LEABHARLANN CHOLÁISTE NA TRÍONÓIDE, BAILE ÁTHA CLIATH | TRINITY COLLEGE LIBRARY DUBLIN
Ollscoil Átha Cliath | The University of Dublin

Terms and Conditions of Use of Digitised Theses from Trinity College Library Dublin

Copyright statement

All material supplied by Trinity College Library is protected by copyright (under the Copyright and Related Rights Act, 2000 as amended) and other relevant Intellectual Property Rights. By accessing and using a Digitised Thesis from Trinity College Library you acknowledge that all Intellectual Property Rights in any Works supplied are the sole and exclusive property of the copyright and/or other IPR holder. Specific copyright holders may not be explicitly identified. Use of materials from other sources within a thesis should not be construed as a claim over them.

A non-exclusive, non-transferable licence is hereby granted to those using or reproducing, in whole or in part, the material for valid purposes, providing the copyright owners are acknowledged using the normal conventions. Where specific permission to use material is required, this is identified and such permission must be sought from the copyright holder or agency cited.

Liability statement

By using a Digitised Thesis, I accept that Trinity College Dublin bears no legal responsibility for the accuracy, legality or comprehensiveness of materials contained within the thesis, and that Trinity College Dublin accepts no liability for indirect, consequential, or incidental, damages or losses arising from use of the thesis for whatever reason. Information located in a thesis may be subject to specific use constraints, details of which may not be explicitly described. It is the responsibility of potential and actual users to be aware of such constraints and to abide by them. By making use of material from a digitised thesis, you accept these copyright and disclaimer provisions. Where it is brought to the attention of Trinity College Library that there may be a breach of copyright or other restraint, it is the policy to withdraw or take down access to a thesis while the issue is being resolved.

Access Agreement

By using a Digitised Thesis from Trinity College Library you are bound by the following Terms & Conditions. Please read them carefully.

I have read and I understand the following statement: All material supplied via a Digitised Thesis from Trinity College Library is protected by copyright and other intellectual property rights, and duplication or sale of all or part of any of a thesis is not permitted, except that material may be duplicated by you for your research use or for educational purposes in electronic or print form providing the copyright owners are acknowledged using the normal conventions. You must obtain permission for any other use. Electronic or print copies may not be offered, whether for sale or otherwise to anyone. This copy has been supplied on the understanding that it is copyright material and that no quotation from the thesis may be published without proper acknowledgement.

Optimization of Vehicle Front Shape for Pedestrian Protection

Guibing Li, BENG., MSC.

A thesis submitted to the University of Dublin, Trinity College in partial fulfilment of the requirements for the degree of

Doctor of Philosophy

2017

Supervisor

Dr. Ciaran K. Simms

Co-Supervisor

Dr. Jikuang Yang

Internal Examiner

Dr. Gareth J. Bennett

External Examiner

Dr. Jason R. Kerrigan

TRINITY COLLEGE DUBLIN
18 JAN 2017
ACADEMIC REGISTRY
PhD
ENGINEERING

TRINITY LIBRARY
0 8 MAR 2017
DUBLIN

Thesis 11256

Declaration

I declare that this thesis has not been submitted as an exercise for a degree at this or any other university and it is entirely my own work.

I agree to deposit this thesis in the University's open access institutional repository or allow the library to do so on my behalf, subject to Irish Copyright Legislation and Trinity College Library conditions of use and acknowledgement.

Signature:

Date:

Abstract

The design of a vehicle front has a significant influence on pedestrian injury risk in the event of a vehicle collision. Although significant progress has been made in understanding which features of vehicle design are crucial for minimizing pedestrian injuries, an optimal vehicle design has not been achieved. A particular challenge is that the range of real world accident scenarios is not considered in current assessments of vehicle pedestrian safety performance. Therefore this thesis sets out to develop and evaluate an efficient and reliable approach for the assessment and optimization of vehicle front shape to reduce overall pedestrian injury risk.

The detailed effects of vehicle front shape on pedestrian injury risk were firstly observed from accident data in the German In-Depth Accident Study (GIDAS) database. The results show that the bumper shape and bonnet leading edge height relative to the hip joint have a significant influence on the injury risk of a pedestrian's leg and pelvis, respectively. These estimated effects vary with impact speed and pedestrian age. The influence of vehicle shape on thorax and head injury outcome is less clear. This study also provides real world evidence for evaluating whether the predicted safer vehicle front shapes in optimizations could match the observations in accidents.

The effects of pedestrian gait stance on lower limb kinematics and injury risk were investigated via finite element (FE) and multi-body simulations. The gait analysis results indicate that the lower extremity injury severity of the pedestrian is highly dependent on the gait stance at impact. In particular, the lower extremity of an adult pedestrian has a lower injury risk when its knee is flexed, and the injury risk of the leg is increased when self-contact between the left and right legs occurs.

A virtual test system (VTS) was developed to assess the pedestrian risk of a vehicle front design, based on multi-body simulations and real world pedestrian accident data. This proposed VTS consists of a simulation test sample (STS) for modelling vehicle-to-pedestrian collisions considering a broad range of impact configurations and an injury weighting system (IWS) for measuring the threat of a vehicle front design to pedestrians by weighting the relative frequency

of each impact configuration (represented by a multi-body impact simulation) in real accidents. By defining a weighted injury number (WIN) as the resultant output, the proposed VTS can predict the general injury distribution as a function of pedestrian body region and size, and vehicle impact speed and type in real accidents. The VTS can also significantly distinguish the risk between different vehicle front types (sedan versus sport utility vehicle (SUV) and van) and also shows substantial risk differences for altered shapes within each vehicle type. An STS size of 60 was then selected for front optimization based on the combined consideration of capability of representing the impact configurations and predicting the injury distributions and computational time. The VTS provides a basic approach which can then be employed for vehicle front shape optimization for pedestrian protection.

An optimization framework was then developed based on the approaches proposed in the VTS study and a geometric chain was used to represent the vehicle front in a parametric manner. This optimization framework is a computational system using MADYMO and MATLAB software. A weighted injury cost (WIC) was defined as the fitness function (objective) of the optimization, and this accounted for the medical and auxiliary costs of an injury and the relative frequency of each impact configuration in accidents. A genetic algorithm (GA) was used to find the optimal vehicle shapes based on the predicted WIC values.

The optimal (lowest WIC), 'good' (best 25%) and 'poor' (worst 25%) vehicle front shapes for pedestrian injury minimization were then predicted for sedans, SUVs and vans. The predictions of the optimization framework are generally plausible from the biomechanics and kinematics perspectives. In particular, evidence supporting the results of the sedan optimization was observed from the GIDAS accident data, where the predicted 'good' shapes and 'poor' shapes performed correspondingly in the accidents. The results suggest that it is feasible to apply the proposed optimization framework for vehicle front shape design for pedestrian protection. Sensitivity studies on the effects of the fitness function of the optimization framework on its outputs indicate that the optimal/'good' vehicle front shapes are affected by the impact speed and head injury criterion used in the optimization framework, but in general the needs for leg and head protection are not strongly conflicting and there is clear potential for a vehicle fleet

with a substantially safer front shape.

In conclusion, an optimization framework for vehicle front shape optimization for pedestrian protection was developed, and this considers a broad range of pedestrian impact configurations and their distributions in accidents, injuries from different body regions and ground contacts and the weighting of predicted injuries. This framework is computationally efficient and biomechanically reliable for the optimization of vehicle front shape for pedestrian protection. The findings of the current work provide a useful basis for future vehicle front shape design with the purpose of mitigating overall pedestrian injury risk.

Acknowledgement

This study was sponsored by a Scholarship from the Faculty of Engineering, Mathematics & Science of Trinity College Dublin and the China Scholarship Council (CSC).

I would like to thank all those who have helped and supported me throughout this research. First and foremost, I would like to express my earnest gratitude to my supervisor Dr. Ciaran Simms for his expert guidance, encouragement and continued support. Ciaran always gave me the most rapid and useful feedback in the work. It is my pleasure to have the opportunity to do my PhD study under Ciaran's supervision and I look forward to continuing work with him in the future. I would like to sincerely thank my co-supervisor Dr. Jikuang Yang for his help throughout my academic study since 2009. He was always available to offer suggestions and advice on my research work and life. I hope we can continue our relationship in the future.

I would like to thank Prof. Hongwu Huang from Xiamen University of Technology, China for the great help in applying the CSC funding, Prof. Dietmar Otte from the Medical University of Hannover, Germany for the in-depth pedestrian accident data, Dr. Mirko Junge from Volkswagen, Germany for assistance with the GIDAS data interpretation, Dr. Joe Condon from the Dublin Institute of Technology, Ireland and Dr. Mathew Lyons from Edinburgh Royal Infirmary, UK for advice on statistical analysis, and Tom Daniel, Dan Larner and Atul Gupta from Google[x], US for advice on impact scenario selection.

I also would like to thank all of the staff in the department, and everyone who shared the office with me over the course of my study: Diarmuid, Feng, Gerard, Greg, Mathew, Melika, Michael Gibbons, Michael Takaza, Richard and Rudi.

Finally, I would like to thank my family and friends, they have always been on my side and supportive. I would like to give the most sincere gratitude to my wife, Ting, for her continued company, concern, support and everything she has done for me.

Content

Abstract ..... **I**

Acknowledgement ..... **V**

Content ..... **VII**

List of Figures ..... **XV**

List of Tables ..... **XXV**

Publications ..... **XXVII**

Glossary ..... **XXIX**

Chapter 1 Introduction **1**

1.1 Background 1

1.2 Objective and approaches 2

1.3 Contributions 5

Chapter 2 Literature Review **7**

2.1 Pedestrian accidents and injury epidemiology 7

2.1.1 Overview of pedestrian accidents 7

2.1.2 Distribution of pedestrian injuries by body region 8

2.1.3 Distribution of pedestrian injuries by impact source 9

2.1.4 Distribution of vehicle type 10

2.1.5 Distribution of vehicle impact speed 12

2.1.6 Distribution of pedestrian age, height and sex 13

2.1.7 Distribution of pedestrian motion 13

2.2 Pedestrian injury biomechanics and criteria 14

2.2.1 Head injury 15

2.2.1.1 Head injury biomechanics 15

2.2.1.2 Head injury criteria 17

2.2.2 Thorax injury 20

2.2.2.1 Thorax injury biomechanics 20

2.2.2.2 Thorax injury criteria 21

2.2.3 Pelvis injury 23
2.2.3.1 Pelvis injury biomechanics 23
2.2.3.2 Pelvis injury criteria 23
2.2.4 Lower extremity injury 24
2.2.4.1 Lower extremity injury biomechanics 24
2.2.4.2 Lower extremity injury criteria 26
2.3 Pedestrian kinematics and injury research techniques 29
2.3.1 Cadaver and dummy tests 29
2.3.2 Subsystem test 31
2.3.3 Numerical simulation 33
2.3.3.1 Multi-body modelling 33
2.3.3.2 Finite element (FE) modelling 36
2.4 Fundamental considerations of pedestrian protection 38
2.4.1 Pedestrian characteristics 39
2.4.1.1 Pedestrian age, sex and height 39
2.4.1.2 Pedestrian walking speed and gait stance 40
2.4.2 Vehicle characteristics 41
2.4.2.1 Vehicle impact speed 41
2.4.2.2 Vehicle front stiffness 41
2.4.2.3 Vehicle front shape 43
2.4.3 Ground impacts 46
2.5 Optimization on vehicle front design 47
2.6 Summary 49
Chapter 3 Detailed Effects of Sedan Front Shape on Pedestrian Injury Risk Observed from In-depth Accident Data 53
3.1 Introduction 53
3.2 Methods 54
3.2.1 Accident data 54
3.2.2 Sedan front profiles 55

3.2.3 Potential relationships 55
3.2.4 Statistical analysis 58
3.2.4.1 Detection of multicollinearity 58
3.2.4.2 Logistic regression 63
3.3 Logistic regression results 64
3.3.1 Bumper vs AIS2+ lower extremity injury risk 64
3.3.2 Bonnet Leading Edge (BLE) vs AIS2+ femur/pelvis injury risk 68
3.3.3 BLE and bonnet vs AIS3+ thorax injury risk 70
3.3.4 BLE, bonnet and windscreen vs AIS3+ head injury risk 71
3.4 Discussion 73
3.4.1 Injury risk estimated by the logistic regression 73
3.4.2 Effects of bumper profile on lower extremity injury risk 73
3.4.3 Effects of bonnet leading edge profile on femur/pelvis injury risk 76
3.4.4 Upper body injuries 77
3.5 Summary 78
Chapter 4 Effects of Pedestrian Gait Stance on Lower Extremity Kinematics and Injury Risk 81
4.1 Introduction 81
4.2 FE simulation 82
4.2.1 FE human body model 82
4.2.2 Vehicle front FE models 83
4.2.3 Setup for FE simulation 85
4.2.4 Injury assessment metrics 85
4.2.5 FE simulation results 86
4.2.5.1 Lower extremity overall kinematics 86
4.2.5.2 Von-Mises stress in the tibia and femur 87
4.2.5.3 Relationship between bone stress and gait stance 89
4.2.5.4 Knee lateral shearing displacement and bending angle 89
4.2.6 Discussion for FE simulation 90

4.2.6.1 Gait effects on tibia loading 91
4.2.6.2 Gait effects on knee reaction 93
4.2.6.3 Gait effects on femur loading 95
4.2.6.4 Knee flexed effects on internal/external rotation 96
4.3 Multi-body simulation 97
4.3.1 Multi-body pedestrian and vehicle models 97
4.3.2 Setup of multi-body simulations 98
4.3.3 Multi-body simulation results 99
4.4 Summary 102
Chapter 5 A Virtual Test System for Assessing Vehicle Front Safety Performance 105
5.1 Introduction 105
5.2 Accident data 106
5.2.1 Accident distribution 106
5.2.2 Injury distribution 107
5.3 Virtual Test System (VTS) 110
5.3.1 Simulation Test Sample (STS) 110
5.3.2 MADYMO pedestrian models 112
5.3.3 Injury Weighting System (IWS) 114
5.3.3.1 Injury number 114
5.3.3.2 Weighting the injury number 115
5.4 Setup of vehicle-to-pedestrian impact simulation 117
5.4.1 Vehicle models tested using the STS 117
5.4.2 Vehicle-to-pedestrian impact modelling 119
5.5 Evaluation of VTS using GIDAS data 119
5.5.1 Setup of STS 119
5.5.2 Combined Injury Number (CIN) 123
5.5.3 Comparison results between VTS and GIDAS 123
5.5.4 Computational time 128
5.5.5 Selection of the STS for optimization 129

5.6 Evaluation of VTS using PCDS data 132
5.6.1 Inputs data 132
5.6.2 Comparison between VTS and PCDS 134
5.7 Sensitivity of WIN to vehicle shape 136
5.7.1 Setup of the sensitivity study 136
5.7.2 Sensitivity study results and discussion 137
5.8 Summary 138
Chapter 6 A Framework for Optimizing Vehicle Front Shape 141
6.1 Introduction 141
6.2 Impact configurations 141
6.3 Vehicle model 143
6.4 Vehicle-to-pedestrian impact simulation 144
6.5 Weighted Injury Cost (WIC) 145
6.6 Optimization method 148
6.7 Optimization process 149
6.7 Summary 150
Chapter 7 Optimization of Vehicle Front Shape 151
7.1 Introduction 151
7.2 Methods 151
7.2.1 Design spaces 151
7.2.2 Setup of the optimizations 152
7.2.2.1 Population size 152
7.2.2.2 Crossover fraction 153
7.2.2.3 Stopping criterion 155
7.3 Optimization results 156
7.3.1 Sedan 156
7.3.1.1 Convergence of the optimization 156
7.3.1.2 Optimal sedan front shape 158
7.3.1.3 The 'good' and 'poor' sedan shapes 159

7.3.2 SUV 161
7.3.2.1 Convergence of the optimization 161
7.3.2.2 Optimal SUV front shape 162
7.3.2.3 The 'good' and 'poor' SUV shapes 163
7.3.3 Van 164
7.3.3.1 Convergence of the optimization 164
7.3.3.2 Optimal van front shape 166
7.3.3.3 The 'good' and 'poor' van shapes 167
7.4 Discussion 168
7.4.1 Feasibility of the optimization framework 168
7.4.2 Sedan front shape optimization 171
7.4.2.1 Optimal sedan front shape 171
7.4.2.2 The 'good' and 'poor' sedan designs 178
7.4.3 SUV front shape optimization 183
7.4.3.1 Optimal SUV front shape 183
7.4.3.2 The 'good' and 'poor' SUV designs 186
7.4.4 Van front shape optimization 190
7.4.4.1 Optimal van front shape 190
7.4.4.2 The 'good' and 'poor' van front shapes 193
7.5 Summary 196
Chapter 8 Effects of the Fitness Function on the Optimal Sedan Front Shape 199
8.1 Introduction 199
8.2 Methods 199
8.2.1 Risk of permanent medical impairment (RPMI) 199
8.2.2 GAMBIT head injury criterion 200
8.3 Results 202
8.3.1 Optimization using the WRPMI 202
8.3.3 Optimization using the GAMBIT 203
8.4 Discussion 205

8.4.1 WRPMI vs WIC.....205
8.4.2 GAMBIT vs HIC.....207
8.5 Summary.....214
Chapter 9 General Discussion.....217
9.1 Effects of vehicle front shape on pedestrian injury risk.....218
9.2 Pedestrian gait stance study.....223
9.3 Virtual test system (VTS).....224
9.4 Optimization framework and its applications.....227
9.4.1 Optimization framework.....227
9.4.2 Applications of the optimization framework.....230
9.4.2.1 Feasibility of the optimization framework.....230
9.4.2.2 Considerations in the optimization framework.....237
9.4.2.3 Comparison of vehicle front shape optimizations from different studies.....243
Chapter 10 Conclusions and Future Work.....247
10.1 Conclusions.....247
10.2 Further work.....249
References.....253
Appendix.....267

List of Figures

Figure 1.1 Thesis structure....3

Figure 2.1 Distribution of pedestrian AIS2+ injuries as body region for different countries, adapted from (Hu and Klinich, 2012)....9

Figure 2.2 Vehicle types in pedestrian accidents, adapted from (Mizuno and Kajzer, 2000)....11

Figure 2.3 Front shape corridors for different vehicle classes, adapted from (Mizuno and Ishikawa, 2003)....11

Figure 2.4 Impact speed distribution (a) and cumulative frequency (b) for different countries, adapted from (Mizuno, 2005)....12

Figure 2.5 Anatomy of human head: bony structure (top), the brain and meninges (bottom), adapted from (Netter and Carios, 2003)....15

Figure 2.6 WSTC head injury tolerance curve, adapted from (Lissner et al., 1960)....17

Figure 2.7 Thoracic anatomy, adapted from (Netter and Carios, 2003)....21

Figure 2.8 AIS2+ injuries as functions as TTI values, adapted from (Cavanaugh et al., 1993). 22

Figure 2.9 Anatomy of the human pelvis, adapted from (Sobotta, 1997)....23

Figure 2.10 Anatomy of the lower extremity skeleton (a), adapted from (Sobotta, 1997) and the knee joint (b), adapted from (Tandeter et al., 1999)....25

Figure 2.11 Knee injury criteria for different impact velocities, adapted from (Mo et al., 2014). 29

Figure 2.12 Global kinematics of pedestrian in PMHS test, adapted from (Kerrigan et al., 2005). 30

Figure 2.13 Pedestrian dummies: (a) RSPD (Aldman et al., 1985), (b) Polar-II (Akiyama et al., 2001), Chalmers-Autoliv (c) adult (Björklund and Zheng, 2001) and (d) child (Renaud and Tapia, 2004)....31

Figure 2.14 EEVC subsystem impactor test methods, adapted from (EEVC, 2002)....32

Figure 2.15 Multi-body pedestrian models: (a) CPM, (b) MADYMO ellipsoid models....35

Figure 2.16 Facet pedestrian human body model (a), adapted from (MADYMO, 2012) and lower extremity segment model (b), adapted from (Kerrigan et al., 2009b)....36

Figure 2.17 Human body FE pedestrian models: (from left to right) original THUMS (Maeno and Hasegawa, 2001), THUMS version 4.0 (AF05, AM50 and AM95) (Toyota Motor Corporation, 2011), H-model^{TM} (Dokko et al., 2003) and HBMP (Li et al., 2014). 38

Figure 2.18 Simplified average force deflection curves and ±1 standard deviation corridors for different vehicle front areas, adapted from (Martinez et al., 2007). 43

Figure 2.19 Frontal shapes of sedan bumper, adapted from (Otte and Haasper, 2007)..... 44

Figure 3.1 Sedan front shape parameters defined in this study. 55

Figure 3.2 Distribution of AIS2+ injuries as a function of vehicle contact location for different body regions for the analysis sample. 57

Figure 3.3 AIS2+ lower extremity injury risk as a function of BLD and BUH for different speed and age levels. 66

Figure 3.4 AIS2+ lower extremity injury risk as a function of BLH and BUH for different speed and age levels. 67

Figure 3.5 AIS2+ lower extremity injury risk as a function of NBLH and NBUH for different speed and age levels 68

Figure 3.6 AIS2+ femur/pelvis injury risk as a function of NBLEH for different speed and age levels. 70

Figure 3.7 Probability of an AIS2+/AIS3+ injury as a function of the combined predictor. 73

Figure 3.8 Typical loading condition for pedestrian lower extremity when struck by sedan bumper. 75

Figure 3.9 Linear regression between the NBLEH and BLEH. 77

Figure 4.1 THUMS Version 4 AM50 pedestrian model and stances for pedestrian gait study, in simulations the pedestrian was struck from the right lower extremity (dark red). 83

Figure 4.2 Impact simulation of vehicle front FE models to THUMS: (a) sedan-to-THUMS, (b) SUV-to-THUMS. 84

Figure 4.3 Geometric constructions used to assess knee lateral bending and shearing. 86

Figure 4.4 Typical pedestrian global kinematics in (a) sedan and (b) SUV impact (10% gait stance). 87

Figure 4.5 The location and timing of maximum von-Mises stress in the tibial and femoral cortical

bone in the ipsilateral and contralateral lower extremity for (a & b) sedan and (c & d) SUV impact. The 10% gait stance is shown, and for each bone the maximum stress and the time of the maximum stress are shown separately for the proximal, shaft and distal regions. 88

Figure 4.6 Maximum von-Mises stress in the tibia and femur cortical bone in the ipsilateral and contralateral lower extremity for sedan (a & b) and SUV (c & d) impacts 89

Figure 4.7 Maximum knee shearing displacement and bending angle in the ipsilateral and contralateral knee in impact against (a & b) sedan and (c & d) SUV. 90

Figure 4.8 Kinematics of pedestrian in sedan impact for the (a) 25% and (b) 75% gait stances. 92

Figure 4.9 Kinematics of pedestrian in SUV impact for the 75% gait stance. 93

Figure 4.10 The change of knee flexion/extension and internal/external rotation angle as functions of knee initial flexed angle in the ipsilateral and contralateral lower extremity in impacts against: (a) sedan, (b) SUV. 94

Figure 4.11 Knee lateral bending moment as functions of the change of knee flexion/extension and internal/external rotation angle in the ipsilateral and contralateral lower extremity in impacts against: (a) sedan, (b) SUV. 95

Figure 4.12 Femur loading in (a) sedan impact and (b) SUV impact 96

Figure 4.13 Knee internal/external rotation simulation (a) and linear regressions between knee axial torque and knee flexion angle (b) 97

Figure 4.14 Multi-body vehicle-to-pedestrian impact simulation models (red lines show the centre-line shape of FE vehicle front models, see Figure 4.2). 98

Figure 4.15 MADYMO 50th% male pedestrian model in different gait stances, in simulations the pedestrian is struck from the right lower extremity (dark red). 98

Figure 4.16 Multi-body simulation results of the ipsilateral lower extremity for different pedestrian gait stances 100

Figure 4.17 Comparison of predicted injury risk for the ipsilateral lower extremity between multi-body and FE simulations. 101

Figure 5.1 Distribution of impact speed and vehicle class for the GIDAS and PCDS data 107

Figure 5.2 Distribution of impact direction and initial contact location in the GIDAS data. 107

Figure 5.3 Diagram of different centre area widths for a midsize sedan 107

Figure 5.4 Distribution of AIS2+ injuries as functions of pedestrian body region, vehicle class and impact speed for the GIDAS and PCDS data. 109

Figure 5.5 MADYMO pedestrian models of different sizes. 113

Figure 5.6 Distributions of impact speed, pedestrian height (GIDAS) and gait stance (assumed uniform distribution) for a STS 116

Figure 5.7 Vehicle models (Crocetta et al., 2015) vs 50^{th}% male model. 118

Figure 5.8 Force/deformation curves of contact characteristics for different vehicle structures. 119

Figure 5.9 Comparisons of AIS2+ injury distributions as pedestrian body region and height between VTSs and GIDAS data 124

Figure 5.10 Comparisons of AIS2+ injury distributions as vehicle impact speed and class between VTSs and GIDAS data 125

Figure 5.11 Comparisons of AIS2+ injury rate between VTSs and GIDAS data. 127

Figure 5.12 Relative errors in AIS2+ injury proportion as pedestrian body region and height, and vehicle impact speed and class between VTSs and GIDAS data. 128

Figure 5.13 Relative errors in AIS2+ injury rate between VTSs and GIDAS data. 128

Figure 5.14. Computational time as a function of STS sample size (red for 120 and green for 60). 129

Figure 5.15 Distribution of impact speed, pedestrian height (PCDS) and gait stance (assumed uniform distribution) for VTS-6-5-2/60. 133

Figure 5.16 Comparisons of AIS2+ injury distributions as pedestrian body region and height, and vehicle impact speed and class between VTSs and PCDS data 135

Figure 5.17 Predicted overall WIN (a) and WIN of the head, thorax, pelvis and lower extremity (b) for different vehicle classes 137

Figure 6.1 MADYMO pedestrian models (MADYMO, 2012) and gait stances (Untaroiu et al, 2009). 142

Figure 6.2 Vehicle front model and the geometric dimension chain. 144

Figure 6.3. Vehicle-to-pedestrian impact simulation. 144

Figure 6.5 Whole process of the optimization framework. 150

Figure 7.1 Population of the generation after 10 iterations for the optimizations using different

crossover fraction values. 154

Figure 7.2 Predicted WIC of the generation after 10 iterations for the optimizations using different crossover fraction values. 155

Figure 7.3 Convergence process of the simplified optimizations for different vehicle types. 156

Figure 7.4 Design points of generation 0 (G0), 5 (G5), 10 (G10), and 15 (G15) for the sedan optimization. 157

Figure 7.5 Predicted WIC data for design points (a) and generations (b) in the sedan optimization. 158

Figure 7.6 Optimal sedan front and pedestrian models. 159

Figure 7.7 The 'good' and 'poor' sedan shapes (a) and their corridors (b). 160

Figure 7.8 Design points of generation 0 (G0), 4 (G4), 8 (G8), and 11 (G11) for the SUV optimization. 161

Figure 7.9 Predicted WIC data for design points (a) and generations (b) in the SUV optimization. 162

Figure 7.10 Optimal SUV front model and pedestrian models. 162

Figure 7.11 The 'good' and 'poor' SUV shapes (a) and their corridors (b). 164

Figure 7.12 Design points of generation 0 (G0), 5 (G5), 9 (G9), and 13 (G13) for the van front shape. 165

Figure 7.13 Predicted WIC data for design points (a) and generations (b) in the van optimization. 166

Figure 7.14 Optimal van front model and pedestrian models 166

Figure 7.15 The 'good' and 'poor' van shapes (a) and their corridors (b). 167

Figure 7.16 Changing of the median WIC for different body regions in the sedan (a), SUV (b) and van (c) optimization process. 170

Figure 7.17 Comparisons of the injury cost distribution as a function of body regions between the simulations and GIDAS data for sedan (a) and van (b) impacts 171

Figure 7.18 Predicted WIC as a function of sedan bonnet leading edge height, the points in green show the case for the optimal sedan. 173

Figure 7.19 Predicted head WIC as a function of sedan bonnet length, the points in green show

the case for the optimal sedan.....174
Figure 7.20 Predicted head linear acceleration curves for the 5th% male model struck by sedan fronts with different bonnet lengths.....175
Figure 7.21 Predicted WIC as a function of sedan bonnet angle (a) and windscreen angle (b) for sedan impacts, the points in green show the case for the optimal sedan. 177
Figure 7.22 Comparisons of the optimal sedan fronts (a) and 'good' shape corridors (b) between the optimizations using different impact configurations. 178
Figure 7.23 Comparisons of the predicted WIC as a function of body region, pedestrian size and impact speed between the simulations using a 'good' and 'poor' shape sedan front.....179
Figure 7.24 Comparisons of the pedestrian kinematics between the simulations using a 'good' and 'poor' shape sedan front.....180
Figure 7.25 Comparisons of pedestrian head resultant and perpendicular impact speed between the simulations using a 'good' and 'poor' shape sedan front (the situation for ipsilateral lower extremity forward is shown).....181
Figure 7.26 Comparisons of the head resultant linear acceleration curve for the 5th% male model between the simulations using a 'good' and 'poor' shape sedan front. 182
Figure 7.27 Profiles of the sedans meeting the trends of 'good' and 'poor' shapes predicted by the optimization framework (Figure 7.7) in the GIDAS data (a) and the average injury costs calculated from the cases involved these sedans (b).....183
Figure 7.28 Predicted WIC as a function of SUV bonnet leading edge height, the points in green show the case for the optimal SUV.....184
Figure 7.29 Predicted head and thorax WIC as a function of bonnet angle for SUV impacts, the points in green show the case for the optimal SUV. 186
Figure 7.30 Comparisons of the optimal SUV fronts (a) and 'good' shape corridors (b) between the optimizations using different impact configurations. 186
Figure 7.31 Comparisons of the predicted WIC as a function of body region, pedestrian size and impact speed between the simulations using a 'good' and 'poor' shape SUV front.....187
Figure 7.32 Comparisons of the pedestrian kinematics between the simulations using a 'good' and 'poor' shape SUV front.....188

Figure 7.33 Comparisons of pedestrian head resultant and perpendicular impact speed between the simulations using a 'good' and 'poor' shape SUV front (the situation for ipsilateral lower extremity forward is shown).....189
Figure 7.34 Predicted WIC as a function of van bonnet leading edge height, the points in green show the case for the optimal van.....191
Figure 7.35 Predicted head and thorax WIC as a function of van bonnet length, bonnet angle and windscreen angle for van impacts, the points in green show the case for the optimal van. 192
Figure 7.36 Comparisons of the optimal van fronts (a) and 'good' shape corridors (b) between the optimizations using different impact configurations.....193
Figure 7.37 Comparisons of the predicted WIC as a function of body region, pedestrian size and impact speed between the simulations using a 'good' and 'poor' shape van front. 194
Figure 7.38 Comparisons of the pedestrian kinematics between the simulations using a 'good' and 'poor' shape van front.....195
Figure 7.39 Comparisons of pedestrian head resultant and perpendicular impact speed between the simulations using a 'good' and 'poor' shape van front (the situation for ipsilateral lower extremity forward is shown).....195
Figure 7.40 Comparisons of the head resultant linear acceleration curve for the 5^{th}% male model between the simulations using a 'good' and 'poor' shape van front.....196
Figure 8.1 Predicted WRPMI data for design points (a) and generations (b) in the sedan optimization.....202
Figure 8.2 Optimal sedan front model predicted by the WRPMI and pedestrian models. 203
Figure 8.3 'good' and 'poor' sedan shapes observed based on the WRPMI (a) and their corridors (b). 203
Figure 8.4 Predicted WIC data for design points (a) and generations (b) in the sedan optimization using the GAMBIT. 204
Figure 8.5 Optimal sedan front model predicted using the GAMBIT and pedestrian models. 204
Figure 8.6 'good' and 'poor' sedan shapes observed using the GAMBIT (a) and their corridors (b). 205

Figure 8.7 Predicted weighted injury outcome for different body regions as a function of generation in the optimizations based on the WRPMI (a) and WIC (b).....206
Figure 8.8 Optimal sedan fronts (a) and 'good' sedan front shape corridors (b) predicted by the optimizations based on the WIC and WRPMI. 207
Figure 8.9 Predicted WIC for different body regions as a function of generation in the optimizations using the GAMBIT (a) and HIC (b) as the head injury criterion. 208
Figure 8.10 Optimal sedan fronts (a) and 'good' sedan front shape corridors (b) predicted based on the HIC and GAMBIT.....209
Figure 8.11 Comparison of pedestrian head impact location between impacts with the optimal sedan fronts predicted based on the HIC and GAMBIT.....210
Figure 8.12 Head resultant linear speed curves (a) and head angular speed curves (b) for the optimal sedan fronts predicted based on the HIC and GAMBIT. 212
Figure 8.13 Peak head angular acceleration observed from the impacts with the optimal sedan fronts predicted based on the HIC and GAMBIT.....212
Figure 8.14 HIC (a) and GAMBIT (b) values observed from the impacts with the optimal sedan fronts predicted based on the HIC and GAMBIT.....213
Figure 8.15 Profiles of the sedans meeting the 'good' shapes predicted by the HIC and GAMBIT in the GIDAS data (a) and the average injury costs calculated from the cases involved these sedans (b).....214
Figure 9.1 Pedestrian kinematics when struck by the sedans with a high BUH/BLEH (a) and a lower BUH/BLEH (b). 220
Figure 9.2 Comparisons of the optimal vehicle fronts predicted by the optimization framework and the real world vehicle fleets for the sedan (a), SUV (b) and van (c).....235
Figure 9.3 Different Euro-NCAP ratings for similar shaped sedans.....236
Figure 9.4 Comparisons of the predicted CIC between the original shapes and optimal shapes for the GIDAS (a) and PCDS (b) inputs. 237
Figure 9.5 Predicted WIC for the child model (6YOC) as a function of the generation number in optimizations for sedan (a), SUV (b) and van (b) front shape. 238
Figure 9.6 Comparison of 'good' van shape corridors between optimizations with and without a

consideration of ground contacts.....240

Figure 9.7 Comparison of the optimal sedan fronts predicted from different studies.....245

Figure A.1 Kinematics of different pedestrian models struck by the optimal sedan front at different impact speeds.....271

Figure A.2 Kinematics of different pedestrian models struck by the optimal SUV front at different impact speeds.....274

Figure A.3 Kinematics of different pedestrian models struck by the optimal van front at different impact speeds.....277

List of Tables

Table 2.1 Pedestrian injuries (AIS2+) distribution as body region and vehicle/ground contact for adult and child, adapted from (Mizuno and Ishikawa, 2003).....10

Table 2.2 Head injuries and related injury mechanisms, adapted from (Yang, 2005). 16

Table 2.3 Thresholds for head injuries in different AIS levels, adapted from (Payne and Patel, 2001). 18

Table 2.4 Thorax lateral impact tolerances, adapted from (Viano et al., 1989). 22

Table 2.5 Thresholds for pelvis injuries in different AIS levels (adults only), adapted from (Payne and Patel, 2001).....24

Table 2.6 Human femur bending tolerance, adapted from (Kerrigan et al., 2003a). 26

Table 2.7 Human tibia bending tolerance, adapted from (Kerrigan et al., 2003a).....27

Table 2.8 Human knee bending and shearing tolerance, adapted from (Mo, 2012). 28

Table 3.1 Sedan front profile corridors for the analysis sample. 56

Table 3.2 Samples for analysis of different relationships.....57

Table 3.3 Potential predictors and injury severities concerned in different pedestrian body regions.60

Table 3.4 Multicollinearity detection results. 61

Table 3.5 Multicollinearity detection results for the new set models.....62

Table 3.6 Multicollinearity detection results for interaction terms. 63

Table 3.7 Logistic regression analysis results for model 1-A1.....65

Table 3.8 Logistic regression analysis for model 1-A2. 66

Table 3.9 Logistic regression analysis results for model 1-B.....67

Table 3.10 Logistic regression analysis results for model 2-A1.....69

Table 3.11 Logistic regression analysis results for model 2-A2.....69

Table 3.12 Logistic regression analysis results for model 2-B.....69

Table 3.13 Logistic regression analysis results for model 3-A.....70

Table 3.14 Logistic regression analysis results for model 3-B.....71

Table 3.15 Logistic regression analysis results for model 4-A.....71

Table 3.16 Logistic regression analysis results for model 4-B.....72

Table 3.17 Logistic regression analysis results for model 5-A.....72

Table 3.18 Logistic regression analysis results for model 5-B.....72

Table 4.1 Material properties of the main frames of vehicle front models. 84

Table 5.1 AIS2+ injury rate in the PCDS and GIDAS.....109

Table 5.2 A STS considering 6 impact speeds, 5 pedestrian heights and 4 pedestrian gait stances. 112

Table 5.3 Anthropometry data of the MADYMO pedestrian models.....113

Table 5.4 Injury criteria for AIS2+ injuries of head, thorax, pelvis and lower extremity. 114

Table 5.5 Geometrical dimensions of vehicle fronts, adapted from Crocetta et al. (2015). 118

Table 5.6 Ranges, mean values and involving proportions (p_s) of impact speed in GIDAS for different discrete groups. 120

Table 5.7 Ranges, mean values and proportions (p_h) of pedestrian height in GIDAS and heights of the representing multi-body models for different discrete groups.....121

Table 5.8 Pedestrian gait stances and the estimated proportions (p_g) for different discrete groups. 122

Table 5.9 Mann-Whitney U test results for the effects of STS size on injury predictive capability 130

Table 5.10 Regression analysis results 131

Table 6.1 Input data for the VTS-6-5-2/60 142

Table 6.2 Injury criteria for AIS level of head, neck, thorax, pelvis and lower extremity. 145

Table 6.3 Medical and auxiliary cost as a function of injury severity, adapted from (ISO: 13232-5, 2005).....146

Table 6.4 Permanent partial incapacity determination, adapted from (ISO: 13232-5, 2005).....147

Table 7.1 Lower and upper limits of vehicle front geometric dimensions for sedan, SUV and van. 152

Table 7.2 Comparison of the dimensions between 'good' and 'poor' sedan shapes. 160

Table 7.3 Comparison of the dimensions between 'good' and 'poor' SUV shapes.....164

Table 7.4 Comparison of the dimensions between 'good' and 'poor' van shapes.....168

Table 8.1 RPMI on 1%+ level, adapted from (Malm et al. 2008).....200

Table 8.2 GAMBIT threshold for different head injury AIS levels.....201

Table A.1 Information for VTSs with different STS sizes (impact scenarios).....267

Publications

Journal publications

Li, G., Yang, J., Simms, C. (2015a). The influence of gait stance on pedestrian lower limb injury risk. *Accident Analysis & Prevention, 85*, 83-92.

Li, G., Yang, J., Simms, C. (2016a). A virtual test system representing the distribution of pedestrian impact configurations for future vehicle front-end optimization. *Traffic Injury Prevention*, 17:5, 515-523.

Li, G., Lyons, M., Wang, B., Yang, J., Otte, D., Simms, C. (2016b). The influence of passenger car front shape on pedestrian injury risk observed from German in-depth accident data. *Accident Analysis & Prevention.* (under review)

Li, G., Yang, J., Simms, C. (2016c). Safer passenger car front shapes for pedestrians: a computational approach to reduce overall pedestrian injury risk in real world accident scenarios. *Accident Analysis & Prevention.* (under review)

Conference full paper/abstracts

Li, G., Yang, J., Simms, C. (2014). Predicting the effects of pedestrian gait on lower limb injuries. IRCOBI Conference Proceedings, 2014, Berlin, Germany. (abstract)

Li, G., Yang, J., Simms, C. (2015b). A fitness function for vehicle front optimization for pedestrian protection accounting for real world collision configurations. IRCOBI Conference Proceedings, 2015, Lyon, France. (abstract)

Li, G., Otte, D., Yang, J., Simms, C. (2016d). Pedestrian injury trends evaluated by comparison of the PCDS and GIDAS databases. IRCOBI Conference Proceedings, Seoul, South Korea. (full paper)

Li, G., Otte, D., Yang, J., Simms, C. (2016e). Can a small number of pedestrian impact scenarios represent the range of real-world pedestrian injuries? IRCOBI Conference Proceedings, Malaga, Spain. (full paper)

Glossary

Term	Definition
ASDH	Acute subdural hematoma (ASDH) is a clot of blood that develops between the surface of the brain and the dura mater.
DAI	Diffuse axonal injury (DAI) is a brain injury in which damage in the form of extensive lesions in white matter tracts occurs over a widespread area.
FMVSS	Federal Motor Vehicle Safety Standards (FMVSS) are U.S. federal regulations specifying requirements for motor vehicles and regulated automobile safety-related components, systems, and design features. The FMVSS 208 is for occupant crash protection and FMVSS 214 is for side impact protection.
HIC	The Head Injury Criterion (HIC) is a measure of the likelihood of head injury arising from an impact.
LTV	Light Truck Vehicle (LTV) is a U.S. classification for trucks or truck-based vehicles, which includes vans, pickups, and sport utility vehicles (SUV).
Multicollinearity	In statistics, multicollinearity (also collinearity) is a phenomenon in which two or more predictor variables in a regression model are highly correlated, meaning that one can be linearly predicted from the others with a substantial degree of accuracy.
NCAP	New Car Assessment Programme (NCAP) is a government car safety program tasked with evaluating new automobile designs for performance against various safety threats.

Chapter 1 Introduction

1.1 Background

More than 1.17 million people are killed worldwide in road traffic accidents each year, and about 65% of injuries are to pedestrians (World Bank Group, 2011). It is predicted that road traffic injuries will rise to become the fifth leading cause of death by 2030 (WHO, 2013). The shape of a vehicle front significantly influences pedestrian injury risk in the event of a vehicle-to-pedestrian collision and much progress has been made in improving vehicle front design for pedestrian protection (Simms and Wood, 2009). However, accident data shows that the current vehicle fleets still pose serious threats to pedestrians in accidents (WHO, 2013). Both active and passive pedestrian protection approaches can help reducing pedestrian injury risk in road traffic accidents. Reducing the stiffness of the vehicle front reasonably and improving the vehicle front shape are the main methods used in passive pedestrian protection (Simms and Wood, 2009). The efficiency of reducing stiffness for pedestrian protection is generally understood and some local optimizations of vehicle front shape have been done for reducing pedestrian injury risk, such as adding a lower bumper structure (secondary bumper) to protect the lower extremity and using a rounded bonnet leading edge to reduce pelvis injury risk (Snedeker et al., 2005; Pinecki and Zeitouni, 2007). However the global effects of the whole vehicle front shape on overall pedestrian injury risk are still not clear, especially when considering a broad range of impact speeds, pedestrian anthropometries and initial positions. Thus an optimized vehicle front shape for pedestrian protection on a population level remains an elusive goal.

Subsystem impactor tests are widely used to evaluate vehicle front design for pedestrian protection in New Car Assessment Programs (NCAP[◊1]) and in legislative tests. However, these approaches only consider limited impact configurations (EEVC, 2002; J-NCAP, 2011;

[1] Words marked with a superscript lozenge (◊) in the text are explained in the Glossary.

Euro-NCAP, 2013; C-NCAP, 2015). These physical test standards are necessarily limited to a small number of conditions to make them practical, but the high variability of real-world pedestrian accidents means it is not clear whether vehicles which perform well in these subsystem tests will also perform well in real accidents. Accordingly, although the subsystem tests are a major advancement, vehicle front optimization for pedestrian protection is likely to be more successful if it is based on the actual distribution of real-world impact configurations rather than on idealized collision scenarios. It is probably not practical to optimize the vehicle front shape for pedestrian protection based on physical impact tests when broad ranges of impact configurations and vehicle front design space are taken into consideration, and numerical simulation is a more promising approach.

With the rapid development of computer technology, numerical simulation using finite element (FE) and multi-body models have become an important tool for researches and development in pedestrian protection and vehicle front design. Many studies have focused on vehicle front shape optimization for pedestrian protection based on the numerical approach (Carter et al., 2005; Subramanian et al., 2012 and 2016; Kausalyah et al., 2014 and 2015). However, none of the vehicle optimization studies considered the effects of impact speed (only one impact speed of 40 km/h was used) and the actual distributions of the impact configurations observed from accident studies even though these are known to greatly influence the kinematics and injuries of pedestrians when struck by vehicles (Simms and Wood, 2006a; Elliott et al. 2012b; Peng et al. 2012a).

1.2 Objective and approaches

Accordingly, the purpose of the current thesis is to derive an efficient numerical approach for vehicle front shape optimization for pedestrian protection accounting for a broad range of real world crash configurations and overall pedestrian injuries, and to use this approach to optimize vehicle front shapes for different vehicle classes for reduction of overall pedestrian injury risk. The current study also aims to develop a further understanding on the effects of impact configurations and vehicle front shape on pedestrian injuries.

To achieve these objectives, pedestrian accidents and injury epidemiology, pedestrian injury biomechanics and prevention knowledge, recent pedestrian accident data, numerical modelling approaches for vehicle-to-pedestrian collisions and global optimization strategy, are employed as research resources. Figure 1.1 shows the structure of the current thesis.

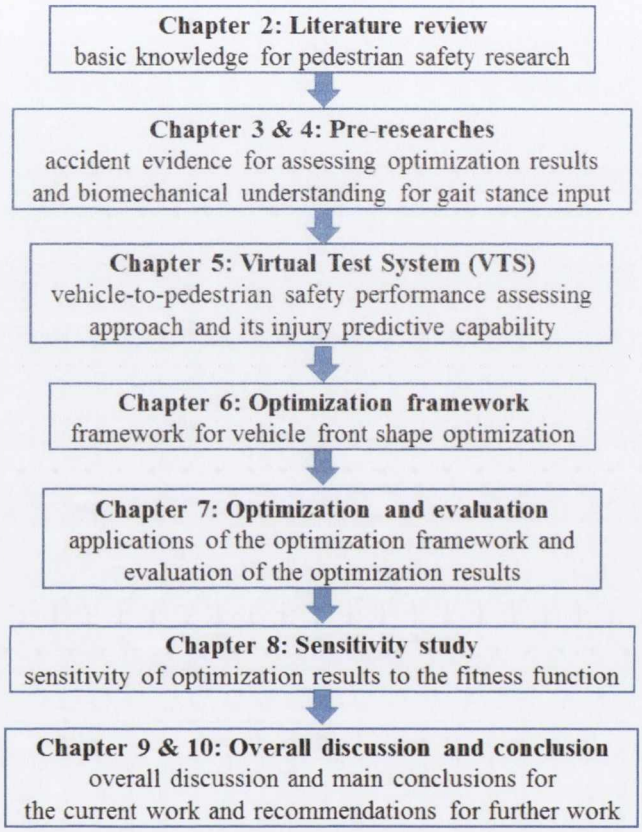

Figure 1.1 Thesis structure.

The detailed content and function of each chapter are summarized as follows:

Chapter 2 summarizes the epidemiology of pedestrian accidents, pedestrian injury biomechanics and criteria, pedestrian safety research techniques, fundamental considerations for pedestrian protection, as well as the state of the art in vehicle front shape optimization for pedestrian protection. This chapter provides with basic biomechanical theory, research approaches and tools, considerations and existing gaps in study of pedestrian protection and vehicle front shape optimization.

Chapter 3 investigates the effects of vehicle front shape on pedestrian injury risk based on

recent in-depth accident data since the quantified relationships between vehicle front geometrical dimensions and pedestrian injury risk in real world accidents are sparse, especially considering the significant recent changes in car front design. The findings of this chapter provide important references for defining vehicle front shape design variables and boundaries for the optimization and evaluating the optimization results (see Chapter 7).

Gait stance has a significant influence on pedestrian head kinematics in vehicle collisions (Untaroiu et al., 2009; Elliott et al., 2012b; Peng et al., 2012b). Thus gait stance is regarded as an important input for vehicle front shape optimization for pedestrian protection, however, its effects on lower extremity injuries are still not clear. Therefore, Chapter 4 conducts finite element (FE) and multi-body simulations to understand how pedestrian gait stance influences lower extremity injury risk. The results of this study help to determine which initial pedestrian gait stances should be included in the optimization (see Chapter 5).

Chapter 5 firstly summarizes pedestrian impact scenarios and injury outcome in real world accidents. According to the accident data, a virtual test system considering a broad range of impact scenarios and their distributions in real world accidents is then proposed to assess the safety performance of a vehicle front shape to pedestrians based on multi-body simulations. The predictions of this virtual test system are evaluated using the corresponding accident data, and a simulation test sample of 60 impact scenarios is then selected for vehicle front shape optimization with the considerations of impact scenarios inclusion (impact speed, pedestrian height and gait stance), injury distribution prediction and computational efficiency. The virtual test system provides basic approaches for assessing the aggressivity of a vehicle front shape in the optimization considering a broad range of pedestrian impact scenarios (see Chapter 6).

Chapter 6 develops a framework for global vehicle front shape optimization for pedestrian protection based on the effective approaches proposed in Chapter 5 in MATLAB and MADYMO environments.

In Chapter 7, the optimization framework defined in Chapter 6 is then applied to optimizations of vehicle front shape for different vehicle classes (sedan, SUV and van). The predictions of the

optimizations are then evaluated by available accident data (e.g. Chapter 3 and Chapter 5), as well as biomechanical and kinematic analyses.

Chapter 8 investigates the influence of the fitness function on the optimization results for the sedan front shape to evaluate the sensitivity of the measuring and weighting methods for predicted injuries to the optimal vehicle front shape.

Chapter 9 makes an overall discussion on the findings observed in the current work and how they link with each other and previous studies.

Chapter 10 summarizes the main conclusions of the current work and recommendations for further work.

1.3 Contributions

First of all this work is the first attempt for overall vehicle front shape optimization for pedestrian protection, which takes into account all major body injuries, a broad range of accident scenarios and which connects back to the available accident data where possible to verify the results. The contributions of this work to the field of vehicle-to-pedestrian safety are summarized as follows:

Firstly, effects of sedan front shape on injury risk to pedestrians' head, thorax, femur/pelvis and lower extremity are estimated based on recent accident data (Chapter 3). This is one of the latest studies on real world pedestrian accidents considering vehicle front shape and the findings may provide useful guidelines for safer vehicle front design. This study is now under review of Accident Analysis & Prevention (Li et al., 2016b, see Publications).

Secondly, according to the study in Chapter 4 we now know how pedestrian gait stance influences lower extremity injury risk and kinematics in vehicle-to-pedestrian collisions. This is the first study on this topic using a set of numerical tests, and further lower extremity protection approaches would be proposed based on the findings. The FE study in Chapter 4 has been published in Accident Analysis & Prevention (Li et al., 2015a, see Publications).

Thirdly, pedestrian impact scenario and injury distributions in German accident data (2000-2015) and US accident data (1994-1998) are summarized in Chapter 5. This study provides useful field information for pedestrian accidents and has been published in proceedings of 2016 Asian conference of International Research Council on Biomechanics of Injury (IRCOBI) (Li et al., 2016d, see Publications).

Fourthly, a novel virtual test system is defined for assessing the threat of a vehicle front design to pedestrians (Chapter 5), which can represent the range of real world accident scenarios, can predict the corresponding distribution of real world injuries and can distinguish the aggressivity between different vehicle front designs. This approach could be considered as a basic guideline for evaluating the performance of a vehicle design for pedestrian protection in future legislative assessment system. The key approach proposed in the virtual test system has been published in Traffic Injury Prevention (Li et al., 2016a, see Publications).

Fifthly, a simulation test sample of 60 impact scenarios is suggested for vehicle front shape optimization for pedestrian protection, based on the application of the proposed virtual test system. This simulation test sample could be employed in further researches on the similar topic. The selection of this reasonable test sample has been published in proceedings of 2016 European conference of IRCOBI (Li et al., 2016e, see Publications).

Finally, a novel framework for overall vehicle front shape optimization for pedestrian protection has been developed in MATLAB and MADYMO environments. This optimization framework is computationally feasible and its predictions for safer sedan design are generally plausible by assessment using available accident data, as well as biomechanical and kinematic analyses. Therefore this optimization framework could be used in future studies on the similar topic and the predictions provide useful guidelines for safer vehicle front shape design for pedestrians. A study of this framework and its application in sedan front shape optimization is now under review of Accident Analysis & Prevention (Li et al., 2016c, see Publications).

Chapter 2 Literature Review

A good understanding of the background of pedestrian injury and protection is crucial for vehicle optimization design with the purpose of reducing pedestrian injury risk. Therefore, this Chapter provides a review of the studies on the epidemiology of pedestrian accidents, pedestrian injury biomechanics and criteria, pedestrian injury and kinematics research techniques, fundamental considerations for pedestrian protection and optimization methods on vehicle front design.

2.1 Pedestrian accidents and injury epidemiology

Real world accidents are the best source to reflect the issues for pedestrian safety, and a good understanding on the epidemiology of pedestrian accidents is the prerequisite of vehicle safety design for pedestrian protection. Pedestrian accidents can happen in various scenarios and lead to different injuries. This section summarizes the main epidemiology that has been observed in the analysis of real world pedestrian accidents. These analyses are mainly based on the following accident database: Advanced Protection Systems (APROSYS), Fatality Analysis Reporting System (FARS), German In-Depth Accident Study (GIDAS), International Harmonized Research Activities (IHRA), Institute for Traffic Accident Research and Data Analysis (ITARDA), In-depth Investigation of Vehicle Accidents in Changsha (IVAC), Pedestrian Crash Data Study (PCDS) and Traffic Administration Bureau of China (TABC).

2.1.1 Overview of pedestrian accidents

The situation of pedestrian accidents varies throughout the world, especially between developed and developing countries. According to a study from the National Highway Traffic Safety Administration (NHTSA), in the U.S nearly 4,500 pedestrians were killed due to motor vehicles related accidents each year from 2009 to 2012, accounting for about 10-14% of traffic accident fatalities (NHTSA, 2012). Statistics from ITARDA show that in Japan pedestrians account for about one third of traffic fatalities in 2010 (ITARDA, 2011). In Europe, about 7,500 pedestrians were killed in road traffic accidents in 2008, which is approximately 20% of all the

traffic fatalities (CARE, 2010). In Australia 2,022 pedestrians were killed in vehicle crashes from 2003 to 2012, accounting for 13.6% deaths of all the road users (ATSB, 2013). These studies indicate that pedestrians account for a big proportion (10%-30%) of traffic accident fatalities in developed countries.

According to the data from the World Health Organization (WHO), in developing countries pedestrians make up a much larger proportion of traffic fatalities than in developed countries (WHO, 2013). As reported by Traffic Administration Bureau of China (TABC), from 2010 to 2015 about 25% of the total traffic fatalities in China were from pedestrians (TABC, 2010-2015). This situation is even more serious in India, where pedestrians account for 42% of traffic accident fatalities in Delhi (Mohan, 2002). As summarized in the book of Simms and Wood (2009), pedestrians account for over 50% of road accident fatalities in Kuwait and Ethiopia and 75% in Ivory Coast.

2.1.2 Distribution of pedestrian injuries by body region

Figure 2.1 shows the distributions of pedestrian AIS[2]2+ (Abbreviated Injury Scale 2-6) injuries as body region for different countries, which were summarized by Hu and Klinich (2012) based on previous studies of accident data (Mizuno, 2005; Yang, 2005; Martin et al., 2011). The head and lower extremities have an obviously higher injury frequency in traffic accidents than other body regions for all countries, followed by the chest and pelvis.

---

[2] Abbreviated Injury Scale (AIS) is an anatomical-based coding system where a scale of one (minor) to six (maximum) is used for representing the threat to life associated with the injury. Injuries can be described as AIS2+ (injuries within the AIS level range from 2 to 6, similarly for AIS1+, AIS3+, etc.) or AIS2-4 (injuries within the AIS level range from 2 to 4).

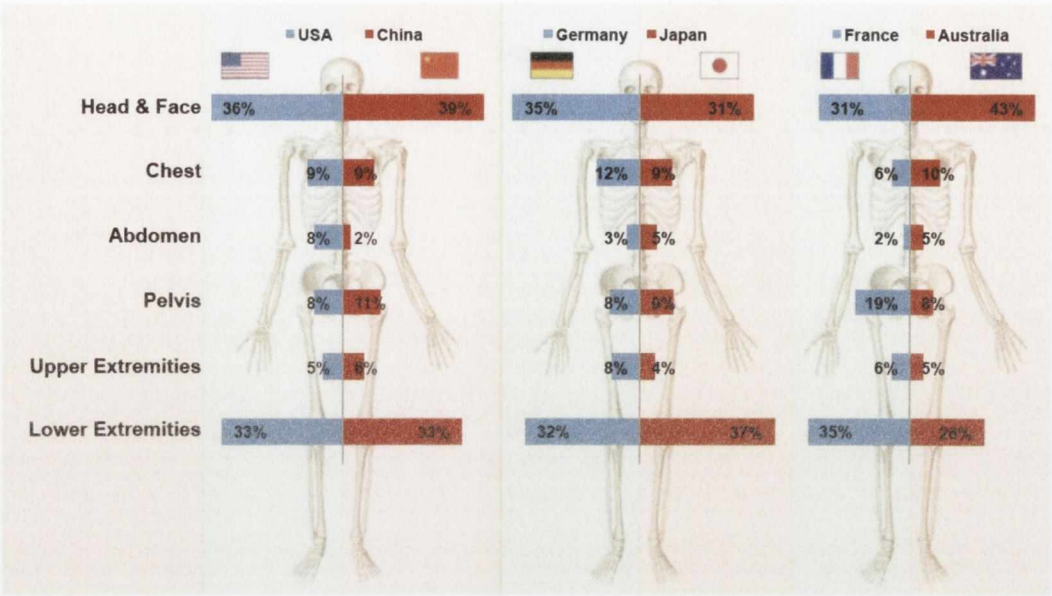

Figure 2.1 Distribution of pedestrian AIS2+ injuries as body region for different countries, adapted from (Hu and Klinich, 2012).

2.1.3 Distribution of pedestrian injuries by impact source

As recorded in the IHRA accident data, nearly 85% pedestrian injuries were due to direct impacts with the vehicle body, in which more than 90% of injuries were attributed to contacts with vehicle front structures (Mizuno and Ishikawa, 2003). However, a previous study of GIDAS data indicates that about 65% of all pedestrians involved in accidents also suffered injuries from the impacts with the ground (secondary impact) (Otte and Pohleman, 2001). For those pedestrians, 38.4% suffered more serious injuries from the impacts with the vehicle (primary impact), about 50% suffered a similar injury severity from the primary and secondary impacts, and 11.2% suffered higher injury severity by secondary impacts (Otte and Pohleman, 2001).

Table 2.1 shows the distribution of pedestrian AIS2+ injuries by body region and vehicle/ground contact in the IHRA data for adults and children. The ratio value indicates the number of AIS2+ injuries from ground impacts divided by that from vehicle impacts for the given body region. It is clear that ground impacts lead to a big proportion of head, face and arm injuries for both adults and children, and ground contact plays a more important role for

children than adults (Mizuno and Ishikawa, 2003). Similar trends were also found in a study based on the APROSYS database (Neal-Sturgess et al., 2007).

Table 2.1 Pedestrian injuries (AIS2+) distribution as body region and vehicle/ground contact for adult and child, adapted from (Mizuno and Ishikawa, 2003).

	Impact	Head	Face	Neck	Chest	Arms	Abdomen	Pelvis	lower extremities
Adult	Vehicle	639	102	17	263	162	149	165	812
	Ground	127	18	2	21	32	2	8	32
	Ratio	0.20	0.18	0.12	0.08	0.20	0.01	0.05	0.04
Child	Vehicle	133	8	3	20	29	11	7	136
	Ground	45	4	0	1	10	0	1	1
	Ratio	0.34	0.50	0.00	0.05	0.34	0.00	0.14	0.01

For injuries resulting from the vehicle structures, IHRA data indicates that about 71% of the AIS2+ lower extremity injuries were from impacts with the vehicle front bumper (Mizuno and Ishikawa, 2003). For the head, about 44% of AIS2+ injuries were caused by contacts with the windscreen, 18% for the windscreen frames and 28% for the top surface of the bonnet/wing. The distribution of impact source for head injuries is different between adults and children. For adults about 67% of AIS2+ head injuries were associated with the windscreen or A-pillar, and 23% with the bonnet top area (including the wing). While most AIS2+ head injuries to children were caused by the bonnet/wing top (53%), only 29% were attributed to the windscreen or A-pillar (Mizuno and Ishikawa, 2003). For the injuries of mid-body regions, the top surface and leading edge of the bonnet/wing are the main vehicle structures for both adult and child (Simms and Wood, 2009).

2.1.4 Distribution of vehicle type

According to a study based on pedestrian accident data from Japan (1992-1996), vehicles involved in pedestrian accidents could be defined as the following types (Figure 2.2): mini-car, sedan (small, medium and large), sports & specialty car, multi-purpose vehicle (MPV), minivan and SUV (Mizuno and Kajzer, 2000). This study also indicates that 'normal' size cars

have the highest frequency resulting in pedestrian fatalities (45%), followed by minivans (25%), while both mini-cars and large vehicles only account for 7% of pedestrian fatalities (Mizuno and Kajzer, 2000). The vehicle type distribution varies between countries. A study of the PCDS database shows that in the U.S 68% of vehicles involved in pedestrian accidents are sedans, 18% are light trucks (pick-up and SUV), and 14% are vans (Klinich and Schneider, 2003). This distribution leads to 63%, 26% and 11% of AIS2+ pedestrian injuries from sedans, light trucks and vans, respectively. Mizuno and Ishikawa (2003) summarized the corridors of vehicle front shape for different vehicle classes based on IHRA data, which show that the front shapes for a given vehicle class vary within a broad geometric range, see Figure 2.3.

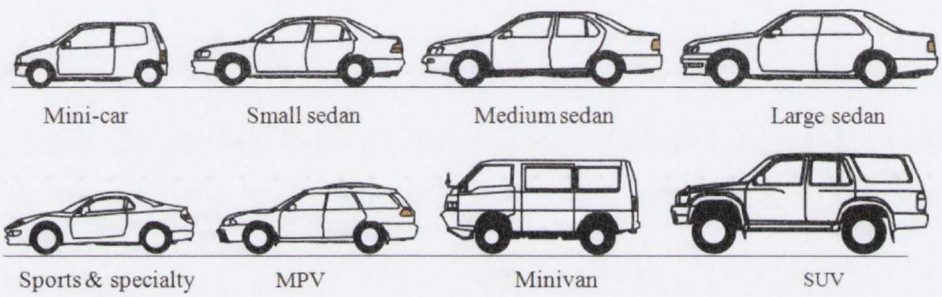

Figure 2.2 Vehicle types in pedestrian accidents, adapted from (Mizuno and Kajzer, 2000).

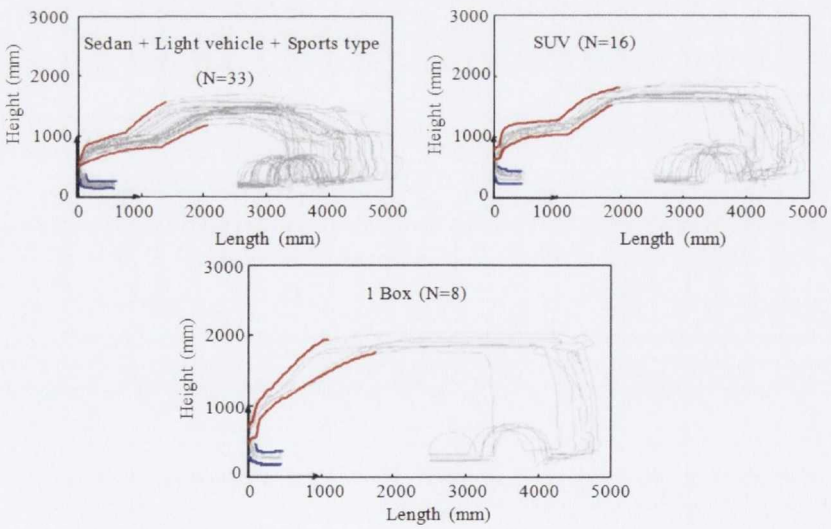

Figure 2.3 Front shape corridors for different vehicle classes, adapted from (Mizuno and Ishikawa, 2003).

According to a study based on three accident databases, vehicle type has a significant influence on pedestrian death risk: pedestrians have significantly higher fatality risk when struck by light truck vehicles (LTV[◊]) than sedans (Lefler and Gabler, 2004). A study using IVAC accident data

(China) indicates that sedan type vehicles are more aggressive to pedestrian's lower extremities than minivans, while the percentage of severe chest injuries for sedan cases (12%) is much smaller than that for minivan collisions (24%) (Li et al., 2012). Another study of the PCDS data shows that LTVs pose higher threats to adult pedestrians than sedans for all body regions (Longhitano et al., 2005). These studies indicate that the change of vehicle geometry (Figure 2.3) may lead to big differences in injury severity and distribution.

2.1.5 Distribution of vehicle impact speed

Figure 2.4 shows the distribution and cumulative frequency of pedestrian accidents as a function of vehicle impact speed for different countries (Mizuno, 2005). Most accidents occurred within the impact speed range from 10 km/h to 50 km/h, and approximately 95% of pedestrian accidents occurred at an impact speed less than 80 km/h. For the U.S. 50% of pedestrian accidents occurred at an impact speed lower than 20 km/h, while this value is 30 km/h for other countries. This difference is probably due to the source of the data where the U.S. data were collected from six urban sites while the data from other countries may cover both urban areas and outskirts.

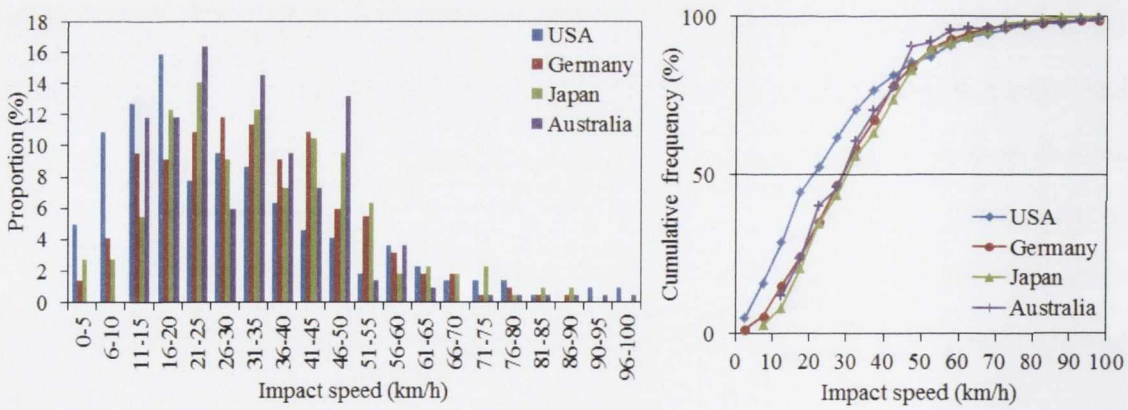

Figure 2.4 Impact speed distribution (a) and cumulative frequency (b) for different countries, adapted from (Mizuno, 2005).

Vehicle impact speed has a strong influence on pedestrian injuries. Nie et al. developed a pedestrian injury risk curve as a function of vehicle impact speed (Nie et al., 2015), based on

accident reconstructions for the IVAC data. Their study indicates that about 60% of pedestrian injuries were caused at impact speeds below 40 km/h, while only about 5% of fatal injuries resulted from this impact speed range and about 60% of fatal accidents occurred at impact speeds below 70 km/h. A study of the APROSYS data (Neal-Sturgess et al., 2007) shows that the average vehicle impact speed for serious pedestrian injuries is 33 km/h, which is much lower than that for the cases resulting in fatal injuries (49 km/h).

2.1.6 Distribution of pedestrian age, height and sex

As recorded in the IHRA accident database, children aged less than 16 years account for about one third of all injured pedestrians, while adults aged between 16 and 60 years account for 47.7% and the old people (60+) account for 21.3% (Mizuno, 2005). The APROSYS pedestrian accident data shows a similar age distribution as the IHRA: 23.4% for pedestrians aged below 16, 45.3% for adults aged 16-60 and 31.3% for adults aged 60+ (Neal-Sturgess et al., 2007). A study of IVAC and GIDAS accident data shows that adults aged below 16 and above 60 account for 7.9% and 9.9% of all injured pedestrians in IVAC respectively, which is significantly lower than that for the GIDAS data (32.5% and 21.4%, respectively) (Yang and Otte, 2007); while pedestrians aged 16-60 account for 82.2% in IVAC, which is about 1.8 times as for GIDAS (46.1%) (Yang and Otte, 2007). The PCDS data shows that pedestrians under 18 years old account for about 30% of accidents, 58% for adults aged 19-65 and 12% for adults aged 65+ (Chidester and Isenberg, 2001).

Data for pedestrian height and sex in accidents is rare in the literature. The PCDS data shows that 22% of pedestrians are with heights of 152 cm or shorter, 39% for 153-168 cm, 33% for 169-183 cm and 6% for 183+ cm (Chidester and Isenberg, 2001). The study of Yang and Otte (2007) indicates that the proportion of male pedestrians (67%) involved in IVAC accidents is obviously higher than that for GIDAS accidents (51.9%).

2.1.7 Distribution of pedestrian motion

Chidester and Isenberg (2001) analysed 521 pedestrian crashes from PCDS data and indicated

that before the impact more than half (55%) of pedestrians were walking, 38% of pedestrians were running, and only 4% of pedestrians were in a stationary situation. A study from Germany shows that 56% of pedestrians were walking when struck by vehicles, 17% were running and only 10% were stationary (Kuehn et al., 2005b). The PCDS data also show that 87% of victims are crossing the road, and most pedestrians (75%) were struck by their left or right side (Chidester and Isenberg, 2001). In the GIDAS database, about 78% of pedestrians were struck laterally, 18% from the front and 4% from the rear (Otte and Haasper, 2005). These studies indicate that most pedestrians were struck from the lateral direction when walking across the road.

For pedestrian walking and running gait stances, no accident data has shown the details. However Chidester and Isenberg (2001) mentioned that 63% pedestrians were with one of their lower extremities forward and both legs with no overlap in the sagittal plane (see Chapter 4 for the detailed gait stances) when struck by vehicles. For the upper extremities orientation, 29% of pedestrians were holding an object in their hand(s) in the accidents, 29% had nothing in their hands and arms, and 29% and 13% were with their arms extended or in other manners respectively (Chidester and Isenberg, 2001). Huang et al. (2008) suggested in their study that pedestrian walking and running speeds for different age groups are in accordance with a normal distribution, and usually children have higher walking or running speed than adults when crossing the road.

2.2 Pedestrian injury biomechanics and criteria

According to the accident data summarized in Section 2.1.2, the head, thorax, pelvis and lower extremity have high injury frequency in pedestrian accidents. Therefore, the injuries to these body regions of a pedestrian are considered in the optimization of this thesis. This section summarizes the studies on injury biomechanics and criteria for the human head, thorax, pelvis and lower extremity, and provides the basic threshold data for assessing pedestrian injury severity in vehicle-to-pedestrian impact simulations.

2.2.1 Head injury

2.2.1.1 Head injury biomechanics

Figure 2.5 shows the basic anatomy of the human head, which is composed of the scalp, skull, meninges and brain from outside to inside (Netter and Carios, 2003). Head injuries include scalp injuries, fractures of the bones (face and skull), laceration and cerebral injuries. In pedestrian accidents skull fractures and cerebral injuries are the most important injuries to the head (Schmitt et al., 2010).

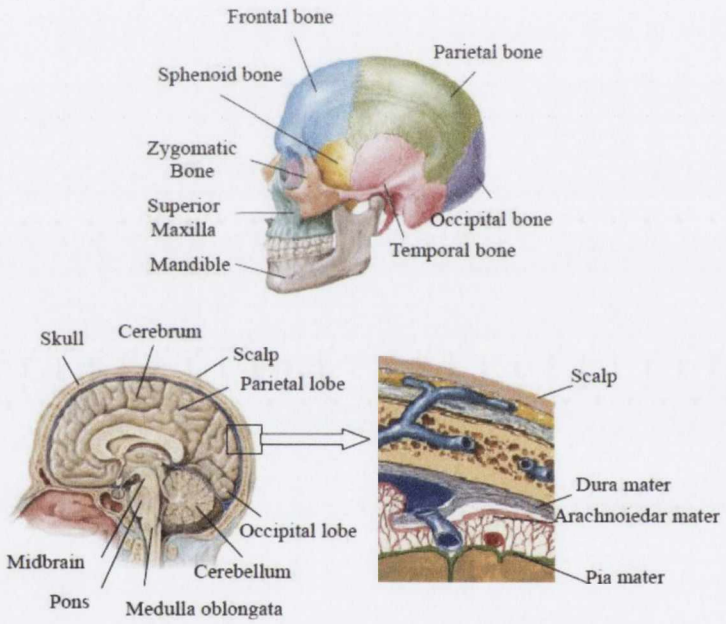

Figure 2.5 Anatomy of human head: bony structure (top), the brain and meninges (bottom), adapted from (Netter and Carios, 2003).

In pedestrian accidents, injuries to the scalp are usually soft tissue injuries, which result in skin bruises, contusion and laceration (Schmitt et al., 2010). But those injuries are not as serious as skull fractures and brain (including the meninges) injuries (Yang, 2005; Schmitt et al., 2010). Skull fractures are divided into basilar and vault fractures. Brain injuries can be classified into two types: diffuse injuries and focal injuries. Diffuse injuries include concussion and diffuse axonal injury (DAI[◊]). Usually, concussion is from a sharp shock or pressure, DAI results from disruption of the axons in cerebral hemispheres and subcortical white matter, focal injuries are caused by localized damage to blood vessels and/or neurological tissue (Schmitt et al., 2010).

Deformation due to direct contact loading is the main mechanism for skull injury, while pressure and shear stress caused by pressure gradients or relative motion between the brain and skull are the major mechanisms for brain injuries (Schmitt et al., 2010), since the brain is an almost incompressible material with high bulk modulus but low shear stiffness (like a gel). Both static and dynamic loadings can cause head injuries. In pedestrian accidents dynamic loading is the main source of head injuries (Schmitt et al., 2010). Dynamic loading can be divided into contact and non-contact loadings. Contact loading is from direct contact of the head with the vehicle structure or the ground in pedestrian accidents, which is the main source of skull fractures. Contact loading may also cause brain injuries by stress waves which can result in a pressure gradient with positive pressure at the struck side and negative pressure to the contralateral side. Inertial forces from acceleration are the source of non-contact loading, which can lead to focal and diffuse brain injuries. Commonly, linear acceleration causes focal brain injury, while rotational acceleration leads to diffuse brain injury (Schmitt et al., 2010). Gennarelli et al. (1972 and 1981) suggested that rotational acceleration plays a dominant role on inducing concussive injuries, diffuse axonal injuries, and subdural hematomas based on tests using live subhuman primates and physical models. They also speculated that these brain injuries may largely be due to shear stress caused by angular acceleration. Table 2.2 shows head injuries and their mechanisms summarized by a previous study (Yang, 2005). Contact force is the source of skull fractures. Diffuse brain injuries are usually from rotational movements, while the causes of focal brain injuries could be contact, acceleration and pressure waves (Yang, 2005).

Table 2.2 Head injuries and related injury mechanisms, adapted from (Yang, 2005).

Head injury		Mechanisms
Skull fracture		Contact forces
Diffuse brain injury	Diffuse axonal injury	Rotational motion
	Concussion	Rotational motion, relative motion of brain to skull
Focal brain injury	Epidural hematoma	Contact force
	Subdural hematoma	Translational and rotational acceleration
	Centre-coup contusion	Contact force and deceleration
	Coup contusion	Contact force

2.2.1.2 Head injury criteria

Figure 2.6 shows the first assessment index for non-penetrating head injuries: the Wayne State Tolerance Curve (WSTC). The WSTC was developed according to a series of tests on cadavers, animals and volunteers. This curve shows the relationship between linear acceleration required for a skull fracture and the duration of the corresponding load. A combination of acceleration and duration located above the curve indicates a high risk of skull fracture, while combinations below the curve means a low risk of skull fracture (Lissner et al., 1960). It is clear from the WSTC that the linear acceleration required for skull fractures for a long duration load is lower than that for a short duration load, see Figure 2.6.

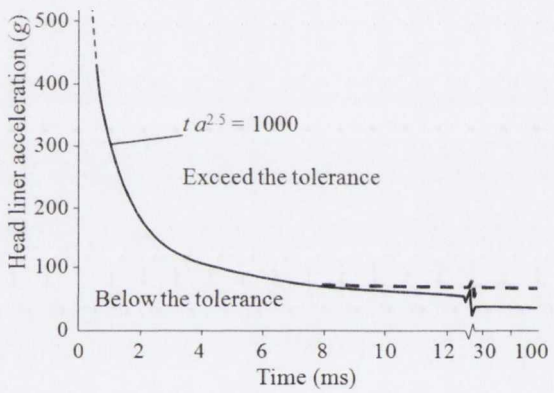

Figure 2.6 WSTC head injury tolerance curve, adapted from (Lissner et al., 1960).

Versace (1971) developed an original version of the HIC◊ and derived the HIC equation based on the WSTC. Then NHTSA proposed a final version of HIC in the subsequent analysis and gave the equation as follows:

$$HIC = max[(t_2 - t_1)\left(\frac{1}{t_2 - t_1}\int_{t_1}^{t_2} a(t)dt\right)^{2.5}], \qquad (2.1)$$

where t_1 and t_2 are two time points in the linear acceleration time history and $a(t)$ is the resultant head linear acceleration. FMVSS 208◊ uses a time window (t_2-t_1) not more than 36 milliseconds (ms) for calculating the HIC. In 1998 NHTSA introduced a time window of 15 ms for the HIC calculation (Kleinberger et al. 1998) and the HIC of 1,000 within a time window of 15 ms is applied by European Experimental Vehicles Committee (EEVC) as the pedestrian

head injury criterion for both adults and children (EEVC, 2002). A study on the relation between skull fracture and HIC value indicated that for adults about 50% of skull fractures occur within a HIC of 1000 (Hertz, 1993). Payne and Patel (2001) proposed HIC thresholds for head injuries in different AIS levels (Table 2.3), which could be applied as main references for assessing head injury severities in later numerical simulations.

Table 2.3 Thresholds for head injuries in different AIS levels, adapted from (Payne and Patel, 2001).

Injury criteria	Injury criteria level	AIS level	Injury level
HIC	<520	1	No fracture
	520-900	2	Linear fracture
	900-1,255	3	Depressed fracture
	1,255-1,575	4	Open fracture
	1,575-1,860	5	Large haematoma
	>1,860	6	Non survivable

Since the HIC only takes linear head acceleration into consideration, a head injury index combining both linear and rotation accelerations was proposed by Newman, which is named Generalized Acceleration Model for Brain Injury Threshold (GAMBIT) (Newman, 1986). Based on the assumption of taking equal weight of the linear and rotation acceleration and using 250 g as the limit of the linear acceleration and 25,000 rad/s^2 as the limit for rotational acceleration, the GAMBIT equation was provided as follows:

$$G(t) = \left(\left(\frac{a(t)}{a_c}\right)^m + \left(\frac{\alpha(t)}{\alpha_c}\right)^n\right)^{\frac{1}{s}}, \tag{2.2}$$

where a and α are defined as the resultant head translational and rotational acceleration time history, respectively, a_c and α_c are thresholds for head translational and rotational acceleration, respectively, and n, m and s are empirical constants selected to fit the available data. A later study proposed values for the parameters in the GAMBIT equation ($n = m = s = 2.5$, a_c=250g, α_c = 25,000 rad/s^2) by fitting the GAMBIT to field accident data (Kramer and Appel, 1990). Since the GAMBIT is a time dependent parameter, the maximum GAMBIT value is used for predicting head injuries and G=1 is set to correspond to a 50% probability of irreversible head

injuries (Newman, 1986; Kramer and Appel, 1990). However the GAMBIT is not used in any regulations due to the lack of validation (Schmitt et al., 2010). A recent study based on simulations using a finite element model of a monkey head suggests that the GAMBIT cannot capture the underlying mechanism for brain stem strain and is not suitable for brain injury prediction (Antona-Makoshi et al., 2013).

Newman et al. (2000) proposed the Head Impact Power (HIP) index, which takes all head motions in six degrees into consideration for assessing brain injury. The *HIP* can be described as follows:

$$HIP = ma_x \int a_x dt + ma_y \int a_y dt + ma_z \int a_z dt + I_{xx}\alpha_x \int \alpha_x dt + I_{yy}\alpha_y \int \alpha_y dt + I_{zz}\alpha_z \int \alpha_z dt, \quad (2.3)$$

where m and I are the mass and moments of inertia for the human head respectively, while a and α are the linear and rotational accelerations of the head respectively. The subscripts show the acceleration and inertial components and the maximum HIP is used as an injury predictor. The HIP was proposed for predicting brain injuries (especially for concussion) and not for skull fractures.

Recently, a kinematically based Brain Injury Criterion (BRIC) was developed for brain injury (Takhounts et al., 2011), which was provided as follows:

$$BRIC = \frac{\omega_{max}}{\omega_{cr}} + \frac{\alpha_{max}}{\alpha_{cr}}, \quad (2.4)$$

where ω_{max} and α_{max} are the maximum resultant head angular velocity and acceleration respectively, and ω_{cr} and α_{cr} are the thresholds for these two parameters respectively. In a later study, Takhounts et al. (2013) proposed another version of BRIC, which was given as follows:

$$BRIC = \sqrt{(\frac{\omega_x}{\omega_{xc}})^2 + (\frac{\omega_y}{\omega_{yc}})^2 + (\frac{\omega_z}{\omega_{zc}})^2}, \quad (2.5)$$

where ω_x, ω_y, and ω_z are the maximum head angular velocities about three different axes respectively, and ω_{xc}, ω_{yc}, and ω_{zc} are the thresholds for these. However, the BRIC, only

considering angular kinematics, was proposed for predicting concussion and DAI and cannot capture skull fractures.

There are some head injury criteria based on finite element (FE) modelling. In 2003 a head injury criterion called SIMon was proposed based on a head finite element (FE) model, which includes a cumulative strain damage measure (CSDM), a dilatational damage measure (DDM) and a relative motion damage measure (RMDM). The CSDM references to DAI, the DDM is for contusions and the RMDM correlates to acute subdural hematoma (ASDH◊) (Takhounts et al., 2003). Another head injury criterion based on a FE head model was proposed by Willinger and Baumgartner at Strasbourg Louis Pasteur University (ULP) called the ULP criterion, which uses the brain von-Mises stress as the index for brain injury (Willinger and Baumgartner, 2003). In 2008, a study investigated the prediction capability of the HIC, HIP, SIMon and ULP head criteria based on reconstructions of the same set of real world human accidents (Marjoux, 2008) using a finite element model. This study suggests that the HIC showed a good prediction of both skull fracture and brain injuries when comparing to accident cases, despite its simplicity.

2.2.2 Thorax injury

2.2.2.1 Thorax injury biomechanics

The thorax is an important part of the human body since serious thorax injuries can result in fatalities. Figure 2.7 shows the anatomy of the human thorax, it includes the rib cage and the interior organs. The ribcage consists of twelve thoracic vertebrae, the sternum, and twelve pairs of ribs. The ribcage structure forms a relatively hard cover around the interior organs, which can protect the organs from external load.

Thoracic injuries can be divided into skeletal injury and soft tissue injury. Skeletal injuries include rib fracture and sternum fracture while soft tissue injuries consist of contusion of bronchus, bronchus tear, lung contusion, heart contusion, lung laceration and aortic laceration (AAAM, 2005). In pedestrian accidents thorax injuries are usually from lateral impacts. The basic mechanisms of thoracic injuries in pedestrian collisions are compression of the ribcage

and viscous loading of the internal soft tissues (Schmitt et al., 2010).

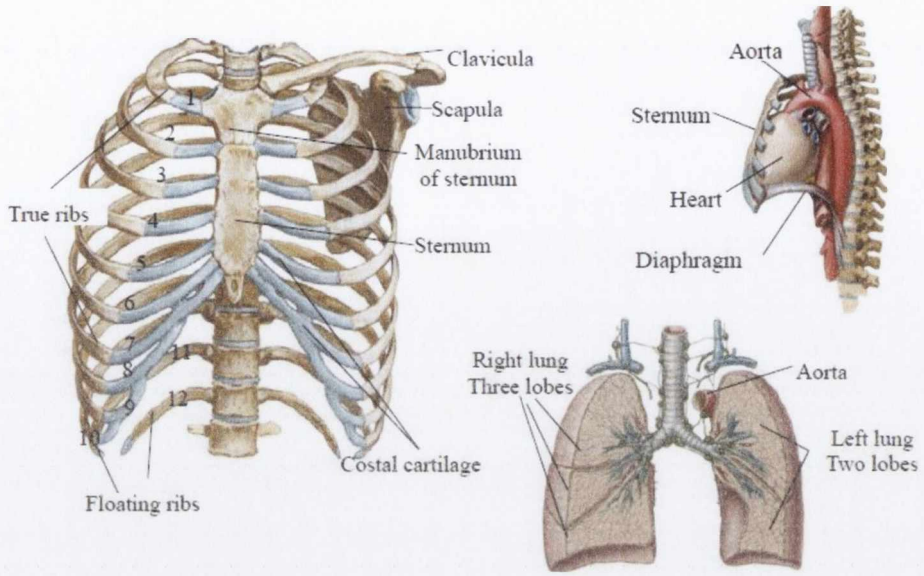

Figure 2.7 Thoracic anatomy, adapted from (Netter and Carios, 2003).

2.2.2.2 Thorax injury criteria

The first thorax injury criterion was proposed in 1984 to assess blunt trauma injuries called Thoracic Trauma Index (TTI) (Eppinger et al., 1984). The TTI is an acceleration criterion which takes account of the age and weight of the test subject as well as the spinal acceleration. The TTI is defined as follows:

$$TTI = 1.4 * age + \frac{1}{2}(RIB_{acc} + T12_{acc})\frac{M}{M_{ref}}, \tag{2.6}$$

where *age* (years) is the age of the subject, RIB_{acc} (g) is the maximum lateral acceleration of the fourth or eighth ribs (depending on which is higher) on the ipsilateral side, $T12_{acc}$ is the maximum lateral acceleration (g) of the twelfth thoracic spine, M (kg) is the subject's mass and M_{ref} (kg) is the reference mass (75 kg as a 50th% adult male). Figure 2.8 shows the TTI values for MAIS2+ thorax injuries observed from cadaver tests (Cavanaugh et al., 1993), which can be applied as an important reference for assessing thorax injury severities.

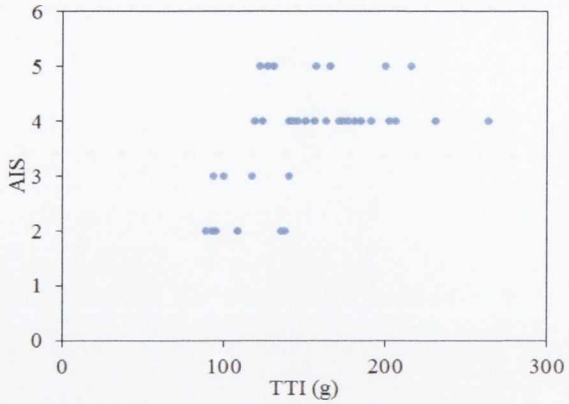

Figure 2.8 AIS2+ injuries as functions as TTI values, adapted from (Cavanaugh et al., 1993).

In 1989 Viano et al. proposed thorax injury functions for viscous response, compression response, spinal acceleration response and force response and corresponding injury criteria named as viscous criterion (VC), compression criterion (C), spinal acceleration criterion (Gsp) and force criterion (F) (Viano et al., 1989). The VC is the instantaneous product of the thorax deformation velocity and thorax compression, which is defined as:

$$VC = V(t) * C(t) = \frac{d[D(t)]}{dt} * \frac{D(t)}{b}, \tag{2.7}$$

where *V(t)* is the velocity of the thorax deformation calculated by differentiation of the deformation *D(t)*, *C(t)* is the rate of thorax deformation calculated as the deformation *D(t)* divided by the initial torso thickness *b*. Gsp is defined as the maximum lateral acceleration measured from the first (T1), eighth (T8) and twelfth (T12) vertebra of the thoracic spine. The force criterion is defined based on the impact force on the thorax. Table 2.4 shows the thresholds of the above four thorax injury criteria for lateral impact (Viano et al., 1989).

Table 2.4 Thorax lateral impact tolerances, adapted from (Viano et al., 1989).

Criteria	Tolerance level	Injury level
Viscous criterion (VC)	1.0 m/s	50% probability of AIS≥3
	1.47 m/s	25% probability of AIS≥4
Compression criterion (C)	Whole thorax 38.4%	25% probability of AIS ≥ 4
Spinal acceleration criterion	T8 45.2 g	25% probability of AIS ≥ 4
(Gsp)	T12 31.6 g	25% probability of AIS ≥ 4
Force criterion (F)	5.5 KN	25% probability of AIS ≥ 4

2.2.3 Pelvis injury

2.2.3.1 Pelvis injury biomechanics

The pelvis connects the upper body by the spine to the lower limbs by the hip joint, with the digestive organs covered within the pelvic ring, see Figure 2.9. The pelvis has two hipbones which form the side and front walls of the pelvic ring, while the coccyx and sacrum form the rear wall. Bone fracture is the main injury of the pelvis, which can be divided into isolated fracture of the pelvic ring, multiple fractures of the pelvic ring and sacrum fracture (Schmitt et al., 2010). Compression is the primary source of pelvis injury. In pedestrian collisions pelvis injuries can be caused by lateral loading, applied to the proximal femur and pelvis, from the contacts with the front structures of a vehicle, such as the bonnet leading edge.

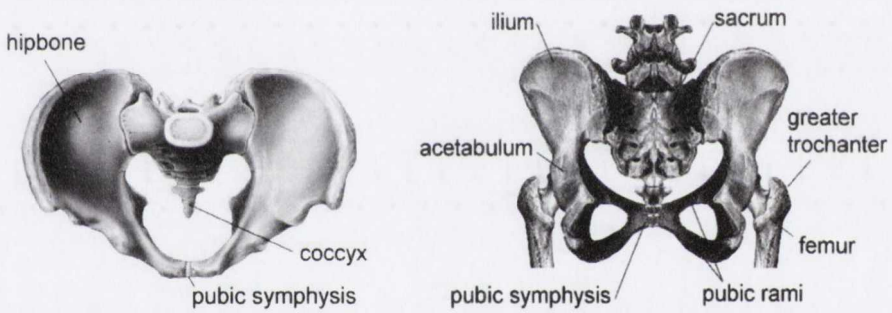

Figure 2.9 Anatomy of the human pelvis, adapted from (Sobotta, 1997).

2.2.3.2 Pelvis injury criteria

Lateral impact force is regarded as the most important index for pelvis injuries. A study of cadaver tests for the pelvis in lateral impacts suggest that the impact force tolerance is 10 kN for the mid-size adult male and 4 kN for the small adult female (Cesari and Ramet, 1982). Payne and Patel (2001) proposed lateral impact force tolerance levels for pelvis injuries (adults only) (Table 2.5), which could be applied as the main reference for assessing pelvis injury severities in numerical simulations.

Another pelvis injury tolerance is a resultant acceleration of 130 g, which was applied in the FMVSS 214$^{\diamond}$ for lateral impact (Haffner, 1985). In the study of Viano et al., the authors

indicated that fracture of the pelvis is associated with compression but not impact force or pelvic acceleration, and proposed a compression of 27% as the pelvic tolerance in lateral impact (Viano et al., 1989).

Table 2.5 Thresholds for pelvis injuries in different AIS levels (adults only), adapted from (Payne and Patel, 2001).

Injury criteria	Injury criteria level	AIS level	Injury level
Pelvis lateral impact force	<4 kN	1	No fracture
	4-6 kN	2-3	Minor pelvis fracture
	6-10 kN	4-5	Major pelvis fracture
	>10 kN	6	Crushed pelvis

2.2.4 Lower extremity injury

2.2.4.1 Lower extremity injury biomechanics

The human lower extremity consists of a skeletal part, ligaments, tendons and soft tissues. The skeletal part includes long bones (femur, tibia and fibula), patella and the bones in the foot (Figure 2.10 (a)). The femur is the upper part of the lower extremity (thigh bone) which links the pelvis to the knee while the leg (tibia and fibula) connects the knee with the foot. The knee is one of the most complicated human body parts, which consists of two joints: the femorotibial joint and the patellofemoral joint (Figure 2.10 (b)). There are four major ligaments in the knee joint: anterior cruciate ligament (ACL), posterior cruciate ligament (PCL), medial collateral ligament (MCL) and lateral collateral ligament (LCL). The LCL and MCL run down the outside and inside of the knee respectively and limit the sideways motion of the knee. The ACL links the front of the tibia to the back of the femoral condyle in the centre of the knee and limits rotation and forward motion of the knee. The PCL links the back of the tibia to the front of the medial femoral condyle and limits rotation and backward motion of the knee (Solomon et al., 2001).

The lower extremity has a very high injury frequency in pedestrian accidents compared to other body regions since it is usually the first contact part for a pedestrian in vehicle-to-pedestrian collisions. Long bone (femur, tibia, and fibula) fractures, knee injuries (ligaments avulsion and

condyle fractures), ankle dislocation and foot bone fracture are the typical lower extremity injuries in pedestrian accidents (Yang, 2005; Schmitt et al., 2010). The main mechanisms of long bone fractures are bending and shearing loads for vehicle impacts, which usually result from the contacts between the pedestrian lower extremity and the vehicle bumper and/or bonnet leading edge (Kerrigan et al., 2003a; Yang, 2005). The main mechanism of knee injuries is the combined effect of bending and shearing loading caused by the vehicle front structures during impacts (Mo et al., 2014).

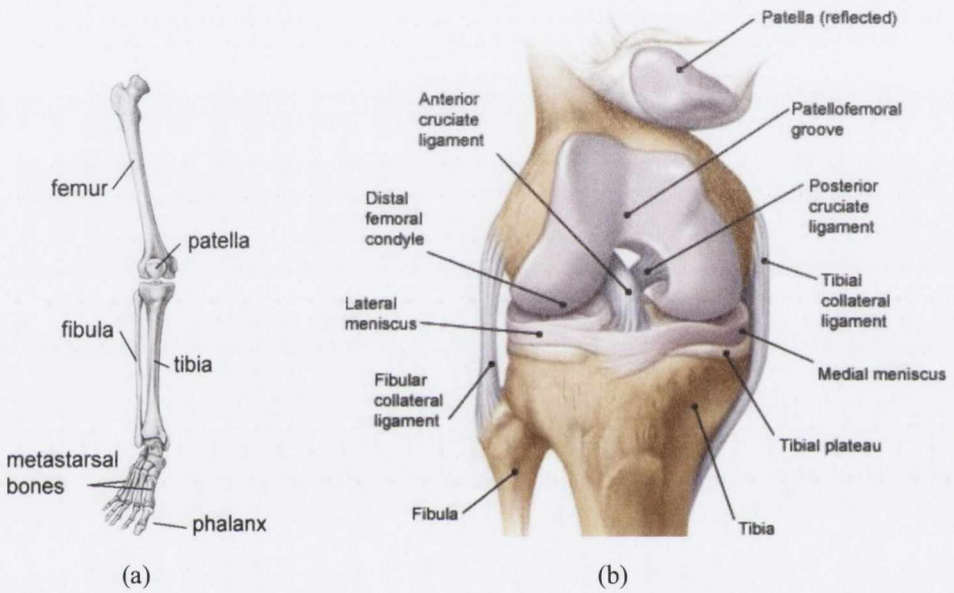

Figure 2.10 Anatomy of the lower extremity skeleton (a), adapted from (Sobotta, 1997) and the knee joint (b), adapted from (Tandeter et al., 1999).

Fibula fractures generally occur together with tibia fracture. According to an analysis of GIDAS data, 54% case of all the pedestrian accident cases with leg long bone fractures have both tibia and fibula fractures (Otte and Haasper, 2007). A study of Edwards and Green (1999) based on the UK hospital records indicates that the tibia has the most frequency of skeletal injury in pedestrian fatalities (30%), followed by the fibula (25%), pelvis (21%) and femur (14%). A tibia fracture may reduce the injury risk to the knee, femur and pelvis (Edwards and Green, 1999).

2.2.4.2 Lower extremity injury criteria

In order to investigate the tolerance of the human lower extremity, many studies have been done via cadaver tests focusing on the bending moment for long bone fractures, and the results of those studies have been summarized in a previous study from Kerrigan et al. (2003a), see Table 2.6 and Table 2.7. This data shows that the thresholds for long bone fractures vary from loading type and sex. The thresholds from a study of Kerrigan et al. (2003a) show a high standard deviation (SD), e.g. failure moment of 412±114 Nm and 310±60 Nm for the femur and tibia respectively. Another study of Kerrigan et al. (2004) proposed injury risk curves for the long bones as a function of bending moment based on cadaver test data. Their injury risk curves show that the bending moment for 50% probability of fracture to the femur is 372 Nm when loading at the distal third, 447 Nm for loading at mid shaft, and 312 Nm to tibia for loading at mid shaft. Takahashi et al. (2000) summarized the yield stresses of tibial and femoral cortical bone from cadaver tests. In their study average yield stresses of 129 MPa and 114 MPa were proposed for the tibial and femoral cortical bone respectively, which can be used as the criteria for modelling bone fractures in numerical human body models.

Table 2.6 Human femur bending tolerance, adapted from (Kerrigan et al., 2003a).

Fracture moment	Test load	Test sample	Study
233 Nm (male) 182 Nm (female)	Quasi-static	9 (4 M, 5 F)	Weber 1859 in Messerer 1880
310 Nm (male) 182 Nm (female)	Quasi-static	12 (6 M, 6 F)	Messerer 1880 in Nyquist 1986
318 Nm (male) 202 Nm (female)		145 (91 M, 54 F)	Mather 1968
324 Nm (20-39 yrs) 213 Nm (40-49 yrs) 203 Nm (50-59 yrs) 201 Nm (60-69 yrs) 184 Nm (70-89 yrs)	Quasi-static	35 (M and F)	Motoshima 1960 in Yamada 1970
373 Nm	Dynamic	33 (26 M, 7 F)	Martens et al., 1986
412±114 Nm	Dynamic	14 (10 M, 4 F)	(Kerrigan et al., 2003a)

At the meantime, a study from Matsui et al. (2004) suggests that the impact force for 50% probability of femur fracture is 9.5 kN according to an injury risk curve for femur fracture probability as a function of impact force based on cadaver test data. The study of Matsui et al. also indicates that femur acceleration is not a reasonable indicator for femur fracture since the mean fracture acceleration is lower than that for no fracture (Matsui et al., 2004). A recent study of tibia tolerance based on FE simulation indicated that the bending tolerance developed from loading at the mid-shaft cannot be applied to other impact conditions for the pedestrian tibia (Mo et al., 2012).

Table 2.7 Human tibia bending tolerance, adapted from (Kerrigan et al., 2003a).

Fracture moment	Test load	Test sample	Study
165 Nm (male) 125 Nm (female)	Quasi-static	9 (4 M, 5 F)	Weber 1859 in Messerer 1880
207 Nm (male) 124 Nm (female)	Quasi-static	12 (6 M, 6 F)	Messerer 1880 in Nyquist 1986
208 Nm (20-39 yrs) 180 Nm (40-49 yrs) 175 Nm (50-59 yrs) 172 Nm (60-69 yrs) 164 Nm (70-89 yrs)	Quasi-static	35 (M and F)	Motoshima 1960 in Yamada 1970
241±49 Nm 408±115 Nm 311±96 Nm	Dynamic	10 (avg. age 51) 12 (avg. age 68) 9 (avg. age 72)	Schreiber et al. 1997
308±79 Nm	Dynamic	21 (16 M, 5 F)	Nyquist et al. 1985
310±60 Nm	Dynamic	9	(Kerrigan et al., 2003a)

For the knee, injury criteria usually are predicated on the bending and shearing response in pedestrian impact. Thresholds for knee shearing force/displacement and bending moment/angle from different studies based on cadaver tests have been summarized in Mo's PhD thesis (Mo, 2012), see Table 2.9. According to Table 2.8, the injury threshold range for knee bending angle is from 9 to 16.3 degrees and for the shearing displacement is from 12 to 25.2 mm. Mo et al. (2013a) indicated that medial displacement of the tibia results in ACL injury while lateral displacement leads to PCL injury, based on shearing tests on human knee joints. This study also

suggests that the threshold of the knee shearing displacement is within a range from 11.4 mm to 17.6 mm, the mean value is 14.4 mm (Mo et al., 2013a). A knee injury criterion combining the knee shearing displacement and bending angle have been proposed based on impact tests using 7 isolated lower extremities from post-mortem human subjects (PMHS) and FE simulations by another study of Mo et al. (2013b). They suggested that an average shearing threshold (15 mm) for initial cruciate ligament failures and a combined injury function of bending and shearing levels (started from 9 degrees to 17 degrees) for MCL injuries. Recently, knee injury criteria for vehicle-to-pedestrian collision environments at different impact speeds have been proposed in a study of Mo et al. (2014) based on FE simulations, which suggest that knee injuries could be caused by a pure lateral bending angle of 14.5-16.5 degrees or a pure lateral shearing displacement of 14-15 mm or combined bending and shearing as in the curves shown in Figure 2.11.

Table 2.8 Human knee bending and shearing tolerance, adapted from (Mo, 2012).

Bending		Shearing		Test load (km/h)	Study
Moment (Nm)	Angle (deg)	Force (kN)	Displacement (mm)		
101	9	-	-	16	(Kajzer et al., 1993)
123	11			20	
129	16	-	12 (micro) 22 (macro)	Quasi-static	(Ramet et al., 1995)
284	14.6	2.7	23	40	(Kajzer et al., 1997)
356	12.3	2.4	16	20	(Kajzer et al., 1999)
137	12	1.1	-	2.2/4	(Kerrigan et al., 2003a)
117	13.9	-	-	40	(Ivarsson et al., 2005)
	16.3	-	25.2	Dynamic	(Bose et al., 2008)

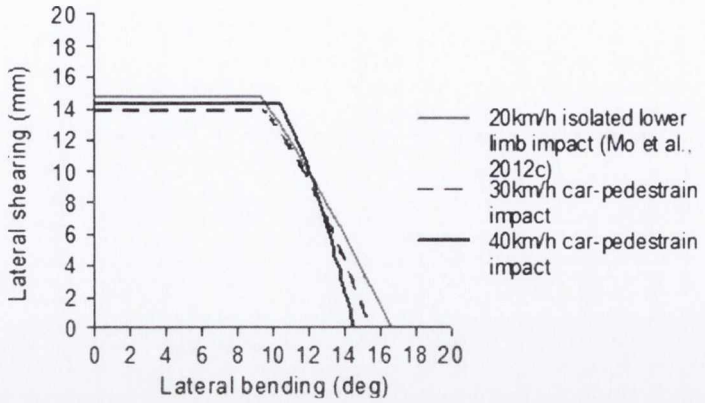

Figure 2.11 Knee injury criteria for different impact velocities, adapted from (Mo et al., 2014).

2.3 Pedestrian kinematics and injury research techniques

Impact tests using cadavers, dummies and sub-system impactors are the main physical research approaches for pedestrian injury and kinematics. With the rapid development of computer technology, numerical modelling of vehicle-to-pedestrian impact is also widely used as an indispensable tool in vehicle design and academic research processes. This section provides a summary of the research techniques on pedestrian kinematics and injury.

2.3.1 Cadaver and dummy tests

Cadaver tests using isolated body regions or a full-scale human body are the most valid way to understand the details in pedestrian collisions since the kinematics and injury biomechanics of pedestrians in real world accidents are hard record and measure. The cadaver tests of isolated body part are usually applied to study the biomechanics and estimate the injury thresholds for a particular human body region. In 1960 Lissner et al. (1960) proposed the WSTC for assessing head skull fracture based on a combination of cadaver and animal tests. In 1977 Nahum et al. (1977) analysed intracranial pressure dynamics during head impact based on tests on human cadavers' head loaded at a certain speed. During the 1980s Viano et al. (1989) developed a series of impact tests on cadavers to analyse the force, acceleration and viscous compression response in the human thorax and abdomen during lateral impact. For pelvis injury biomechanics, Viano et al. (1989) and Bouquet et al. (1994) conducted lateral impact tests on human cadavers. Kajzer et al. (1997 and 1999) studied knee injury biomechanics in lateral

impact at high and low speed based on shearing and bending tests using cadavers. Kerrigan et al. (2003a, 2003b, 2004 and 2008b) analysed pedestrian lower extremity kinematics and injury thresholds based on tests using isolated cadaver body regions and vehicle impact tests using full-scale human cadavers. For global pedestrian kinematics in vehicle collisions, Kerrigan et al. (2005, 2007, and 2008a) developed vehicle-to-pedestrian impact tests for post-mortem human surrogates (PMHS) using different size of cadavers and vehicles. Recently, Pass et al. (2012 and 2015) analysed pedestrian head, shoulder and spine kinematics based on full-scale PMHS tests. Figure 2.12 shows the typical global kinematics of a vehicle-to-pedestrian collision in cadaver tests (Kerrigan et al., 2005). Results from the above cadaver tests are generally applied as either pedestrian injury criteria or references for validation of mathematical human body models.

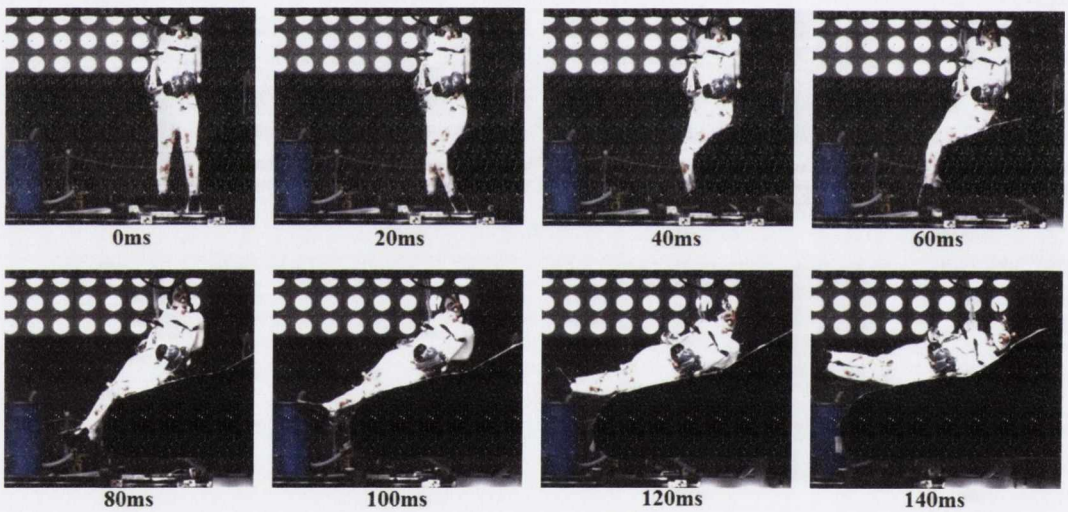

Figure 2.12 Global kinematics of pedestrian in PMHS test, adapted from (Kerrigan et al., 2005).

Pedestrian physical dummies developed according to human physical characteristics are widely used to predict pedestrian kinematics and injuries in vehicle crashes and to assess the safety performance of vehicle front designs. In 1985, the first pedestrian dummy was developed by Aldman et al. (1985), named rotational symmetrical pedestrian dummy (RSPD), see Figure 2.13 (a). Then the POLAR-I was developed in 1999 based on the Hybrid III and THOR occupant dummies (Huang et al., 1999). This dummy is the first generation with human geometry and can be representative of a 50th% adult male. The improved version of this

dummy is called POLAR-II, and it was validated against PMHS test data with various vehicle front shapes, see Figure 2.13 (b) (Akiyama et al., 2001). POLAR-III is the current version (Akiyama et al., 2009; Okamoto et al., 2009; Takahashi et al., 2009). Two dummies have been developed by combination work of Autoliv and Chalmers University, called Chalmers-Autoliv dummies, see Figure 2.13 (c) and (d). The adult dummy is representive of a 50^{th}% adult male, while the child dummy represents a 6-year-old child. Both the Chalmers-Autoliv dummies have been validated based on the kinematics of the Chalmers Madymo pedestrian model in vehicle impact simulations. Thereby the Chalmers-Autoliv dummies can only be used for studying the kinematic response (Renaud and Tapia, 2004; Björklund and Zheng, 2001).

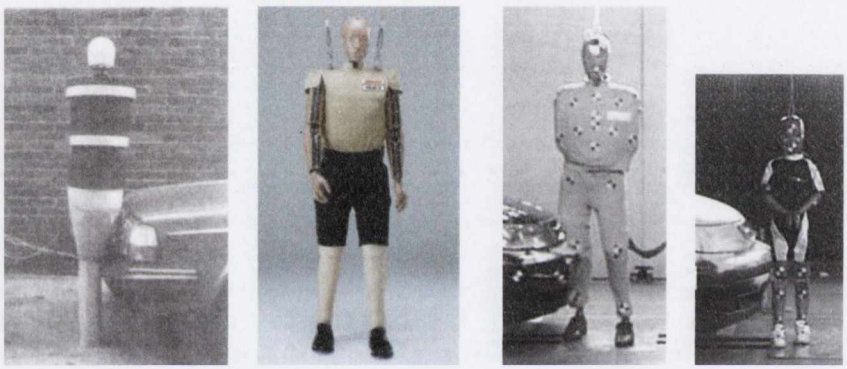

(a) (b) (c) (d)

Figure 2.13 Pedestrian dummies: (a) RSPD (Aldman et al., 1985), (b) Polar-II (Akiyama et al., 2001), Chalmers-Autoliv (c) adult (Björklund and Zheng, 2001) and (d) child (Renaud and Tapia, 2004).

2.3.2 Subsystem test

Cadaver and dummy tests are not the optimal methods for assessing vehicle safety performance for pedestrians in a legislative purpose due to the ethics and high cost. Therefore the European Enhanced Vehicle Safety Committee (EEVC) working group (WG) proposed the pedestrian subsystem impactor test methods (Figure 2.14) to evaluate pedestrian protection performance of the vehicle front structures (EEVC, 1994, 1998 and 2002). The EEVC pedestrian subsystem test methods include three types of impact tests using different impactors: a lower legform to bumper impact test to indicate injury risk of the adult knee and leg struck by the vehicle front using lateral knee-joint shear displacement and bending angle, and tibia acceleration; upper

legform to bonnet leading edge impact test to predict the injury risk of adult thigh and pelvis struck by vehicle front using bending moments and forces; child and adult headform impactors to bonnet impact tests to indicate head injury risk using accelerations. The impact speed of 40 km/h is applied for all these subsystem impact tests. The EEVC test scheme is applied in the European New Car Assessment Programs (Euro-NCAP) for assessing car safety performance (Euro-NCAP, 2013).

The International Standards Organization (ISO) (ISO, 2000) and IHRA (Mizuno, 2005) also proposed similar test methods as the EEVC. Later the United Nations Economic Commission for Europe (UNECE) Working Party on Passive Safety proposed a pedestrian Global Technical Regulation (GTR) head impact test procedure (UNECE, 2007; GTR, 2009). What is more, the subsystem tests methods are also used in the NCAP of China and Japan (J-NCAP, 2011; C-NCAP, 2015). The test speed for the headform impactors varies from 32 km/h to 40 km/h for these different test procedures. The impact angle and location also differ for test procedures provided by different institutions.

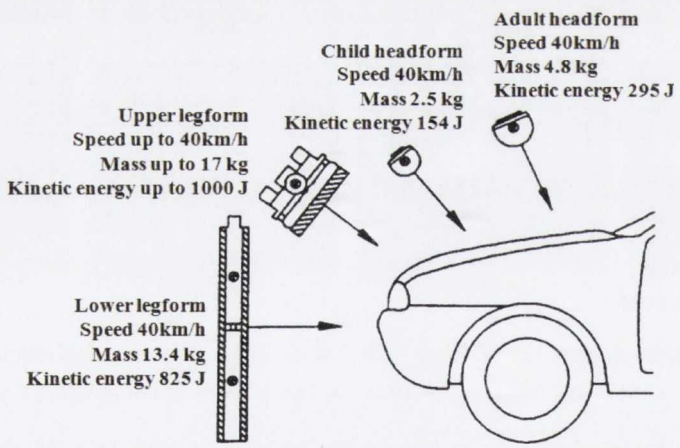

Figure 2.14 EEVC subsystem impactor test methods, adapted from (EEVC, 2002).

These subsystem tests have led to significant changes in vehicle front design for pedestrian protection. However the current testing methods using isolated impactors mainly focus on the stiffness and energy absorbing capability of isolated vehicle front structures. The overall vehicle front shape, the global kinematics of the pedestrian body and the geometry differences between vehicle classes (i.e. sedan, SUV and van) cannot be fully evaluated. Although a

comparison of Euro-NCAP scores with pedestrian accident outcomes in Sweden showed a reduction of injury severity for cars with higher pedestrian scores, cars with a high Euro-NCAP score could not be studied due to lack of cases (Strandroth et al. 2011). A German study of almost 700 pedestrian accidents found a correlation between the Euro-NCAP score and moderate pedestrian injuries, but reported significant injury ranges within a single Euro-NCAP score (Liers et al. 2011).

2.3.3 Numerical simulation

Computational simulations using multi-body models and finite element (FE) models are the commonly-used approaches for vehicle-to-pedestrian impact modelling.

2.3.3.1 Multi-body modelling

Multi-body modelling uses rigid bodies and joints to simulate the mechanical properties of an object. The geometry of the multi-body model is usually modelled using ellipsoids and/or facets. The contact characteristics of the multi-body parts are usually defined using supplied loading/unloading functions, hysteresis paths and damping. Different joint types (e.g. spherical joints, translational joints, revolute joints, etc.) can be defined. For multi-body human body models, different contact properties and joint motion properties are usually defined to simulate the mechanical characteristics of the human body regions and joints. Similarly the geometric and mechanical characteristics of vehicle fronts can also be modelled using multi-body systems.

The MADYMO pedestrian models and Chalmers pedestrian model (CPM) are the main ellipsoid multi-body human body models which are widely used in pedestrian safety studies (Figure 2.15). The MADYMO ellipsoid pedestrian model consists of 52 rigid bodies. The outer surface is described by 64 ellipsoids and 2 planes. The MADYMO 50th% male ellipsoid pedestrian model is scalable and has been validated extensively considering a large range of PMHS impactor tests on various body parts and different sets of full size PMHS vehicle-to-pedestrian impact tests (Hoof et al., 2003). The validation results indicate that the MADYMO 50th% male ellipsoid

pedestrian model show good predictions for global kinematics in vehicle-to-pedestrian collisions, but this model is limited in predicting detailed pedestrian injuries when compared to cadaver tests (Hoof et al., 2003). In particular, comparisons for head kinematics showed correlation scores over 90 %, but the correlation score for the bumper forces and accelerations of various body parts was lower (47-64%) due to the limitations in modelling vehicle contact characteristics used in cadaver tests (Hoof et al., 2003). For lower extremity fracture predictions, the comparison results between the MADYMO 50th% male pedestrian model and cadaver tests are dependent on the fracture tolerances employed (Hoof et al., 2003). Generally the model can predicted similar lower extremity fractures when reasonable thresholds for shearing force (6 kN and 4kN for femur and tibia, respectively) and bending moment (430 Nm and 285 Nm for femur and tibia, respectively) were defined for the corresponding joints (Hoof et al., 2003). A study using MADYMO pedestrian models (50th% male and stocky female) and detailed vehicle front models for reconstructions of real world vehicle-to-pedestrian accidents indicates that the MADYMO pedestrian models can generally predicted the injuries observed in accidents by using HIC (head), TTI (upper torso), and bending angle (knee) for the corresponding body regions (Van Rooij et al., 2003). But the knee shear displacement in the model is not a good predictor for knee injury, and no good predictors are available in the model for shoulder and abdomen injuries (Van Rooij et al., 2003). For long bone fractures in the lower extremity, the predicted bending moments resulted an under-estimation when thresholds of 524 Nm and 450 Nm were defined for thigh and leg, respectively (Van Rooij et al., 2003). However, the thresholds used in Van Rooij et al. (2003) are obviously higher than that for the study of Hoof et al. (2003) where good predictions of lower extremity fracture were observed.

The MADYMO 50th% male ellipsoid pedestrian model has been scaled to a 3-year-old child, a 6-year-old child, a small female and a large male model based on the anthropometries of the corresponding human (small female and large male model) or dummies (3-year-old child and 6-year-old child model) (MADYMO, 2012). However these scaled models have not been validated. Another widely use multi-body pedestrian model is the Chalmers model, which is also scalable and has been validated against cadaver tests in terms of kinematics (Yang and Lovsund, 1997). With the good kinematic prediction, both MADYMO models and Chalmers

pedestrian model are widely used in reconstructions of real world pedestrian accidents and analysis of pedestrian dynamic response (Liu et al., 2002; Van Rooij et al., 2003; Yao et al., 2008; Elliott et al., 2012a; Li et al., 2012; Lyons and Simms, 2012; Nie et al., 2015). However the multi-body pedestrian models are rarely used for detailed injury prediction and biomechanical analysis. Some other multi-body ellipsoid pedestrian models are available as well, for example the JARI, RARU, and Honda pedestrian models. However these models are without frangible lower extremities and are limited for understanding the dynamic responses of pedestrians in vehicle-to-pedestrian crashes (Garrett, 1998; Okamoto et al., 2000; Neal et al., 2003; Anderson et al. 2007).

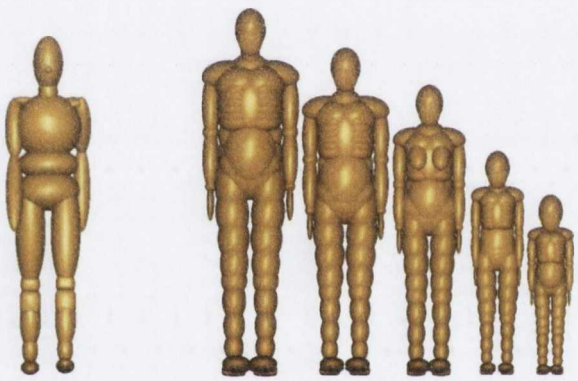

(a) (b)

Figure 2.15 Multi-body pedestrian models: (a) CPM, (b) MADYMO ellipsoid models.

A 50th% male facet pedestrian model has also been released by MADYMO (Figure 2.16 (a)). This pedestrian model was also validated against volunteer tests and PMHS test data and is recommended for impacts with a finite element (FE) vehicle model in an FE simulation environment (MADYMO, 2012). However facet pedestrian models in other sizes are not available and the released 50th% male facet pedestrian model is not scalable. Kerrigan et al. (2009b) developed a lower extremity facet model based on the University of Virginia (UVA) 50th% male FE lower limb model (Untaroiu et al., 2005) via the multi-body system, see Figure 2.16 (b). This lower extremity model was validated against their PMHS test data (Kerrigan et al., 2007 and 2008b) and was found to be more biofidelic in internal and external structure and injury predication than the MADYMO pedestrian model (Kerrigan et al., 2009b).

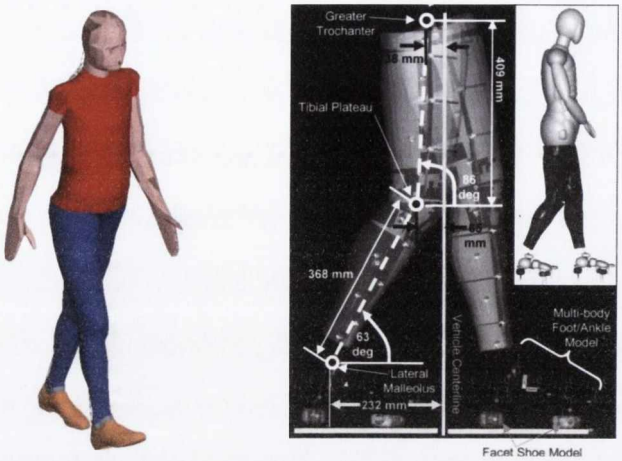

(a) (b)

Figure 2.16 Facet pedestrian human body model (a), adapted from (MADYMO, 2012) and lower extremity segment model (b), adapted from (Kerrigan et al., 2009b).

As summarized above both ellipsoid and facet multi-body pedestrian models are available for kinematics and injuries analysis. The injury outputs of multi-body models are physical quantities, such as force, moment, acceleration and so on. Thus detailed injury features like deformation, stress and fracture are not predicable in multi-body pedestrian models. The advantage of using multi-body models is to save computational time and these models could also be used when the detailed material data is not available. Even though the biofidelity of the MYDAMO pedestrian model is still questionable, it is a numerically fast tool to predict injury mechanisms and injuries (using reasonable injury criteria) in vehicle-to-pedestrian collisions (Hoof et al., 2003; Van Rooij et al., 2003). Overall the MADYMO ellipsoid pedestrian models are computationally fast and robust for more largescale and conceptual analysis, which meet the requirements of the current work.

2.3.3.2 Finite element (FE) modelling

Finite element (FE) models use elements (1-dimension, 2-dimension and 3-dimension) to form the geometry of an object, and define materials and properties to the elements according to the constitutive properties of the simulated structure. This method is widely used in modelling vehicle-to-pedestrian impact by using vehicle and human body FE models.

Isolated head and lower extremity FE models are widely used in pedestrian injury analysis,

such as the HBM-head model (Yang et al., 2008; Yang, 2011), HBM-lower limb model (Han et al., 2011), SIMon head model (Takhounts et al., 2003), ULP head model (Willinger and Baumgartner, 2003), UVA lower limb model (Untaroiu et al., 2005) and the Lower Limb Model for Safety (LLMS) model (Arnoux et al., 2005). For full human body pedestrian models, Maeno and Hasegawa (2011) developed the first version of the Total Human Model for Safety (THUMS) pedestrian model in 2001. The original THUMS pedestrian model was validated against pedestrian cadaver lateral impact data of the pelvis, lower extremity and whole human body. However the biofidelity of the original THUMS model was not good (Maeno and Hasegawa, 2001). The lower limb model of THUMS was improved by Kuwahara et al. (2007) and validated against cadaver test data from Kerrigan's study (Kerrigan et al., 2003a). The current THUMS models are the 4^{th} generation, including three body sizes: 50^{th}% adult male model (AM50), 5^{th}% adult female model (AF05) and 95^{th}% adult male model (AM95) (Toyota Motor Corporation, 2011). The biofidelity of the THUMS Version 4.0 AM50 pedestrian model has been verified by comparing to cadaver test data (Shigeta et al., 2009; Watanabe et al., 2011). Another total human body FE pedestrian model named the Honda H-model^{TM} pedestrian model was developed by Dokko et al (2003). The H-model^{TM} pedestrian model was validated against cadaver tests and the validation results of the H-model^{TM} pedestrian model show good agreements with cadaver data in terms of kinematics (Dokko et al., 2003). Recently a full human body FE pedestrian model, called human body model of pedestrian (HBMP) has been developed based on existing segment models of head, neck, thorax and lower limbs from Hunan University, China (Li et al., 2014). However, this human body model did not show good agreements with cadaver test data in its validation (Li et al., 2014). As shown in Figure 2.17 are the full scale FE pedestrian human body models.

FE whole body dummy models developed based on the geometric and mechanical properties of existing pedestrian dummies are also available for pedestrian safety studies. Shin et al. (2006) developed and validated the POLAR II full body FE model. The validation results indicate that this model can be used to represent the POLAR II dummy in vehicle impact. Yao et al. developed a full scale FE model based on the Autoliv-Chalmers adult pedestrian dummy and validated this model against dummy test data (Yao et al., 2011).

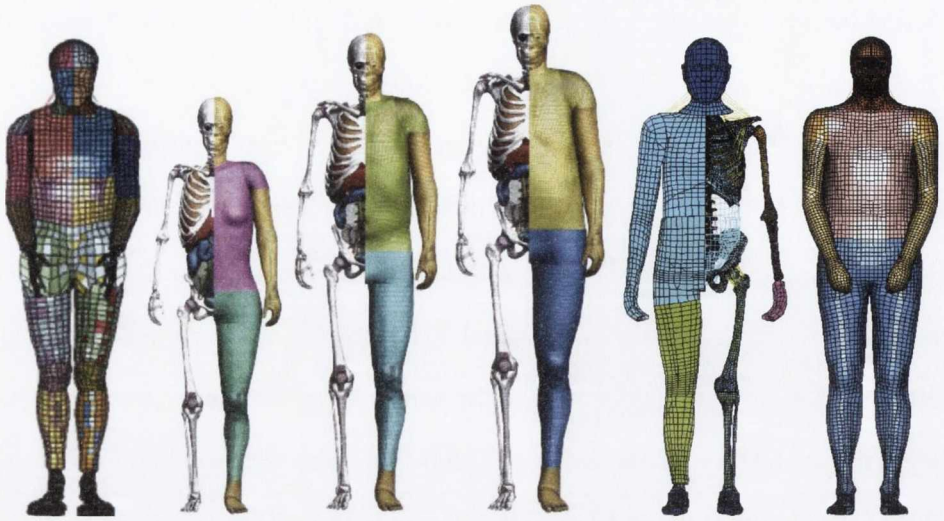

Figure 2.17 Human body FE pedestrian models: (from left to right) original THUMS (Maeno and Hasegawa, 2001), THUMS version 4.0 (AF05, AM50 and AM95) (Toyota Motor Corporation, 2011), H-model™ (Dokko et al., 2003) and HBMP (Li et al., 2014).

FE human models can predict detailed stress and strain distributions, bone fractures and ligament ruptures. The geometry and contact interface of finite element models are more detailed than multi-body models. But the FE modelling needs detailed material characteristics and geometry data and is much more computationally time consuming than the multi-body simulation. Furthermore valid FE pedestrian models for children are not available due to the lack of material characteristics and the scaled data for FE modelling of human body may lead to unsubstantiated predictions. Thus the FE modelling is more suitable for analysis of injury biomechanics based on limited impact conditions.

2.4 Fundamental considerations of pedestrian protection

Human, vehicle and environment are the basic factors for a pedestrian accident. However it is impractical to consider all the factors in the optimization of vehicle front shape since some of them cannot be defined in the numerical simulation (such as environment parameters). Thus the optimization will focus on the important factors. This section summarizes the effects of the pedestrian characteristics, vehicle characteristics and ground impacts on pedestrian injury risk in vehicle-to-pedestrian collisions. The factors that have a significant influence on pedestrian

injury risk should be considered in the vehicle front optimization.

2.4.1 Pedestrian characteristics

2.4.1.1 Pedestrian age, sex and height

As summarized in Section 2.16, pedestrian age is in a broad range from child to old age. Studies of accident data show that age is a very important factor influencing pedestrian injury outcome (Kong and Yang, 2010; Mizuno, 2005; Mizuno and Ishikawa, 2003; Zhang et al., 2008). Nearly all of these studies indicate that young individuals generally have a lower risk for serious injuries than older people in an accident. This is largely due to the differences in skeletal microarchitecture between individuals in different age (Phelps et al., 2000). According to Section 2.2.4.2, long bone fracture thresholds for females are generally lower than that for males (see Table 2.6 and Table 2.7). The thorax threshold is age dependent (Eppinger et al., 1984; Viano et al., 1989). The EEVC report indicates that a different HIC threshold should be used in assessing vehicle design for child head impactor tests than for adults (EEVC, 2002). However, the detailed injury criteria for different individuals are not available, and even for individuals in the same group (i.e. males with a similar age, height and weight) the tolerance level for a given injury varies in a wide range (Takahashi et al., 2000; Kerrigan et al., 2004; Mo, 2012). Therefore it is impractical to model all the physiological characteristics for each pedestrian in the simulation. A study of NASS and PCDS pedestrian accident data indicates that sex is not a statistically significant factor influencing pedestrian injury outcome in vehicle collisions (Zhang et al., 2008). This suggests that the effects of sex on injuries could be generally ignored in the optimization.

According to Section 2.1.3, pedestrian height has strong effects on the head impact point on the vehicle front, which may result in different levels of impact loading and injury severities to the victims. Usually the vehicle bumper and bonnet leading edge area is the most important part for shorter pedestrian protection, while the whole vehicle front, even the roof, should be considered for taller pedestrian protection. Accident data also shows that short pedestrians have a higher risk of suffering injuries caused from impacts with the ground (Mizuno and Ishikawa, 2003),

while tall individuals have a higher frequency of receiving AIS3+ injuries from impacts with the vehicle front since they are more likely to contact the stiff area such as the windscreen frame (Chidester and Isenberg, 2001). The accident data suggests that the effects of pedestrian height on injury outcome should be accounted for in the optimization of vehicle front.

2.4.1.2 Pedestrian walking speed and gait stance

The detailed influences of pedestrian walking/running speed on injury risk are still not clear. However, according to the accident reconstruction methods proposed in a previous study, the pedestrian walking speed is usually much lower than the vehicle impact speed and could be ignored in accident reconstructions (Brach and Brach 2005). A study of multi-body simulations indicates that pedestrian walking speed can influence the head impact position and orientation (head transverse offset and rotation angle) but has no effect on head impact speed (Elliott et al., 2012b). These two studies suggest that walking speed is not a crucial factor influencing pedestrian injury severity. But for vehicle active safety design the pedestrian walking/running speed is an important factor for the development of detecting sensor systems (Huang et al., 2008).

Many studies have indicated that pedestrian gait stance has a significant influence on pedestrian dynamic response and injury (Untaroiu et al., 2009; Elliott et al., 2012b; Peng et al., 2012b). Elliott et al. reported that pedestrian gait stance has a cyclical effect on head impact condition on the vehicle front (Elliott et al., 2012b). A study of Untaroiu et al. (2009) suggests that pedestrian kinematics in a vehicle collision are highly sensitive to pedestrian gait stance and it is a very important factor in pedestrian accident reconstructions. Peng et al. (2012b) proposed that pedestrian gait stance has strong effects on head impact conditions including head contact point, wrap around distance (WAD) and impact velocity and angle. It is therefore clear that a broad range of pedestrian gait stances should be considered in the optimization of vehicle front. However, how pedestrian gait stance affects the lower extremity injury is still not clear. Therefore, a detailed study on the effects of pedestrian gait stance on lower extremity injury risk is necessary to understand the injury outcome from the optimization conducted in the current thesis.

2.4.2 Vehicle characteristics

2.4.2.1 Vehicle impact speed

According to Section 2.1.5, pedestrian accidents occur over a broad range of impact speeds. Accident analysis shows that pedestrian injury risk generally increases with increasing vehicle impact speed (Simms and Wood, 2009). Multi-body simulations also indicate that vehicle impact speed strongly influences the kinematics and injuries of pedestrians (Liu et al., 2002; Elliott et al., 2012b; Peng et al., 2012b). Head impact speed and WAD increases with increasing vehicle impact speed (Peng et al., 2012b). Higher vehicle impact speeds lead to higher value of HIC, thigh impact force, tibia acceleration and knee shearing displacement (Liu et al., 2002). Headform and Hybrid III head impact test data show that a reduction of head impact speed can significantly decrease the HIC of the headform in vehicle collisions (Fredriksson et al., 2007b). FE simulations indicate that reducing the head impact speed from 30 km/h to 20 km/h can decrease the CSDM by about 100% in the brain of the FE head model (Fredriksson et al., 2007b). A study of PCDS data indicates that pedestrian knee ligament injuries mainly occur at impact speeds of 20-30 km/h, while long bone fractures in the pedestrian lower extremity mainly occur at impact speeds of about 40 km/h (Matsui, 2005). It is clear that reducing the vehicle impact speed is an efficient approach to reduce pedestrian injury risk. But it is not clear whether a vehicle front shape which shows a good pedestrian safety performance to pedestrian at a particular impact speed is also safe at other impact speeds, since the impact speed will affect the distribution of the injuries through the pedestrian's body (e.g. head injuries might be more important in high impact speed cases, while lower extremity injuries might be more important for low impact speed impacts) and the head contact location on the vehicle front. Therefore the broad range of impact speed should be considered in the optimization of vehicle front shape for pedestrian protection.

2.4.2.2 Vehicle front stiffness

The stiffness of vehicle front structures varies from vehicle types and manufactures. Stiffness corridors for vehicle bumper, bonnet leading, middle and rear area and windscreen base were

developed based on pedestrian subsystem impact tests in a previous study (Martinez et al., 2007). Figure 2.18 shows simplified average force deflection curves and ±1 standard deviation corridors for those five vehicle front areas. Different colours of the curves associate with different safety levels based on the Euro-NCAP pedestrian impact assessment methods, where red is for poor, yellow is for intermediate and green is for good (Martinez et al., 2007). In general lower stiffness vehicle fronts yielded safer outcomes to pedestrians in Euro-NCAP impact tests, even though this trend is not very clear for the bonnet middle (Martinez et al., 2007).

Studies based on cadaver tests, accident analysis and numerical simulations also show that reducing the stiffness of vehicle front structures can generally decrease pedestrian injury risk (Pritz et al., 1975; Bunketorp et al., 1983; Matsui et al., 1999; Mizuno et al., 2001; Liu et al., 2002; Schuster, 2006; Elliott et al., 2012a;). However, stiffness is not the only factor affecting pedestrian injuries. Ishikawa et al. (1992) claimed that soft bumpers can reduce shearing force in the knee but have no effect on knee bending moment, which would be influenced by the bumper shape. Studies based on FE simulations of sedans and SUVs to pedestrian impacts indicate that reducing the whole stiffness of the bumper is not a suitable method for pedestrian lower limb protection but an optimum stiffness distribution for the vehicle bumper can reduce pedestrian knee injury (Yasuki, 2007a and 2007b). The deformation space under the surface of the bonnet is also a key factor for pedestrian head injury since some stiff structures like the engine and hinge lie under the bonnet surface (Simms and Wood, 2009). These findings suggest that reducing the stiffness of the vehicle front and keeping enough deformation space can generally reduce pedestrian injury risk when the vehicle shape is given. Therefore, the focus is on optimization of vehicle front shape for pedestrian protection in the current thesis.

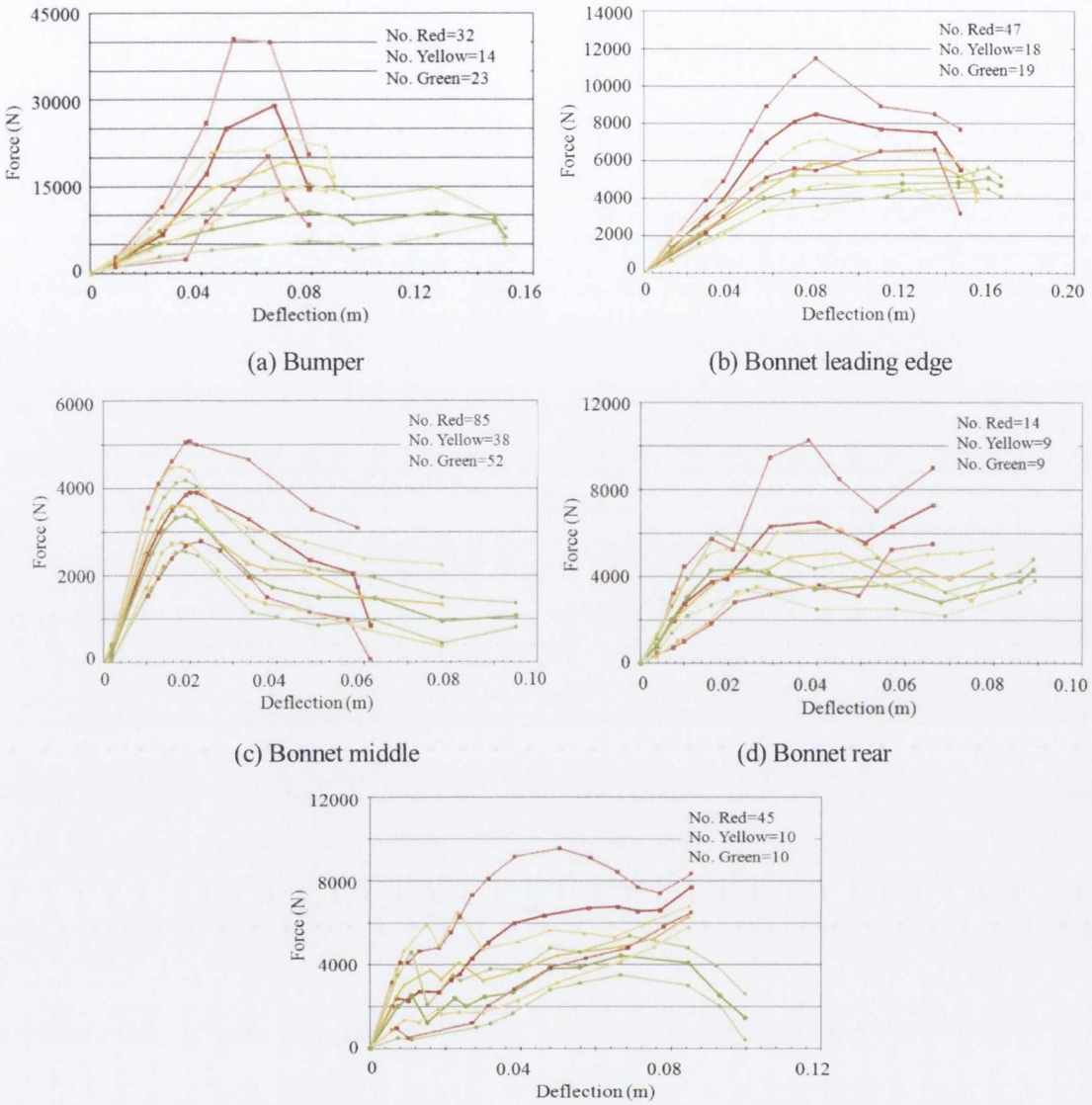

Figure 2.18 Simplified average force deflection curves and ±1 standard deviation corridors for different vehicle front areas, adapted from (Martinez et al., 2007).

2.4.2.3 Vehicle front shape

The vehicle front generally consists with the following structures: bumper, bonnet leading edge (BLE), fender, bonnet and windscreen. As summarized in the book of Simms and Wood (2009), vehicle front design has a significant influence on pedestrian kinematics and injuries by affecting the contact time, impact location, impact velocity and impact force for each body region of the pedestrian.

Generally, the front bumper is the first part that contacts with the pedestrian in vehicle collisions, and the lower limb is the first contact body part of pedestrians. So firstly the shape of the vehicle bumper can influence pedestrian lower limb injuries (Simms and Wood, 2009). According to GIDAS accident data, there are four common types of sedan bumpers: Type A and Type B are protruding and rather rectangular, Type C and Type D are rounded see Figure 2.19 (Otte and Haasper, 2007). The accident data also shows that Type A and B bumpers are much more aggressive than Type C and D bumpers to pedestrian lower extremities (Otte and Haasper, 2007).

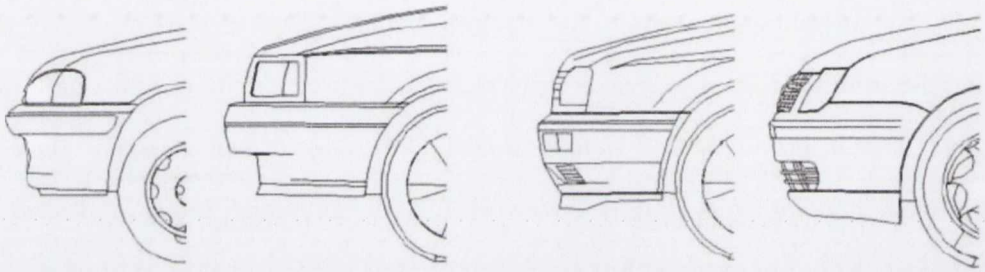

Figure 2.19 Frontal shapes of sedan bumper, adapted from (Otte and Haasper, 2007).

Another study of GIDAS data shows that most pedestrian knee injuries in accidents result from vehicle bumpers higher than the knee height, and smoother vehicle bumpers lead to lower frequency of knee injuries than those bumpers with protruding and rectangular shape (Otte and haasper, 2005). According to a study of Matsui et al., the relative height of vehicle bumper and pedestrian knee is the key factor of vehicle bumper shape influencing pedestrian lower extremity injuries. Their results show that the mean normalized bumper lower edge height (bumper lower height divided by knee height) for femur fracture is 0.95, for knee ligament injury is 0.79 and for tibia fracture is 0.78 (Matsui, 2005). A study on the effects of vehicle front shape on pedestrian injury risk based on multi-body simulations indicates that vehicle bumper height has a significant influence on pedestrian knee injury: higher bumpers result in large knee lateral bending angle, and the pedestrian knee has highest lateral shearing displacement when the bumper centre height is just below knee (Liu et al., 2002). Their simulation results also show that the head impact speed increases with the bumper centre height

when fixing the bonnet leading edge height since the large knee lateral deflection in the higher bumper height cases reduces the pelvis slipping on the bonnet surface but intensifies the rotation of upper body forward to the vehicle. (Liu et al., 2002).

The bonnet leading edge is usually the second vehicle structure that contacts the pedestrian in accidents. The bonnet leading edge is the main source for thigh and pelvis injuries for adult pedestrians and thorax and head injuries for children (Simms and Wood, 2009). PCDS accident data shows that vehicles with a high bonnet leading edge lead to more injuries to pedestrians' hip and mid-body than low bonnet leading edge vehicles (Longhitano et al., 2005). Accident data from JARI and ITARDA indicate that the normalized height of the bonnet leading edge (bonnet leading edge height divided 50% of pedestrian height) is the most important factor for pedestrian pelvis and femur injuries, followed by the stiffness and curvature of the bonnet leading edge (Matsui et al., 1999). Meanwhile, many studies have shown that the head kinematics and injuries are strongly influenced by the height of the bonnet leading edge (Pritz and Pereira, 1983; Matsui et al., 1999 and 2002; Liu et al., 2002; Longhitano et al., 2005). Dummy test data show that the impact speed and WAD of the dummy head for sedan impacts are significantly higher than that for SUV impacts (Matsui et al., 2002). Previous studies based on multi-body simulations also indicate that lower bonnet leading edge heights can reduce the thigh and pelvis loading but may lead to higher head impact speed or impact force for adult pedestrians (Pritz and Pereira, 1983; Liu et al., 2002). The study of Pritz and Pereira (1983) also claimed that lower bonnet leading edge heights may result in lower head impact force and higher pelvis impact force for children. These findings suggest that it is necessary to consider the effects of bonnet leading edge design on injuries from different pedestrian heights and body regions in the optimization of vehicle front shape.

There are fewer studies focusing on the effects of bonnet surface and windscreen design on pedestrian injuries. A study of GIDAS accident data shows that short bonnets lead to higher frequency of head impacting with the vehicle windscreen than a long bonnet, resulting in more serious head injuries to pedestrians (Otte, 1994b). The effects of bonnet top angle on pedestrian injury outcome are rarely reported. Otte (1994a) also suggested that windscreens with small

inclination angle are safer for pedestrians in accidents. However, multi-body model simulation results show that vehicle windscreens with a steep inclination angle are safer for pedestrian head in terms of linear and angular accelerations when a non-linear stiffness characteristic of the windscreen is defined (Lyons and Simms, 2012). But the head acceleration versus windscreen angle trends using a linear windscreen stiffness are opposite to those observed from simulations using a non-linear stiffness (Lyons and Simms, 2012). Furthermore, Lyons and Simms re-analysed Otte's accident data and indicated that the correlation between head injury risk and windscreen angle is very low if removing the cases with the head impact located on the frame (Lyons and Simms, 2012). Accordingly, further analysis on the effects of windscreen on pedestrian injuries should be performed, especially using accident data.

2.4.3 Ground impacts

As mentioned in Section 2.1.3, ground impact is an important source for pedestrian head injuries. Many studies have focused on investigating pedestrian ground contact mechanisms in vehicle-to-pedestrian collisions based on multi-body simulations (Simms and Wood, 2006a and 2006b; Simms et al., 2011; Crocetta et al., 2015). The above studies suggest that the vehicle front design has a significant influence on pedestrian contact mechanisms with the ground. In general, impact mechanisms for adults resulting in a head-first contact with the ground are more severe for high fronted vehicles compared to low fronted vehicles (Crocetta et al., 2015). The study of Crocetta et al. (2015) also indicates that for impacts with SUVs and vans (with a high front) the pedestrian is mainly pushed forward and this leads to high head ground contact speeds for children. These studies also indicate that the effects of vehicle front design on ground impact mechanisms are highly dependent on the impact speed. Previous studies based on real world accident data suggest that vehicle impact speed is a crucial factor influencing the role of ground impacts in vehicle-to-pedestrian collisions: at low speeds (less than about 35 km/h) ground contact injuries are frequently the most severe injuries, whereas at higher speeds vehicle contact injuries are generally more severe (Ashton and Mackay, 1983; Guillaume et al., 2015). Therefore, it is necessary to account for the injuries from ground impacts in the optimization of vehicle front shape for pedestrian protection, especially for collisions at low

impact speeds.

2.5 Optimization on vehicle front design

Optimization of vehicle fronts can be conducted for local structures or the global design to reduce pedestrian injury risk. For local structure design, optimizations mainly focus on the injuries from the body region which directly contacts with a particular structure in vehicle-to-pedestrian collisions. Optimizations for the global vehicle front design may consider the overall pedestrian injuries and the whole body kinematics.

Optimizations of the vehicle bumper usually consider additional structures for the lower bumper (shape) and energy absorbers (stiffness) in the bumper area to reduce pedestrian lower extremity impact force and bending moment (Konosu et al., 2005; Pinecki and Zeitouni, 2007). Many studies suggest that a secondary bumper (lower absorber) can reduce knee injury risk (Ishikawa et al., 1992; Kajzer and Schroeder, 1992; Kuwahara et al., 2007; Pinecki and Zeitouni, 2007). However, the lower absorber may increase tibia fracture and ankle injury risks unless it is in a very low height level (Kuwahara et al., 2007).

Optimization of the bonnet leading edge is generally with the purpose of reducing its aggressivity to a pedestrian's femur/pelvis and mid-body. This can be achieved by using a softer material, lower bonnet leading edge height and more rounded angle for the bonnet front structure (Simms and Wood, 2009). Additionally, a bonnet edge airbag can be applied for improving vehicle safety performance (Fredriksson et al., 2007a). These optimization designs may ignore the effects of bonnet leading edge on upper body (i.e. thorax and head) kinematics in vehicle collisions (Pritz and Pereira, 1983).

For the bonnet top and windscreen (with frame) area, optimizations mainly focused on stiffness rather than shape. Some studies suggest the inner structures (sandwich hood structures) with uniform stiffness and energy absorption to reduce pedestrian head injury risk (Kerkeling et al., 2005; Liu et al., 2009; Peng et al., 2012c). An uplifting bonnet (pop-up/reversible bonnet) is also a method to reduce pedestrian torso and head injury risk (Kuehn et al., 2005a; Nagatomi et

al., 2005; Huang and Yang, 2010). For the windscreen area, new materials for the windscreen panel and airbag are potential solutions for pedestrian protection. Pedestrian airbags covering the A-pillars and lower windscreen frame can significantly reduce pedestrian injury risk from impacts with the bonnet and the area covered by the airbag (Kuehn et al., 2005a; Jakobsson et al., 2013).

During the last decade, some studies have involved optimization of overall vehicle front shape for pedestrian protection. Carter et al. (2005) demonstrated a feasible method of applying multi-body simulations and a simple Genetic Algorithm (GA) to optimize the centre-line geometry of car fronts for the reduction of pedestrian head and thoracic injuries from primary impacts. In their study three pedestrian models (6-year-old child, 5th % female and 50th % male) and two gait stances were used in the impact simulations at 40 km/h. However this optimization did not converge satisfactorily.

Recently, Subramanian et al. (2012 and 2016) proposed a similar approach of using multi-body simulations and GA to optimize the vehicle front centre-line geometry by considering the cost of injuries (from primary contacts) for four body regions (head, neck, thorax and lower extremity). In their studies, different pedestrian sizes (6-year-old child, 5^{th}% female, 50^{th}% male and 95^{th}% male for the study of 2012, while 6-year-old child, 5^{th}% female, 50^{th}% male for the study of 2016), but only one gait stance and one impact speed (40 km/h) were accounted for. Their study in 2012 used contact force for predicting lower extremity injuries (Subramanian et al., 2012), which is not a good choice according to the injury biomechanics of the lower extremity where bending is the key dynamic response (Section 2.2.4.1). In their later study, the leg bending moment was considered in its injury criterion but the thigh injury criterion was based on the axial compression force and injuries from the knee have not been considered (Subramanian et al., 2012). The vehicle front models used in their studies have large gaps between different structures (such as the bumper and bonnet), which leads to invalid contacts between the pedestrian models and the vehicle front as clarified in their studies (Subramanian et al., 2012 and 2016). The lack of a suitable consideration of the injury criteria, knee injuries and impact speeds and the drawback of vehicle front modelling in these studies may lead to erroneous predictions. What is more, these studies have not provided detailed analyses on evaluating and validating their predictions. Thus the optimization of vehicle fronts with detailed analyses of the

predictions will help to build a solid foundation for future reference.

Kausalyah et al. (2014) provided an approach of using multi-body simulations, response functions and GA to optimize the overall vehicle front geometry with the purpose of reducing head injury risk of an adult and a child pedestrian model. This study suggests that an optimized vehicle front shape for adults are significantly different from that for a 6-year-old child in terms of head injury risk reduction and the optimal shape for both adult and child head protection has been proposed with consideration of avoiding run-over occurrences (Kausalyah et al., 2014). In their study of 2015 (Kausalyah et al. 2015), a Central Composite Design method was proposed to create the simulation experiments, and then a multi linear regression analysis was performed to derive the response surface models between adult head injury risk and vehicle shape parameters. This study was aiming at comparing the feasibility of the use of Central Composite Designs (CCD) between a Circumscribed Design (CCC) and a Faced Design (CCF) rather than optimizing vehicle front shape for pedestrian protection. The studies of Kausalyah et al. (2014 and 2015) only focused on head injury at an impact speed of 40 km/h.

The above studies on optimization of overall vehicle front geometry for pedestrian protection more or less considered the influence of pedestrian size and gait stance on injury outcome. However, the broad range of impact speed and injuries from secondary impacts have not been accounted for in these previous studies. Furthermore, none of these vehicle optimization studies considered the actual distributions of the relevant input parameters observed from accident data even though these distributions may influence the optimal vehicle front shapes which lead to low injury risk to pedestrians in accidents. Basically these studies demonstrate the computational methods of using multi-body simulations and appropriate optimization algorithms to find the optimal vehicle front shape for pedestrian protection based on the defined impact configurations and fitness function, but an optimal vehicle front shape for pedestrian protection remains a research goal.

2.6 Summary

According to Section 2.1, it is clear that pedestrians are vulnerable road users at a high risk for injury in vehicle collisions all through the world, especially for developing countries.

Pedestrian accident data indicates that the head and lower extremity have significantly high injury frequency when struck by a vehicle, followed by the chest and pelvis. Therefore vehicle safety design should consider all injuries or at least the main injuries from these body regions. Pedestrian injuries can be caused by impacts with either the vehicle front or the ground. A broad range of vehicle type, impact speed and pedestrian status (age, sex, height, orientation, gait stance and so on) are involved in pedestrian accidents. These pedestrian accident epidemiological data suggest that an optimization of the vehicle front should consider the broad range of impact configurations in real world accidents.

As discussed in Section 2.3, cadaver and dummy tests are not practical methods for assessment of vehicle safety performance for pedestrians, where a big range of impact configurations needs to be tested, such as the optimization of the current thesis. The subsystem impact tests only focus on limited impact conditions so that a broad range of accident configurations are excluded and the isolated impactors used in the subsystem impact tests cannot reflect the integral kinematics of the whole body. Given these shortcomings of using physical impact tests for the current optimization, the computational simulation using well developed numerical pedestrian models is an efficient approach for the optimization proposed in the current thesis.

The literature summarized in Section 2.2 helps to have a good understanding of the human body anatomy, injury biomechanics of different body regions in vehicle-to-pedestrian impacts and potential criteria which can be used for assessing pedestrian injuries in vehicle collisions. According to the main injury biomechanics of the human body in vehicle-to-pedestrian collisions, the availability of injury threshold references and the injury predicative capabilities of the current assessment methods for pedestrian injuries (Section 2.2 and 2.3), the HIC (head), TTI (thorax), lateral impact force (pelvis), bending moment/yield stress (long bones in the lower extremity) and bending angle/shearing displacement (knee) can be applied as the criteria for assessing pedestrian injuries in the numerical simulation studies of the current thesis.

Section 2.4 discussed the influence of pedestrian and vehicle characteristics and ground impacts on pedestrian kinematics and injuries. It is clear that a vehicle's shape, stiffness and impact speed, as well as a pedestrian's height, age and gait stance have significant effects on

pedestrian kinematics and injury risk. The impacts from the ground are also very important for pedestrian injuries, especially for collisions at low impact speeds. Reducing the contact stiffness and increasing the crush depth of vehicle front structures are essential for pedestrian protection in terms of vehicle stiffness optimization. In contrast, the effects of vehicle front shape on pedestrian injury risk are still in debate or not clear, such as the influence of windscreen angle on head injury and the effects of the overall shape of vehicle front on overall pedestrian injury risk. Furthermore, the effects of pedestrian gait stance on lower extremity injuries (accounting for about 30% of all pedestrian injuries) have not been investigated in detail yet.

According to Section 2.5, previous optimizations of overall vehicle front shape only considered limited impact conditions and the primary impacts. The optimization of overall vehicle front shape based on those methods may not represent the situation in the real world since pedestrian accidents occur in various impact configurations and pedestrian injury outcome is strongly dependent on the initial impact conditions. Accordingly, optimization of overall vehicle front shape for pedestrian protection is likely to be more successful if it is based on the actual distribution of real world impact configurations rather than on idealised collision scenarios. Therefore a global optimization method accounting for a broad range of impact scenarios and their distributions in real world accidents needs to be developed and the optimization results should be evaluated via kinematic analyses and/or accident data. The optimal shapes predicted by this optimization approach are then worth consideration in future vehicle front designs.

Given the above gaps in understanding pedestrian injury and prevention and in the optimization of overall vehicle front shape for pedestrian protection, a number of studies are conducted in the following content of this thesis based on the accessible approaches and reasonable considerations for pedestrian safety research summarized in this chapter.

Chapter 3 Detailed Effects of Sedan Front Shape on Pedestrian Injury Risk Observed from In-depth Accident Data

3.1 Introduction

Pedestrians are vulnerable road users with a high risk of serious injury or fatality in road traffic collisions with motor vehicles. Although vehicle speed is the most important factor for pedestrian injury outcome, the design of the vehicle front has a significant influence on pedestrian injury risk (Matsui et al., 1999; Longhitano et al. 2005; Matsui, 2005; Otte and Haasper, 2005 and 2007). A quantified understanding of the overall effects of vehicle front shape on pedestrian injuries remains lacking and is a pre-requisite for future vehicle front design for pedestrian protection.

Many studies have focused on the effects of vehicle front design on pedestrian injuries based on physical tests (e.g. Kajzer and Schroeder, 1992; Kerrigan et al., 2008a) and numerical simulations (e.g. Han et al., 2012; Liu et al., 2002; Lyons and Simms, 2012; Peng et al., 2012). However, these are usually based on limited impact configurations (e.g. impact speed & pedestrian height) which do not adequately reflect the wide range of actual pedestrian impact scenarios. Accordingly, analysis of detailed accident data is widely used to investigate the effects of vehicle front shape on pedestrian injuries. Li et al. (2012) compared sedans to minivans based on Chinese pedestrian accidents between 2006 and 2012 (In-depth Investigation of Vehicle Accidents in Changsha - IVAC), and found that flat type vehicles lead to a high proportion of thorax injuries while long bonnet type vehicles result in a higher proportion of head injuries (Li et al., 2012). Longhitano et al. (2005) compared injury rates for different pedestrian body regions between 95 LTV cases and 174 sedan cases from the US Crash Data Study (PCDS, 1994-1998), and found that LTVs (with their high vehicle fronts) are more aggressive than sedans (Longhitano et al. 2005). Otte and Haasper (2005 & 2007) used pedestrian accidents from 1985 to 2004 in the German In-Depth Accident Study (GIDAS) database to report that rounded bumpers are safer than angular ones. However, the detailed geometry of the vehicle front was not considered. In a more detailed analysis, Otte (1994a) investigated 76

pedestrian and cyclist cases (speed range 45-60 km/h) in GIDAS from 1985 to 1992 and found a higher injury severity with increasing windscreen inclination angle with respect to the horizontal. Matsui et al. (1999) used 82 cases from the Japanese JARI (1987-1988) and ITARDA (1993-1998) databases and found that higher bonnet leading edges are associated with increased AIS2+ femur & pelvis injury rates, especially when the bonnet leading edge is above the hip. Matsui (2005) used 62 pedestrian cases from the PCDS database to show that injuries to the tibia and knee ligaments can change to an injury to the femur with an increase in bumper height. More recently, Pal et al. (2015) used the PCDS accident data to investigate the influence of bumper and bonnet leading edge design on lower extremity and pelvis injuries, and reported that increasing the bumper lower edge to knee height ratio increases pelvis and femur injuries and decreases tibia and fibula injuries. They also indicated that decreasing bonnet leading edge to hip height ratio can reduce the occurrence of pelvis and femur injuries and increase tibia and fibula injuries.

Thus much in known in general terms about the influence of vehicle design on pedestrian injuries, but quantified relationships derived from accident data are sparse, and conclusions are often based on accident data more than 15 years old, thus not capturing the significant recent changes in vehicle front design. The current study therefore aims to apply logistic regression approaches to recent GIDAS accident data to estimate risk relationships between different pedestrian body region injuries and detailed sedan front design parameters, while controlling for impact speed and pedestrian age. A particular focus was placed on the relationships between sedan front shape and pedestrian head, thorax, pelvis and lower extremity injuries, since in the GIDAS database sedans account for more than 90% of pedestrian accidents and these body regions account for about 80% of AIS2+ injuries. The effects of SUV and van shape on pedestrian injury risk are not analysed due to the lack of sufficient cases.

3.2 Methods

3.2.1 Accident data

Pedestrian accident data from GIDAS were analysed, with the following inclusion criteria: 1) GIDAS pedestrian accident cases collected after 1st January 2000, 2) accidents involving sedans

(accounting for about 90% of GIDAS pedestrian accidents), 3) impact speed from 16 to 80 km/h (accounting for about 80% of GIDAS pedestrian accidents), 4) both pedestrian and vehicle information are available, 5) pedestrian heights > 150 cm, 6) pedestrians hit only once by one vehicle, 7) pedestrian was upright (not lying or sitting) and 8) the event caused at least one AIS1+ injury to the head, thorax, pelvis or lower extremity. In total 594 cases were extracted from an original accident sample of 1,258 cases as the analysis sample based on these criteria.

3.2.2 Sedan front profiles

In total 225 sedan models were included in the analysis sample. The main parameters defined to describe the sedan front shape are shown in Figure 3.1. The values of these parameters for each car model (recorded by brand, model and year in GIDAS) were measured from the corresponding vehicle blueprint (The-Blueprints, 2015) and scaled accordingly. The bumper and bonnet leading edge dimensions were measured using the EEVC WG17 (EEVC, 2002) protocol. A summary of these shape parameters in the analysis sample is shown in Table 3.1.

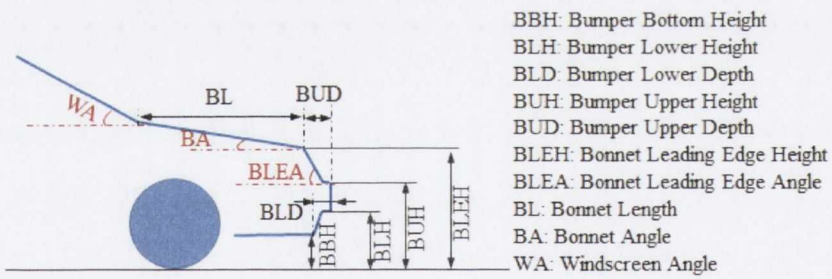

Figure 3.1 Sedan front shape parameters defined in this study.

3.2.3 Potential relationships

In the GIDAS data, injury sources were recorded according to the track information on vehicle front structures, kinematic analysis and reasonable estimations. Figure 3.2 shows that AIS2+ lower extremity injuries are mainly associated with contacts to the bumper (78%), while femur/pelvis injuries are largely due to impacts with the bonnet leading edge (BLE) and bonnet (51%). The bonnet (33%) and windshield (51%) are respectively the main sources of thorax and head injuries. Some body regions are rarely injured by certain car regions (e.g. the windscreen causes negligible lower extremity injuries). Therefore, to limit the relationships to test by logistic regression, the

principal relationships assessed were bumper versus lower extremity, BLE versus femur/pelvis, BLE versus thorax, BLE versus head, bonnet versus thorax, and windshield versus head (Table 3.2). The relationships of BLE versus thorax and head were set to investigate effects of the design of BLE on thorax and head injuries due to the subsequent effects on upper body kinematics (Liu et al., 2002; Han et al., 2012).

Table 3.1 Sedan front profile corridors for the analysis sample.

Parameter	Unit	Min	Median	Max
Bumper bottom height (BBH)	mm	130	237	383
Bumper lower depth (BLD)	mm	0	27	204
Bumper lower height (BLH)	mm	177	269	488
Bumper upper depth (BUD)	mm	12	125	211
Bumper upper height (BUH)	mm	381	537	677
Bonnet leading edge height (BLEH)	mm	630	748	891
Bonnet leading edge angle (BLEA)	°	41	55	85
Bonnet length (BL)	mm	300	980	1200
Bonnet angle (BA)	°	8	13	37
Windscreen angle (WA)	°	23	30	55

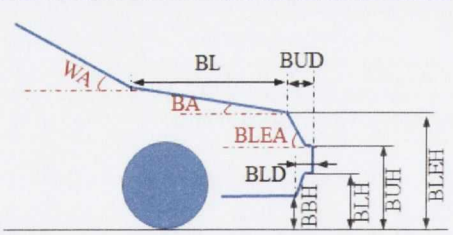

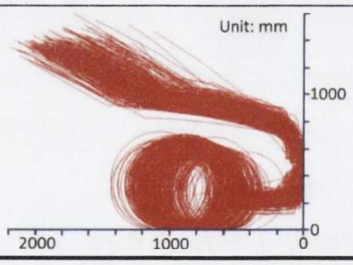

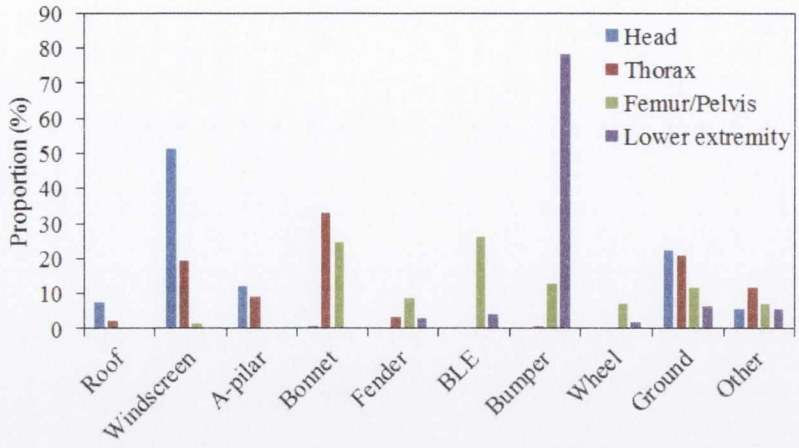

Figure 3.2 Distribution of AIS2+ injuries as a function of vehicle contact location for different body regions for the analysis sample.

Table 3.2 Samples for analysis of different relationships.

Sample	Relationship	Size	Inclusion criteria
1	Bumper vs Lower extremity	306	At least one AIS1+ lower extremity injury caused by bumper
2	BLE vs Femur/Pelvis	130	At least one AIS1+ femur/pelvis injury caused by BLE/bonnet
3	BLE/Bonnet vs Thorax	53	At least one AIS1+ thorax injury caused by bonnet
4	BLE/Bonnet/Windshield vs Head	212	At least one AIS1+ head injury caused by vehicle front
5	BLE/Bonnet/Windshield vs Head	90	At least one AIS1+ head injury caused by windshield centre

The GIDAS database uses the AIS 2005 (Gennarelli and Wodzin, 2006) classification to record injuries and the impact sources (vehicle structure involved, ground etc.) are also recorded. The focused is therefore on accident cases with at least one AIS1+ injury to a particular body region caused by a particular structure of the car front to avoid irrelevant cases. Two samples were defined for head injury analysis, one includes all cases at least having a head injury from vehicle front body; another one only includes the cases with the head impact location being within the windscreen centre area to avoid the effects of windscreen stiffness (due to the distance from the frame) on head injury severity (Mizuno et al., 2001). Five sub samples were set for analysis of the

car region versus pedestrian injury relationships, see Table 3.2.

3.2.4 Statistical analysis

According to previous studies on accident analysis (Kong and Yang, 2010; Nie et al., 2015), logistic regression is the commonly used approach to investigate the quantified effects of predictors on pedestrian injury risk. The logistic regression analysis assumes that the predictors included are not linear combinations (multicollinear) of each other. Multicollinearity◊ can result in incorrect signs and magnitudes of logistic regression coefficients, leading to incorrect relationships estimated between the predictors and dependent outputs (Midi et al., 2010). Therefore, it is first necessary to detect any multicollinearity between the predictors before using the logistic regression model to estimate the quantified effects of sedan front shape parameters on pedestrian injury risk. The multicollinearity diagnostic statistics produced by linear regression analysis are reliable to detect the multicollinearity between the predictors (Midi et al., 2010). Subsequently, logistic regression was applied to further analyse those parameters without multicollinearity between each other.

3.2.4.1 Detection of multicollinearity

Mathematically multicollinearity can mainly be detected by defining a tolerance and its reciprocal, called variance inflation factor (VIF) (Belsley et al., 1980). For a given predictor the tolerance is defined as:

$$Tol = 1 - R^2, \tag{3.1}$$

where R^2 is the coefficient of determination for the regression of that predictor on all remaining independent predictors (Belsley et al., 1980). The *VIF* is defined as:

$$VIF = \frac{1}{Tol} = \frac{1}{1-R^2}, \tag{3.2}$$

A smaller value of tolerance or a larger value of *VIF* indicates a higher likelihood of multicollinearity. However there is no formal threshold for tolerance or *VIF* for determining the multicollinearity. It is suggested that a *VIF* of 5 and above indicates a multicollinearity problem, and for logistic regression case a *VIF* value above 2.5 should be applied (Midi et al., 2010).

In the current study, the impact speed and pedestrian age were included as the predictors together with the shape parameters, since they are important factors influencing pedestrian injuries (Kong and Yang, 2010). The relative heights of the bumper to the knee and the bonnet leading edge (BLE) to the hip are important factors influencing pedestrian kinematics and injuries (Matsui et al., 1999; Matsui, 2005; Simms and Wood 2009). Therefore, the normalized bumper upper height (NBUH, bumper upper height divided by knee height) and normalized bonnet leading edge height (NBLEH, bonnet leading edge height divided by hip height) were estimated for each case from the age and sex of the pedestrian, based on German anthropometric data (Pheasant and Haslegrave, 2006). Table 3.3 shows the potential predictors and the injury severities concerned in different pedestrian body regions (AIS2+ for lower extremity and pelvis and AIS3+ for thorax and head) for the relationships summarized in Table 3.2. Particularly for the head, the effects of bonnet leading edge height and bonnet length on AIS3+ head injury risk were analysed by sample 4 to consider their influences on head impact location, while the effects of bonnet and windscreen angle on AIS3+ head injury risk were emphasize by sample 5 where head contacts were controlled within the windscreen centre. The AIS levels were selected to distinguish reasonable injury severities based on the AIS classification system (Gennarelli and Wodzin, 2006) for the corresponding body parts (AIS0-3 and AIS0-6 are defined for the lower extremity and thorax/head respectively). The injury outcome (dependent variable) was coded 0 and 1 for the cases with and without an injury defined by the injury severities concerned (Table 3.3), while the predictors (independent variables) are continuous data. Then multicollinearity diagnostic statistics conducted by the application of linear regression (between the predictors and injury outcome) was employed to detect multicollinearity between predictors in the samples via SPSS software (Table 3.2 and 3.3). The normalized shape parameters were evaluated separately together with the impact speed and pedestrian age since they are not vehicle shape design variables but factors of interest when analysing pedestrian injuries.

Table 3.4 shows the multicollinearity detection results, where for each sample the model A includes the shape parameters, speed and age, the model B includes the normalized shape parameters speed and age. It is clear from this table that multicollinearity occurs between the BLD and BLH in sample 1, and between the BUD and BLEA in sample 2. No multicollinearity was found between the

normalized parameters and speed and age in sample 1 and 2, or for any predictor in sample 3 and 4 (Table 3.4).

Table 3.3 Potential predictors and injury severities concerned in different pedestrian body regions.

Sample	Relationship	Predictor	Injury severity
1	Bumper vs Lower extremity	Speed, Age, BBH, BLD, BLH, BUH, BUD, NBLH and NBUH	AIS2+ (with=167, without=139)
2	BLE vs Femur/Pelvis	Speed, Age, BUD, BLEH, BLEA and NBLEH	AIS2+ (with=48, without=82)
3	BLE/Bonnet vs Thorax	Speed, Age, BLEH, BA and NBLEH	AIS3+ (with=17, without=36)
4	BLE/Bonnet/Windshield vs Head	Speed, Age, BLEH, BL and NBLEH	AIS3+ (with=39, without=173)
5	BLE/Bonnet/Windshield vs Head	Speed, Age, BLEH, BA, WA and NBLEH	AIS3+ (with=11, without=79)

According to the study of Midi et al. (2010), removing one or some parameters which have multicollinearity from the model is suggested to solve the multicollinearity problem. Therefore a potential set of predictors was arranged for sample 1 using the parameters without multicollinearity and the BLD (model 1-A1) or BLH (model 1-A2), respectively (Table 3.5). Similarly, the BUD (model 2-A1) and BLEA (model 2-A2) were used separately to form a set of predictors together with other parameters without multicollinearity in sample 2. The same approach was applied to detect the multicollinearity between predictors in the new set models, and the results are shown in Table 3.5, where the multicollinearity problems were solved by using the parameters with multicollinearity separately. According to the above results, 1-A1, 1-A2, 1-B, 2-A1, 2-A2, 2-B, 3-A, 3-B, 4-A, 4-B, 5-A and 5-B are the potential models for later logistic regression analysis.

Table 3.4 Multicollinearity detection results.

Sample-model	Parameter	*Tol*	*VIF*
1-A	Speed	0.999	1.001
	Age	0.986	1.014
	BBH	0.667	1.500
	BLD	0.231	**4.321**
	BLH	0.217	**4.610**
	BUH	0.915	1.093
	BUD	0.836	1.197
1-B	Speed	0.997	1.003
	Age	0.979	1.021
	NBLH	0.988	1.012
	NBUH	0.972	1.029
2-A	Speed	0.986	1.014
	Age	0.978	1.022
	BUD	0.181	**5.536**
	BLEH	0.598	1.671
	BLEA	0.205	**4.874**
2-B	Speed	0.992	1.008
	Age	0.990	1.010
	NBLEH	0.985	1.015
3-A	Speed	0.974	1.027
	Age	0.967	1.034
	BLEH	0.941	1.063
	BA	0.905	1.105
3-B	Speed	0.984	1.016
	Age	0.990	1.011
	NBLEH	0.977	1.023
4-A	Speed	0.995	1.005
	Age	0.993	1.007
	BLEH	0.983	1.017
	BL	0.981	1.019
4-B	Speed	0.985	1.016
	Age	0.983	1.017
	NBLEH	0.968	1.033
5-A	Speed	0.976	1.025
	Age	0.933	1.071
	BLEH	0.887	1.128
	BA	0.900	1.111
	WA	0.913	1.096
5-B	Speed	0.977	1.023
	Age	0.998	1.022
	NBLEH	0.979	1.022

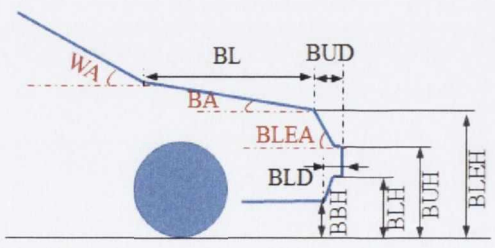

Table 3.5 Multicollinearity detection results for the new set models.

Sample-model	Parameter	*Tol*	*VIF*
1-A1	Speed	0.999	1.001
	Age	0.987	1.013
	BBH	0.981	1.020
	BLD	0.867	1.153
	BUH	0.919	1.088
	BUD	0.836	1.197
1-A2	Speed	0.999	1.001
	Age	0.986	1.014
	BBH	0.870	1.150
	BLH	0.813	1.230
	BUH	0.922	1.084
	BUD	0.865	1.156
2-A1	Speed	0.989	1.012
	Age	0.996	1.004
	BUD	0.879	1.137
	BLEH	0.877	1.140
2-A2	Speed	0.990	1.010
	Age	0.996	1.004
	BLEH	0.991	1.009
	BLEA	0.998	1.002

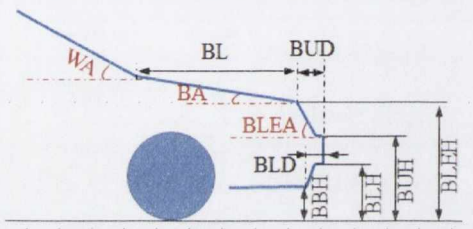

For a consideration of interaction terms (two-way interaction) in later logistic regression analysis, the multicollinearity between the predictors, including interacting parameters (e.g. for model 1-A1 speed, age, BBH, BLD, BUH and BUD) and interacted parameters (e.g. for model 1-A1 speed*BBH, speed*BLD, age*BBH, BBH*BLD and et al.), was evaluated by the multicollinearity diagnostic statistics conducted via the linear regression for each potential model (Table 3.4 and 3.5). Table 3.6 shows the multicollinearity detection results for two-way interaction terms between speed and the shape parameters in model 1-A1 and within all predictors in model 2-A1 (as the examples). Table 3.6 indicates that the interaction terms have serious multicollinearity (high *VIF* values) with the original (interacting) parameters (other interaction terms and models are not shown, but the situation is similar). This suggests that the interaction terms can be linearly predicted from the original parameters. Therefore, it is suggested to exclude the interaction terms in later logistic regression analysis.

Table 3.6 Multicollinearity detection results for interaction terms.

Model	Predictor	*Tol*	*VIF*	Model	Predictor	*Tol*	*VIF*
1-A1	Speed	**0.004**	**223.119**	2-A1	Speed	**0.002**	**492.943**
	Age	0.983	1.017		Age	**0.003**	**384.489**
	BUD	**0.084**	**11.891**		BLEH	**0.028**	**35.955**
	BBH	**0.142**	**7.052**		BUD	**0.003**	**362.707**
	BLD	**0.112**	**8.945**		Speed*BLEH	**0.002**	**560.028**
	BUH	**0.098**	**10.204**		Speed*BUD	**0.035**	**28.792**
	Speed*BUD	**0.046**	**21.749**		Age*BLEH	**0.002**	**440.138**
	Speed*BBH	**0.022**	**44.680**		Age*BUD	**0.035**	**28.260**
	Speed*BLD	**0.099**	**10.080**		BLEH*BUD	**0.002**	**449.112**
	Speed*BUH	**0.005**	**203.191**				

3.2.4.2 Logistic regression

The analysis in 3.2.4.1 selected the potential regression models, without multicollinearity between predictors, for each body region (Table 3.4 and 3.5). Then, the logistic regression approach, with the impact speed, pedestrian age and the car front shape parameters as predictors, was employed to investigate the relationships between the shape parameters and the odds of pedestrian AIS2+/AIS3+ injuries for each selected model (Table 3.4 and 3.5). The logistic model and injury probabilities are described as follows:

$$logit(p) = log\left(\frac{p}{1-p}\right) = \beta_0 + \beta_1 * x_1 \ldots + \beta_i * x_i, \tag{3.3}$$

$$p = \frac{exp\ (\beta_0+\beta_1*x_1\ldots+\beta_i*x_i)}{1+exp(\beta_0+\beta_1*x_1\ldots+\beta_i*x_i)}, \tag{3.4}$$

where p is the probability of an AIS2+/AIS3+ injury, β_i are the estimated coefficients based on the data using the method of maximum likelihood (Dobson, 2002), and x_i are the predictors (speed, age and given shape parameters). In logistic regression the Wald test was employed to determine whether a predictor (x_i) has a significant influence on the injury probability (p) by testing

significance of the corresponding coefficient (β_i). A significance (Sig) value lower than 0.05 indicates that the corresponding predictor has a statistically significant influence on the probability of an AIS2+/AIS3+ injury. This logistic model considers the combined effects of the selected predictors but the interaction terms between the predictors are not accounted for since preliminary studies show that the interaction terms have multicollinearity with the parameters interacted and they are not statistically significant.

Then the Odds Ratio (OR) in logistic regression was applied to assess the effects of each shape parameter on pedestrian AIS2+/AIS3+ injury risk. The OR is a factor which estimates the change in AIS2+/AIS3+ injury odds per unit increase in the corresponding shape parameter, while holding the impact speed, pedestrian age and other shape parameters (if they are included) fixed. Thus OR>1 indicates a rising trend of the injury odds with increasing magnitude of the shape parameter, while OR<1 predict the opposite. Confidence intervals at the 95% level are also constructed.

3.3 Logistic regression results

3.3.1 Bumper vs AIS2+ lower extremity injury risk

Table 3.7 shows the actual range of impact and age and each bumper shape parameter (boundary values) observed in the accident sample, and the significance level and the mean, and 95% Confidence Intervals (CI) of the OR for the logistic regression model 1-A1. Table 3.7 also shows the estimated coefficients of the predictors for this logistic regression model. The significance (Sig) levels for speed, age, BLD and BLH are lower than 0.05, while the significance values for BBH and BUD are much higher than 0.05. The ORs for the speed, age and BLD are larger than 1, indicating that the AIS2+ lower extremity injury odds increase with increasing the magnitudes of them. The OR for the BUH is less than 1, showing that the AIS2+ lower extremity injury odds decrease with increasing BUH.

Table 3.7 Logistic regression analysis results for model 1-A1.

Parameter	Boundary values	β	Sig	OR (95% CI)
Constant	/	-0.906	/	/
Speed	16-80 km/h	0.070	**<0.001**	1.072 (1.048-1.097)
Age	11-94 year	0.042	**<0.001**	1.043 (1.030-1.056)
BLD	0-204 mm	0.007	**0.019**	1.007 (1.001-1.013)
BUH	381-677 mm	-0.007	**0.044**	0.993 (0.991-0.999)
BBH	130-383 mm	0.002	0.597	1.002 (0.995-1.009)
BUD	12-211 mm	-0.004	0.530	0.996 (0.982-1.010)

According to the data in Table 3.7, the AIS2+ lower extremity injury probability (p) can be described as:

$$p = \frac{\exp(-0.906+0.070*speed+0.042*age+0.007*BLD-0.007*BUH)}{1+\exp(-0.906+0.070*speed+0.042*age+0.007*BLD-0.007*BUH)}, \quad (3.5)$$

where all the significant predictors are considered. It is clear from Eq. (3.5) that the relationship between AIS2+ lower extremity injury risk and the shape parameters (BLD and BUH) can be described visually using 3-dimensional plots when the age and speed are fixed. Figure 3.3 compares the AIS2+ lower extremity injury risk as a function of BLD and BUH for different speed and age levels. There are obvious differences in the AIS2+ lower extremity injury risk and the effects of bumper shape parameters on AIS2+ lower extremity injury risk between different speed and age levels.

Table 3.8 shows the logistic regression results for model 1-A2. These results indicate that the speed, age, BLH and BUH have a significant influence on AIS2+ lower extremity injury risk. Again the BBH and BUD are insignificant predictors. It is clear from the ORs that the AIS2+ lower extremity injury odds increase with increasing speed, age and BLH, and decrease with increasing BUH.

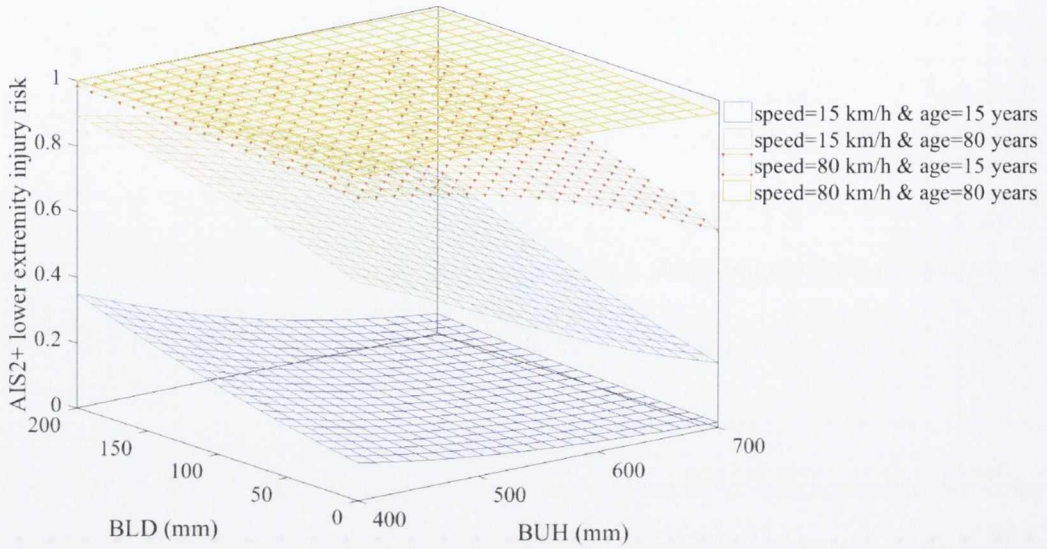

Figure 3.3 AIS2+ lower extremity injury risk as a function of BLD and BUH for different speed and age levels.

Table 3.8 Logistic regression analysis for model 1-A2.

Parameter	Boundary values	β	Sig	OR (95% CI)
Constant	/	-1.318	/	/
Speed	16-80 km/h	0.072	**<0.001**	1.074 (1.050-1.099)
Age	11-94 year	0.042	**<0.001**	1.043(1.030-1.056)
BLH	177-488 mm	0.006	**0.003**	1.006 (1.002-1.010)
BUH	381-677 mm	-0.007	**0.031**	0.993 (0.986-0.999)
BBH	130-383 mm	-0.002	0.649	0.998 (0.990-1.006)
BUD	12-211 mm	-0.005	0.482	0.995 (0.981-1.009)

Similarly, the AIS2+ lower extremity injury risk (p) for model 1-A2 can be estimated according to:

$$p = \frac{\exp(-1.318+0.072*speed+0.042*age+0.006*BLH-0.007*BUH)}{1+\exp(-1.318+0.072*speed+0.042*age+0.006*BLH-0.007*BUH)}, \quad (3.6)$$

including all the significant predictors. Figure 3.4 compares the AIS2+ lower extremity injury risk as a function of BLH and BUH (logically the BLH must be not higher than the BUH) for different speed and age levels. Again the AIS2+ lower extremity injury risk and the effects of bumper shape parameters on AIS2+ lower extremity injury risk vary for different speed and age levels.

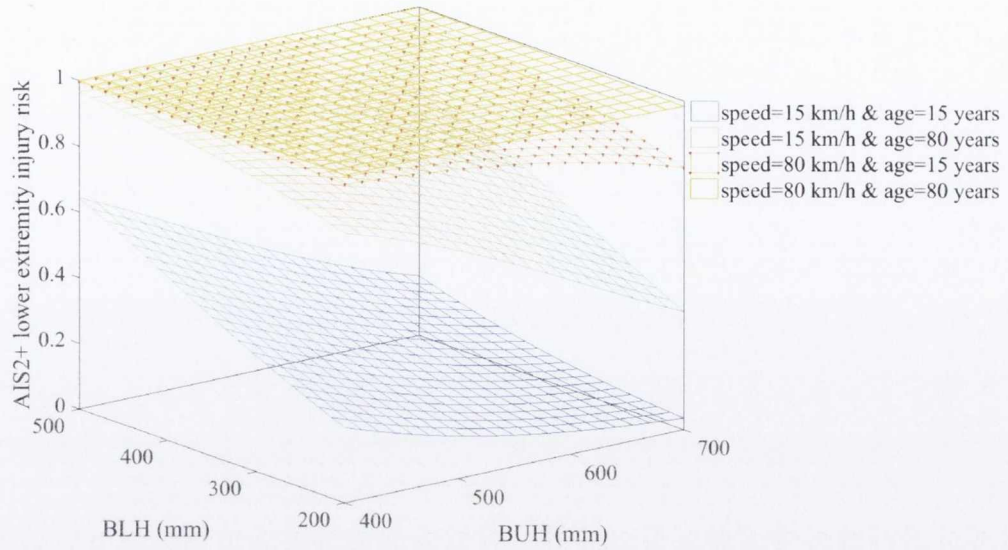

Figure 3.4 AIS2+ lower extremity injury risk as a function of BLH and BUH for different speed and age levels.

Table 3.9 shows the logistic regression analysis results for model 1-B. The Sig values indicate that both NBLH and NUBH have a significant influence on the AIS2+ lower extremity injury risk. The ORs show that the AIS2+ lower extremity injury odds increase by 2.7% (CI 0.8%-4.6%) with each percentage increase in NBLH (controlling for impact speed, pedestrian age and NBUH), and the AIS2+ lower extremity injury odds decrease by 4.1% (CI 1.5%-6.6%) with each percentage increase in NBUH (controlling for speed, age and NBLH).

Table 3.9 Logistic regression analysis results for model 1-B.

Parameter	Boundary values	β	Sig	OR (95% CI)
Constant	/	-1.235	/	/
Speed	16-80 km/h	0.071	**<0.001**	1.073 (1.049-1.099)
Age	11-94 year	0.043	**<0.001**	1.044(1.031-1.058)
NBLH	34-106 %	0.026	**0.006**	1.027 (1.008-1.046)
NBUH	75-144 %	-0.042	**0.002**	0.959 (0.934-0.985)

The AIS2+ lower extremity injury risk as a function of impact speed, pedestrian age, NBLH and NBUH can be described as:

$$p = \frac{\exp(-1.235+0.071*speed+0.043*age+0.026*NBLH-0.042*NBUH)}{1+\exp(-1.235+0.071*speed+0.043*age+0.026*NBLH-0.042*NBUH)}. \quad (3.7)$$

Based on this equation the AIS2+ lower extremity injury risks as a function of NBLH and NBUH for different speed and age levels were calculated and shown in Figure 3.5. The trends of the effects of NBLH and NBUH on AIS2+ lower extremity injury risk are as expected from the ORs. Again the effects of the normalized bumper shape parameters vary for different speed and age levels.

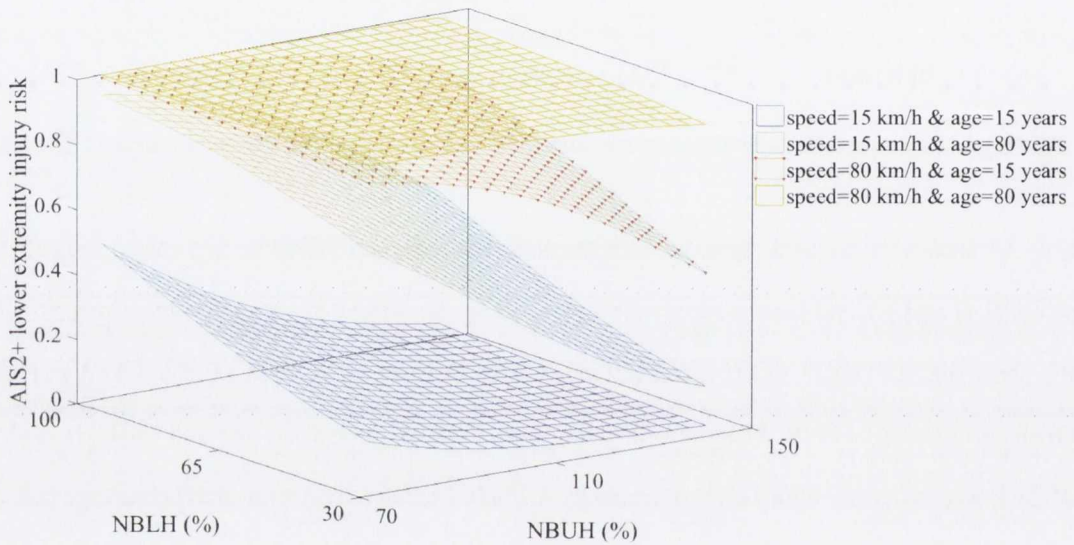

Figure 3.5 AIS2+ lower extremity injury risk as a function of NBLH and NBUH for different speed and age levels.

3.3.2 Bonnet Leading Edge (BLE) vs AIS2+ femur/pelvis injury risk

Table 3.10 and 3.11 show the results from the logistic regression analysis for the effects of BLE shape on AIS2+ femur/pelvis injury odds combining with the impact speed and pedestrian age (model 2-A1 and 2-A2 in Table 3.5, respectively). The results in Table 3.10 and 3.11 indicate that the impact speed and pedestrian age have a statistically significant influence on AIS2+ femur/pelvis injury risk (Sig<0.05), while the BUD, BLEH and BLEA are insignificant predictors for AIS2+ femur/pelvis injury risk.

The logistic regression analysis results for the effects of the normalzed bonnet leading edge height (NBLEH) on AIS2+ femur/pelvis injury odds (model 2-B in Table 3.4) are shown in Table 3.12. The NBLEH (Sig<0.05) has statistically significant effects on AIS2+ femur/pelvis injury odds. The OR

indicates that AIS2+ femur/pelvis injury odds increase with increasing NBLEH.

Table 3.10 Logistic regression analysis results for model 2-A1.

Parameter	Boundary values	β	Sig	OR (95% CI)
Constant	/	-12.214	/	/
Speed	16-78 km/h	0.069	**<0.001**	1.072 (1.034-1.111)
Age	11-94 year	0.038	**<0.001**	1.039 (1.020-1.059)
BUD	12-211 mm	0.007	0.324	1.007 (0.993-1.021)
BLEH	650-850 mm	0.008	0.137	1.008 (0.997-1.019)

Table 3.11 Logistic regression analysis results for model 2-A2.

Parameter	Boundary values	β	Sig	OR (95% CI)
Constant	/	-10.873	/	/
Speed	16-78 km/h	0.070	**<0.001**	1.073 (1.035-1.112)
Age	11-94 year	0.038	**<0.001**	1.039 (1.020-1.059)
BLEH	650-850 mm	0.011	*0.059*	1.011 (0.999-1.022)
BLEA	40-85°	-0.038	0.227	0.963 (0.906-1.024)

Table 3.12 Logistic regression analysis results for model 2-B.

Parameter	Boundary values	β	Sig	OR (95% CI)
Constant	/	-10.908	/	/
Speed	16-78 km/h	0.076	**<0.001**	1.079 (1.040-1.120)
Age	11-94 year	0.035	**<0.001**	1.035 (1.017-1.054)
NBLEH	62-102%	0.072	**0.012**	1.074 (1.016-1.136)

According to the logistic regression results in Table 3.12, the AIS2+ femur/pelvis injury risk as a function of impact speed, pedestrian age and NBLEH can be described as:

$$p = \frac{\exp(-10.908+0.076*speed+0.035*age+0.072*NBLEH)}{1+\exp(-10.908+0.076*speed+0.035*age+0.072*NBLEH)}. \quad (3.8)$$

Similarly, the AIS2+ femur/pelvis injury risks as a function of NBLEH for different speed and age levels were calculated and shown in Figure 3.6.

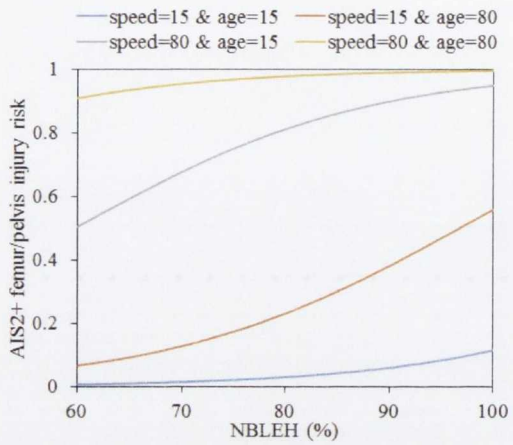

Figure 3.6 AIS2+ femur/pelvis injury risk as a function of NBLEH for different speed and age levels.

3.3.3 BLE and bonnet vs AIS3+ thorax injury risk

Table 3.13 and 3.14 show the logistic regression analysis results for the effects of BLE and bonnet shape (considering impact speed and pedestrian age) on AIS3+ thorax injury odds (model 3-A and 3-B in Table 3.4). The significance confidence values indicate that none of the sedan shape parameters (including the NBLH) has a statistically significant influence on the AIS3+ thorax injury risk, but the impact speed is a significant predictor.

Table 3.13 Logistic regression analysis results for model 3-A.

Parameter	Boundary values	β	Sig	OR (95% CI)
Constant	/	-14.238	/	/
Speed	17-78 km/h	0.064	**0.019**	1.066 (1.011-1.125)
Age	13-94 year	0.030	*0.064*	1.031 (0.998-1.064)
BLEH	650-885 mm	0.012	0.143	1.012 (0.996-1.029)
BA	8-25°	-0.042	0.648	0.959 (0.801-1.148)

Table 3.14 Logistic regression analysis results for model 3-B.

Parameter	Boundary values	β	Sig	OR (95% CI)
Constant	/	-6.297	/	/
Speed	16-78 km/h	0.062	**0.016**	1.064 (1.011-1.120)
Age	11-94 year	0.030	*0.071*	1.031 (0.997-1.064)
NBLEH	63-100%	0.014	0.729	1.014 (0.937-1.097)

3.3.4 BLE, bonnet and windscreen vs AIS3+ head injury risk

The logistic regression analysis results for the effects of BLEH, BL and NBLEH on AIS3+ head injury odds (model 4-A and 4-B, see Table 3.4) without control for head contact location are shown in Table 3.15 and 3.16. The estimated effects of BLEH, BA, WA and NBLEH on AIS3+ head injury odds (model 5-A and 5-B, see Table 3.4) controlling head contacts within windscreen centre are shown in Table 3.17 and 3.18. The Sig values show that all shape parameters are not significant for AIS3+ head injury odds. Impact speed and pedestrian age is significant for AIS3+ head injury odds when head contacts are not controlled (Tables 3.15 and 3.16), but they are not significant for AIS3+ head injury odds when the contacts are fixed in the windscreen centre area (Tables 3.17 and 3.18).

Table 3.15 Logistic regression analysis results for model 4-A.

Parameter	Boundary values	β	Sig	OR (95% CI)
Constant	/	-2.846	/	/
Speed	16-73 km/h	0.054	**<0.001**	1.056 (1.025-1.087)
Age	11-94 year	0.022	**0.008**	1.023 (1.006-1.040)
BLEH	650-886 mm	−0.002	0.637	0.998 (0.989-1.007)
BL	300-1200 mm	-0.001	0.620	0.999 (0.998-1.001)

Table 3.16 Logistic regression analysis results for model 4-B.

Parameter	Boundary values	β	Sig	OR (95% CI)
Constant	/	-3.380	/	/
Speed	16-73 km/h	0.052	**<0.001**	1.053 (1.023-1.084)
Age	11-94 year	0.025	**0.005**	1.025 (1.008-1.044)
NBLEH	62-105%	-0.019	0.310	0.981 (0.945-1.018)

Table 3.17 Logistic regression analysis results for model 5-A.

Parameter	Boundary values	β	Sig	OR (95% CI)
Constant	/	-7.191	/	/
Speed	17-70 km/h	-0.022	0.473	0.979 (0.922-1.038)
Age	12-94 year	0.017	0.272	1.017 (0.987-1.048)
BLEH	650-886 mm	0.013	0.134	1.013 (0.996-1.030)
BA	8-25°	-0.029	0.758	0.971 (0.807-1.169)
WA	24-55°	-0.128	0.271	0.880 (0.702-1.104)

Table 3.18 Logistic regression analysis results for model 5-B.

Parameter	Boundary values	β	Sig	OR (95% CI)
Constant	/	2.235	/	/
Speed	17-70 km/h	-0.033	0.317	0.968 (0.908-1.032)
Age	12-94 year	0.015	0.314	1.015 (0.986-1.046)
NBLEH	62-105%	-0.046	0.295	0.955 (0.877-1.041)

3.4 Discussion

3.4.1 Injury risk estimated by the logistic regression

According to Eq (3.4) the probability of an injury as a function of the predictors can be simplified as:

$$p = \frac{\exp(X)}{1+\exp(X)}, \tag{3.9}$$

where p is the probability of an AIS2+/AIS3+ injury and X is the combined predictor. Figure 3.7 shows the curve of p as a function of X. It is clear from this figure that the effect (the slope of the curve) of the predictor (X) on the injury risk (p) varies with the magnitude of the predictor. For low and high X values the effects are weak, but for the X range from -2 to 2 the effects are strong, see Figure 3.7. This can explain the results in Figure 3.3-3.6 that for the logistic regression models estimated (Eq. (3.5-3.8)) when the impact speed and pedestrian age are both at a low or high level (the injury risk curve has a gentle slope) then the effects of the sedan shape parameters on pedestrian injury risk are weaker than that for the situations where only one of them is at a low level (the injury risk curve has a steep slope).

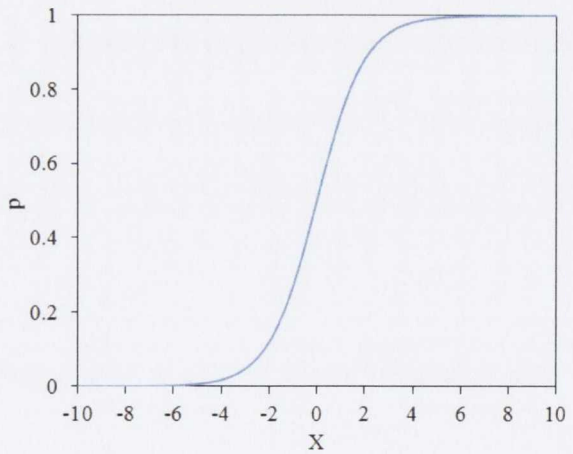

Figure 3.7 Probability of an AIS2+/AIS3+ injury as a function of the combined predictor.

3.4.2 Effects of bumper profile on lower extremity injury risk

As expected the logistic regression results show that the impact speed and pedestrian age have a

statistically significant influence on AIS2+ lower extremity injury risk and they are with a higher significance confidence level than the bumper shape parameters (Table 3.7-3.9). The logistic regression results also indicate that the direct bumper shape parameters of bumper lower depth (BLD), bumper lower height (BLH) and bumper upper height (BUH) are significant predictors for AIS2+ lower extremity injury odds. However the bumper bottom height (BBH) and bumper upper depth (BUD) have no significant effect on pedestrian AIS2+ lower extremity injury risk.

The overall estimated effects of the bumper profile on AIS2+ lower extremity injury risk are shown in Table 3.7 and 3.8. Generally, the AIS2+ lower extremity injury risk increases with increasing BLD and BLH and decreasing BUH. The ORs predict that, when controlling for speed, age and BUH (also the BBH and BUD, but they are not significant predictors), an average 7% (CI: 1%-13%) and 6% (CI: 2%-10%) increase in AIS2+ lower extremity injury odds for every 1 cm increase in BLD (0-20 cm) and BLH (18-49 cm) respectively (Table 3.7 and 3.8). For the BUH, the ORs indicate that 1 cm increase in BUH (38-68 cm) results in 7% (CI: 1%-9%) or 7% (CI: 1%-14%) decreases in AIS2+ lower extremity injury odds when the BLD or BLH is fixed respectively, and again controlling the impact speed and pedestrian age (also the BBH and BUD, but they are not significant predictors). Generally, these estimated effects suggest that a safe bumper for a pedestrian's lower extremity should have a flat (low BLD) and wide (low BLH and high BUH) shape. Although qualitative understanding of the influence of these bumper shape parameters on pedestrian injuries has been available for some time (e.g. Simms and Wood 2009), this is the first time these relationships have been quantified on the basis of accident data rather than staged tests or simulations. For normalized bumper shape parameters, the AIS2+ lower extremity injury odds could be reduced by decreasing the NBLH value and increasing the NBUH value, when the impact speed and pedestrian age is controlled for (Table 3.9). This also indicates that a low BLH and high BUH (a wide bumper) is beneficial for lower extremity injury prevention since for a given pedestrian a low BLH and high BUH lead to a small NBLH and large NBUH.

A general biomechanical explanation lies in the loading condition leading to lower extremity injury from a sedan bumper contacting an adult pedestrian lower extremity as shown in Figure 3.8, where F_U is the inertia force from the upper body, F_C is the impact force from the vehicle bumper, F_L is the

inertia force from the leg/foot below the bumper lower edge and M is the resultant bending moment (force F multiplied by moment arm l) for a particular location in the lower extremity. The bending moment is key for long bone fracture and knee ligament rupture (Schmitt et al., 2010) and is strongly associated with the magnitude and distribution of these forces. It is evident that a small BLD and a low BLH combine to reduce lower extremity bending, and the effects of these are quantified in Table 3.7 and 3.8. Furthermore, a high BUH (consequently a high NBUH) moves the contact location above the knee to the femur and reduces the AIS2+ lower extremity injury risk as long as the BLD and BLH are not too large, since leg injuries account for more than 80% of all the AIS2+ lower extremity injuries in the sample. Particularly, the raw data of sample 1 shows that about 50% of the cases with AIS2+ lower extremity injuries were involved with sedans having a BUH at or lower than the knee area, while this proportion is only 33% for the cases without AIS2+ lower extremity injuries. This indicates that it is better to move the BUH up to the femur area for pedestrian lower extremity protection in sedan impacts. The lower extremity loading condition shown in Figure 3.8 may also explain the insignificance of BBH and BUD, since the bumper bottom is not involved in lower extremity contacts and the BUH only affects the femur loading (most of AIS2+ lower extremity injuries in the accident data are from the leg).

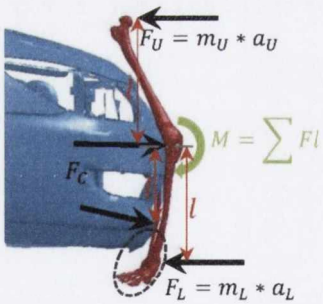

Figure 3.8 Typical loading condition for pedestrian lower extremity when struck by sedan bumper.

In summary, a sedan bumper with a small BLD, a low BLH and a high BUH is a good choice for pedestrian lower extremity injury prevention for pedestrians taller than 150cm (similar findings may apply for shorter pedestrians, but not enough accident cases are available). For example, the modern generation models of the Toyota Corolla, VW Golf and Polo generally fit this profile. The general trends of BLD and BLH predicted here for a safe sedan bumper profile are qualitatively similar to findings of previous studies (Liu et al., 2002; Otte and Haasper, 2005 and 2007; Pal et al., 2015), but

the combination of quantified findings and application to recent accident data makes the current results important for vehicle designers and legislators. For the BUH, this is the first time to propose that a sedan bumper upper edge should be higher than the pedestrian's knee for lower extremity protection. Assessing these proposals with the current dataset shows that 7 out of 10 cases (70%) meeting the profile of a safer bumper (small BLD, small BLH and large BUH) have AIS2+ lower extremity injuries while 10 of 10 cases (100%) not fitting this profile (i.e. large BLD, large BLH and small BUH) have AIS2+ lower extremity injuries when the impact speed and pedestrian age are limited to the range of 36-45 km/h and 18-60 years respectively.

3.4.3 Effects of bonnet leading edge profile on femur/pelvis injury risk

The logistic regression analysis results show that the impact speed, pedestrian age, NBLEH are significant predictors for AIS2+ femur/pelvis injury odds, while the BUD, BLEH and BLEA are not significant (Tables 3.10-3.12). The OR indicates that each 10% increase in NBLEH (62-102%) leads to a 74% (CI: 16%-136%) increase of the odds of an AIS2+ femur/pelvis injury risk (Table 3.12). This finding is well-established qualitatively and is likely due to the reduced direct loading on the pelvis and hip joints in the case of bonnet leading-edges which are significantly below the hip height (Pritz and Pereira, 1983; Matsui et al., 1999; Liu et al., 2002; Schmitt et al., 2010; Han et al., 2012; Pal et al., 2015), but here the effect has been quantified on the basis of recent accident cases. The wide confidence intervals (CI: 16%-136%), even controlling for age and speed, reflect the uncertainty in this relationship, and stiffness is likely to play a significant role here (Matsui et al., 1999).

In practice it is difficult to control the NBLEH with current technology, since this obviously depends on the pedestrian height, and Figure 3.9 demonstrates the weak relationship between BLEH and NBLEH. This may be largely due to the fact that the range for hip height (72-117 cm, maximum relative difference of 63%) is much wider than that for BLEH (65-85 cm, maximum relative difference of 32%) in the sample data (sample 2 in Table 3.2) where only sedan cases were considered. Nonetheless, in the accident data, the Opel Corsa B, BMW E36, Renault Megane I and Suzuki Swift are examples of vehicles with lower bonnet leading edges (<700 mm) and these vehicle models (2 of 13 cases (15%) with AIS2+ femur/pelvis injuries) are also generally associated with

lower AIS2+ femur/pelvis injury risks than the high bonnet leading edge (>800 mm) vehicles (such as Audi 80, Skoda Octavia II, Volvo 300, etc., where 8 of 15 cases (53%) had AIS2+ femur/pelvis injuries) in the sample data (with no significant differences in the impact speed and age between these two groups). Therefore it is proposed to favour lower bonnet leading edges for sedans to provide femur and pelvis protection.

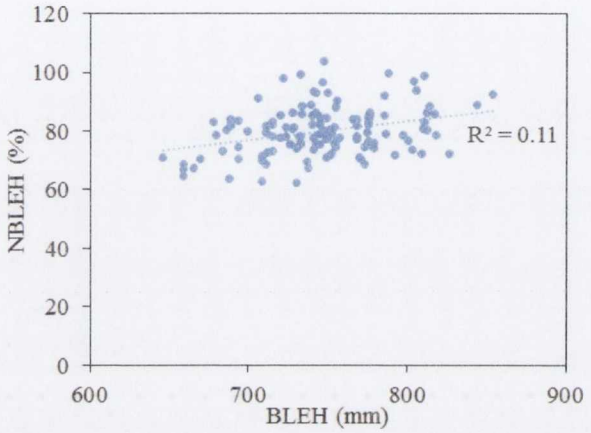

Figure 3.9 Linear regression between the NBLEH and BLEH.

3.4.4 Upper body injuries

The logistic regression analysis results show that none of the sedan shape parameters has a statistically significant influence on the AIS3+ thorax and head injury odds, see Table 3.13-3.18. This may be largely because the upper body kinematics are the cumulative effect of the whole body motion and the injury of the upper body is strongly affected by its impact boundary conditions (impact speed, angle, etc.) during the contacts with the vehicle front structures. Previous studies based on multi-body simulations indicated that a lower BLEH may lead to higher head impact speed (Pritz and Pereira, 1983; Liu et al., 2002) but the current study shows the effect of NBLEH on AIS3+ head injury risk is not statistically significant. Probably, variations in impact configurations in accidents may not be well reflected by published numerical simulations considering only limited impact configurations or there are some other unclear factors besides the head contact speed (such as the neck force, contacting angle, etc.) affecting head injuries. For the thorax, no clear reference is available from other studies to identify the effects of sedan front shape on injury risk. These findings may suggest that the motion of the whole body affects the upper body injury outcome in

vehicle collisions. Therefore, the current subsystem impactor test approach for vehicle safety performance using a simple headform impactor may need to be improved since the mass and motion of the body is not included.

The bonnet length is not significant as observed in sample 4, but a previous study using accident data collected during 1985-1992 shows that that 'short' bonnets (>950 mm and <1,200 mm) lead to a higher risk for serious head injuries than the 'long' bonnets (>1,200 mm) due to a higher proportion for head to bonnet end contacts (Otte, 1994b). This difference is mainly due to the change of vehicle front designs during later 1990's to early 2000's, where more small family cars were introduced to the market. Then most head injuries in recent accidents are from contacts with the windscreen area (Figure 3.2), and hence the bonnet length losses its significant effects on AIS3+ head injury risk.

Surprisingly, the impact speed and pedestrian age are not a statistically significant factor on AIS3+ head injury when head contacts are controlled within the windscreen centre (see Tables 3.17 and 3.18). This finding is not in line with the results for sample 4 where head contacts are not controlled (Tables 3.16 and 3.17) and other studies based on the accident data without a clear inclusion criterion for the head contact location and minimum head injury AIS level, where impact speed is statistically significant for AIS3+ head injuries (Kong and Yang, 2010; Nie et al., 2015). The pedestrian age was also found insignificant for head AIS3+ head injury risk in PCDS accidents without controlling the head contact location (Zhang et al. 2008). These findings may suggest that the head injury risk from contacts with the windscreen centre might be not as sensitive to the impact speed as contacts with other locations (e.g. bonnet, windscreen edge and frame). The analysis results of the current work and previous studies may suggest that the significance level of pedestrian age on head injury risk is dependent on the analysis sample. However, further data collection is also needed to explore these findings.

3.5 Summary

The effects of sedan front shape on pedestrian injury risk were analysed based on GIDAS pedestrian accident data captured after 2000 via statistical methods. In particular, results are presented for the

quantified effects of sedan profile on AIS2+ lower extremity injury risk (with bumper), AIS2+ femur/pelvis injury risk (with bonnet leading edge), AIS3+ thorax injury risk (with bonnet leading edge height and bonnet angle) and AIS3+ head injury risk (with bonnet leading edge height and bonnet and windscreen angle). The results suggest that sedan bumpers should support the leg with a low and forward lower bumper structure and evenly contact the lower extremity up to the femur area with a wide upper bumper which extends above the knee to protect a pedestrian's lower extremity. A low bonnet leading edge helps to reduce pelvis injury risk. Although many of these design features have been proposed previously on the basis of computational models and generalized accident studies, the data presented in this study represents the first attempt to quantify the detailed effects of vehicle shape parameters on pedestrian (>150 cm) injury outcome, and the findings are based on pedestrian accidents since the year 2000. The results also show how the influence of sedan front design on injury outcome varies for different impact speed and pedestrian age levels. The selected sedan front shape parameters are not significant for AIS3+ thorax and head injury risk. The AIS3+ head injury results surprisingly show no statistical dependency on vehicle impact speed and pedestrian age when head contacts are controlled within the windscreen centre.

Chapter 4 Effects of Pedestrian Gait Stance on Lower Extremity Kinematics and Injury Risk

4.1 Introduction

The lower extremity is generally the first body part impacted by the vehicle front in vehicle-to-pedestrian collisions. Accident studies indicate that the lower extremity is one of the most vulnerable parts of the human body when struck by vehicles (Chapter 2). Typical lower extremity injuries include fractures of the long bones (femur, tibia, and fibula), injuries of the knee joint (especially ligament avulsion and condyle fractures), ankle dislocation and foot bone fractures (Otte and Haasper, 2005 and 2007; Yang, 2005). Previous analyses of causation of pedestrian injuries using accident data (Matsui, 2005; Otte and Haasper, 2007), mathematical models (Liu et al., 2002; Han et al., 2012; Mo et al., 2014), and cadaver tests (Kerrigan et al., 2008b) have shown that vehicle front shape and impact velocity have a strong influence on lower extremity injuries. Meanwhile, some studies (Untaroiu et al., 2009; Elliott et al., 2012b; Peng et al., 2012b) have shown that the pedestrian gait phase influences pedestrian kinematics and injury mechanisms. Elliott et al. (2012b) and Peng et al. (2012a) reported that pedestrian gait significantly influences pedestrian head impact conditions. However, the effect of pedestrian gait on lower extremity kinematics and injuries has not been analysed. Understanding this is important since real accidents occur over the full range of possible gait positions since more than half of pedestrians involved in accidents were struck while walking (Chidester et al., 2001; Kuehn et al., 2005b). Therefore pedestrian protection requires knowledge of the influence of these gait positions in real world accidents.

The purpose of this chapter is therefore to investigate the effect of pedestrian gait on kinematics and injuries of the lower extremity. Firstly, the Total Human Model for Safety (THUMS) Version 4.0 50th% adult male (AM50) pedestrian model was used to simulate impact responses and injury biomechanics of pedestrians in vehicle collisions. The FE models of vehicle front structures were developed based on available FE models of a sedan and a SUV used in previous studies (Chen and Yang, 2012; Han et al., 2012). A parameter study was implemented via a set of simulations of vehicle

front to THUMS impacts (in different gait stances) to investigate the effect of pedestrian gait stance on lower extremity injuries. Then multi-body vehicle-to-pedestrian simulations were developed based on the MADYMO 50th% pedestrian model (in different gait stances) and multi-body vehicle models (a sedan and a SUV matching the shape of corresponding FE vehicle models). The multi-body simulation results were compared to FE simulations to assess the findings from FE modelling and the lower extremity injury predictive capability of the MADYMO 50th% pedestrian model in terms of changing gait stance. The findings of the current chapter can provide basic references for selection of pedestrian gait positions in the later optimization of vehicle front design for pedestrian protection.

4.2 FE simulation

4.2.1 FE human body model

The Total Human Model for Safety (THUMS) Version 4.0 AM50 pedestrian model was jointly developed by Toyota Central R&D Labs, Inc. and Toyota Motor Corporation (see Figure 4.1). The THUMS Version 4.0 AM50 pedestrian model contains nearly two million elements and enables prediction of brain and internal organ injuries as well as skeletal and ligament injuries. The lower extremity models of THUMS include all the skeletal parts and the major soft tissues. The skeletal parts were modelled by elastic-plastic material and hyper-elastic material was assumed for flesh, ligaments and tendons (Shigeta et al, 2009). The biofidelity of the models for body region components and the kinematics of the whole body model were verified in previous studies by comparing their impact responses with cadaver tests (Shigeta et al, 2009; Watanabe et al, 2011). The THUMS lower extremity model showed good agreement with post-mortem human subjects (PMHS) test data of static bending and dynamic impact in validations with maximum relative errors within ±15% (Shigeta et al, 2009).

The THUMS model was configured into six gait cycle stances based on a previous study (Untaroiu et al., 2009) and these were used to assess the influence of pedestrian gait on lower extremity kinematics and injuries. To set the gait stance, firstly the joints were rotated according to the angle data from the study of Untaroiu et al. (2009). The ligaments were

modified to keep them taut if they loosened due to joint rotation, then the skin and flesh parts around the rotated joints were remeshed (Toyota Motor Corporation, 2011). Unfortunately, there are no cadaver tests in which different initial gait positions are used, so it is not possible to explicitly validate the biofidelity of the modified models.

The pedestrian model was struck by vehicles from the right side for all simulations. As shown in Figure 4.1, the ipsilateral lower extremity (dark red) standing (10%, 25% and 40% stances) or in swing (60%, 75% and 90% stances), leading (10%, 75% and 90% stances) or lagging (25%, 40% and 60% stances), knee flexed (10%, 60% and 75% stances) or straight (20%, 40% and 90% stances), and legs overlapping in the sagittal plane (25% and 75% stances) or not (10%, 40%, 60% and 90% stances) were considered in the gait stance matrix. This simulation matrix also considered different knee initial positions between the ipsilateral and contralateral lower extremity: both are flexed (10% and 60% stances), both are extended (40% and 90% stances), one is flexed and one is extended (25% and 75% stances).

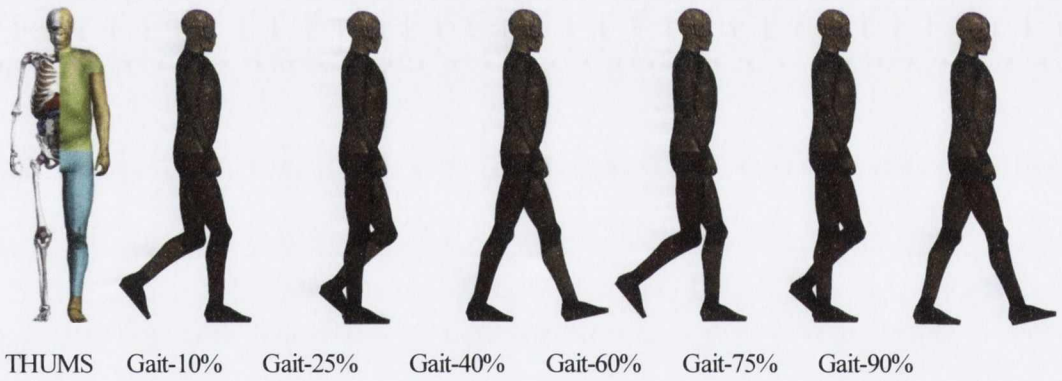

Figure 4.1 THUMS Version 4 AM50 pedestrian model and stances for pedestrian gait study, in simulations the pedestrian was struck from the right lower extremity (dark red).

4.2.2 Vehicle front FE models

FE models of the Sedan front and the SUV front were created for simulations of vehicle-to-pedestrian collisions based on full scale FE models of production vehicles which were validated against results from vehicle-barrier frontal impact tests. The frontal structures were extracted from the original models by cutting off the rear part of both vehicle models from the A-pillar, as shown in Figure 4.2 (a) and (b). The SUV bumper is higher than the knee of the THUMS

model and has no lower bumper structure, while the sedan bumper height is similar to the knee height and has a lower bumper below the knee. The mechanical properties of the vehicle front models were defined as the corresponding part in the original models to maintain the stiffness of front structures, see Table 4.1.

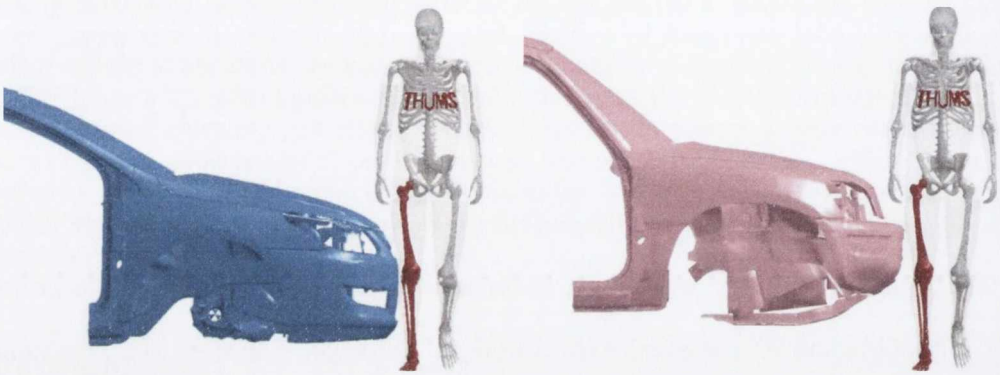

(a) (b)

Figure 4.2 Impact simulation of vehicle front FE models to THUMS: (a) sedan-to-THUMS, (b) SUV-to-THUMS.

Table 4.1 Material properties of the main frames of vehicle front models.

Vehicle	Part	Material model	Density ρ (kg/m3)	Young's modulus E (MPa)	Yield stress δ (MPa)	Poisson ratio
Sedan	Bumper	Elastic-Plastic	1,000	2,000	20	0.3
	Bumper beam	Elastic-Plastic	7,890	210,000	423	0.3
	Front rail	Elastic-Plastic	7,890	210,000	423	0.3
	Hood outer	Elastic-Plastic	7,890	210,000	239	0.3
	Hood inner	Elastic-Plastic	7,890	210,000	129	0.3
	A-pillar	Elastic-Plastic	7,890	210,000	423	0.3
SUV	Bumper	Elastic-Plastic	1,200	1,970	45	0.3
	Bumper beam	Elastic-Plastic	7,890	210,000	417	0.3
	Front rail	Elastic-Plastic	7,890	210,000	276	0.3
	Hood outer	Elastic-Plastic	7,890	210,000	270	0.3
	Hood inner	Elastic-Plastic	7,890	210,000	208	0.3
	A-pillar	Elastic-Plastic	7,890	210,000	305	0.3

The sedan front FE model was established based on a real-world medium-size vehicle. As shown in Figure 4.2 (a), the vehicle FE model includes a total of 277,095 elements and 275,277 nodes and the

mass is 1370 kg. The model consists of hexahedron solid elements, shell elements, beam elements, spring elements and damping units. The full scale sedan FE model was validated against two types of frontal impacts results, including a 100% rigid barrier (RB) crash test at 50 km/h and a 40% offset deformable barrier (DB) crash test at 56 km/h and was used previously (Chen and Yang, 2012) for frontal impact simulations.

The SUV front FE model was based on the FE model from NCAC (2008), which was originally generated for frontal crash simulations. For simulations of the pedestrian impact, the frontal structures forward of the A-pillar were extracted from the original SUV model, as shown in Figure 4.2 (b). The components for modelling the bumper, hood panel, cowl and windshield were re-meshed (Han et al., 2012). The mass and inertia of the removed parts were added to make the reduced model have the same mass and inertia as the original full size model.

4.2.3 Setup for FE simulation

The vehicle-to-pedestrian impact simulations were conducted via LS-Dyna software based on the configurations of six pedestrian gaits and two vehicle front models of the sedan and SUV (Figure 4.2), making a total of 12 simulations at a vehicle impact speed of 40 km/h, since this is the standard speed in the Euro-NCAP tests (Euro-NCAP, 2013). Friction coefficients were applied to the pedestrian to vehicle contact (0.3) and the pedestrian to ground contact (0.7), based on the study from Linder et al. (2004). Only lateral impact in the centre of the vehicle front was analysed in the current study since pedestrians are mainly hit from the side (Otte and Haasper, 2005). Pedestrian walking velocity and vehicle braking were not considered in this study.

4.2.4 Injury assessment metrics

The magnitude of the von-Mises stress in the cortical bone (Bonfield, 1987) and the knee lateral bending angle and shearing displacement (Bose et al., 2008; Mo et al., 2014) were the parameters used to assess lower extremity long bone and knee ligament injury risk. The effect of pedestrian gait stance on lower extremity injury risk was assessed by comparisons of the predicted magnitudes of injury parameters between different gait stances. The predicted knee lateral bending angle and

shearing displacement were measured by the help of two vectors (red in Figure 4.3) defined along the tibia and femur diaphysial axes and two points (yellow in Figure 4.3) defined on the intercondylar eminence of the tibial plateau and the terminal groove of the femoral condyles in the middle of the knee joint, respectively. The average yield stress of tibial (129 MPa) and femoral (114 MPa) cortical bone from cadaver tests (Takahashi et al., 2000) and thresholds of knee lateral bending angle (15 degrees) and shearing displacement (14 cm) for knee ligament rupture (Mo et al., 2014) were applied as a reference for lower extremity injury risk assessment. The current chapter focuses on the relative effects of pedestrian gait position on the knee kinematics and bone loading rather than absolute values. Furthermore, since the fracture/failure thresholds for human body lower extremity structures are within a wide range (Takahashi et al., 2000), tissue failure was not explicitly considered in the modelling.

Figure 4.3 Geometric constructions used to assess knee lateral bending and shearing.

4.2.5 FE simulation results

4.2.5.1 Lower extremity overall kinematics

The typical lower extremity kinematics for the sedan and SUV impacts are shown in Figure 4.4 for the 10% gait stance. The first contact area in the lower extremity is the knee and leg for sedan impacts, while it is the knee and thigh for SUV impacts. These differences in the first contact area lead to different kinematics in the lower extremity during the impact. For sedan impacts, the leg is directly struck by the bumper system and the thigh mainly impacts with the bonnet leading edge due to inertia from the whole upper body, see Figure 4.4 (a). For SUV impacts, the thigh is directly struck by the bumper and the leg moves toward the bumper due to its inertia, see Figure 4.4 (b).

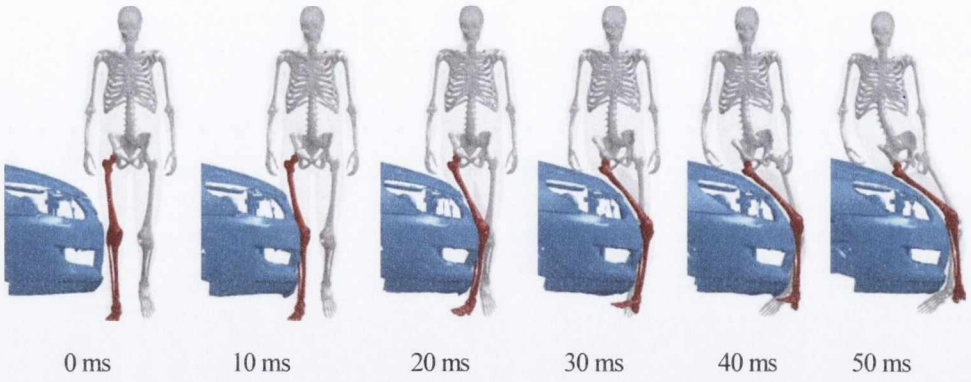

(a)

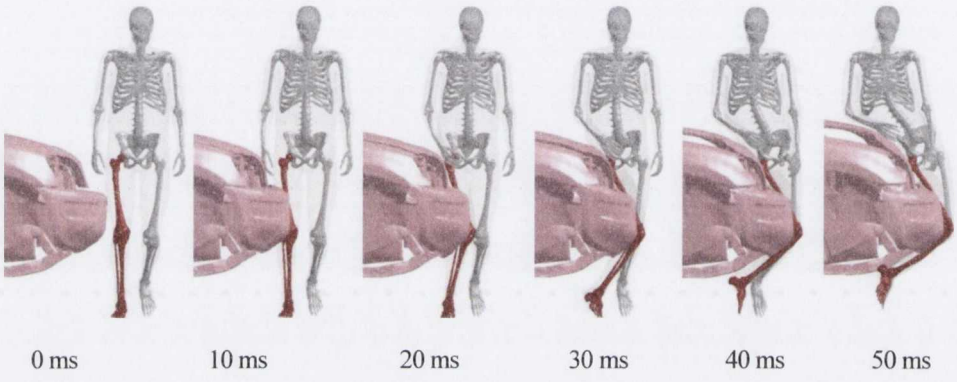

(b)

Figure 4.4 Typical pedestrian global kinematics in (a) sedan and (b) SUV impact (10% gait stance).

4.2.5.2 Von-Mises stress in the tibia and femur

The location and timing of maximum von-Mises stress in the tibial and femoral cortical bone of the ipsilateral and contralateral lower extremities for sedan and SUV impact (10% gait stance) are shown in Figure 4.5. This demonstrates the well-known differences in pedestrian lower extremity kinematics and von-Mises stress distribution for sedan compared to SUV impacts.

For a sedan impact, the leg is supported by both the bumper (proximal tibia) and lower bumper (distal tibia), and the tibia shaft contacts with the soft area between the bumper and lower bumper, see Figure 4.4 (a). The von-Mises stress in the tibia shaft is mainly caused by tibia bending which results from the inertial loading of the lower extremity mass below the lower bumper, see Figure 4.5 (a) and (b). The maximum von-Mises stress in the femur shaft for the sedan impact occurs due to femur bending (ipsilateral and contralateral lower extremity) and direct impact of the bonnet leading edge (ipsilateral lower extremity).

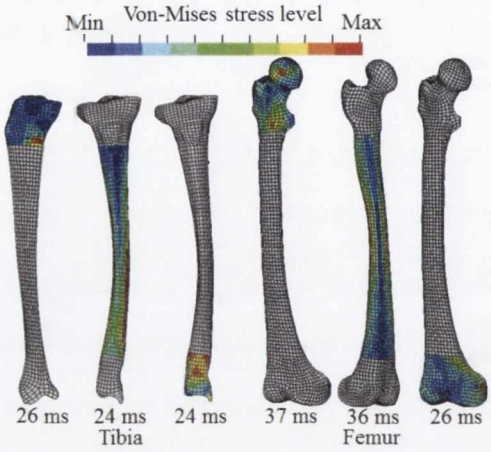

(a) Ipsilateral lower extremity

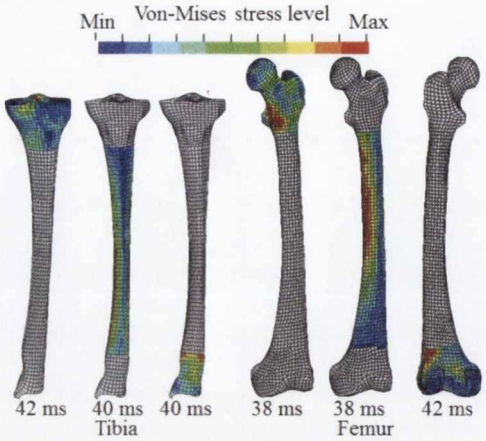

(b) Contralateral lower extremity

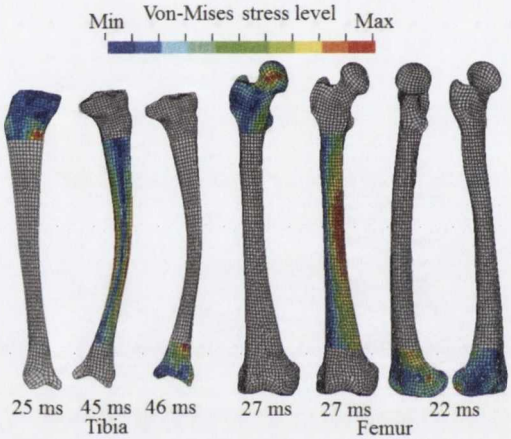

(c) Ipsilateral lower extremity

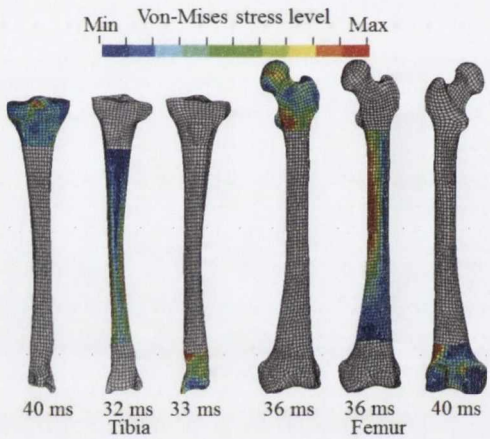

(d) Contralateral lower extremity

Figure 4.5 The location and timing of maximum von-Mises stress in the tibial and femoral cortical bone in the ipsilateral and contralateral lower extremity for (a & b) sedan and (c & d) SUV impact. The 10% gait stance is shown, and for each bone the maximum stress and the time of the maximum stress are shown separately for the proximal, shaft and distal regions.

For the SUV impacts, the maximum von-Mises stress of the femur shaft occurs due to femur bending. However, the leg is now only supported by the bumper (proximal tibia), and the tibia shaft of the ipsilateral lower extremity impacts with the stiff area under the bumper but no severe contact occurs to the contralateral leg, see Figure 4.4 (b). The von-Mises stress in the tibia shaft of the ipsilateral lower extremity results from the direct impact of the SUV structure and bending of the tibia toward the opposite direction of vehicle travel, see Figure 4.5 (c). The maximum von-Mises stress in the tibia shaft of the contralateral lower extremity occurs at an early stage due to bending of the tibia toward the same direction of vehicle speed, see Figure 4.5 (d).

4.2.5.3 Relationship between bone stress and gait stance

The predicted maximum von-Mises stress in the distal end, the shaft and the proximal end of the tibial and femoral cortical bone of the ipsilateral and contralateral lower extremity in different gait stances are shown in Figure 4.6 (a) and (b) for sedan and SUV impacts respectively.

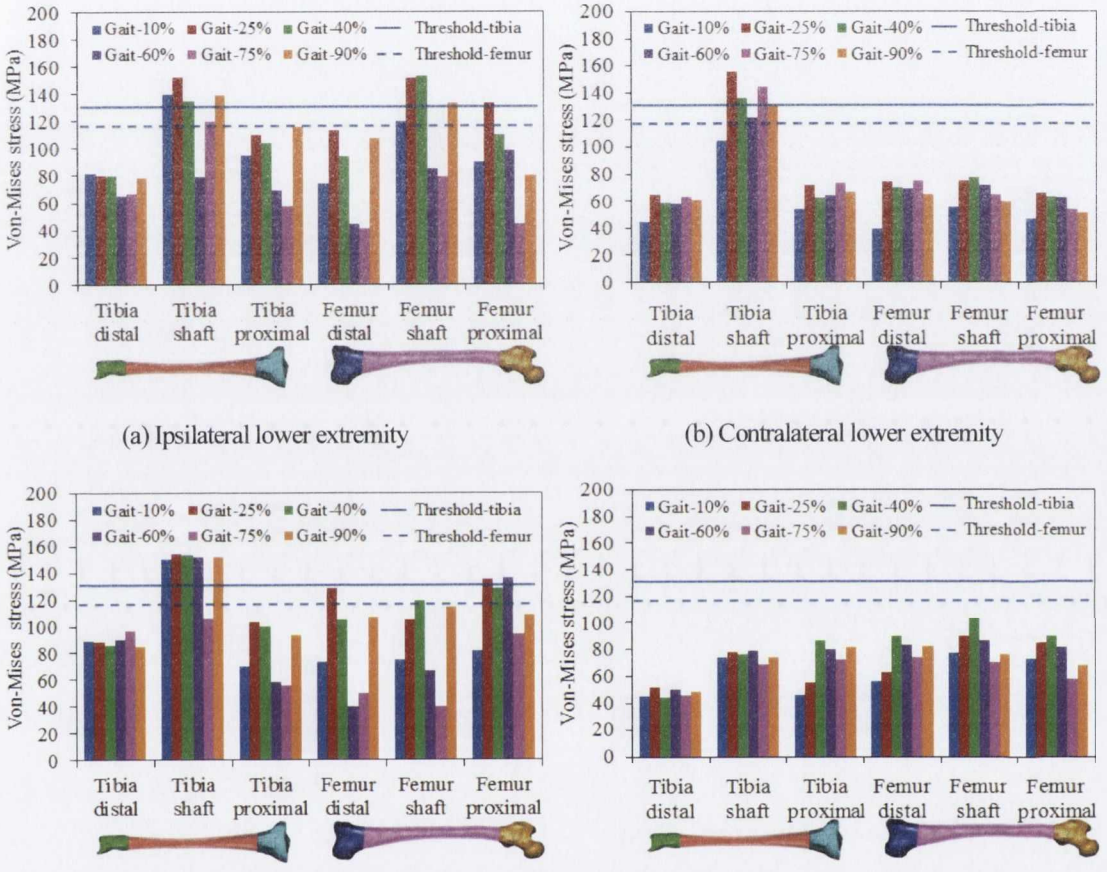

(a) Ipsilateral lower extremity

(b) Contralateral lower extremity

(c) Ipsilateral lower extremity

(d) Contralateral lower extremity

Figure 4.6 Maximum von-Mises stress in the tibia and femur cortical bone in the ipsilateral and contralateral lower extremity for sedan (a & b) and SUV (c & d) impacts.

4.2.5.4 Knee lateral shearing displacement and bending angle

The predicted maximum knee lateral shearing displacement and bending angle in the ipsilateral and contralateral knee for different pedestrian gait stances during the sedan and SUV impacts are shown in Figure 4.7. The simulation results show that pedestrian gait stance has a significant influence on knee loading.

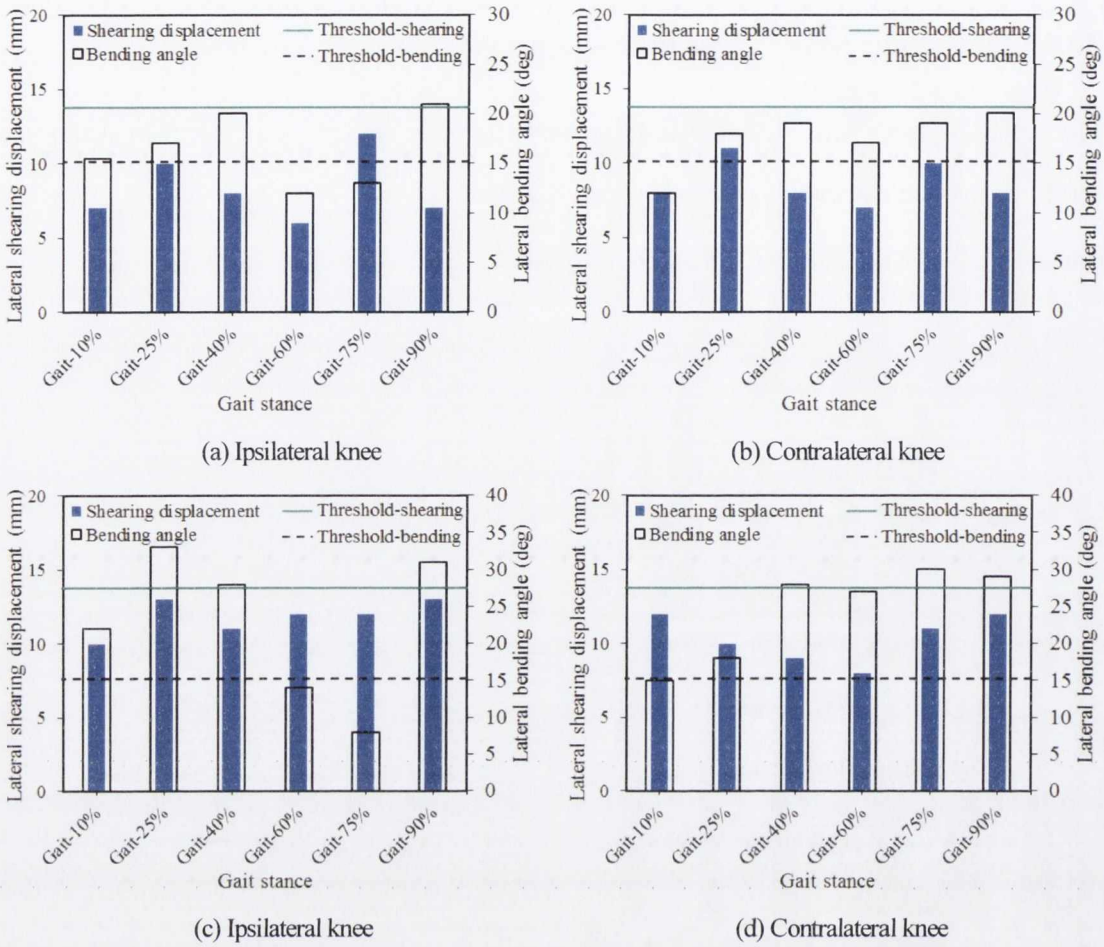

Figure 4.7 Maximum knee shearing displacement and bending angle in the ipsilateral and contralateral knee in impact against (a & b) sedan and (c & d) SUV.

4.2.6 Discussion for FE simulation

As expected for a 40 km/h pedestrian impact, the predicted von-Mises stress magnitudes are close to the failure thresholds for tibial (129 MPa) and femoral (114 MPa) cortical bone (Takahashi et al., 2000), see Figure 4.6. Similarly, the predicted knee lateral bending angle and shearing displacements are close to the thresholds (15 degrees and 14 cm respectively) from the literature (Mo et al., 2014), see Figure 4.7. Therefore, since the main focus of this chapter is the relative influence of pedestrian gait, these findings indicate that the gait stance may contribute to the risk of bony and/or soft tissue (knee ligament) injury. Given the absence of detailed accident data which can be used to assess the predictions from this study, the emphasis here is on predicted injury trends as a function of gait stance rather than absolute values.

Figure 4.6 shows that generally the tibia shaft has a higher von-Mises stress than the distal and proximal tibia for both the ipsilateral and contralateral lower extremities in sedan impacts due to the effects of the kinematics of the tibia (bending toward the opposite direction of vehicle travel). Similarly the femur shaft has generally higher von-Mises stresses than the distal and proximal ends for a sedan impact. This distribution of von-Mises stresses can also be seen in the tibia of the ipsilateral lower extremity for SUV cases. However, for the femur of the ipsilateral lower extremity in the SUV impacts the highest von-Mises stress occurs in the proximal (Figure 4.6 (c)) area since the bonnet leading edge contacts directly with the proximal femur (Figure 4.4 (b)), and inertial loading from the upper body mass leads to a high contact force between the femur head and the hip bone. The contralateral femur loading in both SUV and sedan impact is generally much less than the ipsilateral femur loading and is significantly below the tolerance threshold, see Figure 4.6. However, the contralateral tibia shaft loading magnitude for the sedan case is similar to the ipsilateral tibia shaft loading, and is close to the tolerance threshold.

As shown in Figure 4.4 (b), for SUV impacts no stiff vehicle structure contacts with the leg in the early stage of the impact, which leads to higher inertia force below the knee, resulting in generally higher knee bending angles compared to the sedan cases (Figure 4.7). In the SUV cases, the legs fold under the bumper due to inertial loading (Figure 4.4). Furthermore, no self-contact occurs in the legs for SUV cases, and therefore the knee lateral shearing in all the gait stances is similar in SUV impacts (Figure 4.7).

4.2.6.1 Gait effects on tibia loading

The influence of gait stance on lower extremity injury risk in sedan impacts can be seen from the fact that the 60% and 75% gait stances (ipsilateral knee more flexed, see Figure 4.1) have significantly lower peak von-Mises stress in the whole ipsilateral tibia than other stances (ipsilateral lower extremity straighter), see Figure 4.6 (a). This is partly due to the change of mass below the lower bumper with different gait stances: in the 60% and 75% stances the ipsilateral lower extremity knee is flexed, which raises the leg centre of mass and reduces the inertial bending and deflection in the tibia (see Figure 3.8, Chapter 3, for detailed leg loading conditions). Similarly, for the contralateral lower extremity the predicted peak von-Mises stress in the whole tibia for 10% gait stance

(contralateral lower extremity more flexed) is significantly lower than 40%, 60% and 90% stances (contralateral lower extremity straighter), but the situation for the 25% gait stance (contralateral lower extremity more flexed) is worse (addressed later).

The effects of self-contact force in sedan impacts can be seen from the simulation results (Figure 4.6) where the 25% and 75% gait stances (legs overlapping, see Figure 4.1) have significantly higher peak von-Mises stress in the tibia shaft of the contralateral lower extremity than other stances (legs not overlapping, see Figure 4.1) due to the self-contact force from the ipsilateral lower extremity for the 25% gait stance in the sedan case (green circles in Figure 4.8) which increases bending in the tibia shaft of the contralateral lower extremity. The self-contact force effect can also be observed in the peak tibia shaft von-Mises stress for the 25% gait stance (ipsilateral lower extremity straight and lower extremities overlapped) which is significantly higher than that of the 10%, 40% and 90% gait stances (ipsilateral lower extremity straight but no overlap) and for the 75% gait stance (ipsilateral lower extremity flexed and legs overlapped) compared to the 60% gait stance (ipsilateral lower extremity flexed but no overlap), see Figure 4.6 (a).

(a) (b)

Figure 4.8 Kinematics of pedestrian in sedan impact for the (a) 25% and (b) 75% gait stances.

For the SUV cases, the legs impact with the vehicle structure in a similar way for all gait stances (ipsilateral and contralateral lower extremities respectively), and therefore the gait stance has no significant effect on the peak von-Mises stress in the distal tibia and tibia shaft for SUV impacts for both the ipsilateral and contralateral lower extremities (see Figure 4.6). However, for the 75% gait stance, the ipsilateral ankle impacts the engine support beam (blue circle in Figure 4.9), reducing the

stress from bending in the tibia shaft but slightly increasing the distal tibia stress.

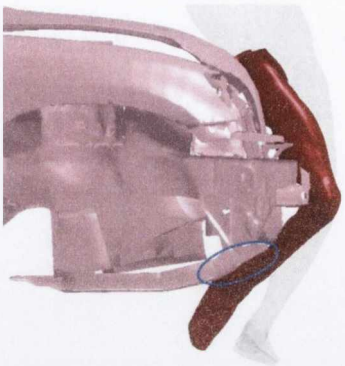

Figure 4.9 Kinematics of pedestrian in SUV impact for the 75% gait stance.

4.2.6.2 Gait effects on knee reaction

For the ipsilateral knee, the influence of the gait stance is reflected in the fact that the 60% and 75% stances (ipsilateral knee more flexed) have significantly lower lateral knee bending angle than the other stances (ipsilateral knee straighter) for both sedan and SUV impacts, see Figure 4.7 (a) and (c). Similarly, smaller lateral knee bending angles were predicted for the contralateral knee for 10% and 25% gait stances (contralateral knee more flexed) than the other stances (contralateral knee straighter) in both sedan and SUV impacts (Figure 4.7). An exception is the 25% gait stance (legs overlapping) in the sedan case due to self-contact from the ipsilateral leg (addressed above). The effect of gait stance on knee shearing is also significant in sedan impacts, with the 25% and 75% gait stances (legs overlapping) having higher lateral shearing displacement than the other stances (legs not overlapping) for both the ipsilateral and contralateral knee, see Figure 4.7 (a) and (b), while no significant effect of gait stance on knee shearing is found for the SUV cases (Figure 4.7). This is due to little variation in inertial loading of the knee in the SUV cases since the bumper is always above the knee height. In the sedan cases the lower bumper reduces the knee bending angle and the leg moves in the same direction as the vehicle, see Figure 4.4 (a). For the 25% and 75% gait stances the self-contact from the contralateral lower extremity restricts the motion of the ipsilateral leg (Figure 4.8), thereby increasing the ipsilateral knee lateral shearing.

Further insight into the effect of gait stance on knee loading can be found from Figure 4.10 and Figure 4.11. Figure 4.10 shows that the change in knee flexion/extension angle and the change in

tibia internal/external rotation angles (up to the instant of maximum knee lateral bending angle) for both the ipsilateral and contralateral lower extremity increases with increased initial flexion angle of the knee. An exception is the 25% gait stance (red circle in Figure 4.10 (a)) in the sedan case, where the supporting effect from the ipsilateral lower extremity at the shaft of the contralateral leg (Figure 4.8) restricts knee flexion and tibia rotation and increases bending in the contralateral knee.

Figure 4.11 shows the inverse relation between the maximum knee lateral bending angle and the change in knee flexion/extension angle and tibia internal/external rotation angle (up to the instant of maximum knee lateral bending angle). The high correlation coefficients and significant slopes for the linear regressions in Figure 4.11 show that the maximum knee lateral bending angle significantly decreases with a greater change in knee flexion/extension angle and tibia internal/external rotation angle. Therefore it is clear that knee flexion/extension motion during impact, which is highly dependent on the initial knee flexion angle (Figure 4.10), can have a protective effect by reducing knee lateral bending.

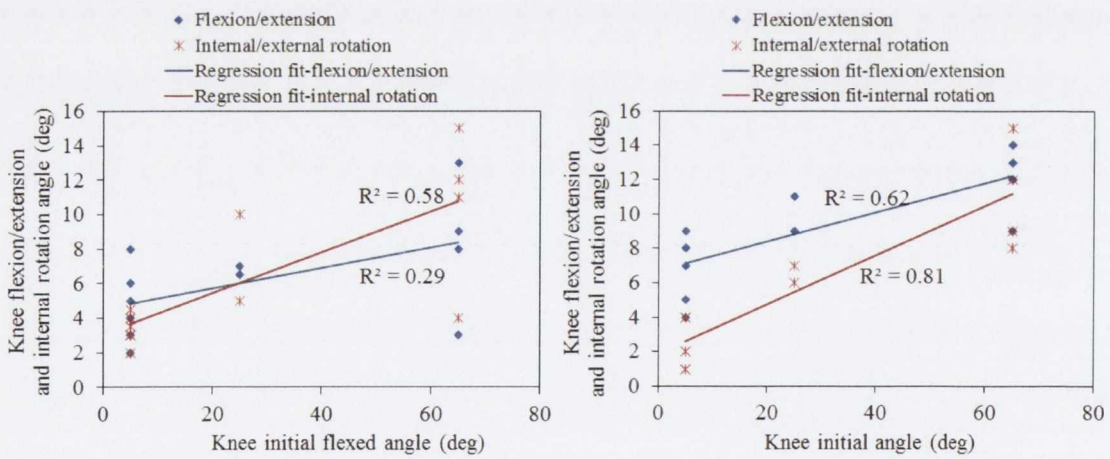

Figure 4.10 The change of knee flexion/extension and internal/external rotation angle as functions of knee initial flexed angle in the ipsilateral and contralateral lower extremity in impacts against: (a) sedan, (b) SUV.

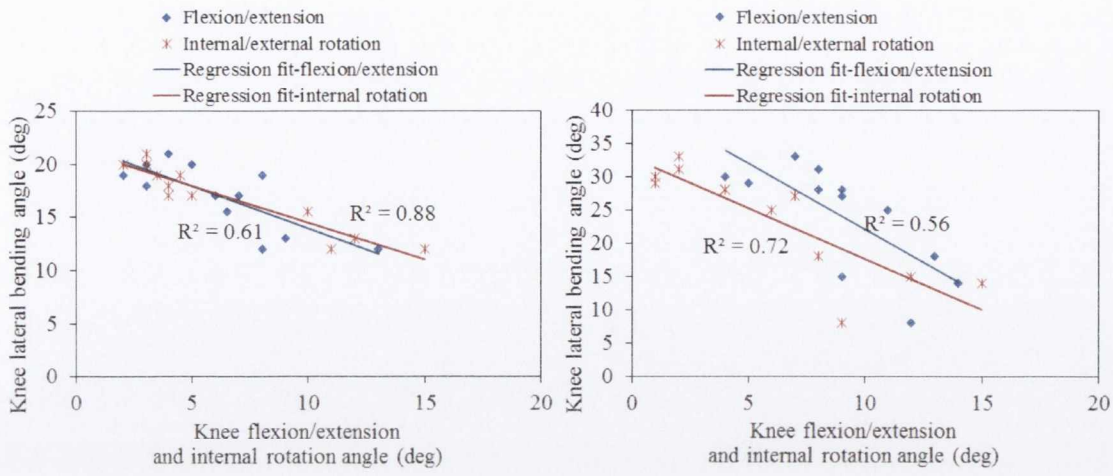

Figure 4.11 Knee lateral bending moment as functions of the change of knee flexion/extension and internal/external rotation angle in the ipsilateral and contralateral lower extremity in impacts against: (a) sedan, (b) SUV.

It is known that tibia internal/external rotation can protect the knee from ligament injuries (Masson et al., 2005; Mo et al., 2014) and the results of this study suggest that more initial flexion in the knee leads to lower knee lateral bending angles (and hence lower knee injury risk), both for the ipsilateral and contralateral knee. This probably also explains why the knee lateral bending angle for cases where the knee is initially flexed slightly (ipsilateral knee in 10% gait stance and contralateral knee in 60% gait stance) is lower than gait stances where the knee is not flexed but higher than gait stances where the knee is significantly flexed. Furthermore, the reduction of knee lateral bending moment can decrease the tension in the knee ligaments and the contact force in the knee joint, thus reducing the peak von-Mises stress in the proximal tibia and distal femur (Figure 4.6), since ligament tension and joint contact between femur and tibia are the source of von-Mises stress for those regions (see Figure 4.5). The effects of knee flexion on lower extremity injury outcome predicted from the FE simulations are similar to that from post-mortem human subjects (PMHS) tests where an initial flexion of the knee decreased the severity of the injuries (Petit et al., 2014).

4.2.6.3 Gait effects on femur loading

Since the peak von-Mises stresses in the femur of the contralateral lower extremity are much lower than the fracture threshold (hence lower injury risk), the effects of gait stance on femur loading are

not further considered. The approximate loading condition on the femur of the ipsilateral lower extremity is shown in Figure 4.12, where F_{upper} is the inertia force from the upper body, $F_{vehicle}$ is the impact force from the vehicle front, F_{lower} is the inertia force from the leg and M_{lower} is the bending moment from the knee. As seen, the gait stances with the ipsilateral knee flexed (especially 60% and 75%) lead to reduced bending moment (M_{lower}) to the knee (Figure 4.7). Therefore for those gait stances where the ipsilateral knee is flexed, the ipsilateral femur has a lower bending moment which reduces the peak von-Mises stress in the femur shaft. This explains why for the 60% and 75% gait stances the pedestrian femur shaft has lower peak von-Mises stress than the other stances for both sedan and SUV cases (Figure 4.6). However for the proximal femur the source of von-Mises stress is the upper body inertia force (F_{upper}) and the same relation does not hold.

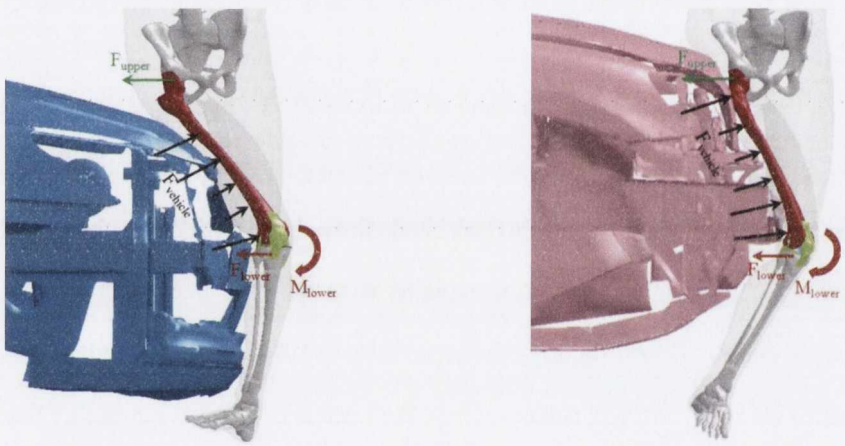

(a) (b)

Figure 4.12 Femur loading in (a) sedan impact and (b) SUV impact.

4.2.6.4 Knee flexed effects on internal/external rotation

It is easy to understand that knee flexion/extension motion (within its physical gait limits) brings no injury to the knee. However the effect of the flexed angle on the loading of the knee joint (ligaments) during internal/external rotation is not clear. It is necessary to have a good understanding of this effect since internal/external rotation is an importance kinematic of the lower extremity during vehicle-to-pedestrian impact as analysed above. Therefore, simulations of applying internal/external rotational velocity to the leg (tibia and fibula), with the femur is fixed, for different knee flexion levels were set, see Figure 4.13 (a). All simulations have the same rotational velocity and end time,

and the maximum internal/external rotation angle is 40 degrees. The maximum axial torque of the knee joint during the simulation as a function of knee flexion angle in terms of internal/external rotation is shown in Figure 4.13 (b). It can be seen from Figure 4.13 (b) that the knee axial torque decreases with increasing knee flexion angle. This means that the restriction of knee ligaments to the leg axial rotation decreases with increasing knee flexion angle or the knee has greater freedom (lower axial torque) of internal/external rotation when it is flexed. It is clear from the simulation results that when the knee is flexed the leg can move in directions of flexion/extension and internal rotation without physical restriction, which is the physiology of the human knee joint (Kinx Learning eBooks, 2014). This finding can support the above effects of pedestrian gait stance on lower extremity kinematics and injuries during vehicle impact.

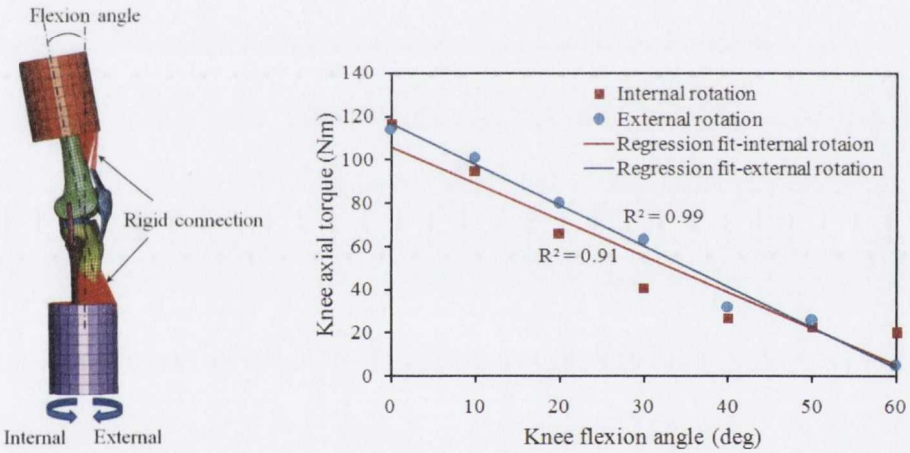

(a) (b)

Figure 4.13 Knee internal/external rotation simulation (a) and linear regressions between knee axial torque and knee flexion angle (b).

4.3 Multi-body simulation

4.3.1 Multi-body pedestrian and vehicle models

The multi-body study is conducted for the following purposes: 1) to double check the findings observed from FE simulations since no physical test and accident data are available to analysis the effects of gait stance on lower extremity injuries; 2) to assess the biofidelity of the MADYMO multi-body pedestrian model in terms of the injury risk trend as a function of gait stance since the

later optimization process is based on multi-body simulations. Thus the multi-body vehicle front models of a sedan and a SUV developed by Crocetta et al. (2015) were firstly modified to fit the centre-line shape of the corresponding FE vehicle front models (Figure 4.2), and then the MADYMO 50th% male pedestrian model was employed and configured into the same six gait stances as the THUMS model (Figure 4.1), see Figures 4.14 and 4.15.

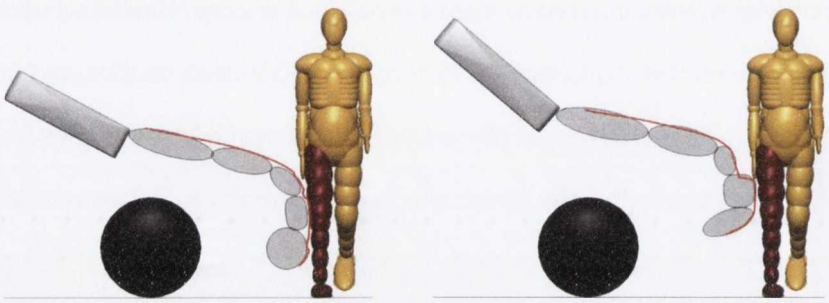

(a) Sedan vs 50th% male model (b) SUV vs 50th% male model

Figure 4.14 Multi-body vehicle-to-pedestrian impact simulation models (red lines show the centre-line shape of FE vehicle front models, see Figure 4.2).

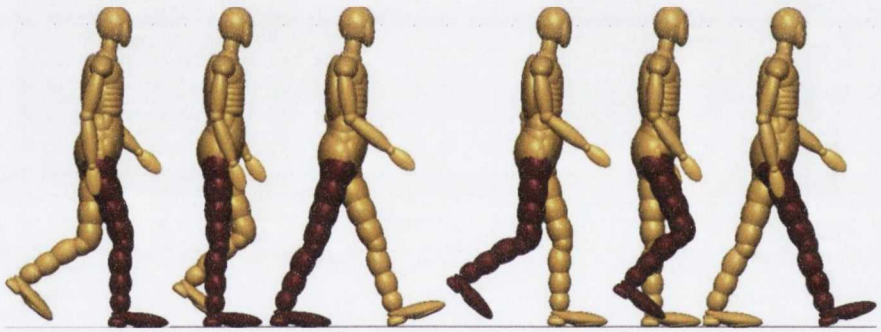

Figure 4.15 MADYMO 50th% male pedestrian model in different gait stances, in simulations the pedestrian is struck from the right lower extremity (dark red).

4.3.2 Setup of multi-body simulations

Same as the FE case, 12 multi-body vehicle-to-pedestrian impact simulations (6 for each vehicle front model) were developed based on the above MADYMO pedestrian in different gait stances and the multi-body vehicle front models (Figures 4.14 and 4.15). Impact simulations were performed at 40 km/h same as the FE simulation. A constant deceleration of 0.75g was applied to the vehicle models to simulate braking at impact on a dry-asphalt surface, similarly to the approach taken in

previous studies (Lyons and Simms, 2012; Crocetta et al., 2015). The pedestrian models (stationary) were struck laterally by the vehicle front from the right side in the simulation.

In the MADYMO application, contact forces between vehicle and pedestrian models are computed according to specified contact characteristics. The contact characteristics of the pedestrian model have been initially defined by the software developer according to cadaver test data (MADYMO, 2012). Since this assessment focuses on the predicted lower extremity injury trend as a function of pedestrian gait stance, the contact characteristics of the original multi-body vehicle front models, defined by Crocetta et al. (2015) according to the data reported in a previous study by Lyons and Simms (Lyons and Simms, 2012), were used. The combined force-deformation characteristics of both contacting surfaces were used for the vehicle-to-pedestrian contact, similarly to previous studies (Lyons and Simms, 2012; Crocetta et al., 2015). The same friction coefficients as for the FE simulation were defined for vehicle-pedestrian contact (0.3) and pedestrian-ground contact (0.7).

4.3.3 Multi-body simulation results

Figure 4.16 shows the maximum lateral bending moment for the leg and thigh, and knee lateral bending angle of the ipsilateral lower extremity as a function of pedestrian gait stance, where thresholds (red lines) for leg and thigh bending moment and knee bending angle provide references for lower extremity injury risk assessment (MADYMO, 2012). The thigh lateral bending moments were extracted from the shaft, and leg bending moments were the maximum values predicted from the distal, shaft and proximal area. Figure 4.17 compares the predicted injury risk (normalized to the corresponding thresholds) for the ipsilateral lower extremity between multi-body and FE modelling. Generally pedestrian gait stance also shows significant effects on lower extremity injury risk for multi-body simulations.

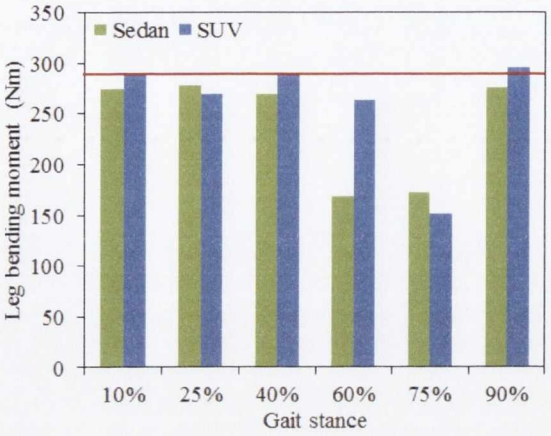

(a) Maximum leg lateral bending moment

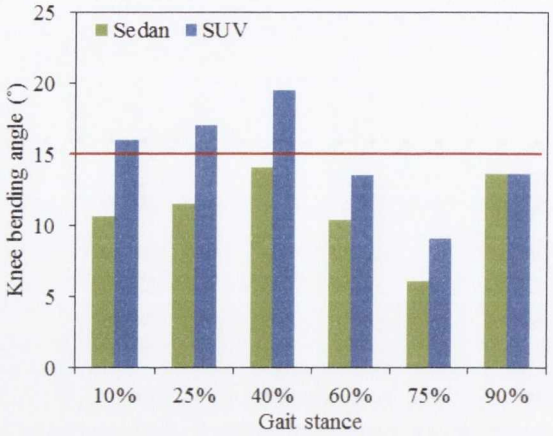

(b) Maximum knee lateral bending angle

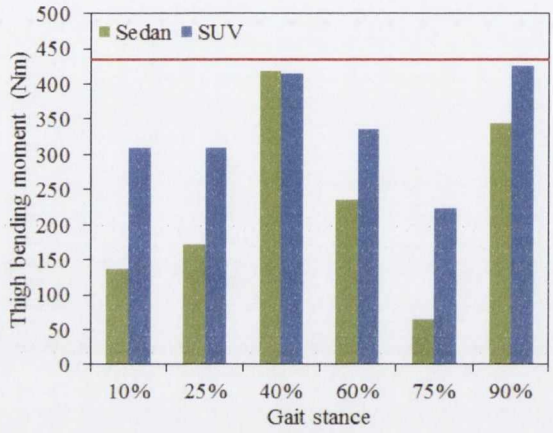

(c) Maximum thigh lateral bending moment

Figure 4.16 Multi-body simulation results of the ipsilateral lower extremity for different pedestrian gait stances.

Figure 4.16 shows that the predicted maximum leg bending moment and knee bending angle for 60% and 75% gait stances (ipsilateral knee flexed, Figure 4.15) are generally lower than other gait positions (ipsilateral knee straighter, Figure 4.15) for both sedan and SUV impacts. This injury risk trend is generally similar to that from the FE simulations (Figure 4.17). For the thigh shaft bending moments in multi-body simulations, 40% and 90% gait stances have an obviously higher injury risk than other cases for both sedan and SUV impacts. These effects on thigh injury risk are not in line with those predicted by the peak von-Mises stress in the femur shaft from FE simulations (Figure 4.17). This might be largely due to the simplification of the multi-body pedestrian lower extremity model and the difference in contact modelling between multi-body and FE models. Generally, the effects of pedestrian gait stance on leg and knee injury risk predicted from multi-body simulations match the findings using detailed human body and vehicle models and

in-depth kinematic analysis. In particular, multi-body simulations also indicate that a flexed keen helps to reduce lower extremity injury risk, which gives strong support to the findings observed from the FE modelling.

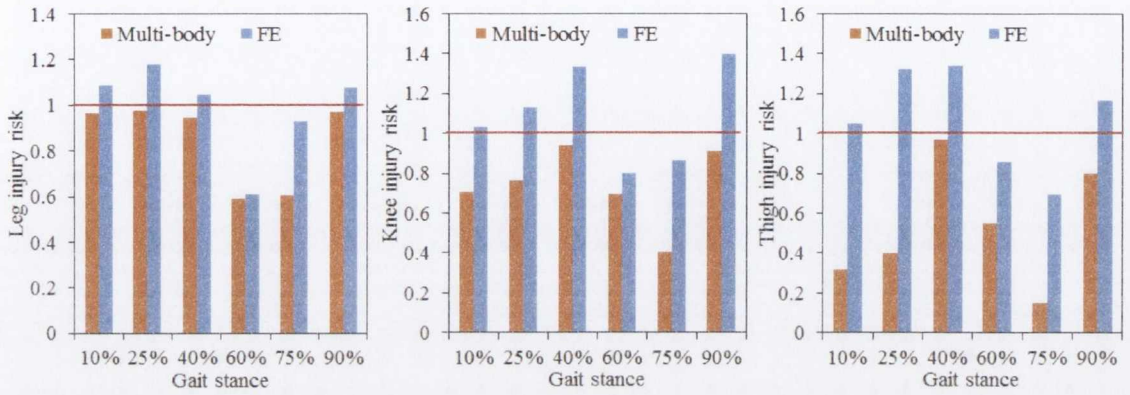

(a) Sedan case

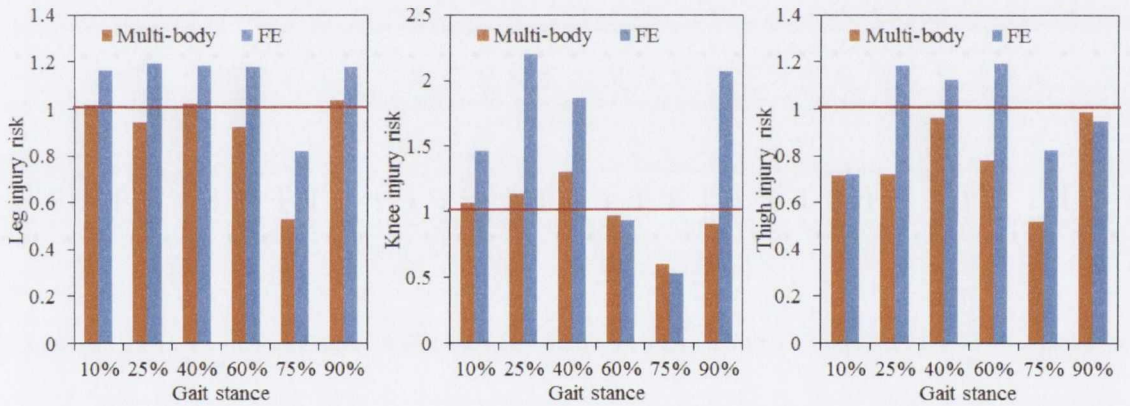

(b) SUV case

Figure 4.17 Comparison of predicted injury risk for the ipsilateral lower extremity between multi-body and FE simulations.

Overall, the maximum knee bending angles predicted from multi-body simulation are significantly lower than that for FE modelling (Figures 4.7 and 4.16). This may be largely due to the fact that the knee of the MADYMO pedestrian model is a complex joint with a strong coupling between the degrees of freedom, so the MADYMO pedestrian model cannot reflect the knee bending motion after it reaches a given limit (MADYMO, 2012). However, the resistance to axial rotation is dependent on the knee flexion angle as defined in the MADYMO pedestrian model (MADYMO, 2012). Not surprisingly, the MADYMO pedestrian model reflects the effects of gait stance on leg and knee injury risk. The definition of the knee joint in the MADYMO pedestrian model also limits

its predictive capability of knee shearing motion (maximum displacement of 6 mm). So the knee shearing displacement has not been considered as a predictor for knee injury in multi-body simulations. Moreover, the MADYMO thigh and leg model are limited to predict detailed loading and injuries in the corresponding body regions. The absolute injury risk predictive capability between the FE and multi-body pedestrian model is not comparable, and the multi-body pedestrian model shows an under-estimation for lower extremity injuries compared to the THUMS pedestrian model (Figure 4.17). However, the biofidelity of the THUMS pedestrian model was also only validated based on cadaver test dada in small sample (Shigeta et al, 2009; Watanabe et al, 2011). Nevertheless, the pedestrian models used here can generally predict the basic biomechanics for lower extremity injuries.

4.4 Summary

This chapter investigated the effects of pedestrian gait stance on lower extremity kinematics and injury risk via FE and multi-body simulations. Both the FE and multi-body simulation results indicate that the lower extremity injury risk for an adult pedestrian struck from the side at 40km/h is strongly dependent on the gait stance when struck by both a sedan and a SUV. The gait analysis shows that generally the lower extremity of an adult pedestrian has lower injury risk when the knee is flexed. Therefore, it seems that certain gait stances induce greater knee flexion and reduced knee lateral bending during impact, and it is predicted that these stances reduce lower extremity injury risk in pedestrian impact cases.

Linear regressions for FE simulation results show high negative correlation between change in knee flexion during impact and knee lateral bending angle and also high negative correlation between leg axial rotation during impact and knee lateral bending angle. FE simulation test results using an isolated knee model indicate that the restriction of knee ligaments to the leg axial rotation decreases with increasing knee flexion angle. FE simulation results also show that in some gait stances a self-contact between the legs occurs, and the lower extremity injury risk is then increased.

The comparisons of outputs between FE and multi-body pedestrian model show that the MADYMO pedestrian model has some limitations in predicting the detailed load and response in lower

extremity under vehicle impact environment due to the definition of mechanical properties in the knee joint. However, the MADYMO pedestrian model can generally predict lower extremity injuries for different regions (leg and thigh, and knee) and reflect the effects of gait stance on leg and knee injury risk comparing to FE simulations.

Since the predicted lower extremity injury risks are strongly dependent on the initial gait position, vehicle safety design for pedestrian protection for a single lower extremity position may not result in significant improvements in accident cases, where a broad range of initial gait positions can be expected. Therefore, the broad range of pedestrian gait stance should be considered in later optimization process. Moreover, the injury predictive capability of multi-body modelling should be evaluated at the population level for vehicle front shape optimization considering a broad range of impact scenarios in accidents.

Chapter 5 A Virtual Test System for Assessing Vehicle Front Safety Performance

5.1 Introduction

The design of a vehicle front has significant influences on pedestrian injury risk in real word accidents according to the study in Chapter 3. As summarized in Chapter 2 the current vehicle designs still pose serious threats to pedestrians and an optimized vehicle front design for pedestrian protection remains an elusive goal. What is more, the pedestrian injury outcome is strongly dependent on the initial impact conditions (Chapter 2 and 4). Accordingly, vehicle front optimization for pedestrian protection is likely to be more successful if it is based on the actual distribution of real world impact configurations rather than on idealised collision scenarios. However, no previous optimization studies directly considered the broad range of impact speed and actual distributions of the relevant input parameters observed from accident studies (Chapter 2 and 4).

As discussed in Chapter 2, a computer-based vehicle front optimization approach which takes into account the broad range of actual pedestrian impact configurations is an increasingly realistic proposition. Accordingly, the purpose of this chapter is to define an efficient Virtual Test System (VTS) to assess the pedestrian safety performance of a vehicle front shape, which can be used for later vehicle front optimization. The VTS is based on MADYMO multi-body vehicle-to-pedestrian impact simulations and the distribution of impact configurations in real world crashes. The VTS should represent real world impact configurations in terms of the distributions of vehicle impact speed, pedestrian gait and pedestrian height. The distribution of predicted injuries should generally match the injuries observed in the accident data. The VTS should also have the predictive ability to distinguish the aggressivity of different vehicle front shapes to pedestrians. If these objectives can be broadly satisfied, this approach can provide the basis for vehicle front optimization, which should result in an appreciable reduction in real world pedestrian injury risk. The VTS will also provide basic knowledge on which impact configurations should be considered in future vehicle front optimization for pedestrian protection, where a large number of vehicle front designs will be evaluated.

5.2 Accident data

The pedestrian accident data from the German In-Depth Accident Study (GIDAS) and US Pedestrian Crash Data Study (PCDS) databases was selected as the source of inputs for the VTS. The GIDAS pedestrian accident cases used here were from the raw data captured during 2000-2015, where the detailed information for vehicle (e.g. manufacturer and model), pedestrian (e.g. injury, age, sex, height and weight) and impact condition (e.g. speed and direction) was recorded. The information of the PCDS data (collected from 1994 to 1998) was extracted from previous studies (Chidester and Isenberg, 2001; Klinich and Schneider, 2003; Mizuno and Ishikawa, 2003). So the PCDS data used here is only at the general level but without detailed information. The PCDS data was selected as a complementary part for VTS inputs and evaluation.

The pedestrian data from GIDAS and PCDS were selected based on the following inclusion criteria: 1) the vehicle was moving forward at impact, 2) the vehicle was a sedan, light truck (LT, i.e. pick-up or SUV) or van and 3) the pedestrian was upright (not lying/sitting on the road) and impacted by the vehicle front (forward of the top of the A-pillar). All the injuries in these databases were recorded using the Abbreviated Injury Scale (AIS) score.

5.2.1 Accident distribution

Figure 5.1 shows the distributions of impact speed, vehicle class and pedestrian age for the GIDAS and PCDS. The vehicle class named LT includes SUVs and pick-ups, while vehicle class van includes MPVs, minivans and vans. Figure 5.1 shows that the impact speed is generally lower in PCDS than GIDAS, and LTVs (SUVs and pick-ups and vans) take significantly higher proportion in PCDS than GIDAS.

Figure 5.2 shows the distribution of impact direction for pedestrians and initial contact location on the vehicle front for different centre area widths (Figure 5.3) in the GIDAS data. It is clear that most pedestrians (about 80%) in the GIDAS database were struck from the lateral side. More than half (55%) cases have a pedestrian initial contact with the vehicle front at the centre area of 800 mm width, this proportion is 65% and 80% for centre area with a width of 1000 mm and 1200 mm,

respectively.

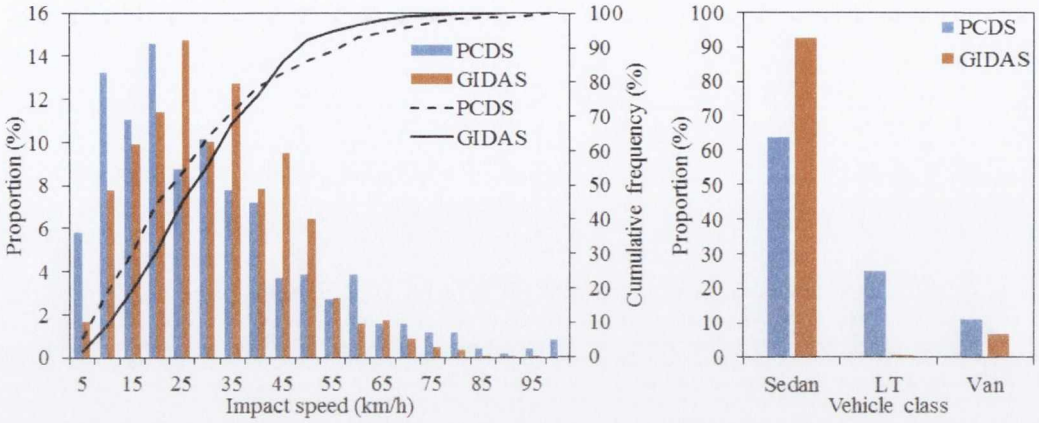

Figure 5.1 Distribution of impact speed and vehicle class for the GIDAS and PCDS data.

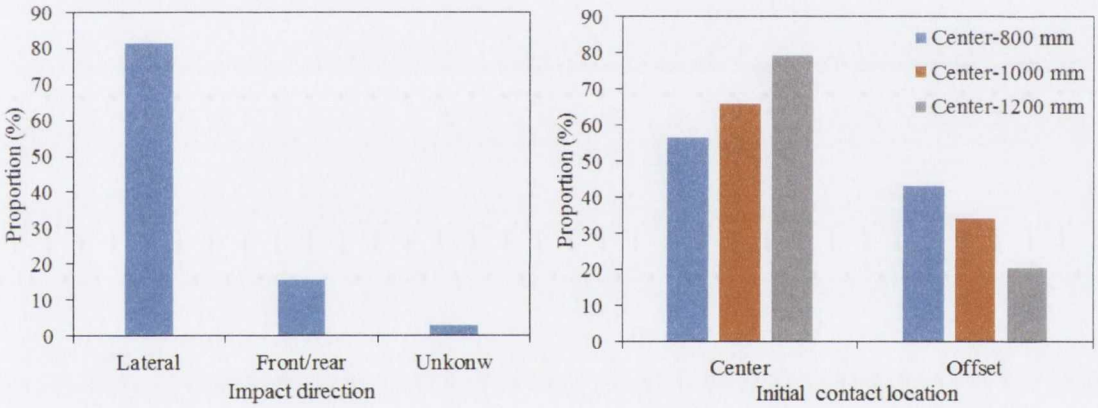

Figure 5.2 Distribution of impact direction and initial contact location in the GIDAS data.

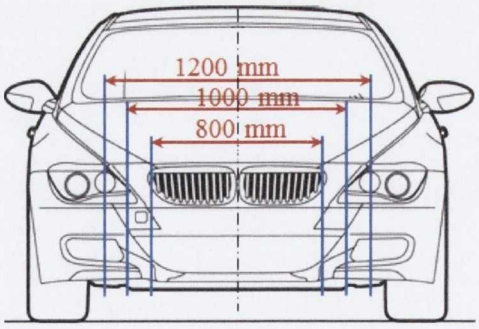

Figure 5.3 Diagram of different centre area widths for a midsize sedan.

5.2.2 Injury distribution

Figure 5.4 shows the distribution of AIS2+ injuries as a function of pedestrian body region, vehicle class and impact speed. It is clear that the PCDS has higher proportions of AIS2+ head and abdomen

injuries but lower proportions for AIS2+ arm and thorax injuries. The proportions of pelvis and lower extremity in the PCDS are similar to those for GIDAS. The higher frequency of AIS2+ thorax injury in the GIDAS data is surprising since an obviously higher proportion of LTVs was observed in PCDS (18%) than GIDAS (1%), and LTVs are observed to be more aggressive to a pedestrian's thorax (Longhitano et al., 2005; Han et al., 2012; Li et al., 2012). The distribution of AIS2+ injuries as a function of vehicle class (Figure 5.4) is generally similar to the involving frequency of vehicle class in the database (Figure 5.1) for both PCDS and GIDAS. Generally, the proportions of AIS2+ injuries for high impact speeds (≥40 km/h, Figure 5.4) are higher than the involving frequencies of these speeds (Figure 5.1) and the low impact speeds (<40 km/h) usually lead to lower proportions of AIS2+ injuries than their occurring frequencies in accidents (Figure 5.1 & Figure 5.4). This indicates that the combined effects of an impact speed range and its involving frequency in accidents affect the outcome of pedestrian injuries.

Table 5.1 shows the AIS2+ injury rate (number of injuries divided by number of cases) for the whole sample, vehicle class (Sed for sedan) and body region between PCDS and GIDAS. Mid-body includes the neck, thorax, abdomen, spine and upper limbs, while lower limbs includes the pelvis and lower extremities. The ratio data shows the injury rate in PCDS divided by the corresponding injury rate for GIDAS. For all conditions the AIS2+ injury rate in PCDS is significantly higher than that for GIDAS. Table 5.1 shows that LTVs have significantly higher AIS2+ injury rate than sedans in PCDS, similar to previously reported (Longhitano et al., 2005). This trend is generally observed in the GIDAS data (excluding the LT cases for its small proportion, Figure 5.1), where the AIS2+ injury rate for vans (1.26) is higher than sedans (1.18). Vans have a generally lower AIS2+ injury rate for the mid-body and lower limbs but higher AIS2+ injury rate for the head/face than sedans in both PCDS and GIDAS. However a previous study indicated that vans have higher aggressivity to pedestrian thorax than sedans in accidents (Li et al., 2012). This difference may largely be due to the influence of arm injuries which account for 32% and 35% of all AIS2+ mid-body injuries in PCDS and GIDAS, respectively. The results in Table 5.1 also indicate that generally SUVs and cars have higher AIS2+ lower limb injury rate than vans in accidents.

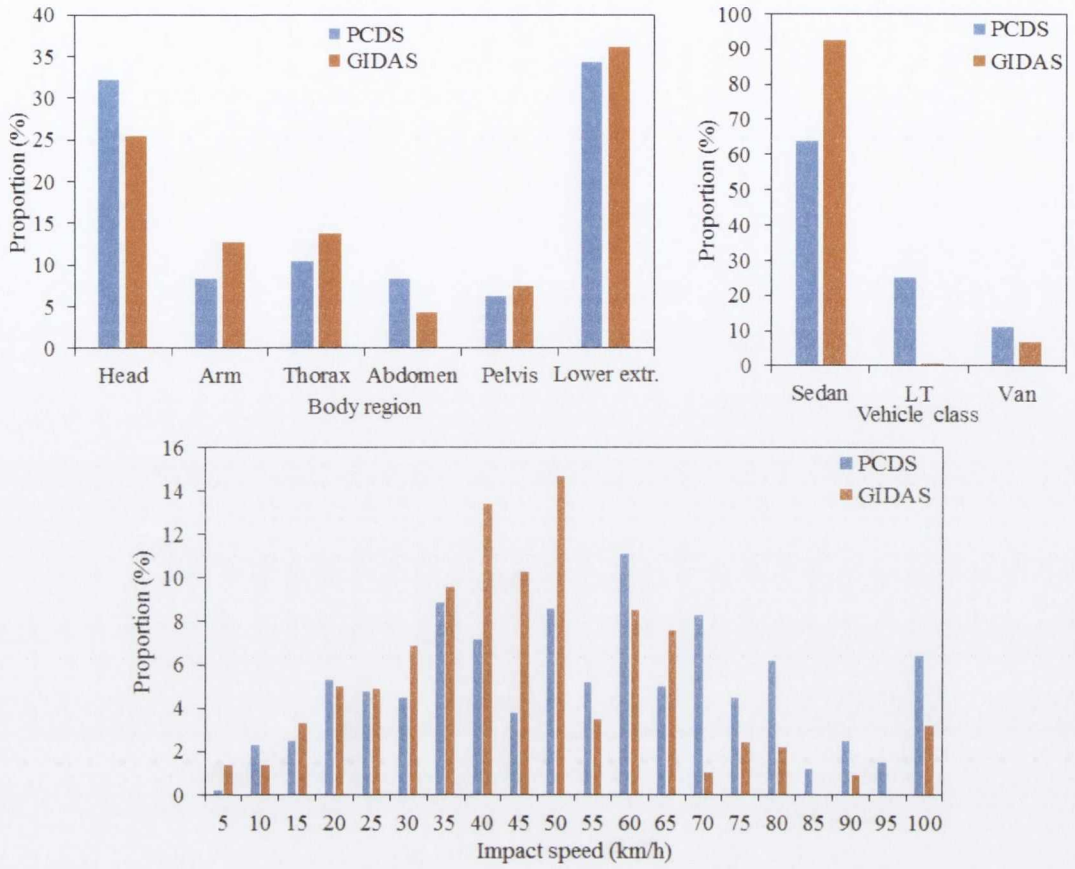

Figure 5.4 Distribution of AIS2+ injuries as functions of pedestrian body region, vehicle class and impact speed for the GIDAS and PCDS data.

Table 5.1 AIS2+ injury rate in the PCDS and GIDAS.

Body region	PCDS				GIDAS				Ratio (PCDS/GIDAS)			
	All	Sed	LT	Van	All	Sed	LT	Van	All	Sed	LT	Van
All	2.70	2.53	3.68	2.21	1.18	1.18	0.9	1.26	2.3	2.1	4.1	1.8
Head/Face	0.97	0.92	1.10	1.07	0.31	0.30	0.20	0.50	3.1	3.1	5.5	2.1
Mid-body	0.83	0.65	1.67	0.56	0.40	0.41	0.20	0.32	2.1	1.6	8.4	1.8
Lower limbs	0.90	0.96	0.91	0.58	0.47	0.47	0.50	0.44	1.9	2.0	1.8	1.3

A significantly higher AIS2+ injury rate is observed for a given vehicle class in PCDS than GIDAS, see Table 5.1. For cars, the AIS2+ injury rate in PCDS is 2.1 times as that in GIDAS, and higher again for the head (3.1 times). For light trucks, the AIS2+ injury rate in PCDS is 5.1 times as that in GIDAS, and for the head and mid-body the ratios are 5.5 and 8.4, respectively. Similarly 1.8 times higher overall AIS2+ injury rates were observed in PCDS than GIDAS for vans, and 2.1 and 1.8

times higher for the head/face and mid-body in van cases, respectively. However, the impact speed is generally lower in PCDS than GIDAS (Figure 5.1). It is not immediately clear why these large differences in injury rate between PCDS and GIDAS are observed, but it is possible to make some speculative comments. The shapes of the vehicles in the PCDS database reflect designs of late 1980s/early 1990s in the US, which have significantly sharper vehicle fronts than the late 1990s/early 2000s vehicles which dominate the GIDAS database (accounting for 80% of cases). It is likely that the stiffness reductions in the European car fleet associated with the EU Directive on pedestrians and with the inclusion of pedestrian testing in Euro-NCAP are not a strong factor, since most of the GIDAS vehicles predate these changes. Nonetheless, it is possible that the European fleet is less stiff, though this remains to be assessed.

The above accident data provides basic information for the distributions of impact configuration and injury, which can be used in the VTS development and evaluation, even though there are some differences between the accident data from different countries.

5.3 Virtual Test System (VTS)

The proposed Virtual Test System (VTS) has two main parts: a Simulation Test Sample (STS) based on MADYMO multi-body vehicle-to-pedestrian impact simulations accounting for the range of vehicle impact speeds, pedestrian heights and pedestrian gait stances to represent real world impact configurations and an Injury Weighting System (IWS) based on distributions of these impact parameters in accidents (the above data) to weight the predicted injuries in the STS.

5.3.1 Simulation Test Sample (STS)

A Simulation Test Sample (STS) was developed to assess the safety performance of a vehicle front design considering the broad range of impact configurations in real world pedestrian accidents. The pedestrian accident data from the PCDS and GIDAS databases was primarily used as the source of inputs. The STS was designed to take most impact configurations into account considering the impact parameters of the vehicle impact speeds, pedestrian heights, pedestrian gait and walking speed since these are the main factors influencing the severity of pedestrian injuries in a vehicle

collision apart from the vehicle front design (Untaroiu et al., 2009; Elliott et al., 2012b; Peng et al., 2012b). To control the computing time the STS was developed by applying discrete values for each input parameter to represent different continuous ranges of the parameters in the accident data.

The range of vehicle speed from 16 km/h to 75 km/h, covering nearly 85% accidents for AIS+ injuries in both PCDS and GIDAS databases (Figure 5.4), was selected as the original range of impact speed. Then this range can be divided into discrete groups (e.g. an interval of 10 km/h) according to the accident data. Similarly, the pedestrian height range from the accident data can also be divided into different discrete groups according to the population of pedestrian height and the availability of the MADYMO pedestrian models, including released models and scalable models (MADYMO, 2012). The discrete pedestrian gait stances proposed by Untaroiu et al. (2009) were considered in the STS since there is no data on gait stance in accidents. For pedestrian speed, the mean values proposed by Huang et al. (2008) were assigned to the corresponding age groups of below 10 years (1.83 m/s), 10-15 years (1.68 m/s) and adults (1.58 m/s) in the STS, so that pedestrian walking speed was fixed for each pedestrian model.

Then a STS can be defined based on the above methods of selecting inputs from accident data. Every combination of each discrete group of these impact parameters in the STS can form an impact configuration, e.g. unique impact configuration is an impact speed of 40 km/h, a pedestrian height of 174 cm and a gait stance of 50%. Thus the sample size of an STS is equal to the number of discrete groups for impact speed, pedestrian height and gait stance. For example, the STS sample size is 120 when considering 6 impact speeds, 5 pedestrian heights and 4 pedestrian gait stances (120=6*5*4). In this way all the impact configurations formed by the discrete groups of impact speed, pedestrian height and gait stance can be tested in the STS to assess the safety performance of a vehicle front design. Table 5.2 shows an example for the STS where 6 impact speeds, 5 pedestrian heights and 4 pedestrian gait stances were considered. This table also shows the mean value of each discrete group for all the impact parameters based on GIDAS accident data and proposed gait stances, which are the references for the inputs of the STS in the multi-body simulations. The choice of discrete groups for impact speed, pedestrian height and gait stance is flexible for different study purposes, e.g. researchers can select more groups (small interval between each) of impact speed to account for

more detailed effects of impact speed, and similarly for other impact parameters.

Table 5.2 A STS considering 6 impact speeds, 5 pedestrian heights and 4 pedestrian gait stances.

Group		1	2	3	4	5	6
Impact speed (km/h)	Range	16-25	26-35	36-45	46-55	56-65	66-75
	Mean	21	31	41	50	61	70
Pedestrian height (cm)	Range	<140	140-157	158-170	171-177	>177	
	Mean	120	151	164	174	185	
Gait stance (%)	Range	20-30	40-60	70-80	90-10		
	Mean	30	50	80	100		

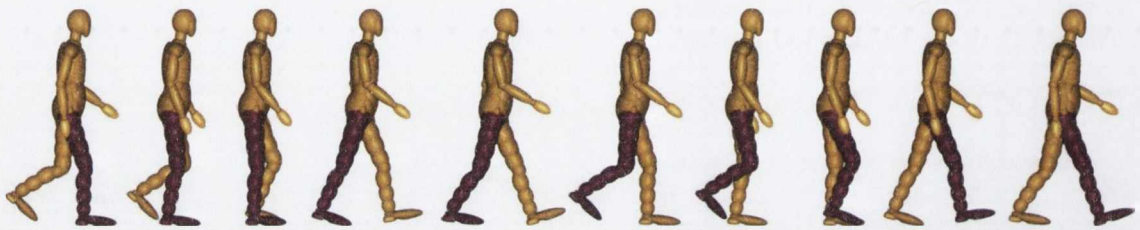

10% 20% 30% 40% 50% 60% 70% 80% 90% 100%

Previous studies have shown that at low speeds (less than about 35 km/h) ground contact injuries are frequently the most severe injuries, whereas at higher speeds vehicle contact injuries are generally more severe (Ashton and Mackay, 1983; Guillaume et al., 2015). To account for ground impacts while reducing computing time, in the STS the most serious injuries from both vehicle and ground contacts for low impact speed collisions (<40km/h) were considered, but for higher impact speed cases (≥40km/h) only injuries from the vehicle contacts were considered. Pedestrians struck from the lateral side account for about 75% of PCDS (Chidester and Isenberg, 2001) and 80% of GIDAS accident cases (Figure 5.2) by vehicle front and thus all cases in the STS were side-struck pedestrians with the pedestrian oriented transverse to the vehicle.

5.3.2 MADYMO pedestrian models

In the STS the MADYMO pedestrian ellipsoid models of different sizes were used to represent pedestrians of different heights. Despite limitations, the mid-sized male pedestrian model and its scaled models have been validated by comparison to accident and cadaver test data in terms of

kinematics and injury prediction (Coley et al., 2001; Van Rooij et al., 2003; Elliott et al., 2012a). Accordingly, they are widely used in accident reconstructions and show generally good correspondence with collision data (Van Rooij et al., 2003; Untaroiu et al., 2009; Peng et al., 2012a). In the current chapter, ten MADYMO pedestrian ellipsoid models (3YOC, 6YOC, 5th% female, 50th% male, 95th% male and 5 scaled adult models using the scaling module MADYSCALE based on the 50th% male model) were used to simulate pedestrians involved in accident collisions, see Figure 5.5. The anthropometry data of the selected pedestrian models is show in Table 5.3, where S1-S5 represent scaled adult male models of different heights. In the simulations, pedestrian models similar to the mean sizes of pedestrian height discrete groups (e.g. Table 5.2) were selected as the inputs for the STS. For the STS shown in Table 5.2, the pedestrian model of 6YOC (117 cm) can be selected to represent the height group <140 cm where the mean height is 120 cm, similarly the pedestrian models of 5th% female, S2, 50th% male and S5 (Table 5.3) can be selected to represent height groups 2-5 (Table 5.2).

Figure 5.5 MADYMO pedestrian models of different sizes.

Table 5.3 Anthropometry data of the MADYMO pedestrian models.

Model	3YOC	6YOC	5th% female	S1	S2	S3	50th% male	S4	S5	95th% male
Height (cm)	95	117	153	160	165	170	174	180	185	191

5.3.3 Injury Weighting System (IWS)

5.3.3.1 Injury number

The Abbreviated Injury Scale (AIS) 2005 was used in the current study to classify predicted injuries (Gennarelli and Wodzin, 2006). According to previous studies on human body injury thresholds, the AIS level of an injury can be estimated from the predicted injury criteria scores for different body regions, which can be extracted from the MADYMO pedestrian model outputs (MADYMO, 2012). Accordingly, predicted injuries from the multi-body simulations were classified into AIS levels using injury criteria for the head (HIC), thorax (TTI), pelvis (impact force), thigh and leg (lateral bending moment) and knees (bending angle). The injury thresholds for these criteria for AIS score calculation were adapted from previous studies (Cavanaugh et al., 1993; Payne and Patel, 2001; MADYMO, 2012; Mo et al., 2014), see Table 5.4.

Table 5.4 Injury criteria for AIS2+ injuries of head, thorax, pelvis and lower extremity.

Body region/Injury criteria	Injury criteria level	Reference
Head/HIC	≥520 (all models)	Payne and Patel 2001
Thorax/TTI (g)	≥100 (all models)	Cavanaugh et al. 1993
Pelvis/Impact force (kN)	≥4.0-6.0 (adult)/1.0-2.0 (child)	Payne and Patel 2001
Thigh/Bending moment (Nm)	≥55 (3YOC) ≥140 (6YOC) ≥265 (5^{th}% female) ≥350-530 (adult male)	MADYMO 2012
Knee/Bending angle (deg)	15 (all models)	Mo et al. 2014
Leg/Bending moment (Nm)	≥50 (3YOC) ≥85 (6YOC) ≥240 (5^{th}% female) ≥270-380 (adult male)	MADYMO 2012

As shown in Table 5.4, similar thresholds for head, thorax and knee AIS2+ injuries were assumed for both adult and child models since no injury criteria data for different body size is available. Different thresholds of long bone and pelvis AIS2+ injuries were used for different pedestrian models, where the data for child models was scaled from those for the adult models (MADYMO, 2012). Based on

the thresholds and injury parameter outputs from each impact simulation, the pedestrian Injury Number (IN) was defined as the sum of all predicted AIS2+ injuries from the above body regions of the struck pedestrian model and this can be calculated for a given collision. For example, the injury parameter outputs from an impact simulation for a 95th% male model are: HIC-685, TTI-150 g, pelvis impact force-8 kN, left thigh lateral bending moment-300 Nm, right thigh lateral bending moment-320 Nm, left knee lateral bending angle-17 degrees, right knee lateral bending angle-13 degrees, left leg lateral bending moment-500 Nm, right leg lateral bending moment-360 Nm. According to the thresholds (Table 5.4) the IN for this collision is 5 (head, thorax, pelvis, left knee and left tibia). The IN was defined to predict the general aggressivity of a vehicle front design to a given pedestrian at a given impact configuration (impact speed and gait stance). Due to the limitations of multi-body modelling and the injury criteria considered, only one injury was considered for each body region listed above, where lower extremity includes thigh (left and right), knee (left and right) and leg (left and right). This is for global rather than detailed local shape evaluation, which is the focus of the current thesis.

5.3.3.2 Weighting the injury number

To account for the proportion of each impact configuration, the involving proportions of vehicle impact speed, pedestrian height and pedestrian gait stance derived from accident data were used in an Injury Weighting System (IWS). Figure 5.6 shows an example of the distributions of the vehicle impact speed, pedestrian height and gait stance, which is for the STS example shown in Table 5.2. The involving proportions of the impact speed and pedestrian height were calculated directly from the GIDAS data, Figure 5.6. A uniform distribution was assumed for pedestrian gait stance since there is no data available in accident and all gait stances are considered equally likely, the proportions for gait stance of 50% and 100% are 30% since each of them represents 3 gait stances (the 50% gait stance represents the gait stances from 40% to 60%, while the 100% gait stance represents the gait stances of 90%, 100% and 10%, see Table 5.2), and a similar proportion of 20% for gait stance 30% (representing 20% and 30% gait stances) and 80% (representing 70% and 80% gait stances) was used, see Figure 5.6.

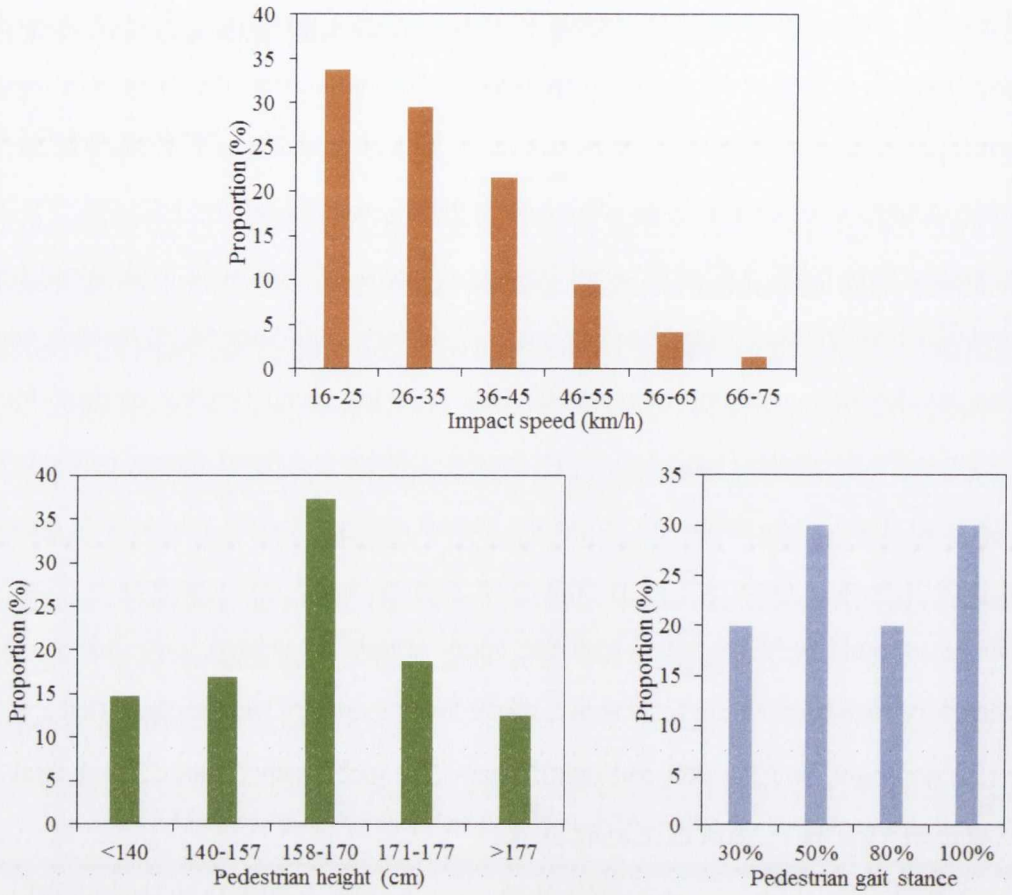

Figure 5.6 Distributions of impact speed, pedestrian height (GIDAS) and gait stance (assumed uniform distribution) for a STS.

Based on the distributions of the impact parameters (e.g. Figure 5.6), the proportion of a given impact configuration (p_i) in the STS can be calculated as the product of the proportion of impact speed (p_{si}), pedestrian height (p_{hi}) and pedestrian gait stance (p_{gi}), see Eq. (5.1). The sum of the proportions for each input parameter is unity, see Eq. (5.2) and Figure 5.2.

$$p_i = p_{si} * p_{hi} * p_{gi}, \tag{5.1}$$

$$\sum_{i=1}^{N} p_i = \sum_{i=1}^{N} p_{si} = \sum_{i=1}^{N} p_{hi} = \sum_{i=1}^{N} p_{gi} = 1. \tag{5.2}$$

To assess the aggressivity of a vehicle front design to pedestrians in real accidents using the STS, the Injury Number (IN) for each impact configuration in the STS is weighted by the frequency of occurrence of this impact configuration in the accident data, see Figure 5.6 and Eq. (5.1-5.3). Thus the Weighted Injury Number (*WIN*) for the STS (size=*N*), is the sum of the product of the Injury

Number (IN_i) and the proportion (p_i) for a given impact configuration in the STS, see Eq. (5.3). Thus the WIN score is the weighted average number of AIS2+ injuries recorded per impact configuration in the STS. The WIN score, regarded as the resulting output of the VTS, can thus be used as a metric to distinguish the aggressivity of different vehicle designs at the general level, as it represents the performance of the vehicles over a range of actual pedestrian collision configurations.

$$WIN = \sum_{i=1}^{N} IN_i * p_i. \tag{5.3}$$

5.4 Setup of vehicle-to-pedestrian impact simulation

5.4.1 Vehicle models tested using the STS

Multi-body vehicle front models of a sedan, SUV and a van (Figure 5.7) developed by Crocetta et al. (2015) were tested using the STSs, respectively. These vehicle models were also used for modelling vehicles involved in PCDS (sedan, SUV and van) and GIDAS (sedan and van, accounting for 99% pedestrian accidents) accidents to evaluate the predictive ability of the proposed STS. The selection of these vehicle models was based on the main vehicle types involved in the accident data. The geometrical dimensions of the vehicle models (Table 5.5) were from real world car shapes (Crocetta et al., 2015).

The vehicle models consist of four structures: bumper, bonnet leading edge (BLE), bonnet and windscreen. Force/deformation curves for the bumper and bonnet leading edge were assumed to be linear, and non-linear relationships were defined for the bonnet and windscreen stiffness, similar to the study of Lyons and Simms (2012). Separate unloading curves based on 10% of the loading curves for bumper, bonnet and windscreen and 1% of the loading curves for the BLE from the same sources were used to apply energy absorption in the impact (Lyons and Simms, 2012; Crocetta et al., 2015). The force/deformation curves of contact characteristics for different vehicle structures are shown in Figure 5.8, where the loading curves for bumper, BLE and bonnet were sourced from impactor test data (Martinez et al. 2007), while the windscreen stiffness was extracted from the study of Mizuno and Kajzer (Mizuno and Kajzer 1999). The contact characteristics for bumper, BLE and bonnet (rear) were selected from their corridors (Martinez et al. 2007) to represent the general

stiffness of the vehicle front structures involved in accidents. It was assumed that the same contact definitions for different vehicle regions could be applied to all the vehicle front models.

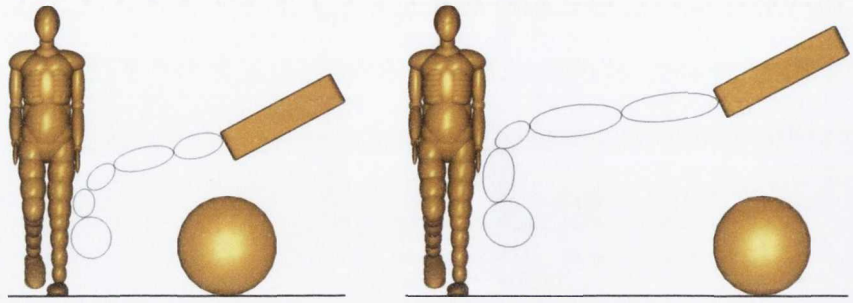

(a) Sedan vs 50th% male model (b) SUV vs 50th% male model

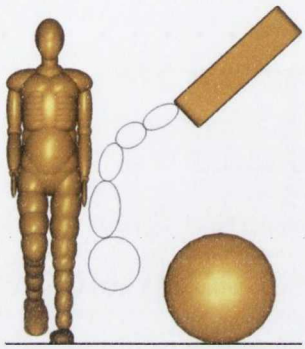

(c) Van vs 50th% male model

Figure 5.7 Vehicle models (Crocetta et al., 2015) vs 50th% male model.

Table 5.5 Geometrical dimensions of vehicle fronts, adapted from Crocetta et al. (2015).

Vehicle	Sedan	SUV	Van
Ground clearance (mm)	230	304	280
BLE height (mm)	694	942	1050
Bonnet length (mm)	795	1272	330
Bonnet angle (°)	13	8	31
Windscreen angle (°)	28	27	43

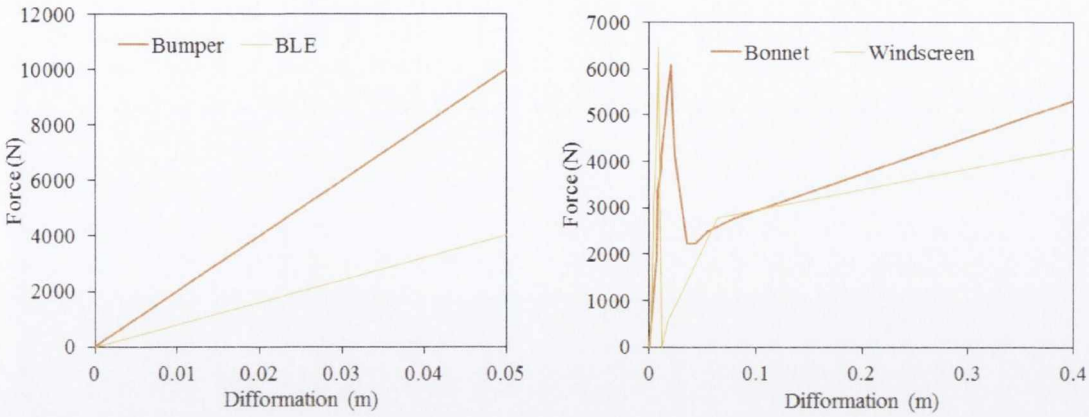

Figure 5.8 Force/deformation curves of contact characteristics for different vehicle structures.

5.4.2 Vehicle-to-pedestrian impact modelling

Only the pedestrian contact characteristics were used for modelling the pedestrian-ground interaction as suggested by Crocetta et al. (2015) since no validated ground contact model is available yet. A friction coefficient of 0.3 for vehicle-pedestrian contacts was used as in previous studies (Lyons and Simms, 2012; Crocetta et al., 2015). To model the friction force in the contact with a dry-asphalt road a friction coefficient of 0.7 for the pedestrian-ground interaction was defined. A constant deceleration of 0.75g was applied to the vehicles to simulate braking at impact on a dry-asphalt surface, similar to the approach taken in previous studies (Lyons and Simms, 2012; Crocetta et al., 2015). Vehicle dipping during braking due to suspension compression and tyre deformation was neglected as done in previous studies (Lyons and Simms, 2012; Crocetta et al., 2015). In the simulation the pedestrian models were configured into one of the 10 gait stances (Table 5.2) proposed by Untaroiu et al. (2009) and struck from the left side by the relevant vehicle front (Figure 5.7).

5.5 Evaluation of VTS using GIDAS data

5.5.1 Setup of STS

The current chapter also aims to find a reasonable simulation sample size for assessing the safety performance in the optimization to keep the computational time at a reasonable level. Therefore STSs of different sizes were defined based on different numbers of discrete groups for impact speed, pedestrian height and gait stance according to the approaches proposed in Section 5.3.1.

The ranges, mean values and involving proportions (p_s) of the impact speed in GIDAS for different discrete groups are shown in Table 5.6. In total four sets (12, 9, 6 and 3 groups) of impact speed discrete groups were chosen to form STSs of different sizes, see Table 5.6.

Similarly Table 5.7 shows the ranges, mean values and involving proportions (p_h) of pedestrian height in GIDAS and the heights of the representing multi-body pedestrian models for different discrete groups. In total four sets of discrete pedestrian heights were selected to form STSs of different sizes (10, 7, 5 and 3 cases). The choice of the height groups was based on the availability of the MADYMO pedestrian models, including released models and scalable models (MADYMO, 2012). Generally, the selected MADYMO models can represent the mean height of each discrete groups (Table 5.7).

Table 5.6 Ranges, mean values and involving proportions (p_s) of impact speed in GIDAS for different discrete groups.

Group	1	2	3	4	5	6	7	8	9	10	11	12
Range	16-	21-	26-	31-	36-	41-	46-	51-	56-	61-	66-	71-
(km/h)	20	25	30	35	40	45	50	55	60	65	70	75
Mean	18	23	28	33	39	43	48	54	59	64	68	73
p_s	0.180	0.158	0.166	0.130	0.121	0.095	0.076	0.020	0.023	0.019	0.007	0.007
Range	16-	23-	30-	36-	44-	50-	56-	63-	70-			
(km/h)	22	29	35	43	49	55	62	69	75			
Mean	19	26	32	40	46	52	59	65	73			
p_s	0.230	0.180	0.223	0.169	0.097	0.046	0.025	0.023	0.008			
Range	16-	26-	36-	46-	56-	66-						
(km/h)	25	35	45	55	65	75						
Mean	21	31	41	50	61	70						
p_s	0.337	0.295	0.216	0.096	0.042	0.014						
Range	16-	36-	56-									
(km/h)	35	55	75									
Mean	26	43	63									
p_s	0.632	0.312	0.056									

Table 5.7 Ranges, mean values and proportions (p_h) of pedestrian height in GIDAS and heights of the representing multi-body models for different discrete groups.

Group	1	2	3	4	5	6	7	8	9	10
Range (cm)	<110	110-139	140-157	158-162	163-167	168-172	173-177	178-182	183-187	>187
Mean	102	126	151	160	165	170	175	180	186	192
Model	95	117	153	160	165	170	174	180	185	191
p_h	0.036	0.111	0.169	0.157	0.114	0.157	0.130	0.068	0.036	0.022
Range (cm)	<140	140-157	158-162	163-167	168-172	173-177	>177			
Mean	120	151	160	165	170	175	183			
Model	117	153	160	165	170	174	185			
p_h	0.147	0.169	0.157	0.114	0.157	0.130	0.125			
Range (cm)	<140	140-157	158-170	171-177	>177					
Mean	120	151	164	174	185					
Model	117	153	165	174	185					
p_h	0.147	0.169	0.372	0.187	0.125					
Range (cm)	<158	158-177	>177							
Mean	130	168	185							
Model	117	170	185							
p_h	0.316	0.559	0.125							

Different sets of discrete groups of pedestrian gait stance were also defined by using all or a part of these 10 gait stances proposed by Untaroiu et al. (2009), see Table 5.8. The choice of the pedestrian gait stance discrete groups was based on their effects on pedestrian lower extremity (Chapter 4) and head kinematics and injuries (Elliott et al., 2012b; Peng et al., 2012b). A uniform distribution was assumed for pedestrian gait stance since there is no data available in accident and all gait stances are considered equally likely. Then involving proportions of the gait stance discrete groups for the cases using less than 10 gait stances were calculated based their representing range, see Table 5.8.

Table 5.8 Pedestrian gait stances and the estimated proportions (p_g) for different discrete groups.

Group	1	2	3	4	5	6	7	8	9	10
Gait	10%	20%	30%	40%	50%	60%	70%	80%	90%	100%
p_g	0.1	0.1	0.1	0.1	0.1	0.1	0.1	0.1	0.1	0.1
Range	10%	20%-30%	40%-50%	60%	70%-80%	90%-100%				
Gait	10%	30%	50%	60%	80%	100%				
p_g	0.1	0.2	0.2	0.1	0.2	0.2				
Range	20%-30%	40%-60%	70%-80%	90%-10%						
Gait	30%	50%	80%	100%						
p_g	0.2	0.3	0.2	0.3						
Range	20%-60%	70%-10%								
Gait	50%	100%								
p_g	0.5	0.5								
Range	10%-100%									
Gait	50%									
p_g	1.0									

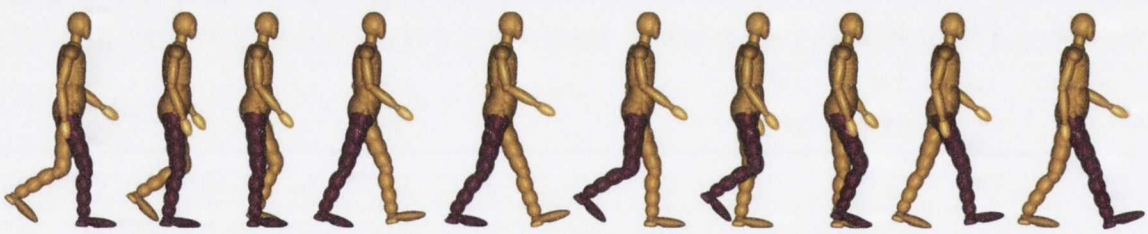

10% 20% 30% 40% 50% 60% 70% 80% 90% 100%

A STS can then be defined by the discrete groups of impact speed, pedestrian height and gait stance selected from Table 5.6-5.8, and the size of the STS is the product of the numbers of discrete groups for these three impact parameters, i.e. the size for a STS using 9 impact speeds, 7 pedestrian heights and 6 gait stances is 9*7*6=378. In total 35 STS candidates were developed based on different combinations of impact parameters, see Table A.1 (Appendix). The VTSs were named using the format VTS-No. speed-No. height-No. gait/No. scenarios, e.g. VTS-9-7-6/378 means that 9 impact speeds, 7 pedestrian heights and 6 gait stances were used in the STS of 378 impact configurations.

5.5.2 Combined Injury Number (CIN)

The WINs for the sedan and van model were calculated based on the simulation outputs and the involving proportions of impact speed, pedestrian height and gait stance (p_s, p_h and p_g in Table 5.6-5.8) via the proposed injury weighting system. To assess the capacity of the proposed VTS to predict the injuries observed in the GIDAS data, a combined injury number (CIN) for AIS2+ injuries for the sedan and van was calculated from the individual WIN (WIN_{sed}-sedan and WIN_{van}-van) for each vehicle class and the frequency (p_{sed}-sedan = 0.94 and p_{van}-van = 0.06, Figure 5.1) of occurrence of each vehicle class in the GIDAS database, see Eq. (5.4). The sum of proportions for all vehicle types is unity, see Eq. (5.5).

$$CIN = WIN_{sed} * p_{sed} + WIN_{van} * p_{van}, \tag{5.4}$$

$$p_{sed} + p_{van} = 1. \tag{5.5}$$

To investigate the sensitivity of the results to the number of impact configurations included in the VTS, combined injury numbers (CINs) were calculated for all the VTSs with different STSs (Table A.1). Comparisons were then made between the predicted AIS2+ injury distributions from the CIN and the actual AIS2+ injury distribution in the GIDAS, as well as the predicted CIN (average number of AIS2+ injuries per impact simulation) from the VTS and the AIS2+ injury rate (number of AIS2+ injuries divided by number of accident cases, i.e. the average number of AIS2+ injuries for each case) in GIDAS. The AIS2+ injury distribution comparisons were made on the basis of proportions of injuries to the different body regions, pedestrian heights, vehicle classes and impact speeds.

5.5.3 Comparison results between VTS and GIDAS

Figure 5.9 and 5.10 show the predicted AIS2+ distributions as a function of pedestrian body region and height, and vehicle impact speed and type between the CINs predicted by different sized VTSs. The GIDAS data is also shown as the reference. The proportions of AIS2+ injuries to these five body regions and thirteen impact speeds from the GIDAS were normalized to keep a summation of 100% since injuries relating to other body parts and impact speeds were excluded in the simulation test sample. The comparisons conducted in Figure 5.9 and 5.10 were also 'normalized' to use the

minimum number (three) of pedestrian height and impact speed groups considered in the VTSs (e.g. the predictions using three impact speeds cannot compare to the accident data for ten impact speed bins, but the predictions using ten impact speeds can compare to the accident data for three impact speed bins). This can also avoid the exaggerated relative differences between the predicted injury proportions and the accident data for the VTSs where large numbers of pedestrian height and/or impact speed groups are used since for those cases the injury proportion of each group is very small (the relative error will be too large).

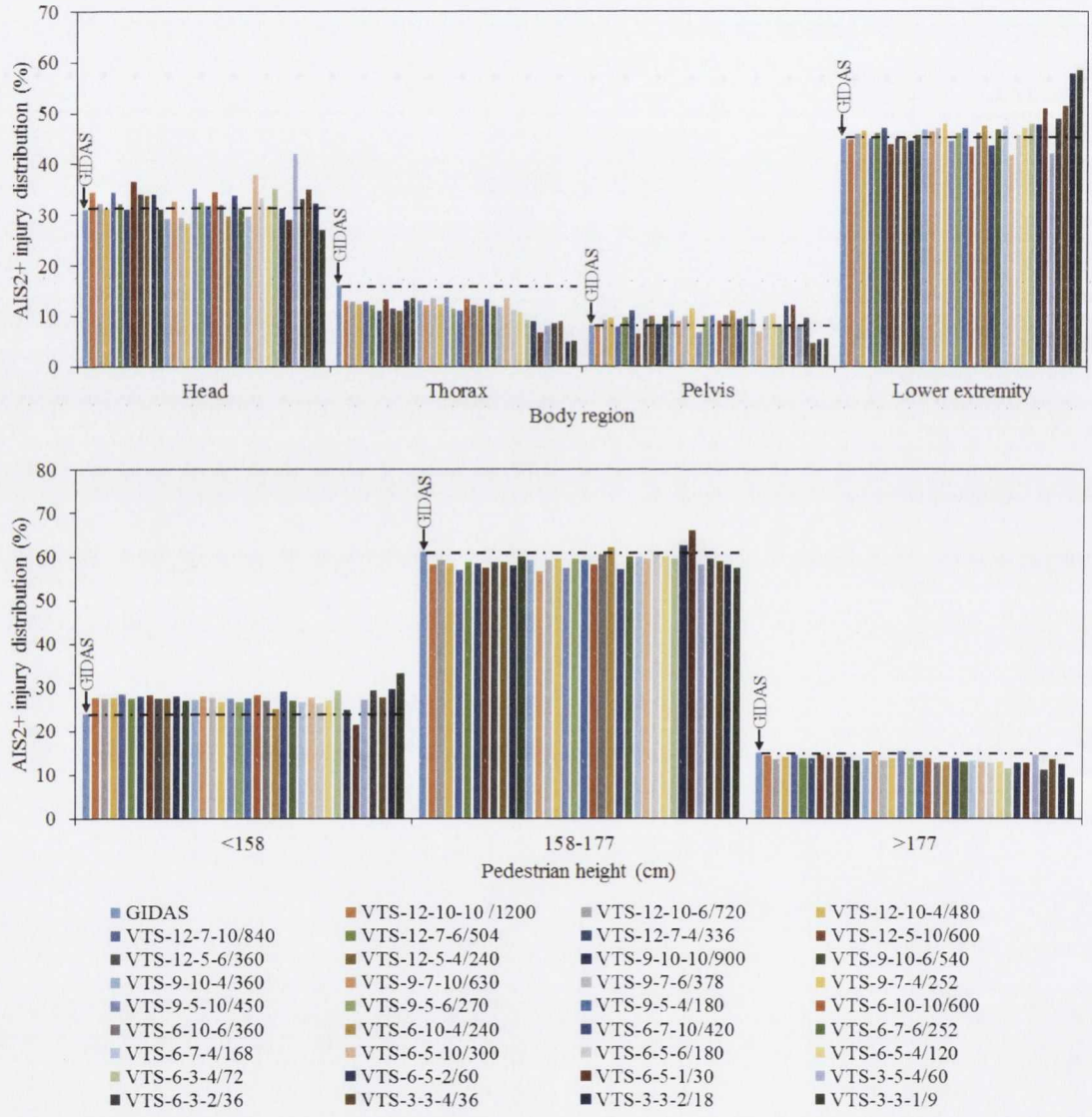

Figure 5.9 Comparisons of AIS2+ injury distributions as pedestrian body region and height between VTSs and GIDAS data.

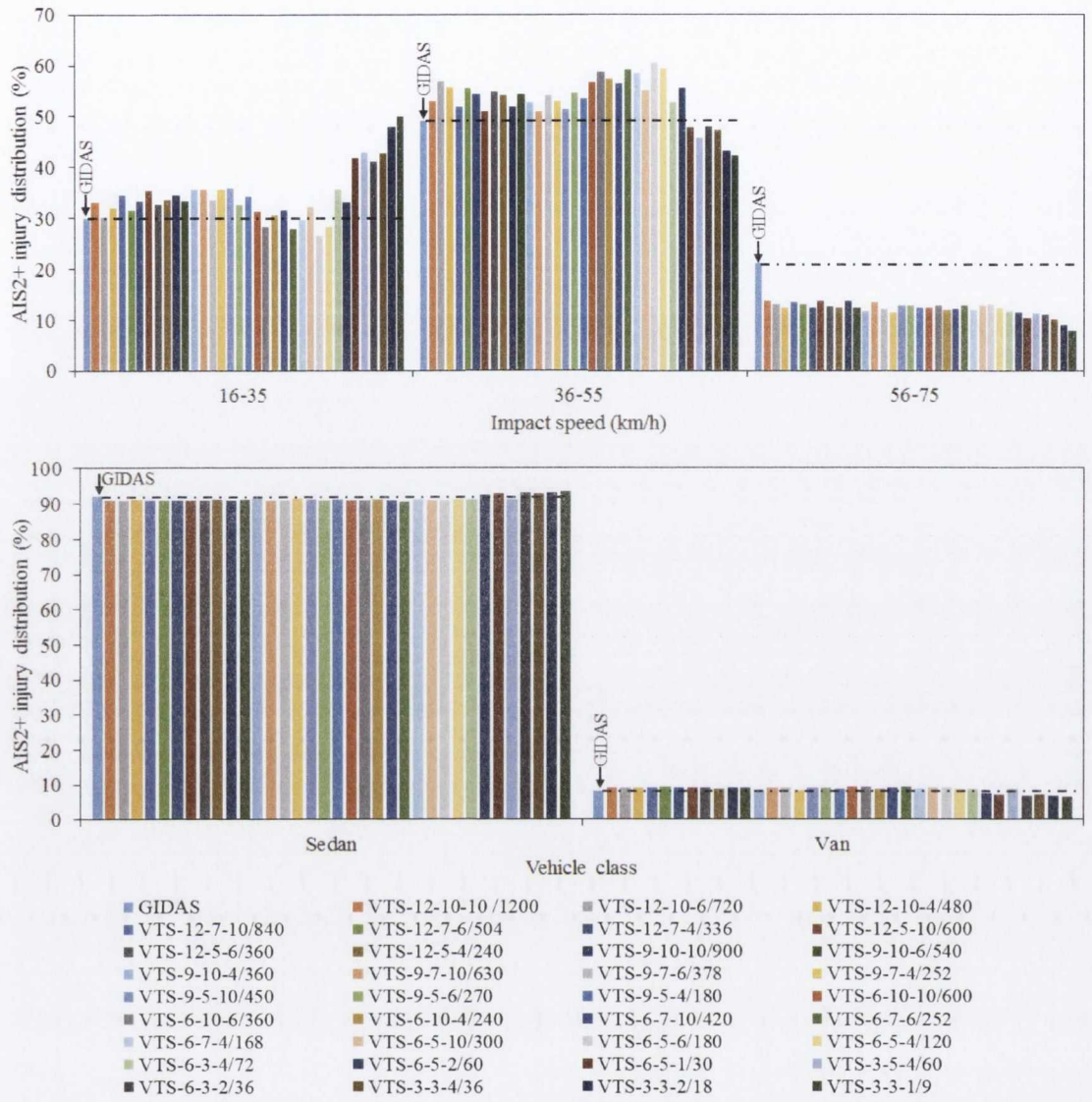

Figure 5.10 Comparisons of AIS2+ injury distributions as vehicle impact speed and class between VTSs and GIDAS data.

Generally, the AIS2+ injury distributions predicted from the VTSs are very similar to that in GIDAS data except those cases where very small STS samples were used, see Figures 5.9 and 5.10. The differences in AIS2+ injury distributions between VTSs using different STS sizes and GIDAS data are more evident for body region and impact speed than for pedestrian height and vehicle class. Figure 5.9 shows that the distribution of AIS2+ injuries by body region for the GIDAS accident data and the VTSs are very similar. The head (about 30%) and lower extremity (about 45%) are the dominant body regions for AIS2+ injuries (Figure 5.9), which is also similar to the trend observed in the accident data from different countries (Hu and Klinich, 2012).

For the comparison of AIS2+ injury distribution as a function of pedestrian height, Figure 5.9 shows that the VTSs slightly over-predict the proportion of injuries associated with shorter individuals, and somewhat under-predict the proportions for midsize and taller pedestrians. These differences may be partly because the impact locations were fixed in the central area of the vehicle front for the STS. A consequence of this is that the stiff A-pillar to head contact which can occur (especially for impacts away from the vehicle midline) for adult pedestrians is not represented in the VTS. In contrast, for children the head often contacts with the stiff bonnet leading edge area regardless of the pedestrian position with respect to the vehicle midline. This likely leads to the over-representation of the shorter pedestrians with respect to taller pedestrians in the VTSs observed in Figure 5.9.

The predicted distribution of AIS2+ injury as a function of vehicle class shows good agreement with the GIDAS data, see Figure 5.10. However, the predicted injury frequencies at high impact speeds (>55km/h) are lower than observed in the GIDAS accident data. This may be largely because of the simplification of impact scenarios and limitations in the modelling (contact, pedestrian model etc.). Another possible reason for this is that the injuries from ground impacts are not accounted for high impact speed cases, thus leading to under-predictions of injuries for the cases within the speed range.

Apart from the injury distributions, the normalized AIS2+ injury number (injury rate) from the VTS and the GIDAS was compared in Figure 5.11, where the accident data within the impact speed range from 16 to 75 km/h (the speed range considered in the VTS) was used. The predicted AIS2+ injury rate is sensitive to the pedestrian gait stance, and the predicted AIS2+ injury rate increases when decreasing the number of gait stances included in the VTS. For example, the predicted AIS2+ injury rate for VTS-6-5-2/60 (1.353) is obviously higher than that for VTS-6-5-4/120 (1.140), VTS-6-5-6/180 (1.081) and VTS-6-5-10/300 (1.042). This may be because the high proportions of gait stances with straight lower extremities in the VTSs where less gait stances are used (Table 5.8) raise the AIS2+ injury rate in pedestrian lower extremities (accounting for about 45% of all AIS2+ injuries, see Figure 5.9), since the gait stances with straight lower extremities have a higher injury risk to the lower extremity than the flexed knees (Chapter 3).

Figure 5.11 Comparisons of AIS2+ injury rate between VTSs and GIDAS data.

Figure 5.12 shows the mean relative differences in AIS2+ proportions for pedestrian body region and height, and vehicle impact speed and class between the CINs predicted by the VTSs in different STS sizes and GIDAS data shown in Figure 5.9 and 10. The mean and standard deviation of relative error (with respect to the GIDAS data) of a VTS for a given distribution (body region, pedestrian height, impact speed and vehicle class) were calculated based on the relative differences of all the comparisons for a VTS in this distribution (i.e. for body region comparison, mean and standard deviation of the relative differences in AIS2+ proportion for head, thorax, pelvis and lower extremity). From this figure we can see that the sample size has visible effects on AIS2+ injury distributions as a function of pedestrian body region and vehicle impact speed, but the effects for sample size on AIS2+ injury distributions as a function of pedestrian height and vehicle class are not so obvious. Figure 5.13 shows the relative errors in the AIS2+ injury rate between the VTSs using different STSs and GIDAS data. These comparisons help to reflect the representativeness of a VTS compared to the GIDAS accidents.

Figures 5.12 and 5.13 indicate an obvious decrease in predictive capacity (increased relative error) with increasing the sample size when less than 120 impact configurations (red point) were employed in the STS. But the relative errors have no obvious reductions when a sample size bigger than 120 was applied.

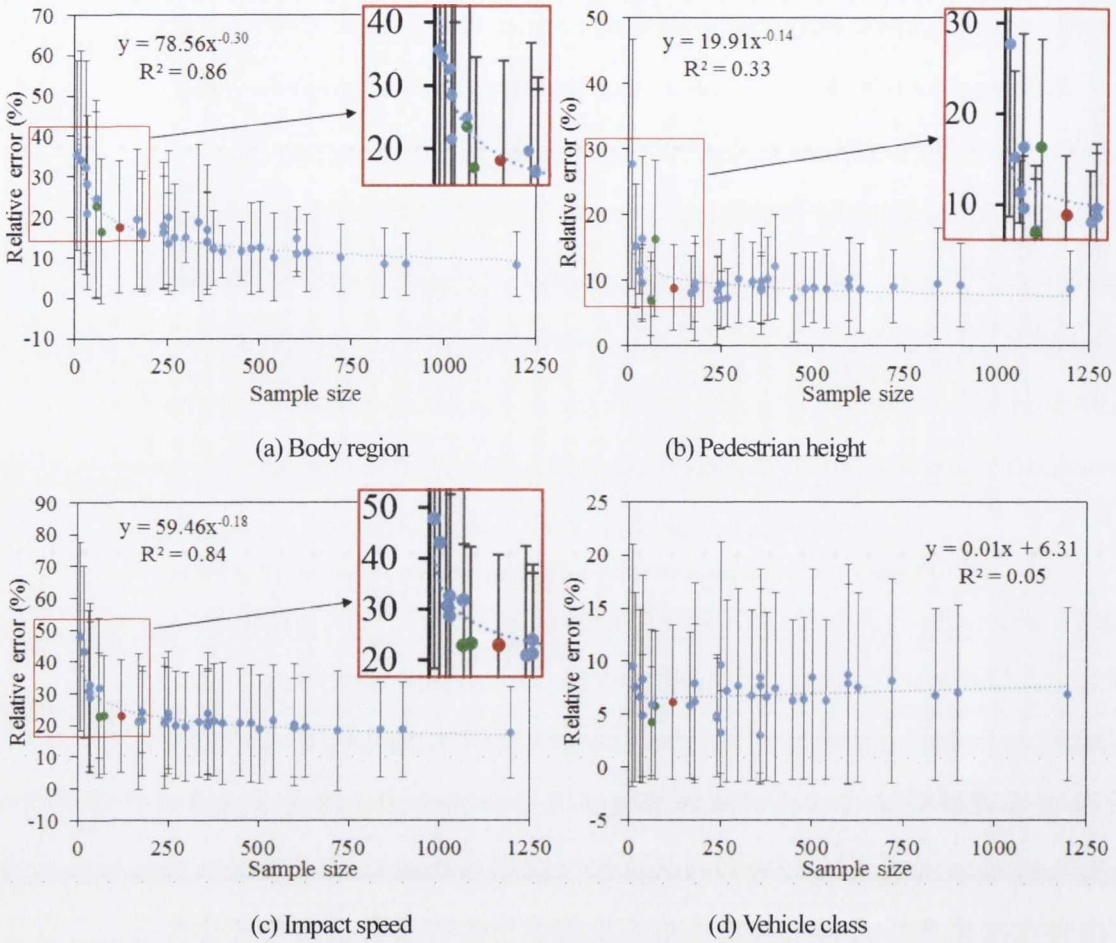

Figure 5.12 Relative errors in AIS2+ injury proportion as pedestrian body region and height, and vehicle impact speed and class between VTSs and GIDAS data.

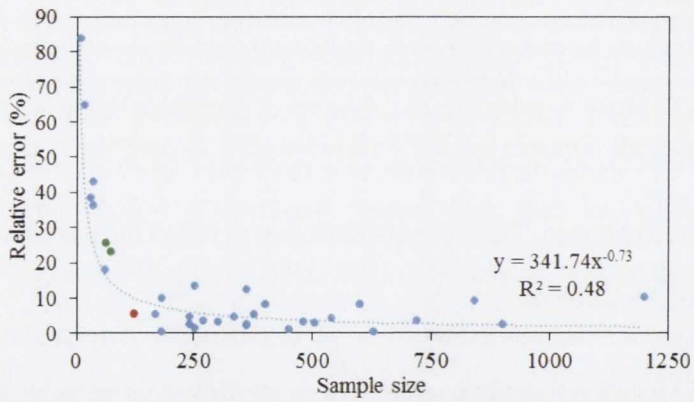

Figure 5.13 Relative errors in AIS2+ injury rate between VTSs and GIDAS data.

5.5.4 Computational time

Figure 5.14 shows the computational time (for a single vehicle model) as a function of the STS

sample size for a given computer with parallel computing of four cores. For the given computer, the computational time increases linearly with increasing the STS sample size. The computational time shown in Figure 5.14 is for a single vehicle model, including the time for impact simulation and WIC calculation. For the optimization work where a very large number of vehicle designs need to be evaluated, a small STS sample size can reduce the computational time substantially.

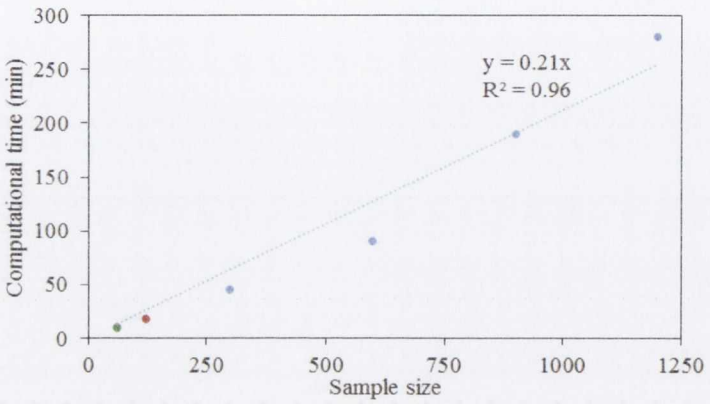

Figure 5.14. Computational time as a function of STS sample size (red for 120 and green for 60).

5.5.5 Selection of the STS for optimization

The Mann-Whitney-U test (data is not normally distributed) was applied to check the differences in the predicted relative errors shown in Figure 5.12 and 5.13 between the VTSs using a STS size smaller than 120 and those VTSs with a bigger STS size (≥120). Table 5.9 shows the Mann-Whitney-U test results, including the median relative errors for VTSs with a small or large STS size and the significance level for the differences in the predicted relative errors between these two groups. The Mann-Whitney U test results show that the predicted relative errors in AIS2+ injury distribution as a function of body region and impact speed and the AIS2+ injury rate for the VTSs with a STS size smaller than 120 are significantly (p-value<0.05) higher than that for those VTSs having a larger STS size (≥120). The STS size is not significant (p-value>0.05) for the prediction of AIS2+ injury distribution as a function of pedestrian height and vehicle class.

Table 5.9 Mann-Whitney U test results for the effects of STS size on injury predictive capability

AIS2+ injury distribution/injury rate	STS size < 120 Median	STS size ≥ 120 Median	p-vale
Body region	26.46	13.65	**<0.001**
Pedestrian height	13.31	8.78	0.056
Impact speed	31.39	20.65	**<0.001**
Vehicle class	6.30	6.89	0.603
Injury rate	37.31	4.37	**<0.001**

A linear regression model was then used to establish the relationship between the mean relative errors in the predicted AIS2+ injury distribution as a function of body region and impact speed (Figure 5.12 (a) and (c)), as well as the relative error in the predicted AIS2+ injury rate (Figure 5.13) and the number of impact parameter groups used in the STS. The model is:

$$REs = C + B_s * N_s + B_h * N_h + B_g * N_g, \tag{5.6}$$

where the *REs* are the predicted relative errors for a given comparison described above, C is the constant of the regression model, B and N are the coefficient and number of groups for each impact parameter, respectively. The subscripts in Eq. (5.6) are the impact speed (s), pedestrian height (h) and gait stance (g).

Table 5.10 shows the regression analysis results. The R-square values (0.48-0.79), which are the coefficients of determination of the regression models reflecting the correlation between the input data (relative errors) and that estimated from the regression functions, indicate that the regression models can generally represent the relationships between the numbers of impact parameters and the predicted relative errors. Table 5.10 also shows the coefficients and p-values for these impact parameters in each comparison, where the coefficient reflects the importance and significance level of the corresponding impact parameter in the regression. It is clear that the three impact parameters are statistically significant (p-value<0.05) for the predicted relative errors of AIS2+ injury distribution as a function of body region and impact speed. The negative coefficients for all of these impact parameters indicate that the relative error decreases with increasing the number of groups for impact speed, pedestrian height and gait stance used in the STS. For the prediction of AIS2+ injury

distribution as a function of body region in GIDAS, the number of pedestrian gait stance (B=-1.10) is more important than the number of groups for impact speed (B=-0.68) and pedestrian height (B=-0.76). The number of impact speed is the most importance factor influencing the prediction of AIS2+ injury distribution as a function of impact speed in GIDAS. For the prediction of AIS2+ injury rate in GIDAS, the effect of pedestrian height number is more significant. These results suggest that the number of groups for all impact parameters (impact speed, pedestrian height and gait stance) considered in the STS has a significant influence on the injury predictive capability of the VTS since these parameters are all important factors for the pedestrian injury outcome in vehicle collisions.

Table 5.10 Regression analysis results

Relative error (RE)	Impact parameter	Constant	B	R-square	p-vale
Body region	Impact speed	33.00	-0.68	0.79	**0.001**
	Pedestrian height		-0.76		**0.002**
	Gait stance group		-1.10		**0.000**
Impact speed	Speed group	36.53	-0.82	0.64	**0.001**
	Height group		-0.53		**0.047**
	Gait stance group		-0.64		**0.007**
Injury rate	Speed group	44.25	-1.49	0.48	**0.042**
	Height group		-1.81		**0.044**
	Gait stance group		-1.54		**0.045**

According to the above analysis, a sample size of 120 (VTS-6-5-4/120) is a good choice based on the current selected impact configurations and numerical methods. But the computational time for a STS size of 120 is twice that for a sample size of 60, which would enlarge the total simulation time in the optimization where a huge number of vehicle designs need to be evaluated. Considering the absolute effects of the impact parameters (impact speed, pedestrian height and gait stance) on pedestrian injuries and the difference between discrete groups of each parameter, it is suggested to use more groups of impact speed (an interval bigger than 10 km/h may lead to a large different in the injury outcome) and pedestrian height (important for the head contact location and selection of a safe vehicle shape in the optimization) but less gait stances (most gait stances are similar to each other) in

the STS when controlling the computational time for the vehicle front shape optimization. Therefore it is reasonable to consider the VTS-6-5-2/60 as the candidate for the optimization since it includes the same impact speed (six groups from 16 to 75 km/h) and pedestrian height (five sizes from child to large adult male) groups as the VTS-6-5-4/120. The only difference between these two STSs is in the gait stance (Table 5.8), but all gait stances considered in the VTS-6-5-2/60 are with straight lower extremities, which may result in more severe lower extremity injuries in the collision. Therefore the optimization based on VTS-6-5-2/60 can take the severe situation into consideration. Moreover, the VTS-6-6-2/60 can predict the AIS2+ injury distributions and AIS2+ injury rate observed from GIDAS data with mean relative errors less than 25% (the green point in Figure 5.12 and 5.13), which is generally acceptable.

5.6 Evaluation of VTS using PCDS data

5.6.1 Inputs data

As discussed above a STS of 60 impact configurations (VTS-6-5-2/60, Table A.1) is the choice for later vehicle front optimization. For a further evaluation, the injury predictive capability of the VTS-6-5-2/60 was assessed by comparing to the PCDS data. Therefore, the sedan, SUV and van multi-body models (Figure 5.7) were tested using the VTS-6-5-2/60. Similarly, the distributions of vehicle impact speed, pedestrian height and pedestrian gait stance used in the STS were derived based on PCDS accident data (Mizuno and Ishikawa, 2003) and US anthropometric data (Pheasant and Haslegrave, 2006) or reasonable assumptions.

Figure 5.15 shows the distributions of the impact speed, pedestrian height and gait stance discrete groups for VTS-6-5-2/60, and the proportions of each impact parameter were normalized to maintain a sum of 100%. The distribution of the vehicle impact speed (Figure 5.15) was extracted directly from a study on PCDS data (Mizuno and Ishikawa, 2003), the mid-value of each discrete group (e.g. 20.5 km/h for group 16-25 km/h) was assumed as the input impact speed in the simulation since no detailed data is available. The distribution of pedestrian height was calculated by the proportions of the pedestrian ages (Mizuno and Ishikawa 2003) and the estimated heights based on US anthropometric data (Pheasant and Haslegrave, 2006), see Figure 5.15. The mean heights of these

discrete groups were calculated based on the height data estimated, and these values are very close to the height of the selected pedestrian models (Figure 5.15 and Table 5.7). The same distribution of gait stance as shown in Table 5.8 for the case of using two gait stances were employed here based on the assumed uniform distribution since there is no detailed data available for gait position in PCDS either. Then the WINs for the sedan, SUV and van model were calculated based on the simulation outputs and the involving proportions of impact speed, pedestrian height and gait stance (Figure 5.15) via the proposed IWS.

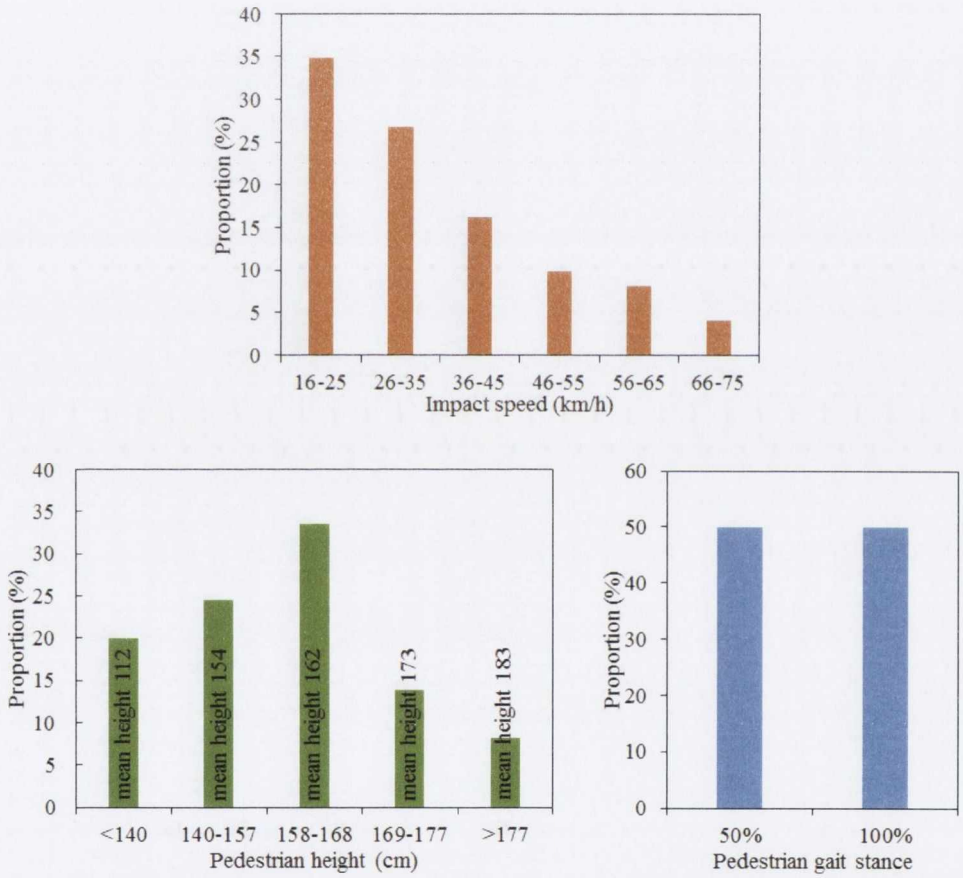

Figure 5.15 Distribution of impact speed, pedestrian height (PCDS) and gait stance (assumed uniform distribution) for VTS-6-5-2/60.

Similarly, the CIN for AIS2+ injuries for these three vehicle classes was calculated from the individual WIN (WIN_{sed}-sedan, WIN_{suv}-SUV and WIN_{van}-van) for each vehicle class and its frequency (p_{sed}-sedan = 0.68, p_{suv}-SUV/pick-up = 0.18 and p_{van}-van = 0.14, Figure 5.1) of occurrence in the PCDS (Chidester and Isenberg 2001), see Eq. (5.7). As before, the sum of the proportions for

all vehicle classes is unity, see Eq. (5.8). Then the AIS2+ injury distributions as a function of body region, pedestrian height, vehicle class and impact speed and AIS2+ injury rate predicted from the CIN were compared to that from the PCDS data.

$$CIN = WIN_{sed} * p_{sed} + WIN_{suv} * p_{suv} + WIN_{van} * p_{van}, \tag{5.7}$$

$$p_{sed} + p_{suv} + p_{van} = 1. \tag{5.8}$$

5.6.2 Comparison between VTS and PCDS

Figure 5.16 compares the distributions of the predicted (VTS) and actual (PCDS) AIS2+ injuries for different body regions, pedestrian heights, vehicle types and impact speeds. The injury data for PCDS was adapted from previous studies (Chidester and Isenberg, 2001; Klinich and Schneider, 2003; Mizuno and Ishikawa, 2003) and the proportions for the body region and impact speed were normalized to keep a summation of 100% since injuries relating to other body parts and impact speeds were excluded in the simulation test sample. Generally the predicted AIS2+ injury distributions are very similar to the PCDS data although there are differences in some cases.

The results in Figure 5.16 show that the distribution of AIS2+ injuries by body region for the PCDS accident data and the VTS are very similar. The head and lower extremity are the dominant body regions for AIS2+ injuries, which is also similar to the trend of GIDAS data and IHRA data reported by Mizuno and Ishikawa (2003). Figure 5.16 shows that the VTS over-predicts the proportion of AIS2+ injuries associated with shorter individuals (<168 cm) by about 19%, and under-predicts the proportions for taller pedestrians (≥168 cm) by 13%. Similar to before, these differences may be partly because the impact locations were fixed in the central area of the vehicle front for the VTS. A consequence of this is that the stiff A-pillar-head contact which can occur for taller pedestrians is not represented in the STS, but this accounts for about 10% AIS2+ injuries in PCDS accidents (Chidester and Isenberg, 2001). The VTS over-predicts the proportion of AIS2+ injuries for vans but under-predicts the injury proportion for sedans (Figure 5.16). These differences may be due to the limitation in ground contact definition where the ground is modelled as a rigid surface since the impact mechanisms for head-to-ground contact are more severe with vans compared to sedans (Crocetta et al., 2015). In general, the predicted relationship between injury proportion and impact

speed is similar to the PCDS cases, see Figure 5.16. However, the predicted injury frequencies at low impact speeds (≤35km/h) are significantly lower than observed in the PCDS accident data. Similarly, this may be largely because of the simplification of impact scenarios and limitations in the modelling (ground contact, pedestrian model etc.). Generally, the results in Figure 5.16 indicate that the VTS can also predict the general distribution of pedestrian injuries in PCDS data as a function of body region, pedestrian height, vehicle class and impact speed.

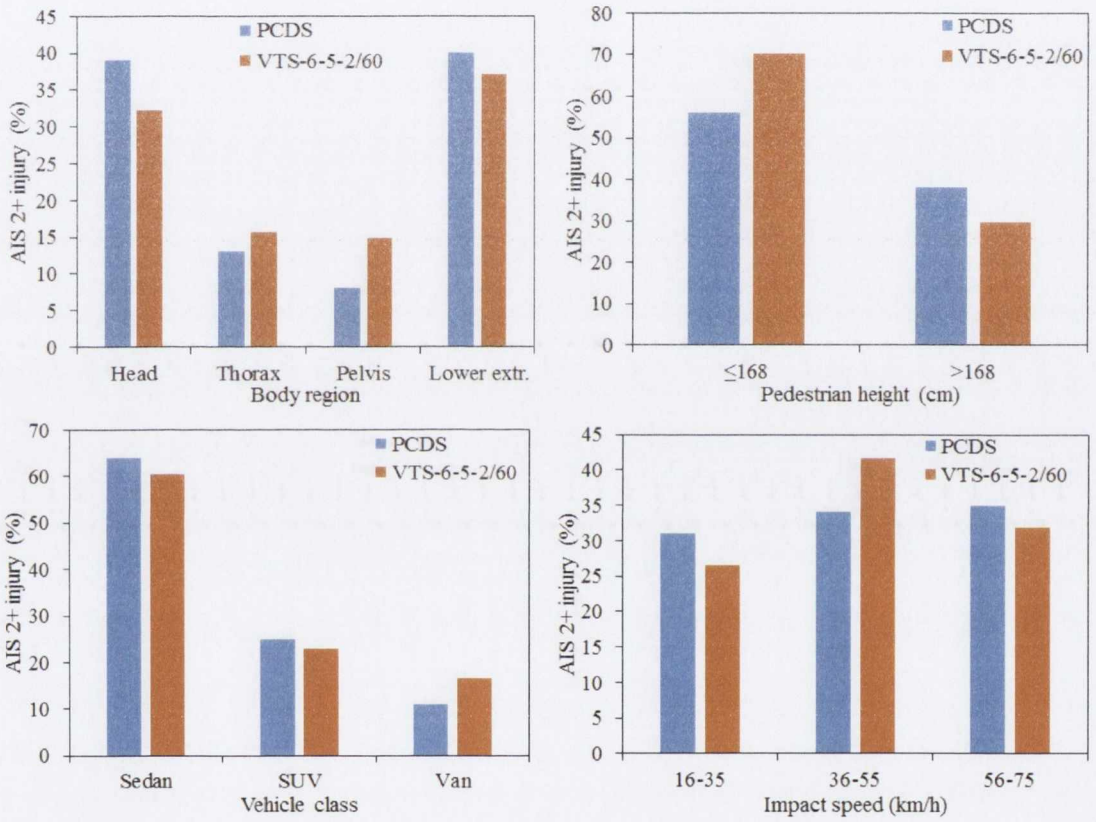

Figure 5.16 Comparisons of AIS2+ injury distributions as pedestrian body region and height, and vehicle impact speed and class between VTSs and PCDS data.

The normalized AIS2+ injury numbers from the VTS and the PCDS were also compared. There are 1040 AIS2+ injuries from the body regions accounted in the current study for 552 accidents in the PCDS data, so the AIS2+ injury rate in the accident data is 1.88 (1040/552). For the predicted CIN derived from the VTS, the normalized AIS2+ injury number is 1.43. Thus the predicted average AIS 2+ injuries per impact is considerably lower than that in the PCDS accidents. This may be because only one injury is currently recorded per body region in the VTS and the variations of vehicle front

stiffness in the accidents, but only one contact characteristic was considered for each vehicle structure and the same contact characteristics were defined for all the three vehicle classes. The differences between the predicted CIN and the AIS2+ injury rate in PCDS and GIDAS data also reflect the differences in the injury risk in raw data shown in Table 5.1.

5.7 Sensitivity of WIN to vehicle shape

5.7.1 Setup of the sensitivity study

The main application of the VTS will be as a means to discriminate different vehicle front designs for pedestrian safety. This can be done with the Weighted Injury Number (WIN), see Eq. (5.3), which reflects the global threat of a vehicle front design for pedestrians. However, the effectiveness of the VTS in discriminating different vehicle designs depends on the WIN being sufficiently different when the vehicle shape (class) is changed. Accordingly, the sensitivity of the predicted injury risks to variations in vehicle shape (class) is an important consideration: if the VTS is to be successful in optimizing a vehicle front for pedestrian protection, the injury predictions should obviously be sensitive to changes in vehicle shape. The benefits of reducing effective stiffness are obvious (e.g. keeping enough space between the deformed surfaces and the bottom stiff structures), but there should also be clear differences in the predicted injury risk when the VTS is applied to a conventional sedan shape compared to an SUV or a van, since accident data indicates clear differences in pedestrian injury risk between these vehicle classes (Li et al., 2012; Longhitano et al., 2005), and analysis show this is substantially a function of differences in vehicle shape (Simms and Wood, 2006b; Han et al., 2012).

Therefore, an assessment of the influence of changes in vehicle front shape (class) on the predicted injury outcome for the VTS was carried out. Three different vehicle front shapes (sedan, SUV and van) developed by Crocetta et al. (2015), with the same contact definitions for the corresponding vehicle structures, were tested using the selected VTS with a STS size of 60 (VTS-6-5-2/120, see Table A.1). Then the predicted WINs from these three vehicle types were compared to each other to investigate the sensitivity of the predicted injury risks to variations in vehicle shape.

5.7.2 Sensitivity study results and discussion

Figure 5.17 (a) shows the predicted WINs for different vehicle shapes (classes) tested using the VTS-6-5-2/60 based on the inputs from GIDAS and PCDS data, respectively. Figure 5.17 (b) shows these predicted WINs for pedestrian head, thorax, pelvis and lower extremity, and different vehicle shapes (classes). As defined above the WIN is the weighted average number of AIS2+ injuries recorded per impact configuration in the STS, so it reflects the aggressivity of a vehicle front design to pedestrians considering the distributions of impact configurations in real world accidents. Generally, the SUV and van have a higher predicted WIN than the sedan (Figure 5.17 (a)), but the difference in the predicted WIN between these three vehicle classes varies between body regions (Figure 5.17 (b)).

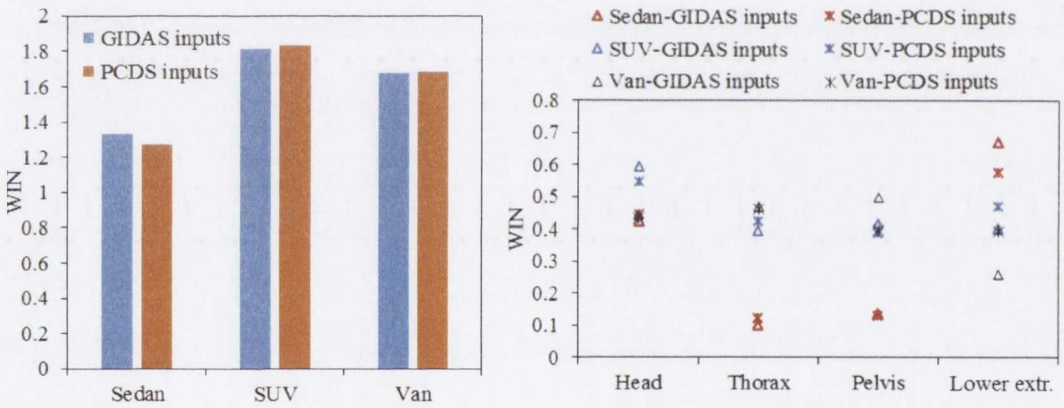

(a) (b)

Figure 5.17 Predicted overall WIN (a) and WIN of the head, thorax, pelvis and lower extremity (b) for different vehicle classes.

Although it is already known that higher injury risks are associated with SUV and van shapes compared to sedans (Klinich and Schneider, 2003; Longhitano et al., 2005), Figure 5.17 (a) shows for the first time the magnitude of the potential benefits/deficits which might accrue to the population of pedestrians by changing the shape of the vehicle population. As shown in Figure 5.17 (a), the SUV (WIN≈1.8) and van (WIN≈1.7) models have a higher predicted WIN than the sedan (WIN≈1.3) model. This predicted trend is similar to the accident data (Table 5.1). Figure 5.17 (b) shows that generally the SUV and van have a higher WIN to the pedestrian's head than the sedan. This prediction is also similar to the accident data (Table 5.1). The results

in Figure 5.17 (b) also indicate that the van model has an obviously higher WIN to a pedestrian's thorax and pelvis but a lower WIN to the lower extremity than the sedan model. Again these findings are in line with the GIDAS data, where the AIS2+ thorax injury rate between vans and sedans is 0.375 vs 0.164, AIS2+ pelvis injury rate is 0.208 vs 0.083 and AIS2+ lower extremity injury rate is 0.375 vs 0.485. The predicted trend of a higher lower extremity injury risk for sedan cases compared to van impacts is also similar to that in the PCDS data (Table 5.1). Even though the detailed thorax injury data from different vehicle classes are not available, a previous study on PCDS indicates that the AIS2+ thorax injury rate for LTV cases (0.68) is obviously higher than that for sedan cases (0.38) (Longhitano et al., 2005). Generally, the results in Figure 5.17 show that the predicted WIN is sensitive to changes in vehicle front shape, and the predicted trends for the effects of vehicle front shape on pedestrian injury risk are similar to those observed in accident data.

5.8 Summary

This chapter proposed a Virtual Test System (VTS) for assessing the aggressivity of a vehicle front shape to pedestrians considering a broad range of impact configurations and their distributions in real world accidents, as well as pedestrian injuries from different body regions. The proposed VTS consists of a Simulation Test Sample (STS) with a set of multi-body simulations accounting for broad ranges of impact speed, pedestrian height and gait stance and an Injury Weighting System (IWS) based on the distributions of these impact parameters in accidents.

The results indicate that the VTSs using a reasonable STS size can provide a good prediction of the distribution of pedestrian injuries observed from the GIDAS and PCDS database when the same vehicle type distribution as the accident data is employed. In particular, by defining a Weighted Injury Number (WIN), comparisons of AIS2+ injury distributions as a function of different pedestrian body regions and height groups, vehicle types and impact speeds between the VTS and the GIDAS accident data show good agreement. Furthermore, the VTS can predict the average AIS2+ injury number for every collision in the STS using the WIN, and the predicted WINs from the VTSs using a reasonable STS size are very similar to the AIS2+ injury rate in GIDAS data but lower

than the PCDS data. A sensitivity study shows significant variations in the WIN when vehicle shape is altered. The general trends of the WIN changing as vehicle shapes are similar to those in accidents.

The VTS can thus be considered as an effective approach for assessing pedestrian safety performance of a vehicle front shape at the generalized level. A simulation sample of 60 impact configurations (six impact speeds, five pedestrian heights and four pedestrian gait stances) is a good choice for future vehicle front optimization considering its computational efficiency, representativeness of impact configurations and injury predicative capability. The good matches between the predictions of MADYMO pedestrian models and accident data are from the combination of using reasonable injury criteria and thresholds, vehicle front shape and stiffness, as well as the injury weighting approach. Therefore similar definitions for these important factors will be used in the optimization process to keep plausible injury predictions.

Chapter 6 A Framework for Optimizing Vehicle Front Shape

6.1 Introduction

The study in Chapter 5 shows that the proposed virtual test system (VTS), where a broad range of impact configurations and their distributions in real world accidents are considered, can be used as an effective approach for assessing pedestrian safety performance of vehicle front designs at the generalized level. The proposed weighted injury number (WIN) can predict the average AIS2+ injury number for a vehicle front design considering a broad range of impact configurations by a simulation test sample (STS) and an injury weighting system (IWS). However, the injuries from different body regions may result in different threats and permanent influences to pedestrians. Therefore the predicted injuries from the STS need to be weighted further to reflect the importance of each injury observed. For vehicle front optimization issue, the fitness function, optimization strategy and optimization algorithm need to be defined appropriately. Accordingly, the purpose of this chapter is to develop an efficient framework for optimizing vehicle front shape for pedestrian protection accounting for real world accident configurations and overall pedestrian injuries.

6.2 Impact configurations

The Simulation Test Sample (STS) has been proposed in Chapter 5 (Section 5.3.1) to take most impact configurations into account considering the vehicle impact speed, pedestrian height and pedestrian gait stance for assessing the safety performance of a vehicle front design in real world pedestrian accidents. In the optimization it is necessary to limit the computational time at a reasonable level while maintaining the injury predicative capability of the simulation sample. According to the analysis in Chapter 5 (Section 5.5.5), the STS with 60 impact configurations (VTS-6-5-2/60, see Table A.1) was selected for the optimization framework, and the GIDAS data was employed as the inputs for the STS. The input data of the selected STS is shown in Table 6.1, where the values of p_s, p_h and p_g are the involving proportions for the impact speeds, pedestrian heights and gait stances, respectively. The 60 impact configurations in the STS are formed by the six

vehicle impact speeds, five pedestrian heights and two gait stances, see Table 6.1.

Table 6.1 Input data for the VTS-6-5-2/60

Impact parameter		Group 1	Group 2	Group 3	Group 4	Group 5	Group 6
Impact speed (km/h)	Range	16-25	26-35	36-45	46-55	56-65	66-75
	Mean	21	31	41	50	61	70
	p_s	0.337	0.295	0.216	0.096	0.042	0.014
Pedestrian height (cm)	Range	<140	140-157	158-170	171-177	>177	
	Mean	120	151	164	174	185	
	Model	6YOC	5^{th}%F	5^{th}%M	50^{th}%M	90^{th}%M	
	& height	117	153	165	174	185	
	p_h	0.147	0.169	0.372	0.187	0.125	
Pedestrian gait stance	Range	30%-70%	80%-20%				
	Mean	50%	100%				
	P_g	0.5	0.5				

These six mean impact speeds can be directly applied to the simulation in the STS. According to the mean values of the pedestrian heights for different ranges (Table 6.1), five MADYMO models (6YOC, 5^{th}%F (female), 5^{th}%M (male), 50^{th}%M and 90^{th}%M) were selected to represent the discrete pedestrian height groups in the STS, see Figure 6.1.

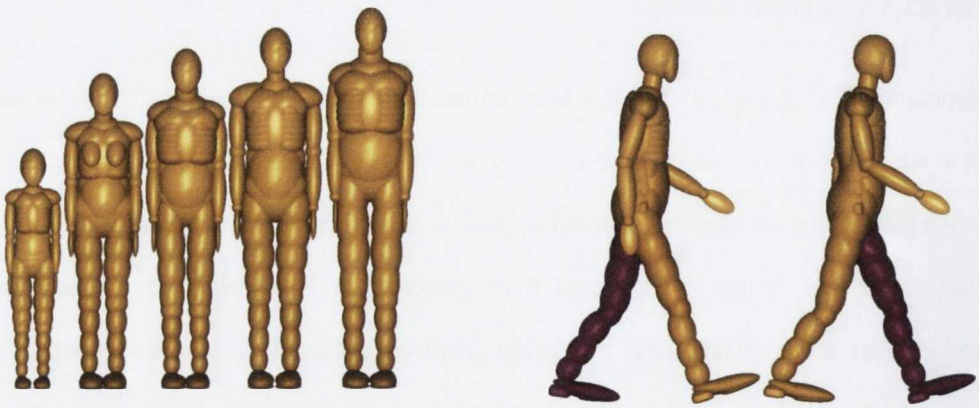

Figure 6.1 MADYMO pedestrian models (MADYMO, 2012) and gait stances (Untaroiu et al, 2009).

Generally the selected pedestrian models can represent the mean pedestrian sizes of different height groups in accidents, see Table 6.1. These pedestrian models cover a broad range of pedestrian heights

from small child (<140 cm) to big adults (>177 cm) in accidents. This can reflect the variations of the relative height of vehicle bumper to the knee, bonnet leading edge to the hip and thorax and head impact location on the vehicle front structure, which will give a broad evaluation of the vehicle front shape for pedestrian safety performance. The selected gait stances are also shown in Figure 6.1 (struck from the left side in the simulations), including positions of forward or backward, and straight knee or flexed knee. These gait stances are associated with the highest lower extremity injury risk (Chapter 4) and also consider the forward and backward rotation of the upper body (Elliott et al., 2012b).

6.3 Vehicle model

In order to test thousands of different vehicle front shape designs in a reasonable time, the vehicle model should be simplified enough to reduce the computing time. According to the GIDAS accident data summarized in Chapter 5 (Section 5.2), most pedestrian accidents occur in the centre area of the vehicle front in the horizontal direction (Figure 5.2 and 5.3, Chapter 5). Thus in this study the optimization focuses on the vehicle centre line shape design. Therefore, simplified multi-body ellipsoid models are used for modelling the vehicle front. As shown in Figure 6.2, six ellipsoids are used to form the centre-line profile of the vehicle front: lower bumper, bumper, bonnet leading edge, bonnet and windscreen. The shape of a particular structure (i.e. bumper, bonnet leading edge, and so on) and the overall vehicle front shape can be controlled by nine parameters (#1-#9, see Figure 6.2). In the optimization some constraints are defined to keep the vehicle shape in a normal geometry since there are overlaps between dimensions. For example, #3 is fixed at a reasonable level as the reference of the chain, #4 must be lower than #5 and #7 must be not larger than #9.

The optimization is defined as a consecutive process, so the vehicle model should be automatically created during the optimization process. As all ellipsoids in MADYMO are positioned relative to a global origin, a geometric dimension chain (crossing the centre of the ellipsoids) is developed as a string of numerical parameters to describe the centre-line geometry of the vehicle front, see Figure 6.2. MATLAB codes were created to control all the parameters and generate vehicle shapes for MADYMO simulation, which allow new shapes to be generated automatically from the geometric

dimension chain. This geometric dimension chain maintains a continuous vehicle shape without any gaps between each ellipsoid for any changes to some or all of the dimensions in the optimization. The same contact characteristics for the vehicle front structures as Chapter 5 were employed for the vehicle model in the optimization framework, see Figure 5.8.

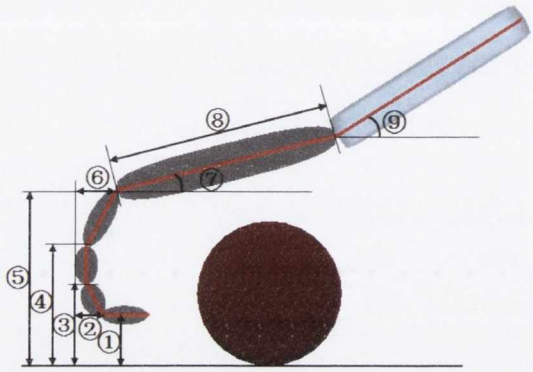

Figure 6.2 Vehicle front model and the geometric dimension chain.

6.4 Vehicle-to-pedestrian impact simulation

A frontal crash configuration with a pedestrian being struck from the left side is considered as the basic simulation condition (Figure 6.3). The impact configuration can be modified by changing vehicle impact speed, pedestrian size and gait stance according to the inputs of the STS. The simulation time was defined to cover the whole process of the primary and secondary impacts for low speed (<40 km/h) cases and cover the whole process of the primary impact for high speed (≥40 km/h) cases. The contact characteristic and friction coefficient for vehicle-pedestrian and ground-pedestrian contacts were defined similarly as described in Chapter 5 (Section 5.4.2).

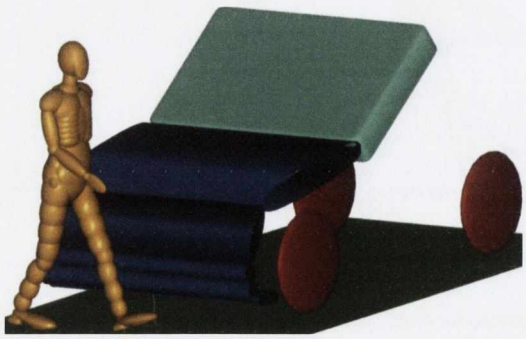

Figure 6.3. Vehicle-to-pedestrian impact simulation.

6.5 Weighted Injury Cost (WIC)

Same as the virtual test system (Chapter 5), in the optimization framework injury criteria of HIC (head), TTI (thorax), impact force (pelvis), bending moment (long bone in lower limbs) and bending angle (knee) were used for predicting injuries. The thresholds of these injury criteria from the literature were applied for assessing AIS levels of the predicted injuries, see Table 6.2. For the head, thorax, and knee the standard injury indices in Table 6.2 are applied for all pedestrian models since the data for pedestrians of different sizes and ages are not available. For lower limbs and the pelvis, fracture thresholds are assumed for the multi-body human models according to the size (Table 6.2).

Table 6.2 Injury criteria for AIS level of head, neck, thorax, pelvis and lower extremity.

Body region/Injury criteria	Injury criteria level	AIS level	Reference
Head/HIC	135-520	1	(Payne and Patel, 2001)
	520-900	2	
	900-1,255	3	
	1,255-1,575	4	
	1,575-1,860	5	
	>1,860	6	
Thorax/TTI (g)	80-100	1	(Cavanaugh et al., 1993)
	100-125	2	
	125-160	3	
	160-200	4	
	>200	5	
Pelvis/Lateral load (kN)	4.0-6.0 (adult)/1.0-2.0 (child)	2-3	(Payne and Patel, 2001)
	6.0-10.0 (adult)/2.0-4.0 (child)	3-4	
Thigh/Bending moment (Nm)	≥55 (3YOC)	3	(MADYMO, 2012) selected/scaled from (EEVC WG17, 1998)
	≥140 (6YOC)		
	≥265 (5^{th}% female)		
	≥350-530 (adult male)		
Knee/Bending angle (deg)	15 (all models)	2	(Mo et al., 2014)
Leg/Bending moment (Nm)	≥50 (3YOC)	2	(MADYMO, 2012) selected/scaled from (Nyquist et al., 1985)
	≥85 (6YOC)		
	≥240 (5^{th}% female)		
	≥270-380 (adult male)		

As reported in ISO: 13232-5 (2005), injury cost (medical cost and auxiliary cost) to the human body can be calculated based on AIS levels of injuries suffered in the corresponding body regions. Table 6.3 shows the medical cost and auxiliary cost of different body regions as a function of AIS level, where the values for the head, thorax and lower extremity were directly extracted from ISO: 13232-5 (2005). For the pelvis, 80% of the costs for an AIS3 and AIS4 abdomen injury were used for an AIS2-3 and AIS3-4 pelvis injury respectively, since no clear injury threshold for each AIS level (Table 6.2) and cost standard are available for the pelvis.

Table 6.3 Medical and auxiliary cost as a function of injury severity, adapted from (ISO: 13232-5, 2005).

Body region	AIS level	Medical cost ($)	PPI	Auxiliary cost ($)
Head	1	784	-	2,664
	2	3,807	-	10,818
	3	14,169	-	47,819
	4	72,349	-	91,497
	5	263,306	-	320,571
Thorax	1	696	-	1,372
	2	3,410	-	10,886
	3	10,147	-	31,051
	4	19,577	-	46,853
	5	32,790	-	64,256
Pelvis	2-3	8,118	-	24,841
	3-4	15,662	-	37,482
Lower extremity	2	7,881	07	27,370
	3	22,732	15	58,650
			22	86,020
			27	105,570
			38	148,580
The cost of fatality (AIS6) is $596,580				

The auxiliary costs of lower limb injuries were calculated based on the permanent partial incapacity (PPI) level which is assessed according to the AIS level in the femur, knee and tibia (Table 6.4). These injury costs were proposed to represent average costs based on a simplified model of samples of bio-economic data but not for the exact costs in a particular situation (ISO: 13232-5, 2005).

Table 6.4 Permanent partial incapacity determination, adapted from (ISO: 13232-5, 2005).

If		PPI
$N_{F,3}+N_{K,2}+N_{T,3}+N_{T,2}$	≥3	38
$N_{F,3}+N_{K,3}+N_{K,2}+N_{T,3}+N_{T,2}$	=2	27
$N_{F,3}$ or $N_{K,2}$ or $N_{T,3}$	=1	15
$N_{T,2}$	=1	07

Where: $N_{I,J}$ is the number of damaged frangible lower extremity components I of AIS injury severity level J, F is the femur component, T is the tibia component, and K is the knee component.

According to the above data, higher medical costs are proposed for body parts with a higher risk for death. Thus the injury cost provides a possible approach to consider the importance of the predicted injuries in the optimization framework. Then injury cost (IC) for a given vehicle-to-pedestrian impact simulation (configuration) can be calculated, which is the sum of the medical cost and auxiliary cost of all injuries to a pedestrian's head, thorax, pelvis and lower extremities. Therefore the injury cost data used in the optimization framework is a quantitative reference for predicted injuries.

Based on the approach of the injury weighting system (IWS) proposed in Chapter 5, the IC for each impact configuration in the STS is then weighted by the frequency of occurrence of this impact configuration in the real accident data to assess the aggressivity of a vehicle front shape to pedestrians. Similarly, the Weighted Injury Cost (WIC) for the STS (N=60) is the sum of the product of the IC (IC_i) and the proportion (p_i) for a given impact configuration in the STS, which is the product of the corresponding proportion of impact speed (p_{si}), pedestrian height (p_{hi}) and pedestrian gait stance (p_{gi}), see Table 6.1 and Eq. (6.1-6.2). Thus the WIC score is the weighted average cost of all injuries (head, thorax, pelvis and lower limbs) recorded per impact configuration in the STS. The WIC score,

regarded as the optimization objective, can thus be used as a metric to distinguish the aggressivity of different vehicle front shapes when the broad range of impact configurations in accidents and overall pedestrian injuries are considered.

$$p_i = p_{si} * p_{hi} * p_{gi}, \tag{6.1}$$

$$WIC = \sum_{i=1}^{60} IC_i * p_i. \tag{6.2}$$

6.6 Optimization method

According to the above approaches, the optimization problem of the vehicle front shape for pedestrian protection can be described briefly as follows:

$$\text{Min } WIC(x), \text{ with } x=\{x_1, x_2, x_3 \ldots x_9\}, X_L<x<X_U, \tag{6.3}$$

where $WIC(x)$ is the objective function, which is a function of independent variables x (design variables, see Figure 6.2), n is the number of design parameters, X_L *and* X_U are the lower and upper boundaries (design space) of the design variables. A given string of x forms a unique vehicle shape (design point). This is a highly nonlinear optimization problem since the injury output of the pedestrian body is not in a linear relationship with these vehicle shape parameters (Liu et al., 2002).

To find the optimal vehicle front shape for pedestrian protection based on nine design variables within a wide design space (Eq. (6.3)), a global optimization algorithm should be employed in the optimization framework. However, applying a global optimization algorithm in this highly nonlinear problem requires a huge computational effort to search the design space fully and it is difficult to avoid finding the local minima. Therefore, heuristic algorithms (e.g. a genetic algorithm) are usually applied for engineering optimization problems, where complex numerical (FE or multi-body) simulations are used (Untaroiu et al., 2009). In the current optimization framework, a genetic algorithm (GA) defined in the MATLAB Global Optimization toolbox was used for the vehicle front shape optimization.

GA is a probabilistic search technique that generates solutions to optimization problems using the

evolutionary concepts of natural selection and genetics (Chong and Zak, 2001). The GA starts with an evaluation for the design points of an initial population and the fitness values (calculated using the fitness function) of these design points are sorted. Then the design points are selected via a fitness-based process based on those sorted fitness values and a new population is created from these selected design points by specific genetic operators such as cross-over and mutation. The GA continues this process generation by generation until it reaches the stopping criteria. The stopping criteria of GA in MATLAB can be defined by setting a limit of generation, fitness value, and computational time. For the current optimization problem, a maximum generation number is a good choice for stopping criteria of the GA since the fitness value and computational time is uncertain while the maximum generation can be pre-checked by preliminary studies.

6.7 Optimization process

To control the simulations automatically, the whole optimization process was developed based on interactions between MATLAB and MADYMO. In the optimization framework MATLAB applications are employed for controlling impact configurations and vehicle shapes, processing the output data and conducting the GA, while MADYMO was used for conducting the impact simulations.

Figure 6.5 shows the whole process of the optimization framework. The optimization process starts with an initial set of values for the vehicle front shape parameters defined in Figure 6.2, which are usually randomly selected by the GA based on the boundaries of the design parameters, and this is called the initial generation. Then a set of vehicle front models are created by MADYMO based on these parameters. In the evaluation system each vehicle front model is tested by the selected STS (60 impact configurations) in MADYMO and the predicted injuries are processed via the weighting approaches proposed above in MATLAB. When all the vehicle models in the initial generation have been tested, the GA creates a new generation based on its defined algorithms described above. Then the optimization process continues from the start until it reaches the stopping criteria (maximum generation number).

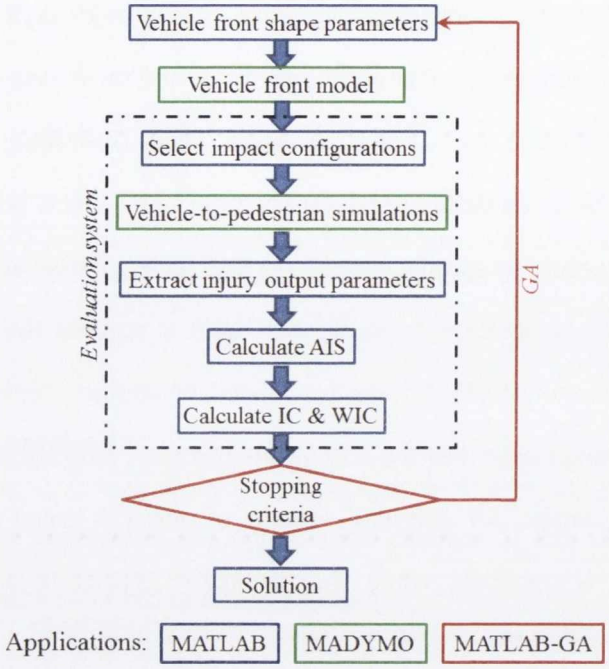

Figure 6.5 Whole process of the optimization framework.

6.7 Summary

An optimization framework of vehicle front shape was developed in this chapter. The defined optimization framework consists of a simulation test sample (STS) of 60 simulations for modelling different impact configurations in real world pedestrian accidents, a geometric dimension chain for controlling and creating continuous multi-body vehicle front models, a numerical system for calculating AIS and weighted injury cost (WIC) and a genetic algorithm (GA) for searching the optimal vehicle front shape. The proposed optimization framework provides a computational method for vehicle front shape optimization for pedestrian protection when the broad range of impact configurations and their distributions in accidents and the overall pedestrian injuries and their importance are considered. The proposed optimization framework is expandable for considering more impact scenarios and applicable for using more biofidelic pedestrian models, more detailed vehicle front models and more representative accident datasets.

Chapter 7 Optimization of Vehicle Front Shape

7.1 Introduction

This chapter applies the optimization framework proposed in Chapter 6 to optimize front shapes of different vehicle types for pedestrian protection. The PCDS accident data (U.S.) shows that sedans, SUV/pick-ups and vans are the main vehicle types involved in pedestrian accidents (Chidester and Isenberg, 2001). This situation is similar in other countries such as China and Germany (Yang and Otte, 2007). Therefore the optimization of vehicle front shape focuses on these three vehicle types. Since each vehicle type has its own function (i.e. sedans have a compact structure for urban use, SUV/pick-ups have a high ground clearance for suburban or off-road travel and vans have a high and short front to keep enough space for the passenger compartment) and the differences in the shape between these vehicle types are significant (Figure 2.3), it is reasonable to optimize the shape for each vehicle type separately. To achieve this, a design space (lower and upper boundary) was firstly defined for the sedan, SUV and van front shape, respectively, based on the vehicle data involved in real world accidents. Then the optimal shape of the vehicle front was obtained for each vehicle type via the optimization framework considering these design spaces.

7.2 Methods

7.2.1 Design spaces

To control the vehicle shape within a reasonable geometry (similar to the existing designs) in the optimization, a design space (lower and upper boundary) should be defined for the genetic algorithm (GA). For the current optimization framework, the lower and upper boundary should be defined for all nine dimensions of the geometric chain (Figure 6.2). Therefore design spaces for the sedan, SUV and van front shape were defined based on the data extracted from the IVAC, IHRA and GIDAS databases with the lowest and highest values of the corresponding dimension observed from these databases being used. For the sedan shape design space, the

data for the mini cars (e.g. Smart Fortwo, Hyundai i10, Sachsenring Trabant 601, Geely LC, etc.) is not considered since the pedestrian head is likely to impact the roof when struck by a mini car, which is beyond the consideration of the current optimization framework. Table 7.1 summarizes the lower and upper limits of the geometric dimension for each vehicle type. In the optimization these values were employed to control the vehicle front geometric dimension chain by the GA.

Table 7.1 Lower and upper limits of vehicle front geometric dimensions for sedan, SUV and van.

Dimension		#1	#2	#3	#4	#5	#6	#7	#8	#9
Unit		mm	mm	mm	mm	mm	mm	°	mm	°
Sedan	Lower	180	50	400	400	550	80	8	700	20
	Upper	350	250	400	700	950	300	20	1,200	55
SUV	Lower	250	50	500	590	750	120	7	800	25
	Upper	450	250	500	900	1,200	300	17	1,200	45
Van	Lower	200	50	500	600	750	65	15	400	30
	Upper	420	280	500	850	1,150	280	40	700	50

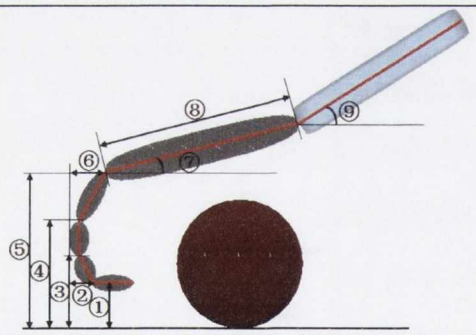

7.2.2 Setup of the optimizations

7.2.2.1 Population size

To search a large number of designs in the optimization, 100 design points (shapes) were defined as the population for each generation in the GA, as suggested in previous studies (Untaroiu et al., 2009; Subramanian et al., 2016). The initial population (100 shapes) was selected

randomly with a uniform distribution according to the boundaries defined in Table 7.1 for each vehicle type.

7.2.2.2 Crossover fraction

The crossover is an important operator which determines the creation of a new generation in the GA. For the GA defined in MATLAB, the crossover fraction specifies the fraction of the next generation, other than elite children (top 5% population that are guaranteed to survive to the next generation), that are produced by crossover based on the parents which generally performed well in the previous generation (Vary Mutation and Crossover, 2016). The rest of the design points of the next generation are created by mutation, which randomly generates directions that are adaptive with respect to the last successful or unsuccessful generation based on a direction and step length that satisfies bounds. The crossover fraction can be defined between 0 and 1, and then the population in the next generation will be created based on the defined crossover fraction value. For example, if the population size is 100 and the crossover fraction is defined as 0.8, then the population for the next generation is distributed as: 100*0.05=5 elite children, (100-5)*0.8=76 crossover children and 100-5-76=19 mutation children. Therefore, it is important to select a reasonable crossover fraction to keep the genes of the excellent individuals (by the crossover children) and create enough new genes and maintain the genetic diversity (by the mutation children).

To find a reasonable crossover fraction, a sensitivity study was conducted to investigate the effects of the crossover fraction on the output of the optimization. To reduce the computational time in the sensitivity study, a simplified STS with 10 impact configurations (one impact speed at 40 km/h, five pedestrian heights and two pedestrian gait stances) was applied to the optimization framework. The selection of this STS is also for a further study of the effects of the impact speed on the optimal shapes since 40 km/h is the speed widely used in legislative and consumer evaluation systems for pedestrian safety performance (Chapter 2). The same weighting system for calculating WIC (Eq. 6.1-6.3) was employed, but only one proportion (100%) was used for the impact speed (40 km/h). Then optimizations were conducted for the sedan front using different crossover fraction values (from 0.1 to 0.9) and the new defined STS. For this sensitivity study the same initial population and iterations (10) were defined to ensure the only changing

variable is the crossover fraction.

Figure 7.1 shows the population of the generation after 10 iterations for the optimizations using different crossover fraction values. The optimizations with a crossover fraction lower than 0.7 are largely converged after 10 iterations, while the optimizations with a crossover fraction of 0.7-0.9 are still searching for the optimal design in a quite wide range.

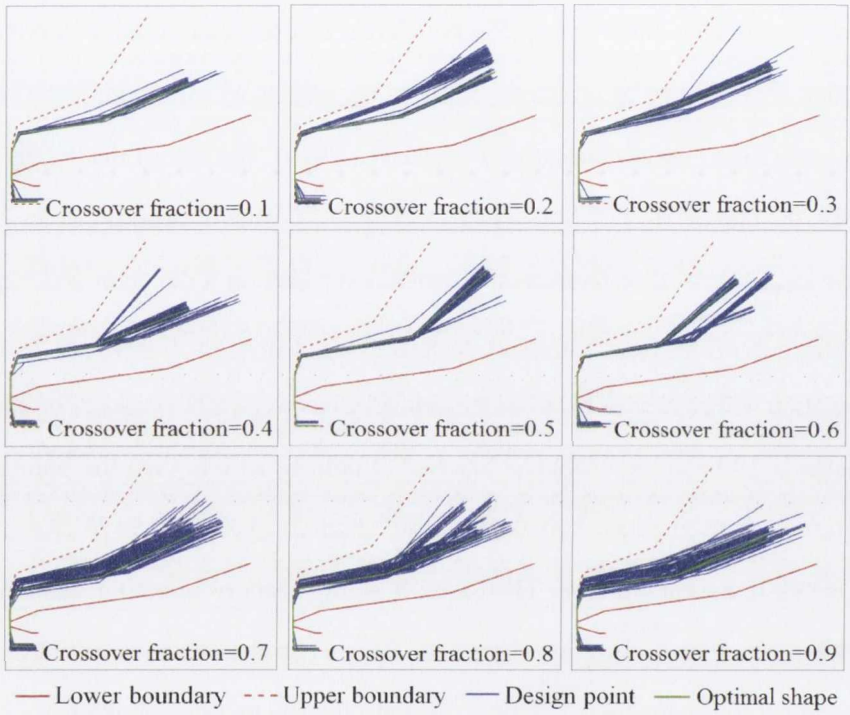

Figure 7.1 Population of the generation after 10 iterations for the optimizations using different crossover fraction values.

Figure 7.2 compares the predicted WICs, including median, interquartile range (IQR) and minimum values, of the generation after 10 iterations for the optimizations and shows that the case with a crossover fraction of 0.8 yields the widest range and a lowest minimum of WIC. According to the above data, it is suggested to select 0.8 as the crossover fraction for the vehicle front shape optimization, which is also the value recommended by the designer of GA in MATLAB (Vary Mutation and Crossover, 2016).

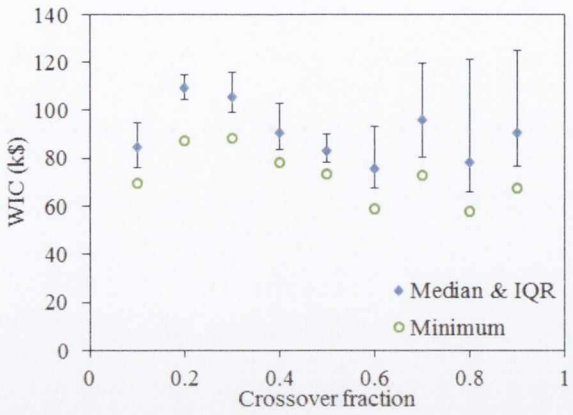

Figure 7.2 Predicted WIC of the generation after 10 iterations for the optimizations using different crossover fraction values.

7.2.2.3 Stopping criterion

The maximum generation number was defined as the stopping criterion since there is no reference for a minimum WIC. It is necessary to use a reasonable maximum generation number for each optimization to achieve the convergence and reduce the computational time by avoiding redundant iterations. Therefore, an optimization using the simplified STS (with 10 impact configurations) and a crossover fraction of 0.8 was conducted for each vehicle type to find a reasonable stopping criterion. A maximum generation number of 15 was initially defined for each optimization according to a preliminary study. Figure 7.3 shows the convergence process of the simplified optimizations, including median, interquartile range (IQR) and minimum values of the predicted WIC for each generation. It is clear from this figure that the sedan front optimization converges at the 14^{th} generation, while the optimizations for the SUV and van converge at the 10^{th} and 12^{th} generation, respectively. Therefore the maximum generation of 15, 11 and 13 were then defined as the stopping criteria for the sedan, SUV and van front shape optimizations, respectively.

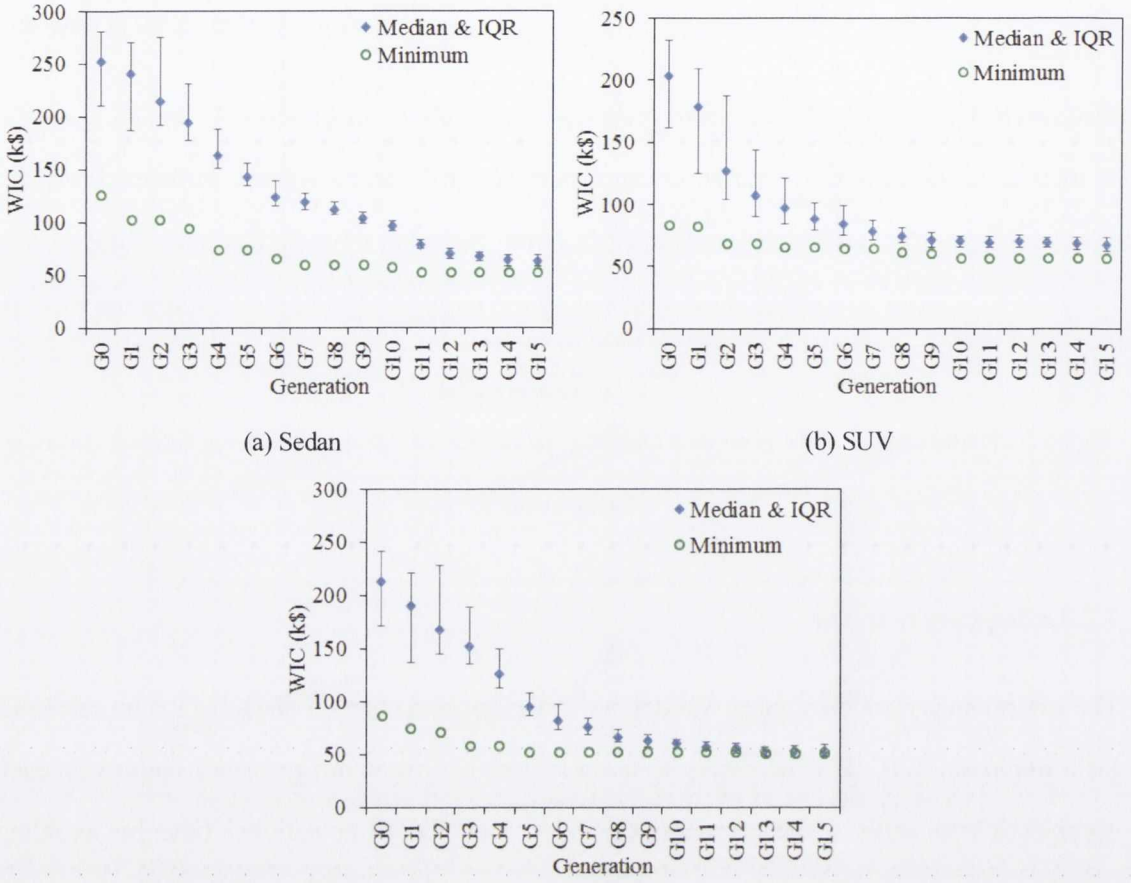

(a) Sedan

(b) SUV

(c) Van

Figure 7.3 Convergence process of the simplified optimizations for different vehicle types.

7.3 Optimization results

7.3.1 Sedan

7.3.1.1 Convergence of the optimization

Figure 7.4 shows the shapes (geometric dimension chain) for four generations (G0, G5, G10 and G15) in the optimization process. The searching range decreases with increasing generation number and reaches a generally stable shape by the end of the optimization (G15). Figure 7.5 shows the predicted overall WICs for all the design points evaluated in the optimization of the sedan front shape (a) and the median, IQR and minimum value of the predicted WIC for each generation (b). The predicted WICs are within a wide range and there is no difference in the minimum WIC between the last three generations (G13-G15). The median WIC decreases

from generation 0 (G0) to generation 15 (G15) and it has no obvious reduction between the last three generations. The data in Figure 7.4 and 7.5 reflect the convergence procedure of the optimization process.

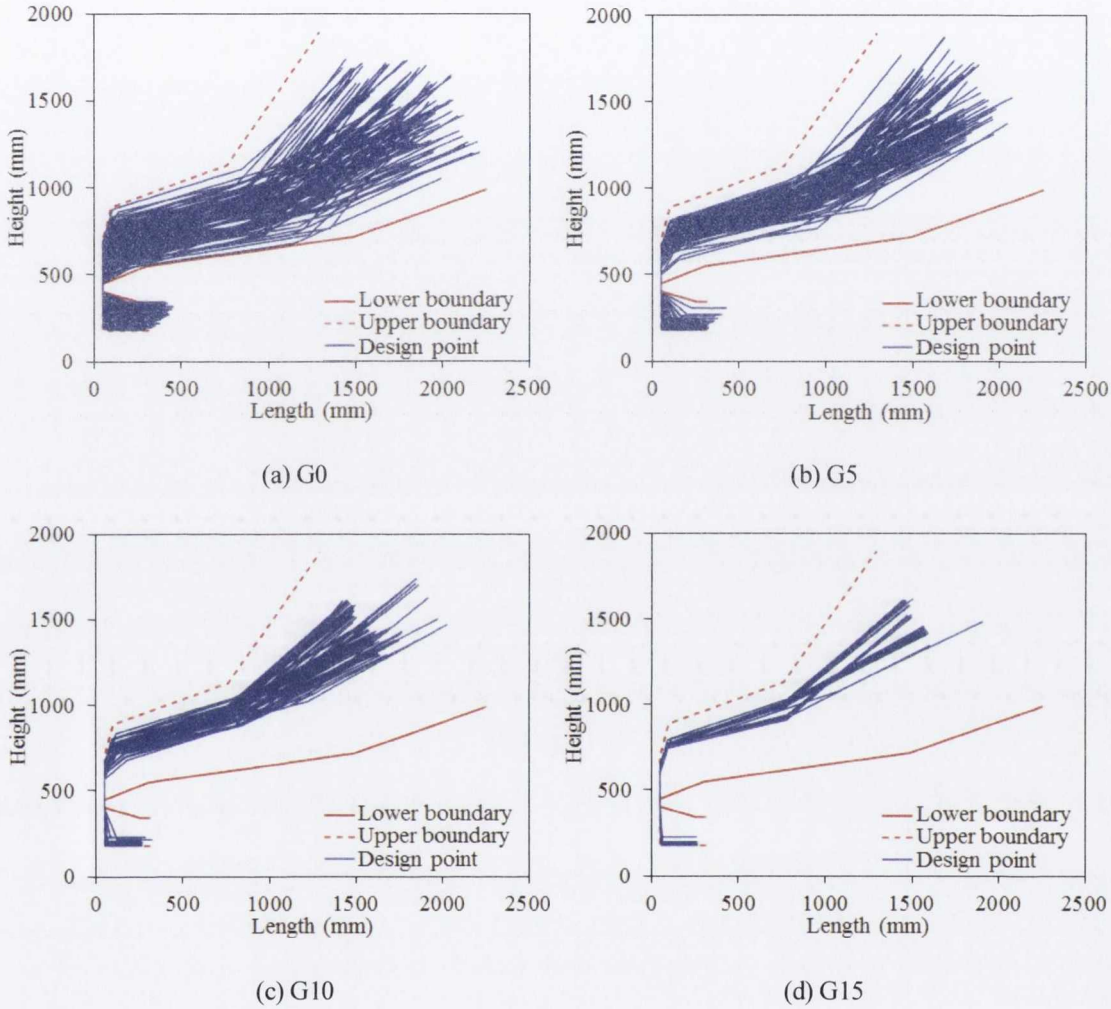

(a) G0

(b) G5

(c) G10

(d) G15

Figure 7.4 Design points of generation 0 (G0), 5 (G5), 10 (G10), and 15 (G15) for the sedan optimization.

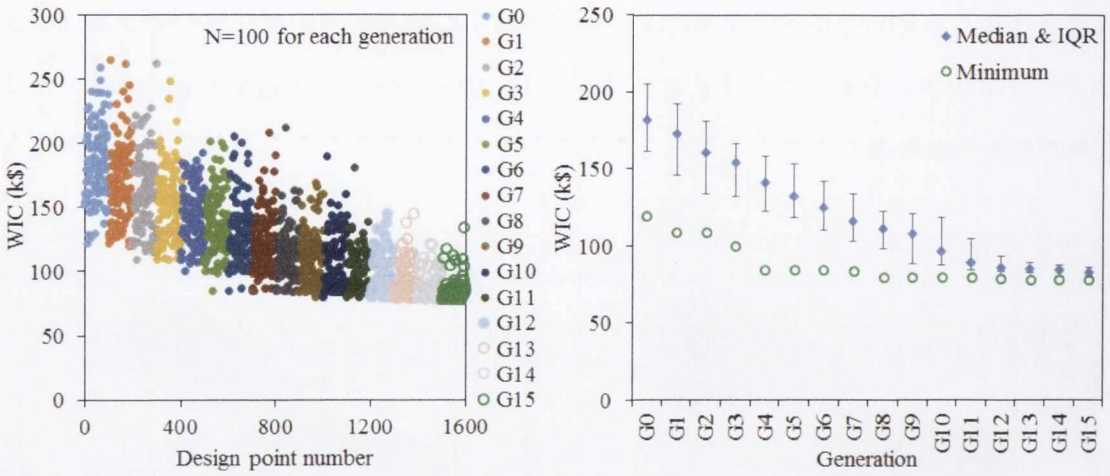

(a) (b)

Figure 7.5 Predicted WIC data for design points (a) and generations (b) in the sedan optimization.

7.3.1.2 Optimal sedan front shape

Figure 7.6 shows the optimal sedan front model together with the differently sized pedestrian models used in the optimization. The optimal sedan front has a wide (from 180 mm to 620 mm above the ground in the height direction) and flat bumper, which covers the pedestrians' lower extremities from the distal leg to the shaft of the thigh with generally even contacts. The bonnet leading edge height (BLEH) of the optimal sedan shape is 750 mm, which is lower than the hip joint of most adults and higher than the child hip (6 years old). The bonnet length is 710 mm with an angle of 19° to the horizontal level and the windscreen angle is 27° to the horizontal level.

Figure A.1 shows the kinematics of different pedestrian models when struck by the optimal sedan front model. It is clear from Figure A.1 that the kinematics varies for pedestrian models of different sizes and impact speeds. For short models (6YOC and 5th% female) the head impact location on the vehicle front is within the bonnet surface, while this goes to the windscreen area for the tall models (adult male). Generally, the head is not the first body part contacting with the ground for pedestrians struck by the optimal sedan front model at 20 km/h. However eight (out of ten) impacts at 30 km/h are with the head contacting the ground first (the ipsilateral lower extremity backward cases are not shown in Figure A.1), and three cases are

with a higher HIC from the ground contacts than that from the vehicle contacts.

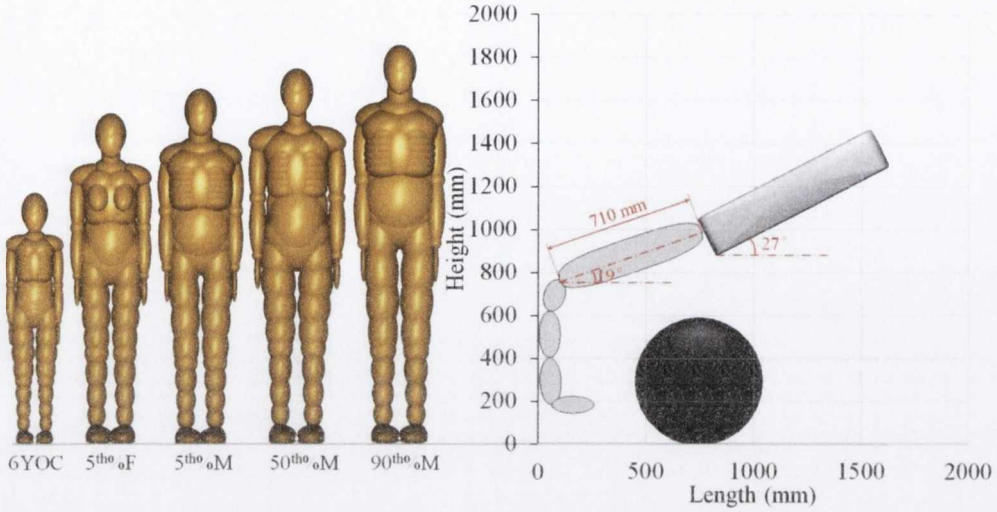

Figure 7.6 Optimal sedan front and pedestrian models.

7.3.1.3 The 'good' and 'poor' sedan shapes

Apart from the optimal sedan front shape, it is interesting to study the differences between the 'good' (resulting in a low WIC) and 'poor' (resulting in a high WIC) designs since the predicted WICs in the optimization show a wide range and there are uncertainties in the optimization algorithm and multi-body simulation. Figure 7.7 (a) shows the 'good' (design points leading to a WIC in the lowest quarter of the WIC range) and 'poor' (design points leading to a WIC in the highest quarter of the WIC range) shapes observed from the optimization process (Figure 7.5). Figure 7.7 (b) shows the corridors for the 'good' and 'poor' shapes, which were developed based on the median and IQR of each dimension. The corridors show obvious differences between the 'good' and 'poor' sedan front shapes.

Table 7.2 compares the magnitudes of the dimensions between the 'good' and 'poor' sedan shapes, where the Mann-Whitney U test (data is not normally distributed) was employed to evaluate the differences and a p-value lower than 0.05 indicates a statistically significant difference in the corresponding dimension between the 'good' and 'poor' shapes. The Mann-Whitney U test results show significant differences in all the dimensions between 'good' and 'poor' sedan shapes. It is clear from Figure 7.7 (b) and Table 7.2 that the 'good' shapes

have a significantly lower bumper lower height (#1), smaller bumper lower offset (#2), higher bumper upper height (#4), higher bonnet leading edge height (#5) and shorter bonnet (#8) than the 'poor' shapes.

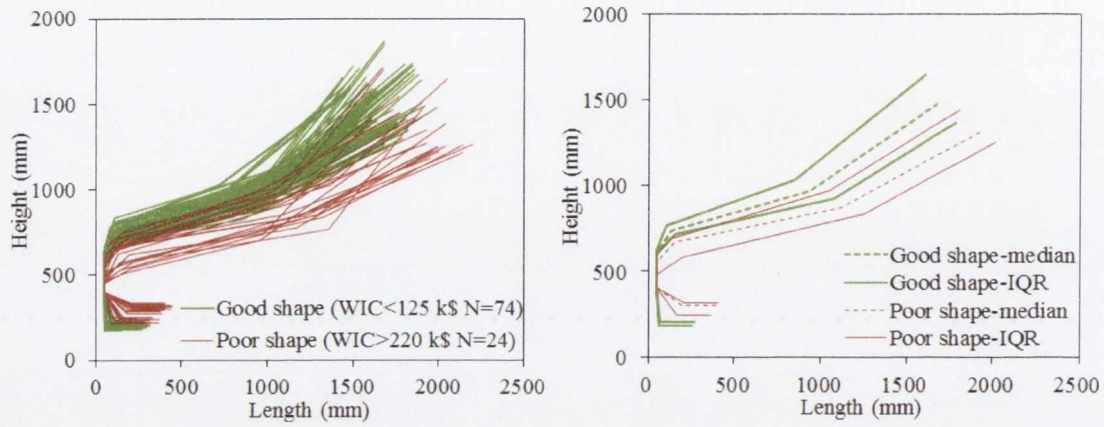

Figure 7.7 The 'good' and 'poor' sedan shapes (a) and their corridors (b).

Table 7.2 Comparison of the dimensions between 'good' and 'poor' sedan shapes.

Dimension		#1	#2	#3	#4	#5	#6	#7	#8	#9
Unit		mm	mm	mm	mm	mm	mm	°	mm	°
Min	Good	180	52	400	536	673	90	9	708	25
	Poor	214	86	400	453	511	108	9	791	21
Median	Good	203	61	400	600	741	135	16	842	30
	Poor	298	194	400	552	669	150	14	1,008	29
Max	Good	238	118	400	661	836	194	20	1,086	53
	Poor	336	245	400	663	772	230	20	1,192	52
p-value		<0.001	<0.001	/	<0.001	<0.001	0.001	0.007	<0.001	0.038

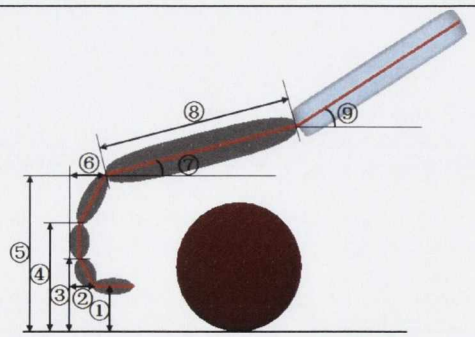

7.3.2 SUV

7.3.2.1 Convergence of the optimization

Figure 7.8 shows the changes in design points from the initial generation (G0) to the final generation (G11). Figure 7.9 shows the predicted WICs, including the data for individual, median and IQR and minimum, for all generations in the optimization of SUV front shape. Again, the minimum and mean WIC have no significant changes between the last three generations (G9-G11). Similarly, the data in Figure 7.8 and 7.9 shows 'good' convergence of this optimization.

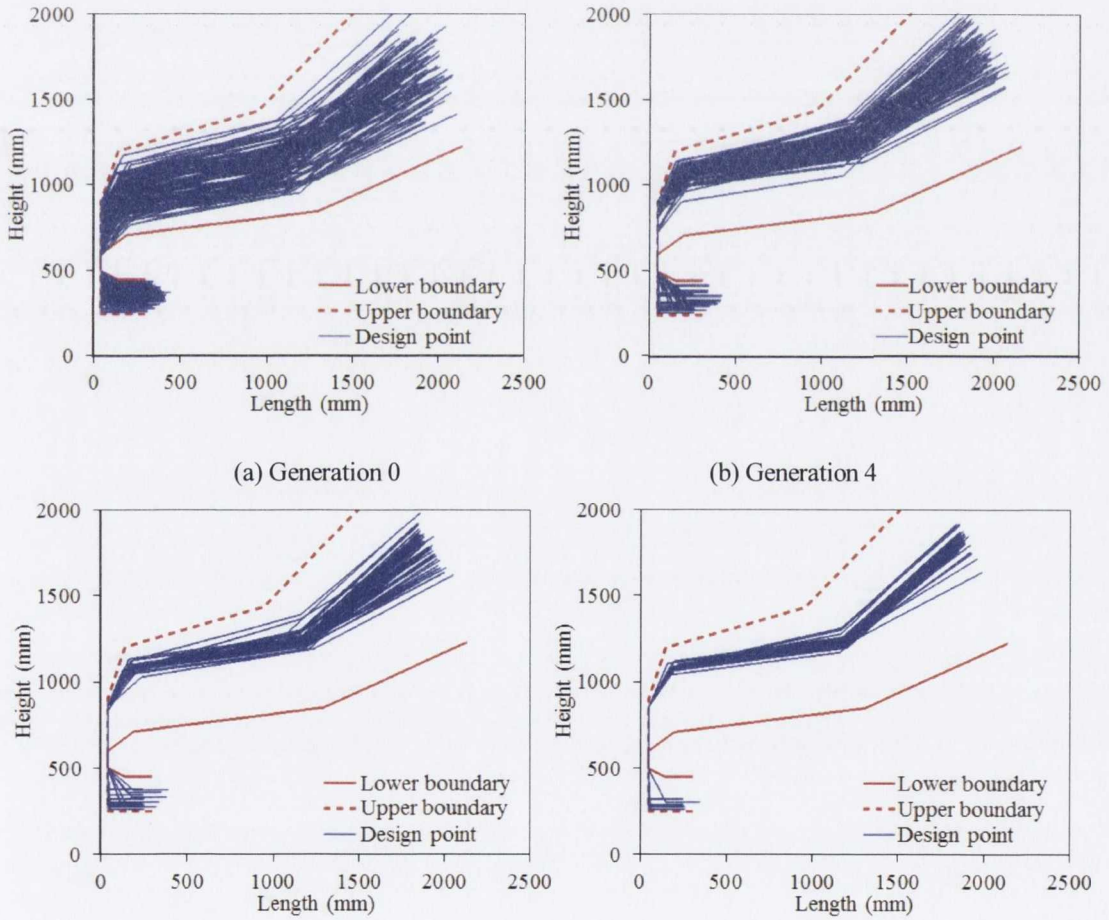

(a) Generation 0

(b) Generation 4

(c) Generation 8

(d) Generation 11

Figure 7.8 Design points of generation 0 (G0), 4 (G4), 8 (G8), and 11 (G11) for the SUV optimization.

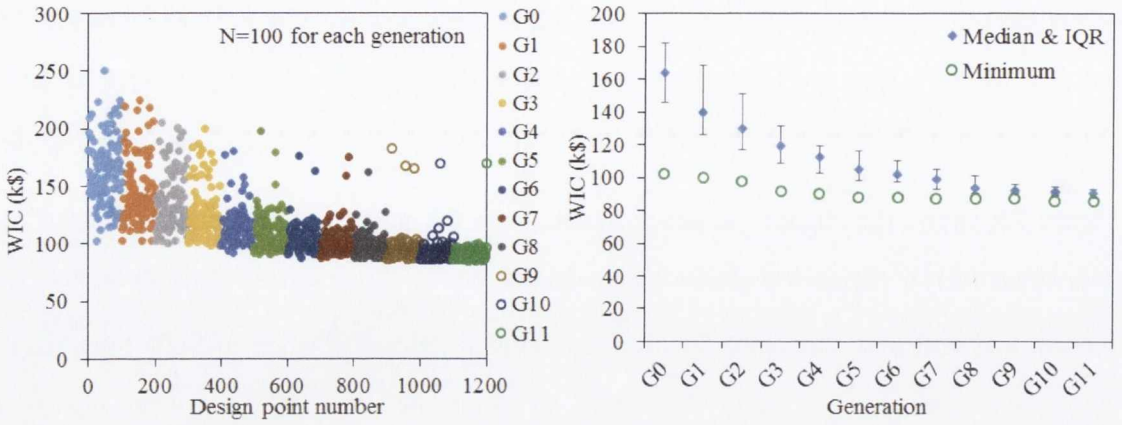

Figure 7.9 Predicted WIC data for design points (a) and generations (b) in the SUV optimization.

7.3.2.2 Optimal SUV front shape

Figure 7.10 shows the optimal SUV front shape observed from the optimization framework. The optimal SUV front shape also has a wide bumper (from 250 mm to 850 mm above the ground) which can nearly cover the whole lower extremity area (from the distal leg to the proximal thigh) of adults and the lower and middle body of the 6YOC child. The bonnet leading edge height is about 1,080 mm and higher than the hip joint of all pedestrians. The bonnet top and windscreen angle is 8° and 42° for the optimal SUV front shape, respectively.

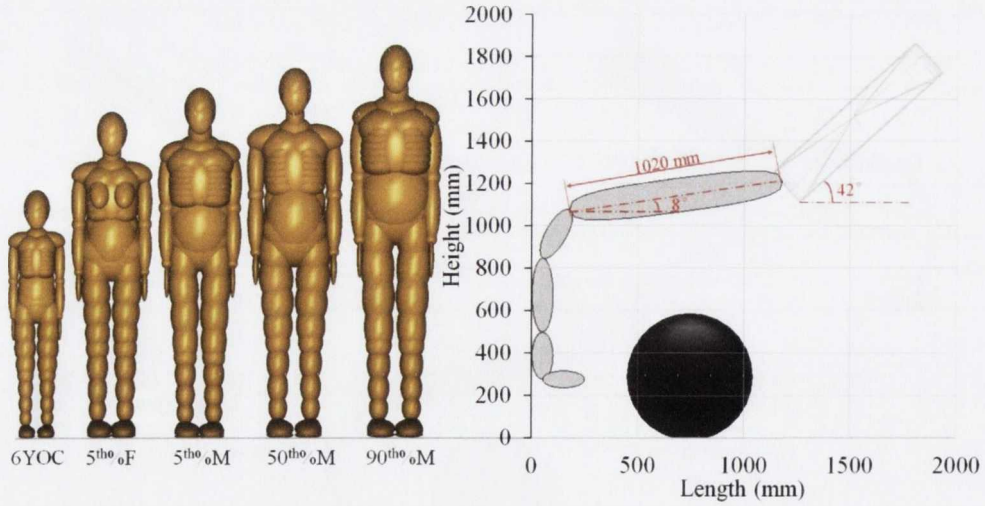

Figure 7.10 Optimal SUV front model and pedestrian models.

Figure A.2 shows the kinematics of different pedestrian models when struck by the optimal

SUV model at different impact speeds. It is clear from Figure A.2 that the lower extremity of short pedestrians (<50th%M) has no significant bending during the collision and the head of adult pedestrians impacts with the bonnet top after the hard contacts of the thorax and shoulder on the SUV front structures. None of the collisions at 20 km/h has the head-to-ground first contact situation, but six (all the cases for adult males) of the ten cases for 30 km/h are with the head-to-ground first contact (the ipsilateral lower extremity backward cases are not shown in Figure A.2) and the head injuries from these ground contacts are more serious than from the vehicle contacts for the corresponding case. For all the cases, the initial head contact location of the adult models is on the bonnet top area and the bonnet leading edge area is the structure for the initial head contact of the child model (Figure A.2). The windscreen design does not matter for the predicted optimal SUV front shape since none of the pedestrian heads reach this area in the collisions simulated, see Figure A.2.

7.3.2.3 The 'good' and 'poor' SUV shapes

The same approaches as the sedan case were applied to the SUV optimization to develop the 'good' and 'poor' shape corridors. Figure 7.11 compares the 'good' and 'poor' SUV shapes and their corridors calculated based on the median and interquartile range (IQR) data. The geometry data in Figure 7.11 shows clear differences between the 'good' and 'poor' SUV shapes. Similarly, the Mann-Whitney U test (data is not normally distributed) was employed to assess the statistical differences in the dimensions between the 'good' and 'poor' SUV shapes and Table 7.3 summarizes the test results. Again, for all dimensions the differences are statistically significant between the 'good' and 'poor' shapes (Table 7.3). Compared to 'poor' SUV shapes, the 'good' SUV shapes have a significantly lower bumper lower height (#1), smaller bumper lower offset (#2), higher bumper upper height (#4), higher bonnet leading edge height (#5) and shallower bonnet (#7), see Figure 7.11 and Table 7.3.

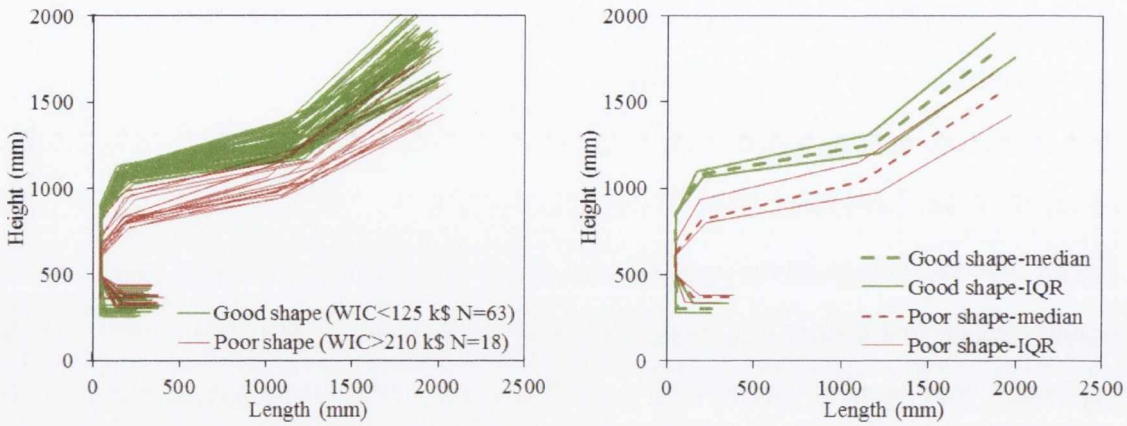

(a) (b)

Figure 7.11 The 'good' and 'poor' SUV shapes (a) and their corridors (b).

Table 7.3 Comparison of the dimensions between 'good' and 'poor' SUV shapes.

Dimension		#1	#2	#3	#4	#5	#6	#7	#8	#9
Unit		mm	mm	mm	mm	mm	mm	°	mm	°
Min	Good	260	50	500	792	1,024	145	7	936	26
	Poor	306	54	500	590	768	183	8	856	25
Median	Good	304	62	500	853	1,077	194	9	1,018	38
	Poor	371	154	500	629	820	203	12	936	33
Max	Good	423	200	500	899	1,134	262	16	1,112	44
	Poor	439	226	500	811	981	257	17	1,092	43
p-value		<0.001	0.002	/	<0.001	<0.001	0.020	0.019	0.015	0.016

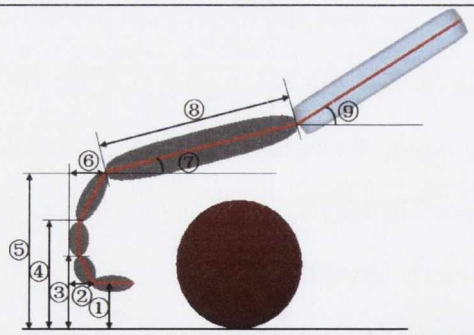

7.3.3 Van

7.3.3.1 Convergence of the optimization

Figure 7.12 and 7.13 show the convergence process of the optimization for the van front shape

in terms of predicted WICs and design points, respectively. Both the predicted WIC and van shape are converged at the last generation and no clear difference in the minimum WIC was observed between the last three generations. Again these results show good convergence of this optimization.

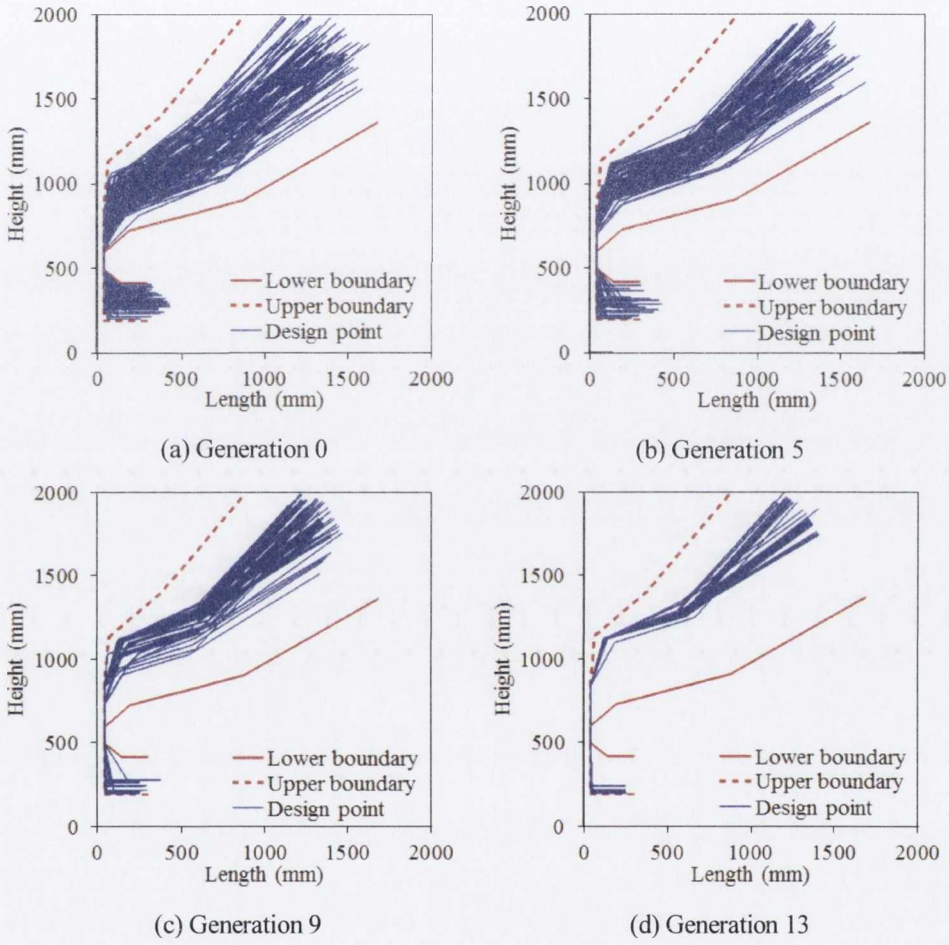

(a) Generation 0 (b) Generation 5

(c) Generation 9 (d) Generation 13

Figure 7.12 Design points of generation 0 (G0), 5 (G5), 9 (G9), and 13 (G13) for the van front shape.

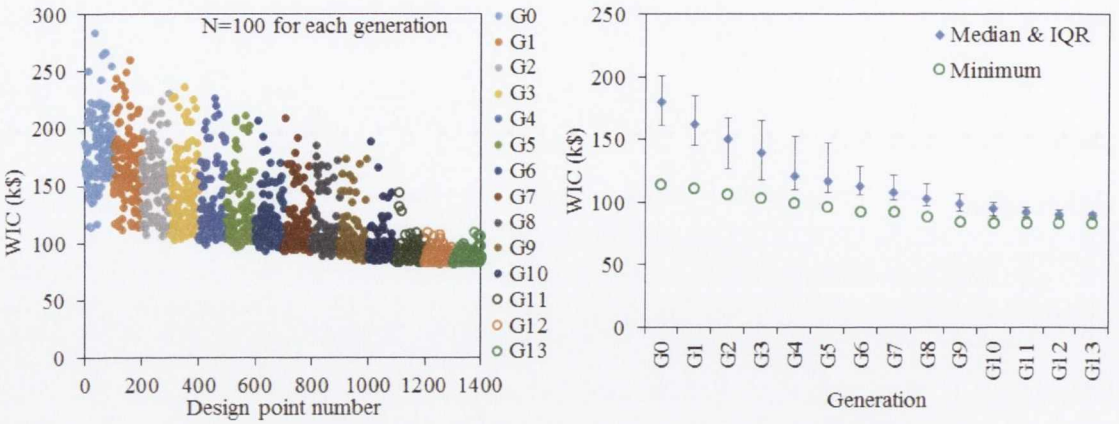

(a) (b)

Figure 7.13 Predicted WIC data for design points (a) and generations (b) in the van optimization.

7.3.3.2 Optimal van front shape

Similarly, the optimal van front shape together with the pedestrian models of different sizes is shown in Figure 7.14. The optimal van front shape also has a wide bumper (from 200 mm to 850 mm above the ground). The bonnet leading edge height for the optimal van front shape is about 1,130 mm above the ground. The bonnet of the optimal van shape is 495 mm in length and with an angle of 17° to the horizontal level. The windscreen angle of the optimal van front shape is 36° to the horizontal level.

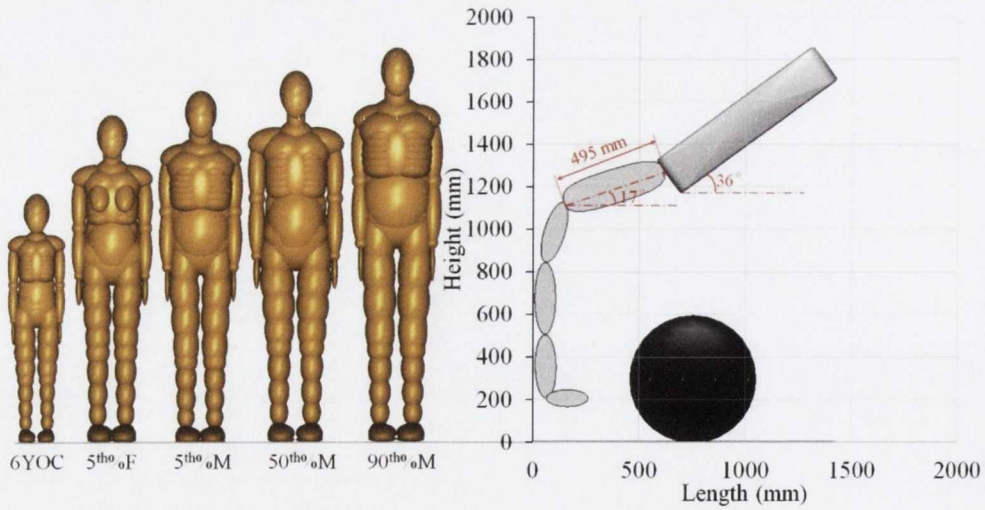

Figure 7.14 Optimal van front model and pedestrian models.

Figure A.3 shows the kinematics of different pedestrian models when struck by the optimal van

front model at different impact speeds. Generally, there is no serious bending response in the lower extremity of the pedestrian models for the cases struck by the optimal van front model at an impact speed lower than 50 km/h, see Figure A.3. The head of the adults mainly impacts with the bonnet top of the optimal van front after the hard contacts between the middle body (mainly the thorax and shoulder) and vehicle front (Figure A.3). The child pedestrian has no obvious wrapping on the optimal van front and its head always impacts with the bonnet leading edge area (Figure A.3). None of the collisions at 20 km/h has the head-ground first contact situation, but nearly all the cases for adult males at 30 km/h are with the head-ground first contact (Figure A.3, the cases for backward gait stance are not shown) and the head injuries from these ground contacts are more serious than from the vehicle contacts for the corresponding case.

7.3.3.3 The 'good' and 'poor' van shapes

Figure 7.15 shows the 'good' and 'poor' van shapes extracted from the van optimization process based on the predicted WICs and Table 7.4 shows the Mann-Whitney U test (data is not normally distributed) results for comparisons of the differences in the dimensions between the 'good' and 'poor' van shapes (the same approaches as the sedan and SUV cases).

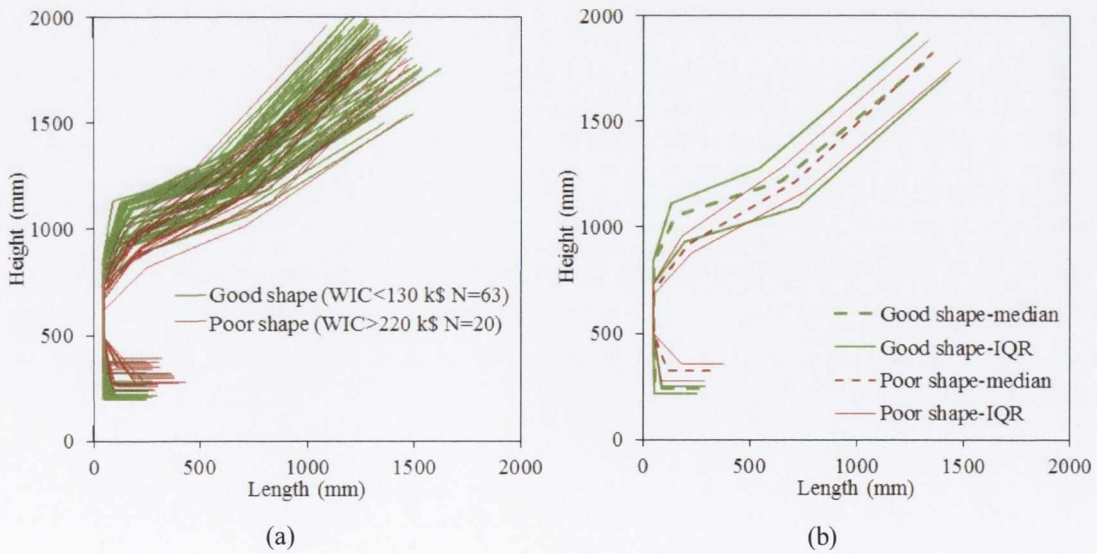

Figure 7.15 The 'good' and 'poor' van shapes (a) and their corridors (b).

Table 7.4 Comparison of the dimensions between 'good' and 'poor' van shapes.

Dimension		#1	#2	#3	#4	#5	#6	#7	#8	#9
Unit		mm	mm	mm	mm	mm	mm	°	mm	°
Min	Good	203	52	500	699	874	68	15	414	31
	Poor	247	51	500	614	819	133	21	447	32
Median	Good	244	58	500	839	1,052	151	17	559	40
	Poor	326	115	500	700	919	210	31	582	42
Max	Good	380	172	500	839	1,131	262	35	694	49
	Poor	397	245	500	794	995	254	40	692	49
p-value		<0.001	<0.001	/	<0.001	<0.001	<0.001	<0.001	0.001	0.501

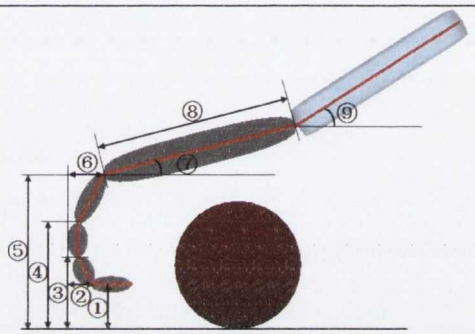

Again, significant differences in geometry were observed between the 'good' and 'poor' van shapes. The data in Figure 7.15 and Table 7.4 show that the 'good' van shapes have a significantly lower bumper lower height (#1), smaller bumper lower offset (#2), higher bumper upper height (#4), higher bonnet leading edge height (#5) and shallower bonnet (#7) than the 'poor' van shapes. The p-value (>>0.05) shows that there is no significant difference in the windscreen angle between the 'good' and 'poor' van shapes.

7.4 Discussion

7.4.1 Feasibility of the optimization framework

The results indicate that the optimizations for the front shape of all the vehicle types show good convergences. The wide variety of predicted WIC value and vehicle shape in the optimization process indicates that the WIC is sensitive to the change of vehicle front shape and the GA can search a broad range of design points under the control of the design spaces. However, it is not

sure if the optimization converges at the global minimum.

Figure 7.16 shows the predicted median WIC and IQR for different body regions as a function of generation number in the sedan, SUV and van optimizations. It is clear from Figure 7.16 that the head has the highest WIC for all vehicle types and the lower extremity WIC is generally the second most important part to form the overall WIC. This distribution is not in line with the distribution of AIS2+ injuries in accidents and in the prediction of multi-body simulations (Figure 5.9, Chapter 5). This is due to the fact that the predicted injuries were weighted further by the injury costs which are associated to the severity of the injuries and body regions (Table 6.3, Chapter 6). The data shows that the GA mainly focuses on reducing the predicted WIC for the lower extremity and head during the optimization process since they play important roles in the overall WIC. The WICs for the thorax and pelvis even increase along with the convergence process for some cases (Figure 7.16). These results show that the GA used in the current optimization framework can take the overall predicted WIC as the objective and focus on the dominant parts of the WIC from different body regions to find the optimal vehicle shapes. This implies that the distribution and weighting factor (such as the injury cost) of the predicted injuries, which together result in the distribution of the weighted injury outcome (such as the WIC), are important factors affecting the optimization results.

Figure 7.17 shows the distributions of the predicted median WIC of the initial generation (the data for generation 0 in Figure 7.16) and the injury cost calculated based on the injuries (AIS level and body region) observed from the GIDAS accident data (speed range of 15-75 km/h, similar to the simulations) and the cost reference (Table 6.3, Chapter 6) as a function of body region for the sedan and van impacts respectively (SUV data is not shown since not enough cases are available). The selection of the initial generation is to consider a broad range of vehicle front shapes since the designs generated by the GA in the later generations become an increasingly concentrated distribution (Figure 7.4). The comparisons (Figure 7.17) are for a further evaluation of the injury distribution predictive capability of the simulation test sample since the detailed severity (AIS1-6) of the predicted injuries were not considered in the virtual test system where the number of AIS2+ injuries was used as the index (Chapter 5). The

distribution of the predicted injury cost as a function of body region is generally similar to that observed from the accidents for both sedan and van impacts (Figure 7.17), even though the pelvis and thorax injury cost proportions observed from the van accidents are surprisingly lower than for the sedan cases in the GIDAS database. However the reasons for this surprising observation are not clear and further detailed analysis of the accident data is needed.

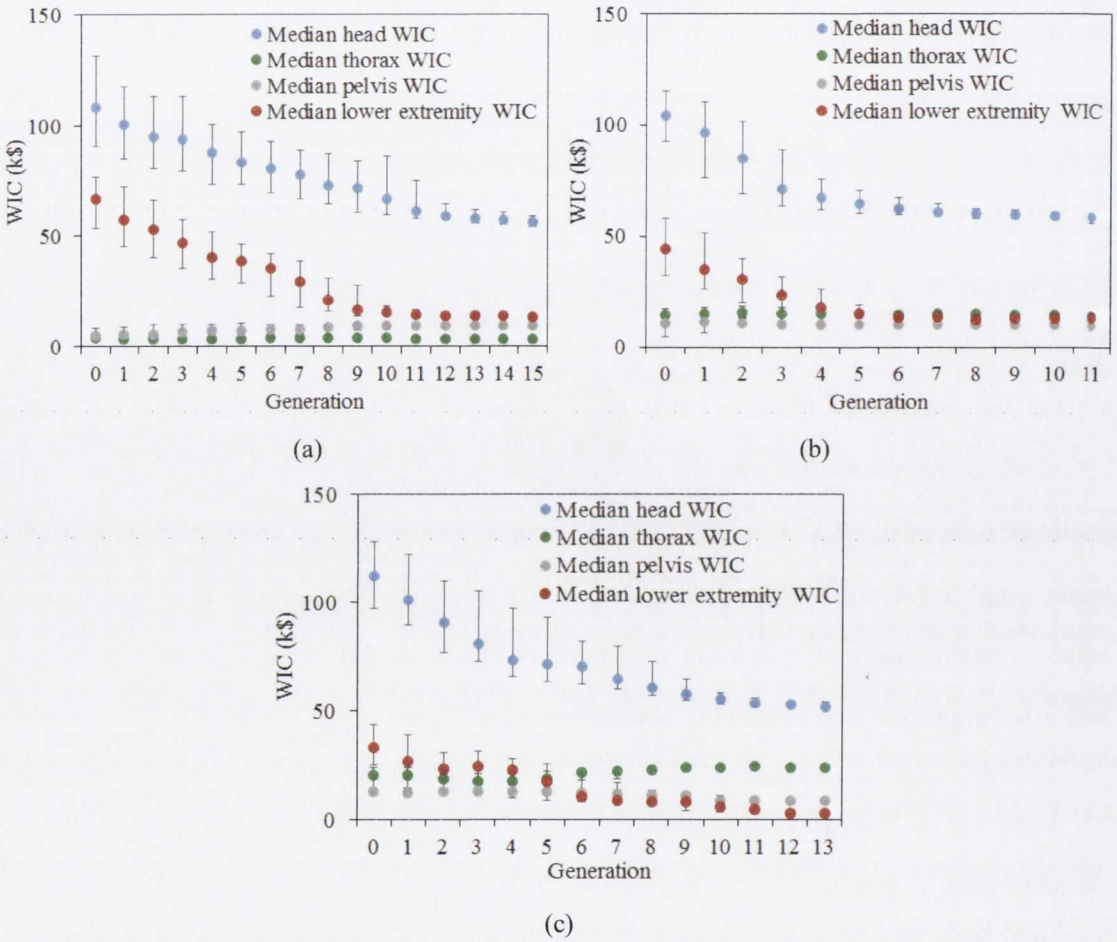

Figure 7.16 Changing of the median WIC for different body regions in the sedan (a), SUV (b) and van (c) optimization process.

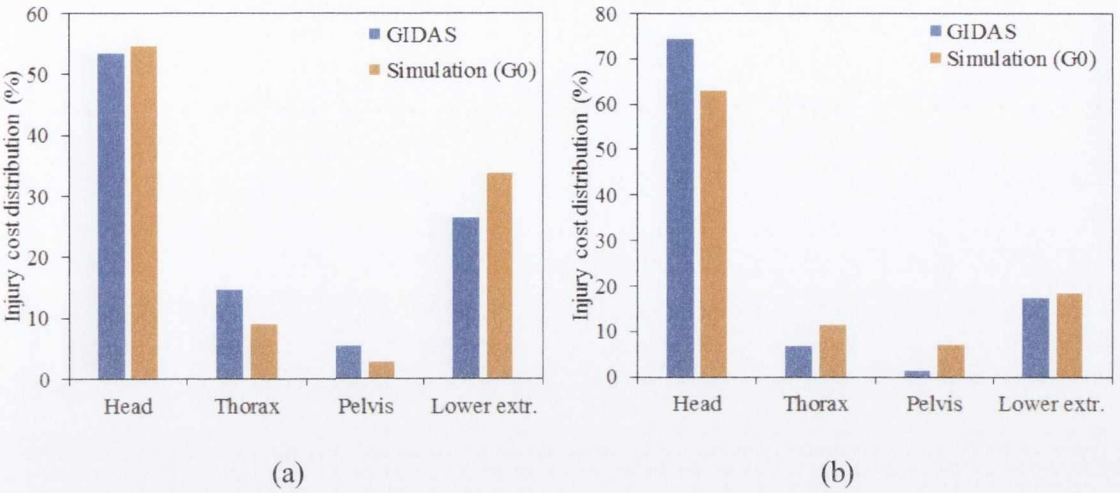

Figure 7.17 Comparisons of the injury cost distribution as a function of body regions between the simulations and GIDAS data for sedan (a) and van (b) impacts.

Nevertheless, the data in Figure 7.16 and 7.17 show that the GA can focus on the objective to find the optimal designs and the approaches of the simulation test sample and injury cost weighting system used in the optimization framework can generally guarantee a valid distribution of the predicted weighted injury outcome. This suggests that the predictions of the optimization framework are generally convincing and it is feasible to use the optimization framework for vehicle front shape optimization for reducing pedestrian injury risk even it is still not clear if the optimal output is the global minimum.

7.4.2 Sedan front shape optimization

7.4.2.1 Optimal sedan front shape

The optimization results for the sedan front shape indicate that the predicted optimal sedan shape nearly takes the lowest bumper lower height (dimension #1), highest bumper upper height (dimension #4) and smallest bumper lower offset (dimension #2) from the design space (Figure 7.6 and Table 7.1). This suggests that a safe sedan front for pedestrians should firstly have a flat and wide bumper which can generally contact the pedestrian lower extremity from the distal leg to the shaft of the thigh with evenly distributed load. This optimal bumper design meets the requirements for a safe sedan bumper observed from the GIDAS accident data (Table

3.7 and 3.8, Chapter 3). Figure A.1 shows that there is no obvious bending response in the pedestrian's lower extremity when struck by the optimal sedan. This is also in line with the analysis of the lower extremity loading condition in Chapter 3 (Figure 3.8), where a wide and flat bumper is suggested for lower extremity injury prevention by reducing the lower extremity bending response. The bumper lower edge height (dimension #1) and bumper lower edge offset (dimension #2) of the optimal sedan reach their lower design limits defined in the optimization, see Figure 7.4 (d) and Figure 7.6. This shows that the lowest height and offset of the bumper lower edge are the best choices for lower extremity protection in sedan impacts. The bumper upper edge (dimension #4) of the optimal sedan (620 mm above the ground) is close to (but does not reach) its upper design limit (700 mm above the ground). This may be to control the bonnet leading edge height for upper body protection.

The bonnet leading edge height of the predicted optimal sedan front (about 750 mm above the ground) is nearly at the lowest level based on this wide bumper design and is generally lower than the pedestrian hip (Figure 7.6). Considering the proportion of different pedestrian heights in the optimization framework (Table 6.1, Chapter 6), nearly 70% of the population represented by the pedestrian models (5^{th}% male-90^{th}% male) have a bonnet leading edge lower than 82% of the hip height when struck by the optimal sedan front, which is helpful for pelvis protection as observed in accident data (Table 3.12, Chapter 3). To investigate the effects of the sedan bonnet leading edge height on the predicted pedestrian injury risk, a sensitivity study was conducted using different bonnet leading edge heights based on the optimal sedan front model, changing dimension #4 in the chain (consequently dimension #5) and keeping other dimensions the same as for the optimal sedan. Then the sedan front models in different bonnet leading edge heights were tested using the STS (Table 6.1, Chapter 6) and the weighted injury cost (WIC) was calculated for each sedan front. Figure 7.18 shows the predicted WIC as a function of bonnet leading edge height for different body regions. As shown in Figure 7.18 the trend of the overall WIC is dominated by the head WIC for all sedan fronts and the effects of the bonnet leading edge height on the predicted head and thorax WIC (injury risk) are complex. This suggests that the upper body injury risk is not linearly dependent on the bonnet leading height due to the complexity of the whole body kinematics and loading conditions (contact

force, constraint force between body regions such as the neck and head, etc.) of the upper body in the impacts, which might be also the reason for the insignificant relationship between the bonnet leading edge height and thorax/head AIS3+ injury risk observed in GIDAS accident data (Table 3.13 and 3.15, Chapter 3). But a highly linear effect of the bonnet leading edge height (also the bumper upper height) on the predicted lower extremity and pelvis WIC (injury risk) was observed, where the predicted pelvis WIC increases with increasing bonnet leading edge height and opposite trend for the lower extremity WIC. These trends are in line with that observed in the GIDAS data (Table 3.7, 3.8 and 3.12, Chapter 3). The trend of the predicted head WIC as a function of the bonnet leading edge height (also the bumper upper height) is similar to that for the lower extremity WIC but opposite to that for the pelvis WIC when the bonnet leading edge is lower than 800 mm, see Figure 7.18. The optimal sedan selects the best bonnet leading edge height to keep the balance between the head, pelvis and lower extremity WIC for minimizing the overall WIC. These findings may imply that to some extent the needs of head and lower extremity protection for a safe sedan are not really conflicting, but the demands of the lower extremity and head protection are partially conflicting with those for pelvis protection.

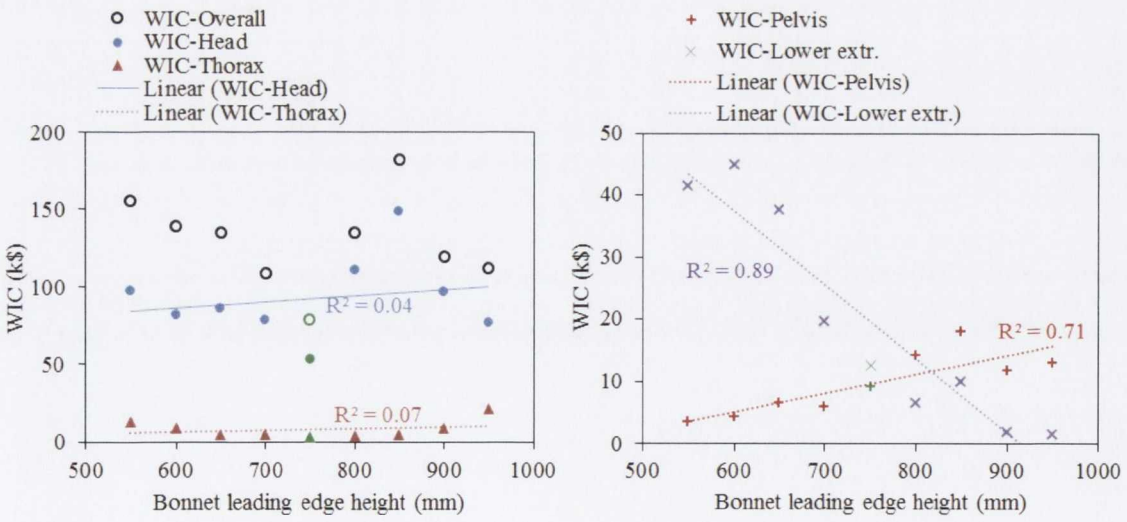

Figure 7.18 Predicted WIC as a function of sedan bonnet leading edge height, the points in green show the case for the optimal sedan.

The predicted optimal sedan front almost has the shortest (710 mm) bonnet from the design space (700-1200 mm), see Figure 7.6 and Table 7.1. To investigate the effects of the bonnet length on the predicted head WIC, a sensitivity study (similar to the bonnet leading height case) was set using different bonnet length values (as the only variable) for the optimal sedan front (Figure 7.6). Figure 7.19 shows the predicted head WIC as a function of the sedan bonnet length. The low R^2 value (0.08) for linear fit of the data shows that the effect of the bonnet length on the predicted head WIC is nonlinear. However the predicted head WIC for a very short (<800 mm) sedan bonnet is lower than for a longer bonnet and the optimization selected a bonnet length with a minimum head WIC as the optimal design.

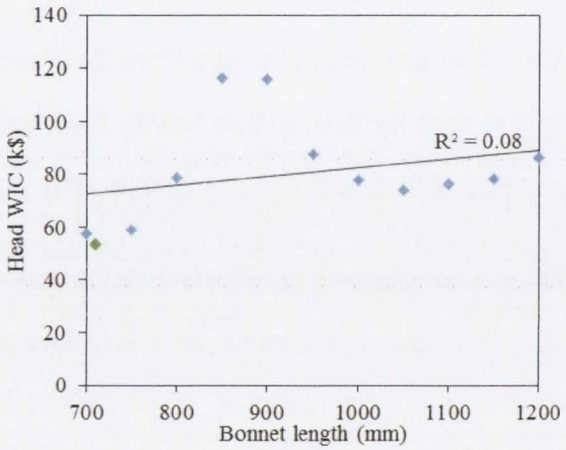

Figure 7.19 Predicted head WIC as a function of sedan bonnet length, the points in green show the case for the optimal sedan.

The bonnet length influences the pedestrian head contact location on the vehicle: short bonnets lead to a high likelihood of the head contact location being at the windscreen area, while long bonnets result in more head impacts on the bonnet top area. This influences head injuries by affecting the head impact boundary conditions, including contact stiffness (varying across vehicle front structures) and the head loading conditions (impact speed, impact angle, neck force, etc.). A detailed analysis of the predicted pedestrian kinematics found that the obviously higher head WIC for the 850-900 mm bonnet length is mainly due to the difference in the head contact location of the 5th% male model which represents about 37% of the population (much higher than other individual models (<19%), see Table 6.1, Chapter 6). For the 850 mm and 900 mm bonnet length cases the head of the 5th% male model contacts with both bonnet and

windscreen at the same time for the impacts at 40 and 50 km/h (important speeds for the WIC, discussed later). This takes the reaction force from both parts into account and leads to a high head linear acceleration peak and HIC (Figure 7.20). For other cases the head of the 5th% male model only contacts with the bonnet or windscreen, consequently a single reaction force and low HIC were predicted (Figure 7.20). Figure 7.20 also shows that the head contact with the bonnet leads to a lower head linear acceleration peak but a higher HIC than the head contacts with the windscreen. This is mainly due to the fact that a sharp reduction (to zero) of the contact force was defined for the windscreen to model fracture and the bonnet contact force has a wide peak pulse (Figure 5.8, Chapter 5). Thus the selection of the short bonnet in the optimal sedan is to keep a high frequency of head-to-windscreen contact for reducing the predicted HIC values, based on the optimal design of the bumper and bonnet leading edge. This implies that the optimal shape is highly stiffness dependent. Even though the stiffness distribution is simplified in the vehicles front models used here, the predictions can generally reflect the HIC (stiffness) distribution observed from head impactor tests for real vehicles (Mizuno et al., 2001).

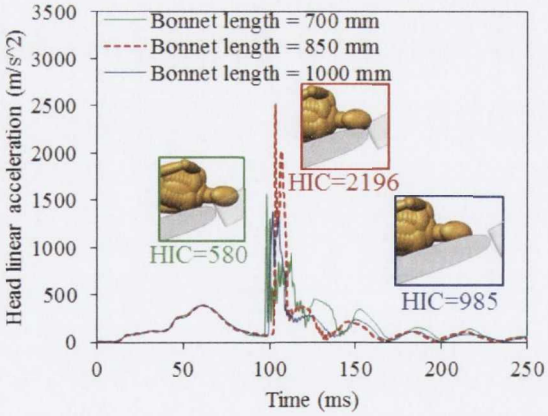

Figure 7.20 Predicted head linear acceleration curves for the 5th% male model struck by sedan fronts with different bonnet lengths.

The predicted optimal sedan front selected a bonnet angle of 19° (close to the upper design boundary of 20°) and a windscreen angle of 27° (design space is 20°-55°), see Figure 7.6 and Table 7.1. Unfortunately, no reference is available from the world accidents to deduce a safe bonnet and windscreen design for pedestrian protection. To investigate the effects of the bonnet

and windscreen angle on the predicted WIC, sensitivity studies were conducted using different bonnet and windscreen angles based on the optimal sedan model, respectively. Similar to before, for the bonnet angle sensitivity study, the only variable is the bonnet angle (8-20°), keeping all other shape dimensions for the optimal sedan front. The same approach was applied for the sensitivity study for the windscreen angle. Figure 7.21 shows the predicted WICs of the body regions affected by changing the bonnet and windscreen angle. The simulation results indicate that changing the sedan bonnet angle can influence the predicted WIC of the pedestrian's head, thorax, pelvis and even the lower extremity (only for adult males), while the windscreen angle only affects head and thorax injuries of adults. Figure 7.21 (a) shows that the effect of bonnet angle on the predicted head WIC is nonlinear (R^2=0.01 for linear fit), its effect on the predicted thorax WIC is not obvious, the predicted pelvis WIC increases with increasing bonnet angle (R^2=0.86) and the lower extremity WIC decreases slightly with increasing bonnet angle (R^2=0.93). The high R^2 value (0.67) for the linear fitting shows that the predicted head WIC generally increases with increasing windscreen angle, while the effect of windscreen angle on the predicted thorax WIC is not obvious, see Figure 7.21 (b). A previous study of Lyons and Simms (2012) based on vehicle-to-pedestrian multi-body simulations at 40 km/h indicates that the head peak linear and angular acceleration increase with increasing sedan windscreen angle, this trend is not in line with that observed in the current sensitivity study using a broad range of impact configurations (impact speed, pedestrian heights and gait stance) based on the HIC. This might be due to the differences in the head injury criteria, impact configuration and the overall vehicle shape. However, the detailed effects of sedan bonnet and windscreen angle on head injuries are still not clear and the complex head kinematics (cumulative effects of the kinematics from previous phases) and impact boundary condition (impact speed, neck force, contact force, etc.) in vehicle collisions are beyond our current understanding. Further studies are need for understanding this issue.

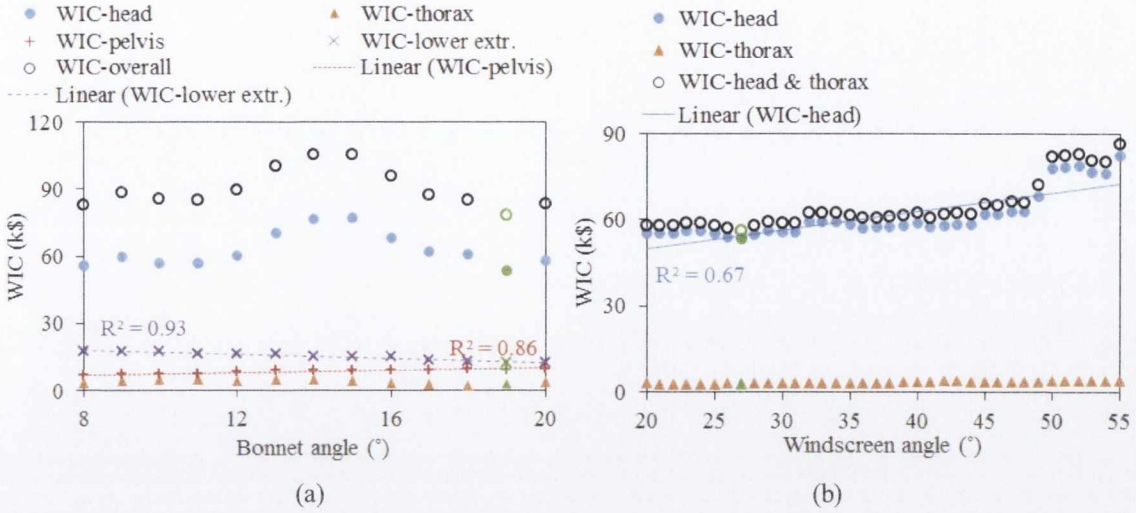

Figure 7.21 Predicted WIC as a function of sedan bonnet angle (a) and windscreen angle (b) for sedan impacts, the points in green show the case for the optimal sedan.

From the above analysis, the optimal sedan front shape was predicted based on the benefit of reducing the overall injury risk (WIC) for pedestrians considering a broad range of impact configurations. The profile for the optimal bumper is easy to be understood from the lower extremity injury mechanism and kinematics. The overall shape of the bonnet leading edge, bonnet and windscreen for the optimal sedan front may mainly be selected based on the head contact location and impact boundary condition since the head injuries (dominating the WIC) are measured by the HIC value, which is the combination of head linear acceleration and duration time and is affected by the head contact stiffness and kinematics. This implies that the optimal sedan front shape could be uncertain when changing the initial impact configuration (e.g. impact speed, pedestrian size, etc.) in the optimization framework and the stiffness of the vehicle structures. However, the stiffness of the vehicle front is not considered as a variable in the current study.

Figure 7.22 compares the optimal sedan shapes and 'good' shape corridors predicted using the original STS (Table 6.1, Chapter 6) and a simplified STS only considering the 40 km/h impact speed (defined in Section 7.2.2.2). It is clear from Figure 7.22 (a) that both optimal sedan shapes have a similar bumper and bonnet leading edge design, but the optimal sedan front predicted using the original STS has a shorter (710 mm vs 825 mm) and steeper (19° vs. 10°) bonnet and a steeper (27° vs. 22°) windscreen compared to the optimal sedan front predicted

via the STS only with the 40 km/h impact speed. The 'good' shape corridor predicted based on the original STS has a lower bonnet leading edge than that predicted using a single impact speed of 40 km/h. These differences may be largely due to the effects of the impact speed on the head contact location and head loading conditions. This suggests that the lower extremity kinematics at 40 km/h can generally reflect the situation for other impact speeds, but the optimization of the overall sedan front shape should consider a broad range of impact speeds.

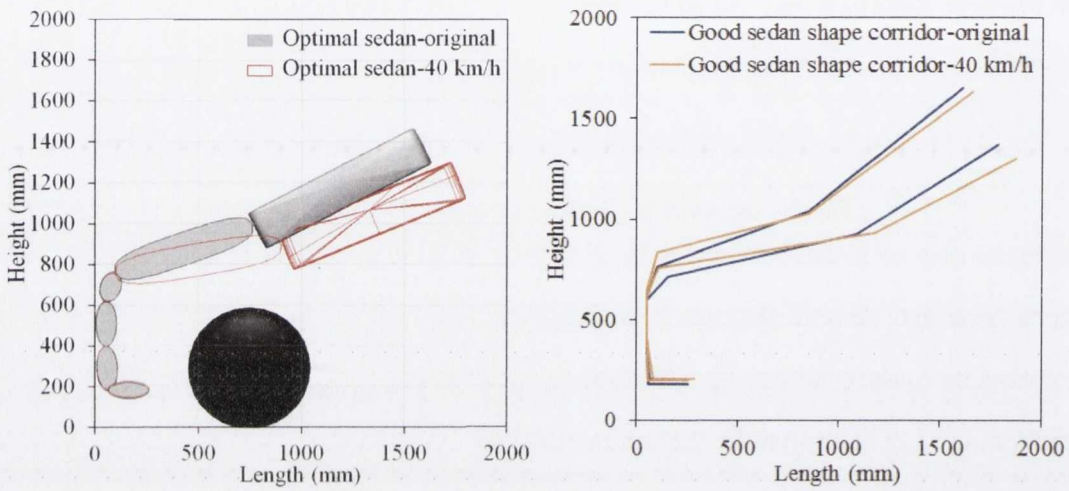

(a) (b)

Figure 7.22 Comparisons of the optimal sedan fronts (a) and 'good' shape corridors (b) between the optimizations using different impact configurations.

7.4.2.2 The 'good' and 'poor' sedan designs

The results in Figure 7.7 and Table 7.2 show that the optimization framework can clearly distinguish the 'good' and 'poor' sedan shapes based on the predicted WIC. To understand the detailed differences in the pedestrian kinematics and predicted WIC between the 'good' and 'poor' shapes, a test using the original STS (Table 6.1, Chapter 6) and injury cost weighting system (Section 6.5, Chapter 6) was conducted on the sedan model with a 'good' shape (the median shape in Figure 7.7) and a 'poor' shape, respectively. Figure 7.23 compares the predicted WICs for different body regions, pedestrian heights and impact speeds between the sedan models with a 'good' and a 'poor' shape. Figure 7.24 shows the typical kinematics of pedestrians in different heights when struck by the sedans with a 'good' and 'poor' shape,

respectively.

It can be seen from Figure 7.23 that the main differences in the predicted WIC between the 'poor' and 'good' shapes are to the head and lower extremity for the body region, to the 5th% male model and to all speeds lower than 70 km/h. There is no obvious difference in the predicted WIC between the 'poor' and 'good' shapes for the thorax, 90th% male model and 70 km/h.

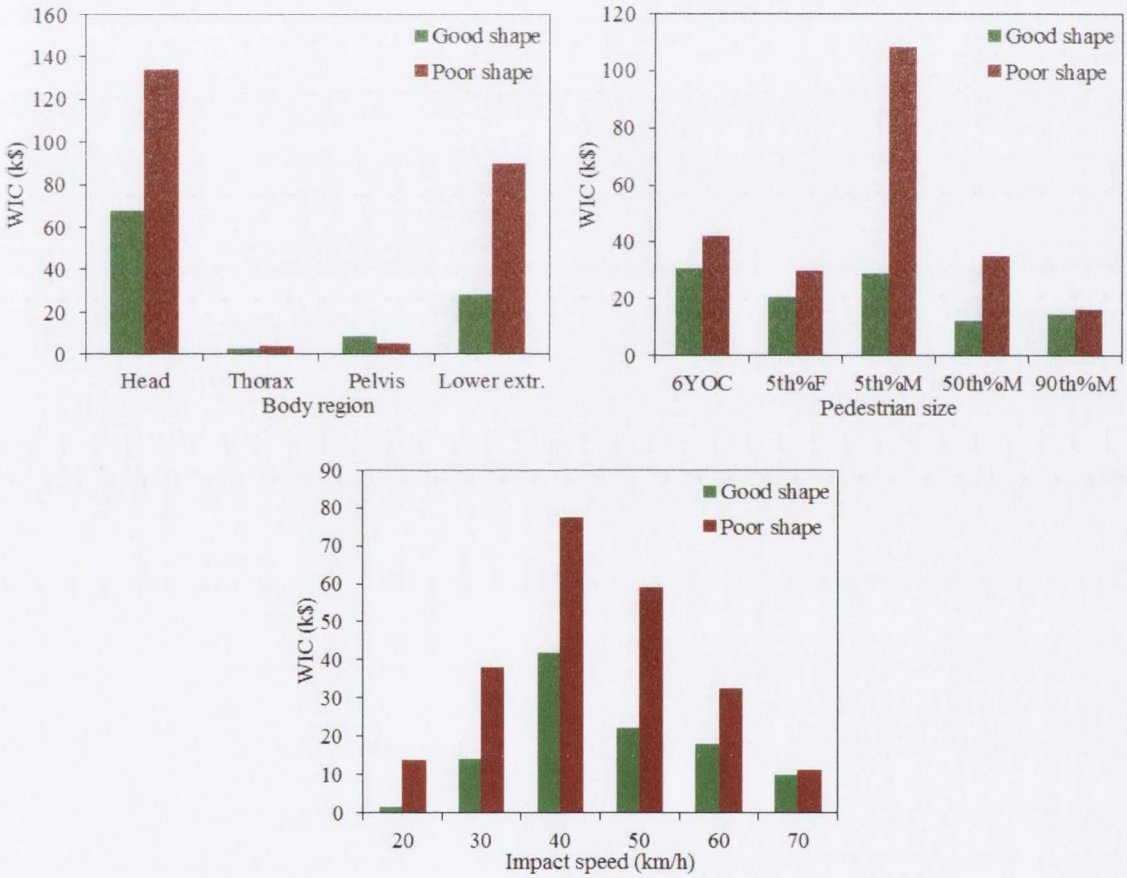

Figure 7.23 Comparisons of the predicted WIC as a function of body region, pedestrian size and impact speed between the simulations using a 'good' and 'poor' shape sedan front.

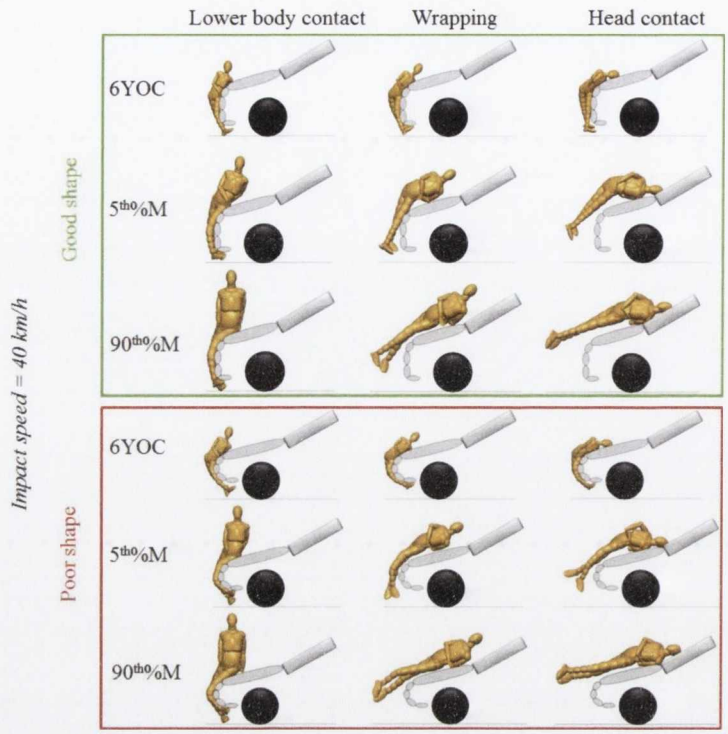

Figure 7.24 Comparisons of the pedestrian kinematics between the simulations using a 'good' and 'poor' shape sedan front.

Compared to the sedan model with a 'good' shape, the 'poor' shaped sedan model has a narrower and sharper bumper and leads to more serious bending to the lower extremity (Figure 7.24), resulting in more lower extremity injuries and higher lower extremity WIC. On the other hand, the 'poor' shapes have a lower bonnet leading edge height than the 'good' shapes. This results in generally higher head impact speeds (resultant and perpendicular to the contact surface) for the cases with the 'poor' shape sedan model than for the corresponding cases with the 'good' shape sedan model (Figure 7.25), leading to a higher head injury risk and head WIC. This may explain the head WIC trend observed in the sensitivity study of the effects of bonnet leading height, see Figure 7.18. The general trend of head impact speed as a function of bonnet leading edge height is also similar to that reported in previous studies based on multi-body modelling (Liu et al., 2002; Peng et al., 2012b), FE simulations (Han et al., 2012), dummy impacts (Matsui et al., 2002) and cadaver tests (Kerrigan et al., 2009a), but this is the first time this trend has been shown at the population level. These results may also suggest that a high bonnet leading edge is beneficial for reducing the head impact speed to some extent, but the

head injury risk might not be always decreasing with increasing the bonnet leading edge height since the head contact location and loading condition could also be affected by the bonnet leading edge height.

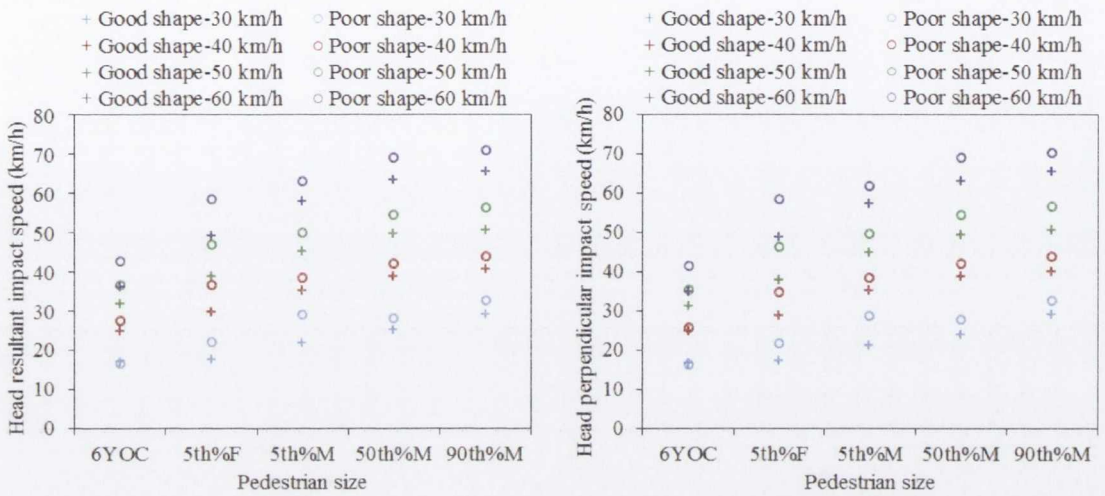

Figure 7.25 Comparisons of pedestrian head resultant and perpendicular impact speed between the simulations using a 'good' and 'poor' shape sedan front (the situation for ipsilateral lower extremity forward is shown).

The head impact location of the 5th% male model for the impacts with the 'good' shape sedan model is at the widescreen area, while this is at the rear edge of the bonnet (also lower edge of the windscreen) for the cases with the 'poor' shape sedan model (Figure 7.24). The differences in head impact location and speed result in a large difference to the head linear acceleration curve and the HIC between the impacts with the 'good' and 'poor' shape sedans, and Figure 7.26 shows an example. Moreover, the proportion of pedestrians represented by the 5th% male model (0.37) is much higher than other individual models (<0.19), see Table 6.1 (Chapter 6). These are the main reasons for the remarkable gap in the WIC of the 5th% male model between the 'good' and 'poor' sedan shapes (Figure 7.23).

The high bonnet leading edge of the sedan model in the 'good' shape leads to a high injury risk to the thigh of the 90th% male model in the simulations, which results in a similar lower extremity WIC as the sedan model in the 'poor' shape where a high knee and leg injury risk is observed. The head of the 90th% male model impacts with the windscreen at the similar area

for both the sedan models with the 'good' and 'poor' shape (Figure 7.24), and the difference in head impact speed between this two sedan models (Figure 7.25) does not lead to obvious differences in the HIC and hence the head WIC. So the head WIC of the 90th% male model for the impacts with the 'good' shape is similar to that for the impacts with the 'poor' shape (Figure 7.23). As observe in the GIDAS accidents, the effects of the sedan shape on pedestrian injury risk are weak at high impact speed and pedestrian age levels (Figure 3.7, Chapter 3). This can explain the small difference in the predicted WIC for 70 km/h cases (pedestrian age is not considered in the simulation), see Figure 7.23.

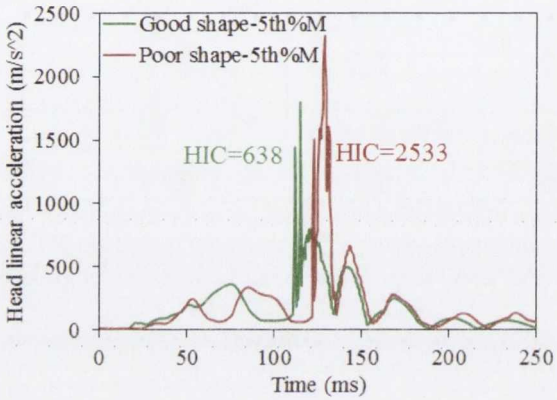

Figure 7.26 Comparisons of the head resultant linear acceleration curve for the 5th% male model between the simulations using a 'good' and 'poor' shape sedan front.

To find more evidence in real world accident data, the sedans that generally meet the profiles for the 'good' and 'poor' shapes (Figure 7.7) were selected from the GIDAS data respectively (named as 'good' and 'poor' sedans), see Figure 7.27 (a). In total there were 14 cases for four different 'good' sedans (meeting the 'good' shapes observed in the optimization) and 9 cases were for four 'poor' sedans (meeting the 'poor' shapes observed in the optimization). To assess the difference in pedestrian safety performance between the 'good' and 'poor' sedans in GIDAS accidents, the injury costs were calculated for each accident case in GIDAS involved with those vehicles. Figure 7.27 (b) compares the calculated average injury cost between the groups of 'poor' and 'good' sedans, based on the condition that there is no statistically significant difference in pedestrian age (p=0.825) and impact speed (p=0.412) between these two groups when the Mann-Whitney U test (data is not normally distributed) was employed.

Clearly, the average injury cost for the cases involved with the 'poor' sedans is much higher than for the cases with the 'good' sedans. No pelvis injury cost was observed for either group and the thorax injury cost was only observed for the 'poor' sedan group due to the small sample size for each group (14 vs 9). Nevertheless, the results in Figure 7.27 give strong support to the predictions of the optimization framework for the threat of sedan front shapes for pedestrians.

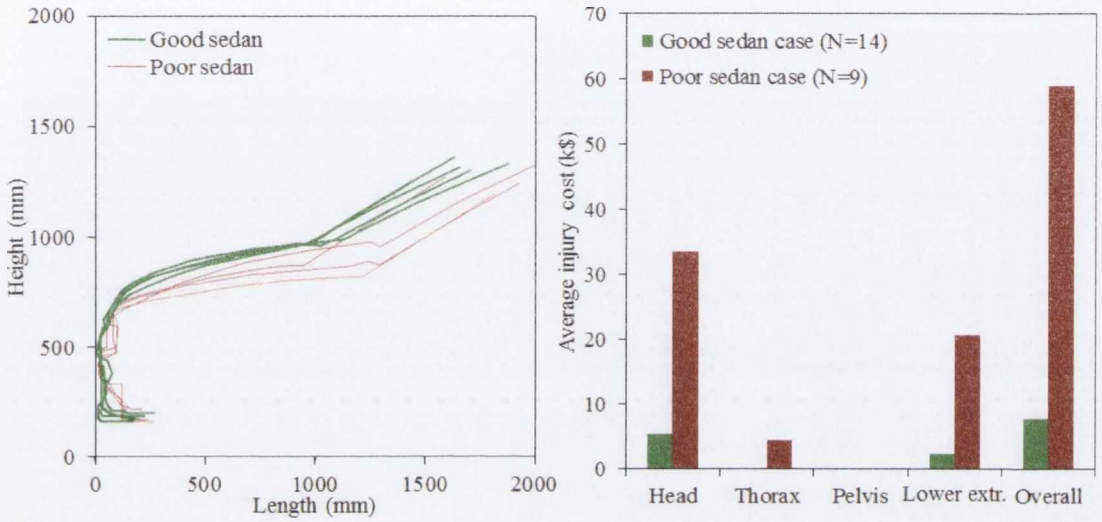

(a) (b)

Figure 7.27 Profiles of the sedans meeting the trends of 'good' and 'poor' shapes predicted by the optimization framework (Figure 7.7) in the GIDAS data (a) and the average injury costs calculated from the cases involved these sedans (b).

7.4.3 SUV front shape optimization

7.4.3.1 Optimal SUV front shape

The optimal SUV front nearly has the lowest bumper lower height (dimension #1) and smallest bumper lower offset (dimension #2) from the design space (Figure 7.10 and Table 7.1). As discussed above this selection is to minimize the lower extremity bending and hence lower extremity injury risk, and the kinematic data shows there is no obvious lower extremity bending when struck by the optimized SUV front (Figure A.2). Similar to the sedan case the bumper upper height (dimension #4) of the optimal SUV front is also close to (but does not reach) its upper design limit. This may also for controlling the height of the bonnet leading

edge. The optimal SUV has a bonnet leading edge of about 1,080 mm above the ground, which does not reach the upper design limit (1,200 mm) but is clearly higher than the hip joint of almost all pedestrians (Figure 7.10). To investigate the effects of the SUV bonnet leading edge height on the predicted pedestrian injury risk, a sensitivity study using the same approach as the sedan case was carried out and the results are shown in Figure 7.28. The head WIC decreases with increasing the SUV bonnet leading edge height when it is lower than 1,100 mm, but then this trend reverses for a higher (>1,100 mm) bonnet leading edge height. The lower extremity WIC decreases linearly (R^2=0.95) with increasing bonnet leading edge height (bumper upper edge height), and an opposite trend was found for the thorax and pelvis WIC. These findings again suggest that the needs of head and lower extremity protection for the SUV are not conflicting when the bonnet leading edge is lower than a certain height (about 1,100 mm). The demands for lower extremity and head protection are generally conflicting with that for the thorax and pelvis protection. Thus this bonnet leading edge design was also selected to minimize the overall WIC by keeping the balance of WICs from different body regions.

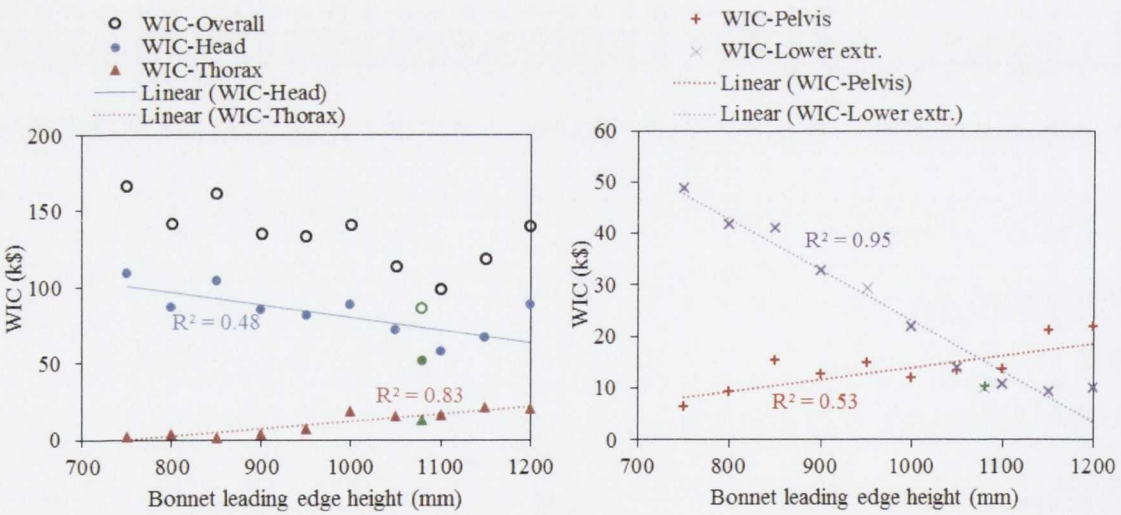

Figure 7.28 Predicted WIC as a function of SUV bonnet leading edge height, the points in green show the case for the optimal SUV.

The optimal SUV front shape has a bonnet with a length of 1,020 mm and an angle of 8° to the horizontal direction. When the shape of the bumper and bonnet leading edge is selected, the bonnet length only affects the head WIC of the 90th% male model by influencing the head

impact location (only for the 70 km/h case, Figure A.2). The simulation results show that the head injuries for the cases of the 90th% male model (in forward and backward gait stances) struck by the SUV fronts with different bonnet lengths (keeping all other parameters at the optimal SUV level) at 70 km/h are all at the AIS6 level (most serious). This suggests that the bonnet length of the optimal SUV front does not matter for pedestrian injuries. This is also the case for the windscreen angle of the optimal SUV front, since even the head of the 90th% male model at 70 km/h impact speed (tallest pedestrian and highest impact speed considered in the optimization) does not reach this area when the optimal bonnet leading edge shape is selected.

According to the predicted kinematics (Figure A.2), when the bumper and bonnet design are fixed, the bonnet angle of the optimal SUV may affect the predicted head and thorax WIC of all adult models for all speeds. Similar to the sedan case, a sensitivity study was conducted to investigate the effects of the bonnet angle on the predicted WIC using different bonnet angles (keeping all other parameters the same as for the optimal SUV). Figure 7.29 shows the predicted head and thorax WIC as a function of the SUV bonnet angle. The predicted head and thorax WICs generally increase with increasing bonnet angle and the optimal SUV has the minimum head WIC values. This suggests that the needs of head and thorax protection for a SUV bonnet angle are similar.

Figure 7.30 shows the optimal SUV front shapes and 'good' shape corridors predicted using the application of the original STS (60 impact configurations, see Table 6.1, Chapter 6) and the simplified STS (10 impact configurations with only 40 km/h speed, Section 7.2.2.2). There is no obvious difference in the SUV shape between the predictions using a broad range of impact speeds and a single impact speed of 40 km/h, largely because adult head contact locations are always in the bonnet area for SUV impacts when a high bonnet leading edge is given, regardless of impact speed.

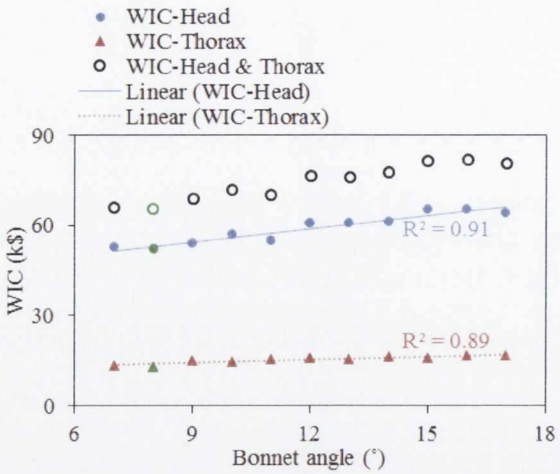

Figure 7.29 Predicted head and thorax WIC as a function of bonnet angle for SUV impacts, the points in green show the case for the optimal SUV.

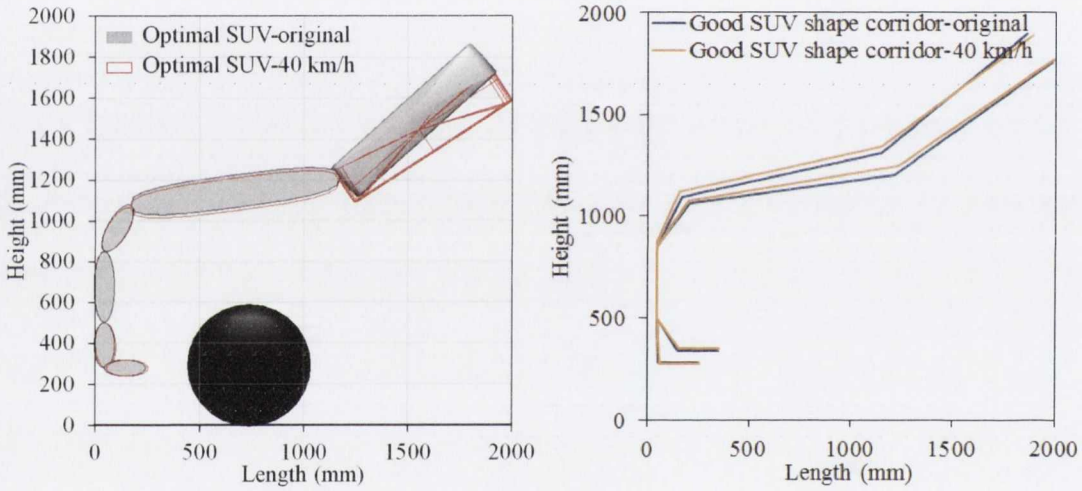

(a) (b)

Figure 7.30 Comparisons of the optimal SUV fronts (a) and 'good' shape corridors (b) between the optimizations using different impact configurations.

7.4.3.2 The 'good' and 'poor' SUV designs

Again, the optimization framework can distinguish the 'good' and 'poor' SUV front shapes based on the predicted WIC, see Figure 7.11 and Table 7.3. The differences in the bumper and bonnet leading edge geometry between the 'good' and 'poor' SUV front shape are similar to the sedan case, where the 'good' shapes have a wider and flatter bumper and a higher bonnet leading edge height than the 'poor' shapes. As discussed this difference mainly affects lower

extremity injuries and upper body kinematics. Similarly, a SUV front model with the median 'good' and 'poor' shape (Figure 7.11 (b)) was tested using the original STS. Figure 7.31 and Figure 7.32 compare the predicted WICs and typical pedestrian kinematics between impacts with these two SUV front models, respectively.

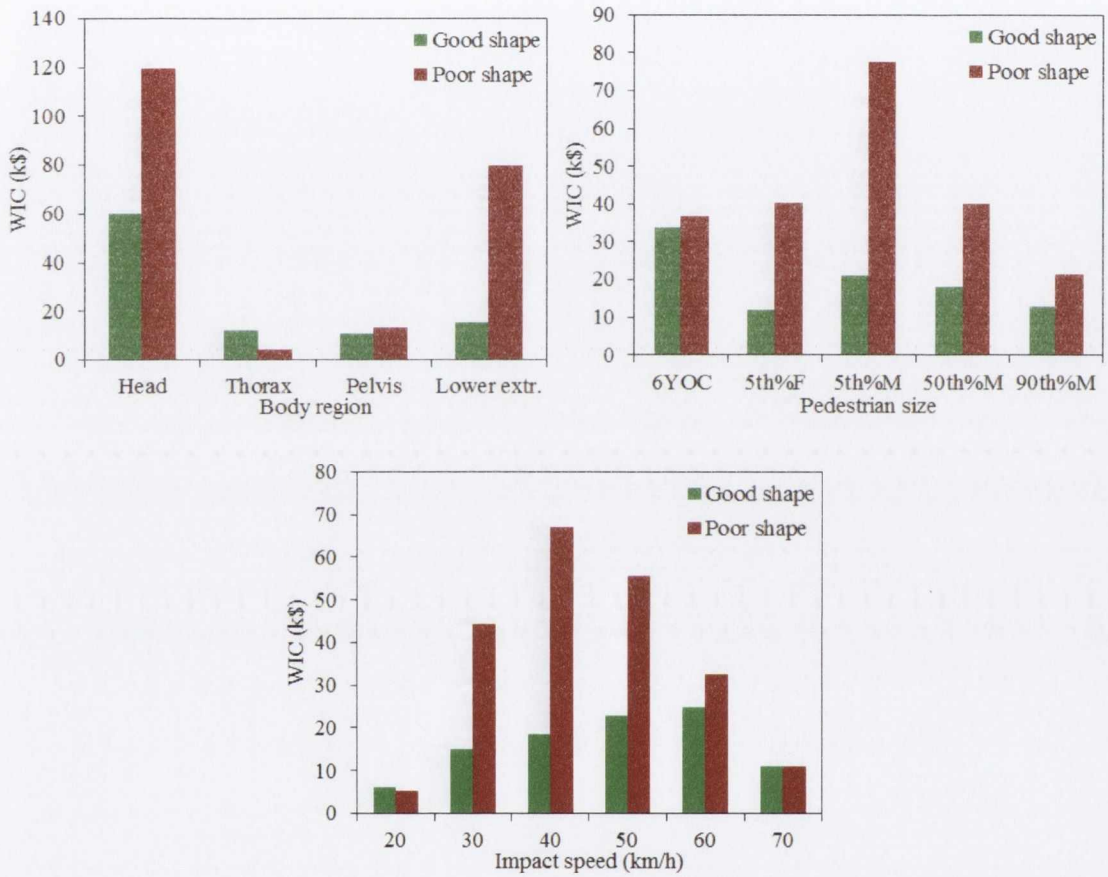

Figure 7.31 Comparisons of the predicted WIC as a function of body region, pedestrian size and impact speed between the simulations using a 'good' and 'poor' shape SUV front.

Figure 7.31 shows that the main differences in the predicted WIC between the impacts of 'good' and 'poor' shape SUV fronts are mainly to the head and lower extremity of adult models and in the speed range from 30 km/h to 60 km/h. There is no obvious difference in the predicted WIC for the pelvis, child model, and low (20 km/h) and high (70 km/h) impact speed case.

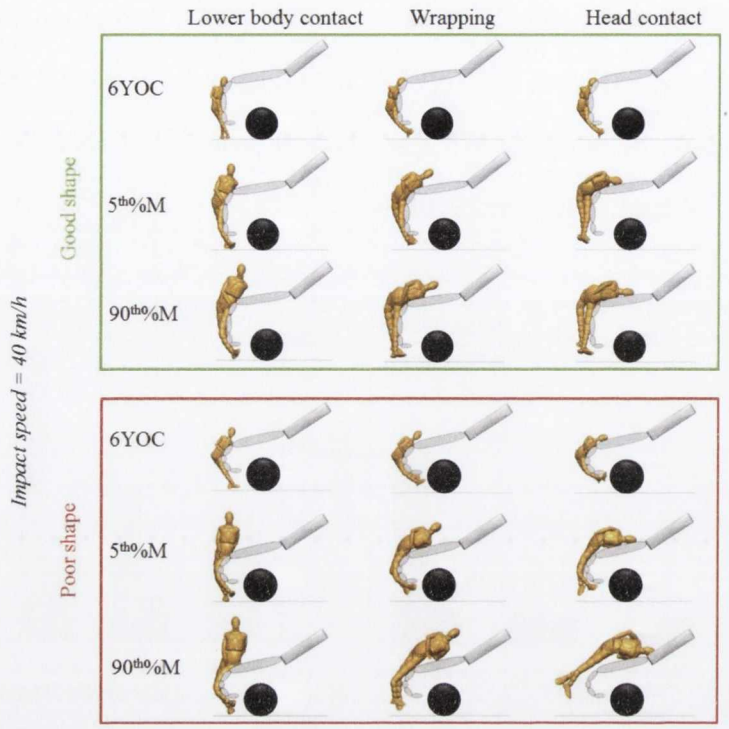

Figure 7.32 Comparisons of the pedestrian kinematics between the simulations using a 'good' and 'poor' shape SUV front.

The difference in the predicted lower extremity injuries can be explained by the lower extremity kinematics, where the lower extremity bending for the 'poor' SUV cases is obviously more serious than for the 'good' SUV impacts, Figure 7.32. For the head, Figure 7.33 compares the head impact speed between the impacts of 'good' and 'poor' shape SUV front. It is clear that the head impact speeds for the adult models in the 'good' SUV shape cases are generally higher than for the 'poor' SUV cases. This might be the main reason for the differences in the predicted head WIC between the impacts with the 'good' and 'poor' SUV shapes. However, the head impact speed for the child model in the 'poor' SUV cases is lower than for the 'good' SUV cases due to the shoulder contact before the head contact in the 'poor' SUV impact cases. Consequently the 'poor' SUV impacts lead to a lower predicted head WIC and a similar overall WIC (the lower extremity WIC is higher) for the child model compared to the 'good' SUV impact cases (Figure 7.31). As discussed the vehicle shape has a weak influence on pedestrian injury risk at a high impact speed, with little difference in the predicted WIC between the impacts with the 'good' and 'poor' SUV fronts for the cases of 70 km/h (Figure 7.31).

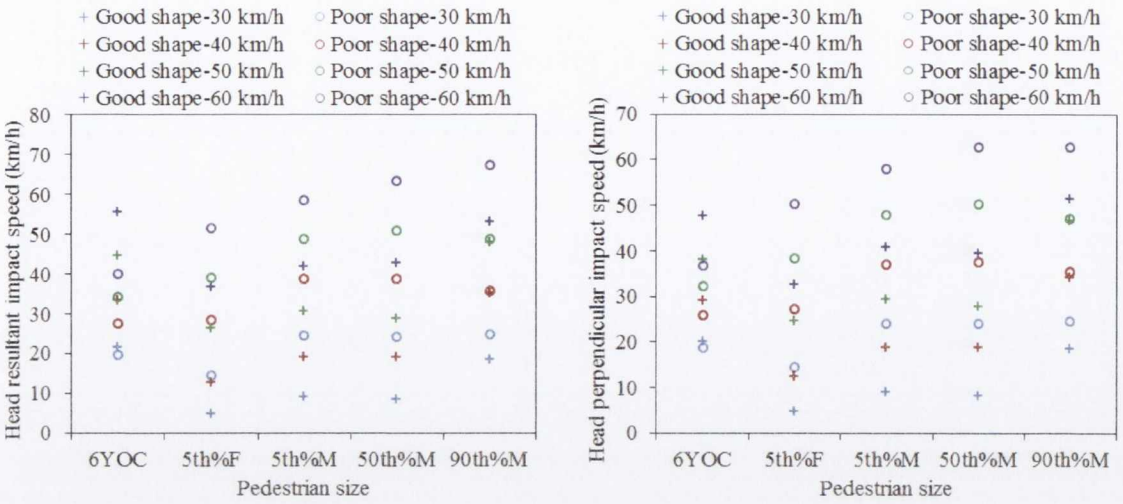

Figure 7.33 Comparisons of pedestrian head resultant and perpendicular impact speed between the simulations using a 'good' and 'poor' shape SUV front (the situation for ipsilateral lower extremity forward is shown).

Unlike the sedan case, there is no obvious difference in the predicted WIC between the impacts with the 'good' and 'poor' SUV shapes at 20 km/h. This is because the 'good' SUV front leads to more serious head injuries for the child model from the ground contacts than the 'poor' SUV front. The thorax WIC predicted from the 'poor' SUV cases is also lower than that predicted from the 'good' SUV impacts due to the absence of a hard contact between the thorax and vehicle front structure (Figure 7.32). Thus the SUVs with a high bonnet leading edge may reduce head impact speed for adult models but increase it for children (6 years old) and cause also more serious head injuries for the child model from ground contacts at 20 km/h than the low bonnet leading edge SUV.

Unfortunately, no evidence from real world accident data is available to support the prediction for the SUV optimization. However, the comparison results between the impacts with the 'good' and 'poor' SUV shapes suggest that the 'good' SUV shapes observed from the optimization framework can strongly reduce the head impact speed of adult pedestrian models (representing 85% of the population involved in GIDAS pedestrian accidents, see Table 6.1 in Chapter 6) and the lower extremity bending response of pedestrians of different heights.

7.4.4 Van front shape optimization

7.4.4.1 Optimal van front shape

Similar to the optimal sedan and SUV front shape, the predicted optimal van front shape nearly takes the lowest bumper lower edge (dimension #1) and offset (dimension #a) from the design space (Figure 7.14 and Table 7.1) to minimize lower extremity bending (Figure A.3). Unlike the sedan and SUV case, the optimal van front shape has a bumper upper height (840 mm) and a bonnet leading edge height (1,130 mm) which nearly reach their upper design limits. Again a sensitivity study was conducted to investigate the effects of van bonnet leading edge height (bumper upper height) on the predicted pedestrian injury risk and Figure 7.34 shows the results. The trend of head WIC as a function of van bonnet leading edge is not straightforward: the bonnet leading edge height seems to have no influence on head WIC when it is lower than 1,000 mm, but the head WIC is nearly doubled at 1,000 mm compared to a lower bonnet leading edge height, after which a decreasing trend was found with increasing bonnet leading edge height. This rapid increase of the predicted head WIC from 900 mm to 1,000 mm is largely due to the change in the head contact location of the 5th% male model at the impact speed of 40-50 km/h (important for the WIC) from the windscreen to the bonnet surface, which lead to a big difference in the predicted HIC. Generally, the thorax and lower extremity WIC are affected linearly by the van bonnet leading edge height, where the thorax WIC increases with increasing bonnet leading edge height and the lower extremity WIC decreases when increasing bonnet leading edge height. Strangely, a decreasing trend was observed for pelvis WIC when increasing the van bonnet leading edge from 850 mm to a higher value. This might be mainly because the bonnet leading edge height of 850 mm is the threshold line for the hip contact location of the 5th% male model on the vehicle front, when it is lower than 850 mm the hip contacts of the 5th% male model is mainly on the bonnet surface and then moving to the bonnet leading edge and the grid area when the bonnet leading edge height reaches 850 mm and above. This changing in the hip contact location would affect the hip loading condition (contact force, impact angle, impact speed, etc.) and hence the hip WIC. This might be also the reason for the turning point of the predicted WIC at the bonnet leading edge height of 850 mm

observed in sedan and SUV cases, see Figures 7.18 and 7.28. This finding suggests the importance of using the population of pedestrian heights and its distribution in the optimization framework. The sensitivity study results (Figure 7.34) indicate that the demands of head, pelvis and lower extremity protection for the *best* van bonnet leading edge height are consistent in the optimization.

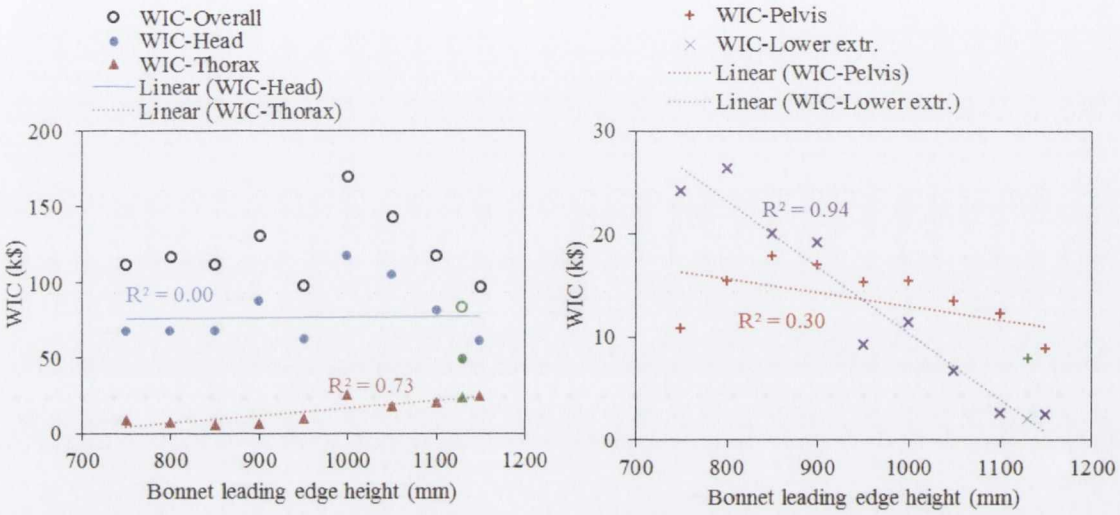

Figure 7.34 Predicted WIC as a function of van bonnet leading edge height, the points in green show the case for the optimal van.

For the bonnet and windscreen design of the optimal van front, Figure 7.35 shows the effects of the bonnet length, bonnet angle and windscreen angle on the predicted head and thorax WICs respectively. These results were predicted based on the same sensitivity study approach used above for the sedan and SUV cases (Sections 7.4.2.1 and 7.4.3.1). The bonnet length and windscreen angle have very little influence on the predicted head and thorax WICs since the changes only affect the tall pedestrians at high impact speeds when the bonnet leading edge height and bonnet angle are fixed at the predicted optimal van level (Figures 7.14 and A.3), and these impact configurations only account for a small proportion (used for weighting the injury cost) of the accidents (Table 6.1 and Eq. (6.1-6.2), Chapter 6). Figure 7.35 shows that the predicted head WIC generally increases with increasing bonnet angle of the van. This trend is similar to the SUV case (Figure 7.29), even though the detailed underlying mechanisms for this effect are not clear due to the complex head loading condition (head impact speed, contact

force, neck force, etc.).

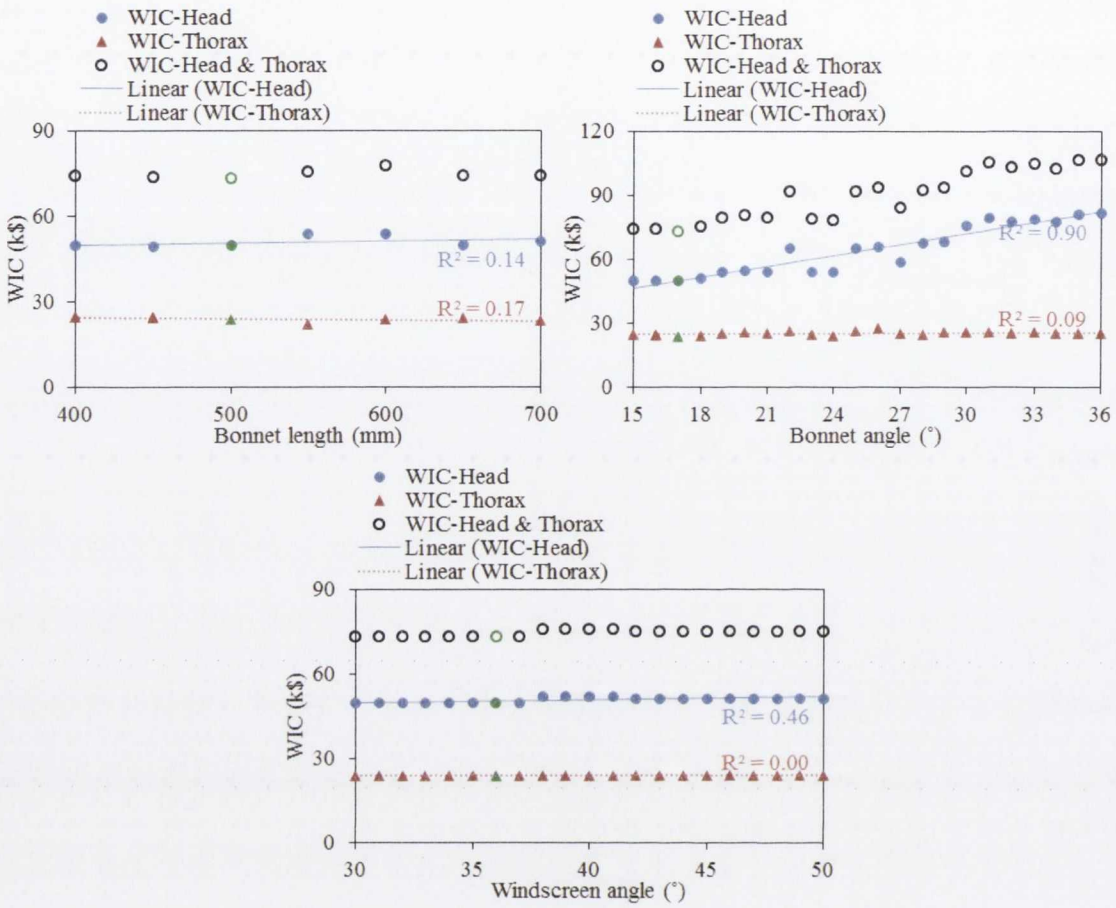

Figure 7.35 Predicted head and thorax WIC as a function of van bonnet length, bonnet angle and windscreen angle for van impacts, the points in green show the case for the optimal van.

Figure 7.36 compares the predicted optimal van front shape and 'good' shape corridors between the optimizations using the original STS (60 impact configurations, see Table 6.1, Chapter 6) and simplified STS (10 impact configurations with only the 40 km/h speed, Section 7.2.2.2). Similarly to the SUV case, there is no clear difference in the optimal and 'good' shape predictions between the cases using different impact speeds and a single impact speed of 40 km/h. This also suggests that the 40 km/h case can generally represent the situation combining different impact speeds.

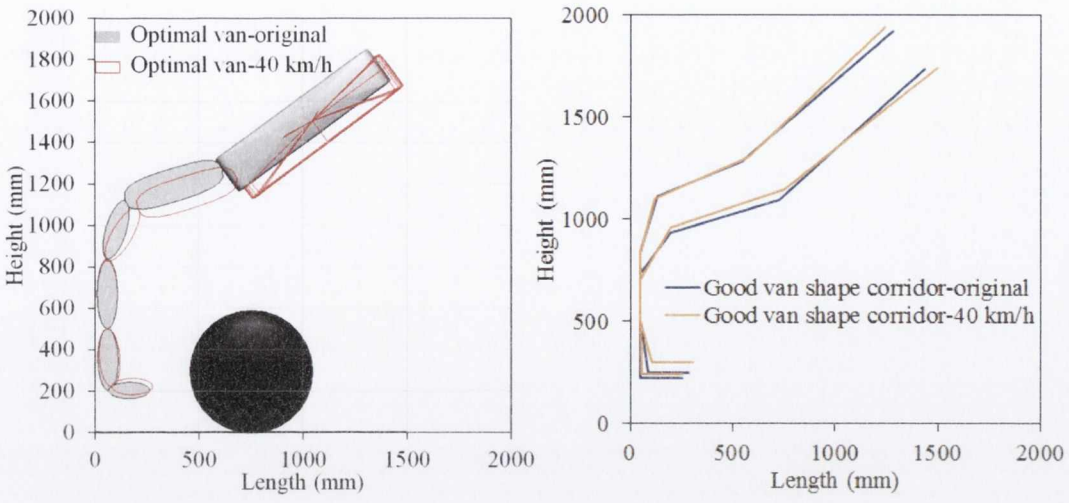

Figure 7.36 Comparisons of the optimal van fronts (a) and 'good' shape corridors (b) between the optimizations using different impact configurations.

7.4.4.2 The 'good' and 'poor' van front shapes

Figure 7.15 and Table 7.4 show the significant differences between the 'good' and 'poor' van shapes. For a further understanding, Figure 7.37 compares the predicted WICs between the impacts (using the original STS) with a 'good' (median in Figure 7.15 (b)) and a 'poor' shape (median in Figure 7.15 (b)) van front. Figure 7.38 shows the typical kinematics of different pedestrian models struck by the 'good' and 'poor' shape van front.

Figure 7.37 shows that the main differences in the predicted WIC between the impacts with the 'good' and 'poor' shape van fronts are to the head and lower extremity, 5^{th}% male model and impact speeds lower than 70 km/h. As discussed above, the difference in the predicted lower extremity WIC is because the 'poor' van shapes have a significantly sharper and narrower bumper than the 'good' van shapes, which leads to a high lower extremity injury risk from bending (Figure 7.38).

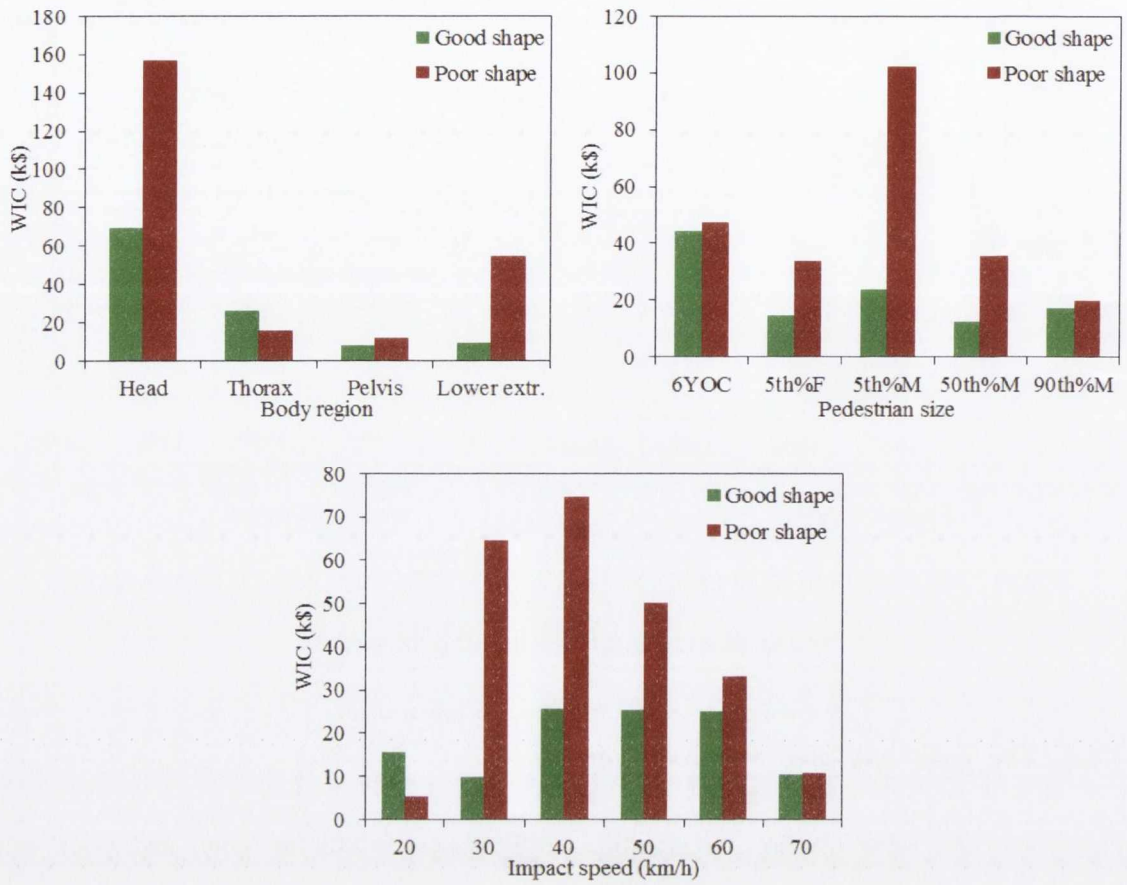

Figure 7.37 Comparisons of the predicted WIC as a function of body region, pedestrian size and impact speed between the simulations using a 'good' and 'poor' shape van front.

For the head, Figure 7.39 compares the head impact speed on the vehicle body for the 'good' and 'poor' shaped van fronts. The head impact speed data shows that the 'poor' shape van front leads to an obviously higher head speed on the vehicle body for the adult models than the 'good' shape van front. This may be the main factor for the big divergence in the predicted head WIC. But the 'poor' shape van front results in a lower head impact speed on the vehicle body for the child model than the 'good' shape van front. This leads to a lower head WIC for the child model in the impacts with the 'poor' shape van front, which generally counteracts the higher WICs to other body regions of the child model in the 'poor' shaped van impacts and then a similar overall WIC for the child model was predicted for the 'poor' and 'good' van shapes (Figure 7.37).

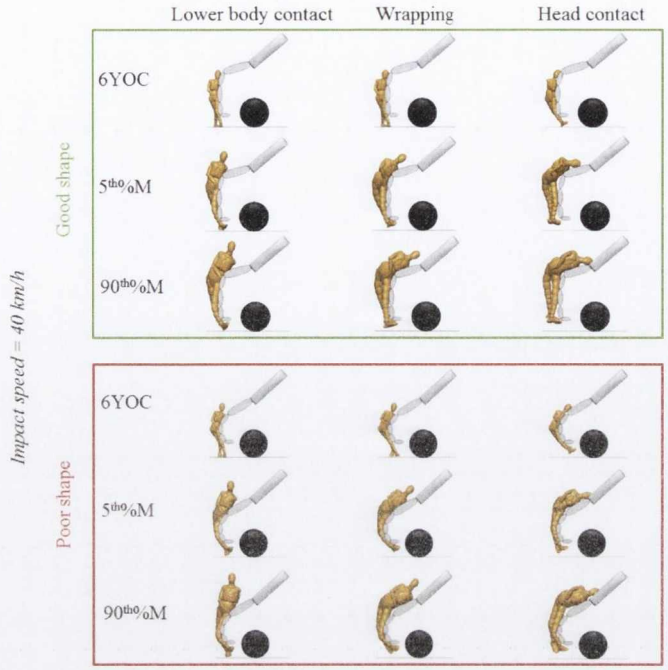

Figure 7.38 Comparisons of the pedestrian kinematics between the simulations using a 'good' and 'poor' shape van front.

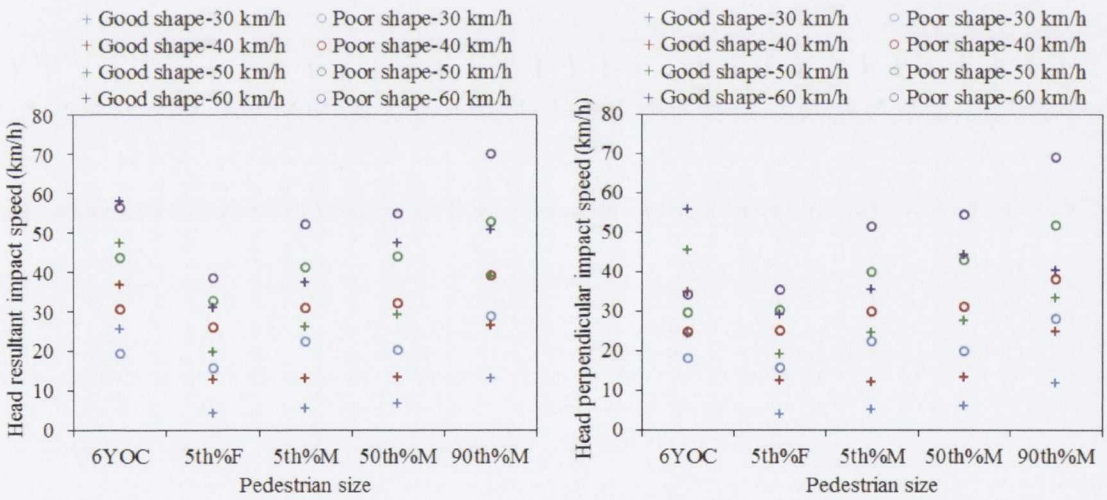

Figure 7.39 Comparisons of pedestrian head resultant and perpendicular impact speed between the simulations using a 'good' and 'poor' shape van front (the situation for ipsilateral lower extremity forward is shown).

Similarly to the sedan case, there is a big gap in the predicted WIC for the 5th% male model between the impacts with the 'good' and 'poor' shape van fronts. This is mainly due to the high proportion of the population represented by this model in accidents (Table 6.1, Chapter 6) and the effects from the head impact location where the head of the 5th% male model mainly

contacts with both bonnet and windscreen of the 'poor' shape van, while this is in the middle bonnet area for the 'good' shape van case (Figure 7.38). The differences in the head impact location and speed lead to a large difference in the predicted head linear acceleration curve and HIC between the impacts with the 'good' and 'poor' vans, Figure 7.40 shows an example. The data in Figure 7.37 shows that the 'good' shape van leads to an obviously higher predicted WIC at 20 km/h than the 'poor' shape van. This is due to the fact that the 'good' shape van front results in more serious head injuries to the child model from the ground contacts than the 'poor' shape van front at this impact speed. The van shape also has a weak influence on predicted WIC for the 70 km/h case due to the strong effects of the impact speed.

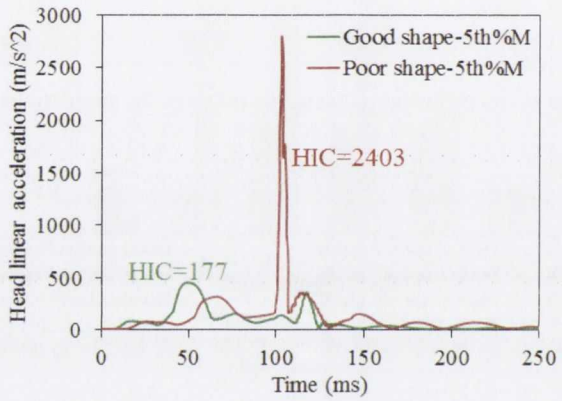

Figure 7.40 Comparisons of the head resultant linear acceleration curve for the 5th% male model between the simulations using a 'good' and 'poor' shape van front.

Again, no evidence from real world accident data is available to support the predictions of the van optimization. Nevertheless, the comparison results between the impacts with the 'good' and 'poor' shape van fronts suggest that the selection of the 'good' van shapes conducted by the optimization framework was based on the objective to reduce the overall predicted WIC (pedestrian injury risk) considering a broad range of impact configurations, even though these predicted 'good' van shapes may lead to a high injury risk for children.

7.5 Summary

This chapter applied the defined optimization framework to the sedan, SUV and van front shape design with the purpose of reducing the overall weighted injury cost (WIC) for

pedestrians. Optimal, 'good' and 'poor' front shapes were observed via the application of the optimization framework for the sedan, SUV and van, respectively.

The results indicate that the defined optimization framework shows good convergence after 10 to 14 iterations of the genetic algorithm when a reasonable design space is given and the simulation test sample (STS) and injury cost weighting system used in the optimization framework can generally predict similar weighted injury distributions as in real world accidents. The genetic algorithm minimizes the optimization objective (overall WIC) by keeping the balance between the injury risk (WIC) from different body regions, pedestrian heights and impact speeds. All the optimal front shapes have a wide and flat bumper which can cover the pedestrian's lower extremity from the distal leg to the shaft/proximal thigh with even contacts. The selection of the bonnet leading edge height for the optimal shapes is mainly for reducing head injury risk by controlling the head impact location and kinematics of the pedestrians. The predicted optimal vehicle front shapes have a particular bonnet and windscreen design to minimize the overall WIC based on the optimal design of the bumper and bonnet leading edge.

The optimal shape is affected by the crossover fraction, definition of the simulation test sample (such as the impact speed) and other factors that have not been assessed in the current study (such as the stiffness, injury measuring and weighting methods, etc.). Thus there is no full confidence to affirm that the predicted optimal output in the current study is the global minimum for each vehicle type. The sensitivity results and comparisons of the predictions between the 'good' and 'poor' shapes indicate that the involving proportions (weight factors for injury cost) of the impact speed and pedestrian height are crucial for the optimization of vehicle front shape. These findings at least imply that a successful optimization of vehicle front shape for pedestrian protection should consider the broad range of impact configurations and their distributions in accident, and ground contacts, even though the global minimum can still not be guaranteed in the optimizations. The optimal shapes were predicted for minimizing the overall pedestrian (considering different heights) injury risk, but not for a particular individual. Thus these optimal shapes may be not good for child protection due to the lower proportion (in accident) of the population represented by the child model (6 years old).

Nevertheless, the comparisons between the 'good' and 'poor' shapes show obvious differences in the geometry, head impact speed on the vehicle front and lower extremity bending response. Particularly, the real accident data from GIDAS indicates that the sedan fronts meeting the 'good' shapes resulted in obviously lower injury cost than those sedans with 'poor' profiles. Therefore the optimization framework can successfully distinguish the aggressivity of vehicle front shapes and the optimal vehicle front shapes observed here are then generally suitable for pedestrian protection.

The results of the sensitivity studies indicate that the effects of the bonnet leading edge on head injury risk observed at the population level are complex and vary between vehicle types. The thorax injury risk increases with increasing the bonnet leading edge height of the SUV and van. The pelvis injury risk increases with increasing bonnet leading edge height for the sedan and SUV. The lower extremity injury risk decreases with increasing bonnet leading edge height (bumper upper edge height) for all vehicle types. A shallow sedan windscreen, and shallow SUV and van bonnet are helpful for head protection. The impact speed and pedestrian population and their distributions have an important influence on the predicted trends of the head and pelvis injury risk resulting from changing the bonnet leading edge and bonnet design. All these findings are for the first time observed at the population level and suggest consideration of the broad range of impact configurations and their distributions in evaluating pedestrian safety performance of vehicle front designs.

Chapter 8 Effects of the Fitness Function on the Optimal Sedan Front Shape

8.1 Introduction

The optimal vehicle front shapes observed in Chapter 7 were from a fitness function using the weighted injury cost (WIC) as the objective, where injuries from four body regions (head, thorax, pelvis and lower extremity) were considered and weighted. The analysis in Chapter 7 indicates that the fitness function is crucial for the optimization since it determines the focuses of the optimization algorithm and hence the optimal vehicle front shapes. Accordingly, this chapter investigates the effects of the fitness function on the optimal sedan front shape, considering a different injury weighting system or a different head injury criterion. The selection of the sedan is due to the fact that this vehicle type accounts for the largest proportion in real world pedestrian accidents (93% in GIDAS and 68% in PCDS).

8.2 Methods

A different fitness function was defined according to the consideration in each section and an optimization was then conducted for the sedan front using the optimization framework proposed in Chapter 6 with the corresponding fitness function and the same definitions for the GA and design space as described in Chapter 7.

8.2.1 Risk of permanent medical impairment (RPMI)

In the original optimization framework the predicted injuries were weighted by the economic injury cost to account for the importance of each injury (ISO: 13232-5, 2005). As proposed in a study from Malm et al. (2008), the importance of a given injury can also be evaluated by the medical impairment (MI) based on the AIS level and location (body region) of this injury. MI is defined by considering the reduction of physical and/or mental functions, independent of cause and without regard to the occupation, hobbies or other special circumstances of the victim (Malm et al., 2008). Based on this conception, a permanent medical impairment (PMI) was

defined as no further improvement in the affected function is expected with additional treatment (Malm et al., 2008). The degree of PMI for a given injury can be between 1% and 99% according to the severity of sustained functional reduction of the injured person from this injury. Therefore the risk of permanent medical impairment (RPMI) can be used to weight the importance of an injury. Malm et al. (2008) calculated the RPMI on the 1%+ level (at least 1% of PMI) for different body regions and AIS levels based on the accident data from Sweden, see Table 8.1.

Table 8.1 RPMI on 1%+ level, adapted from (Malm et al. 2008).

Body region	AIS1	AIS2	AIS3	AIS4	AIS5	AIS6
Head	8%	15%	50%	80%	100%	100%
Thorax	2.6%	4%	4%	30%	30%	100%
Pelvis	17.6%	50%	60%	60%	100%	100%
Lower extremity	17.6%	50%	60%			

Similar to the injury cost, the RPMI for each injury predicted from the STS can be calculated using the injury thresholds (Table 6.5, Chapter 6) and the RPMI data (Table 8.1) for different AIS levels and body regions. Similar to the weighted injury cost (WIC), the sum of RPMI for a pedestrian's head, thorax, pelvis and lower extremity for an impact simulation in the STS can be weighted by the proportion of this impact configuration in accidents, see Eq. (6.1-6.3) in Chapter 6. Therefore the weighted RPMI (WRPMI) can be used instead of the WIC to predict the threat of the vehicle front shape to pedestrians in accidents. Then the WRPMI was defined as the objective of the fitness function and an optimization was conducted for the sedan front shape via the optimization framework and using the same initial population, crossover fraction (o.6) and design space (Table 7.1, Chapter 7).

8.2.2 GAMBIT head injury criterion

In the original fitness function the HIC was employed for assessing head injuries. However, the HIC only accounts for linear acceleration but head angular motion is also very important for

brain injuries (Gennarelli et al., 1972). To account for both linear and angular head kinematics during the impact, the GAMBIT head injury criterion was then used in a modified fitness function. The definition of the GAMBIT has been described in Eq. (2.2), Chapter 2. The maximum GAMBIT was then used as the index for assessing head injuries. Even though the GAMBIT has not been validated, the application of it in the optimization framework may provide some useful information for future vehicle safety design.

Table 8.2 shows the thresholds of the GAMBIT for different head injury AIS levels, which were extracted from the curves of head injury probability as a function of maximum GAMBIT (Kramer and Appel, 1990), and data for the injury probability of 30% was used as the reference. To evaluate the consistency in the head injury prediction between the GAMBIT thresholds (Table 8.1) and HIC thresholds (Table 6.2, Chapter 6), 100 different sedan front models were tested using the STS (60 impact configurations) and WIC was calculated by the AIS levels of the head injuries predicted by the GAMBIT and HIC thresholds respectively for each sedan front. Then the paired t-test was employed to check the difference between the overall head WICs predicted from the GAMBIT and HIC for the same 100 different sedan models (data is generally a normal distribution). The paired t-test result shows that there is no statistically significant ($p=0.47$) difference in the predictions of head WIC between the GAMBIT and HIC when a broad range of sedan shapes were tested. Then an optimization was conducted for the sedan front using the GAMBIT for measuring head injuries and the WIC for weighting the predicted injuries from different body regions. Again the same initial population, crossover fraction (0.8) and design space as for the original sedan front optimization were defined here.

Table 8.2 GAMBIT threshold for different head injury AIS levels.

	AIS1	AIS2	AIS3	AIS4	AIS5	AIS6
GAMBIT	0.56-0.65	0.65-0.85	0.85-0.9	0.9-1.0	1.0-1.05	>1.05

8.3 Results

8.3.1 Optimization using the WRPMI

Figure 8.1 shows the predicted WRPMI for each design point and the median and IQR of the WRPMI for each generation. The optimization shows a good convergence.

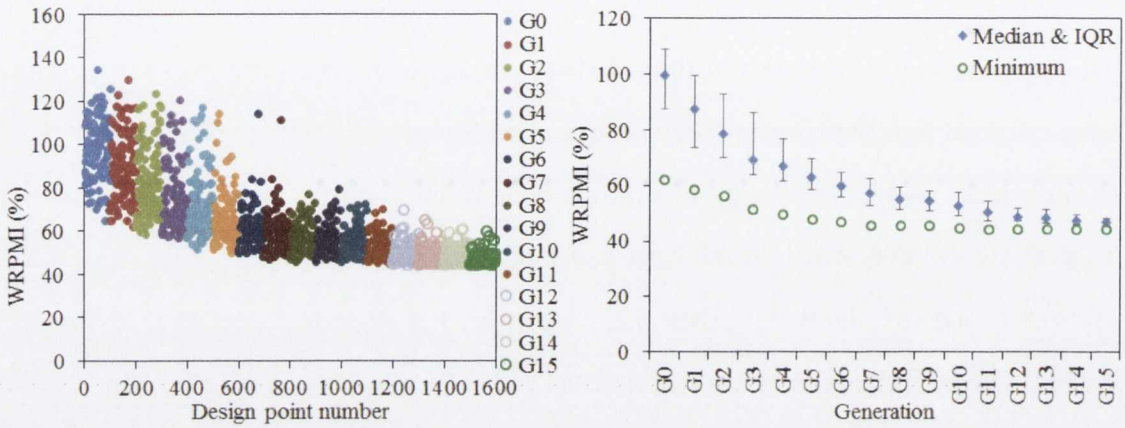

(a) (b)

Figure 8.1 Predicted WRPMI data for design points (a) and generations (b) in the sedan optimization.

Figure 8.2 shows the optimal sedan front model predicted based on the minimum WRPMI value, together with pedestrian models of different sizes. This figure shows that the optimal sedan front has a bumper covering the height range from 180 mm to 620 mm above the ground, without offset in the bumper lower edge. The bonnet leading edge height (BLEH) of this optimal sedan shape is about 730 mm, which is lower than the hip joint of adults and higher than the child hip (6 years old). The bonnet length is 740 mm with an angle of 11°to the horizontal level and the windscreen angle is 24°to the horizontal level.

Figure 8.3 shows the 'good' and 'poor' sedan shapes observed from the predicted WRPMI values shown in Figure 8.1 (a), where the 'good' sedan shapes have a WRPMI value lower than 65% and the 'poor' sedan shapes are with a WRPMI value higher than 110% (same approach as for the WIC used in Chapter 7). A dramatic difference in the bumper shape is observed between the 'good' and 'poor' sedan shapes predicted by the WRPMI data.

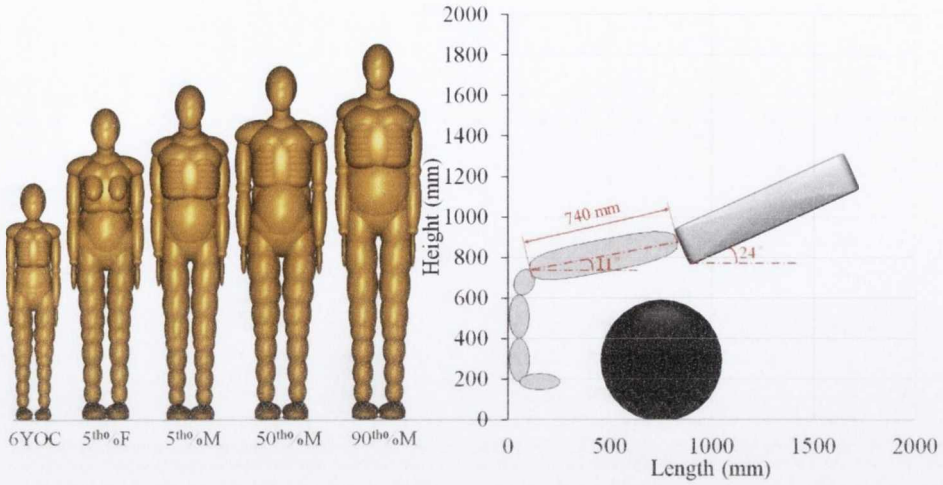

Figure 8.2 Optimal sedan front model predicted by the WRPMI and pedestrian models.

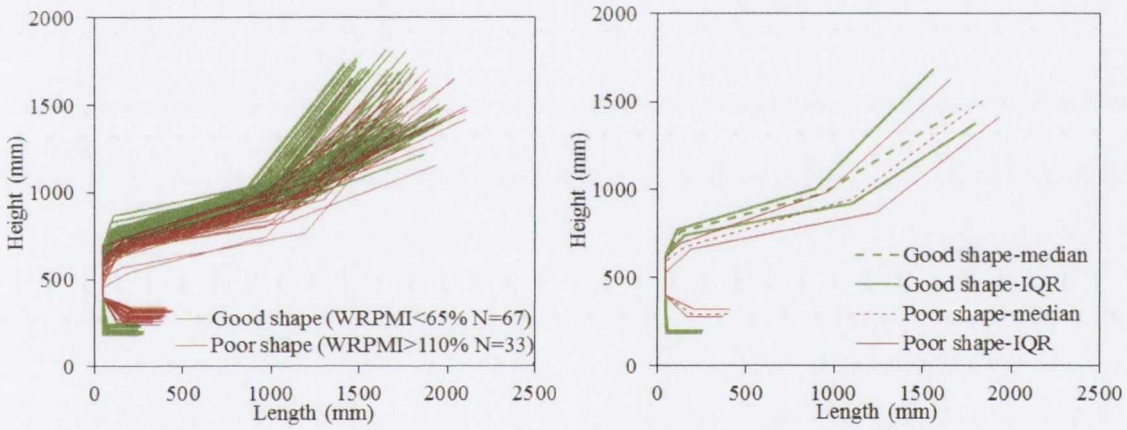

(a) (b)

Figure 8.3 'good' and 'poor' sedan shapes observed based on the WRPMI (a) and their corridors (b).

8.3.3 Optimization using the GAMBIT

Figure 8.4 shows the predicted WIC data, including the WIC for each design point and the median and IQR of the predicted WIC for each generation, as a function of generation in the optimization using GAMBIT instead of HIC. The predicted WIC data shows a good convergence for this optimization. Figure 8.5 shows the optimal sedan front predicted based on the minimum WIC using the GAMBIT as the head injury criterion, together with pedestrian models in different heights. The optimal sedan front predicted using the GAMBIT has a bumper crossing the range from 200 mm to 690 mm above the ground without offset at the lower edge, a bonnet leading edge height of 880 mm above the ground, a bonnet with a length of 1035 mm and an angle of

16° (to the horizontal level) and a windscreen angle of 35° (to the horizontal level), see Figure 8.5. The bonnet leading edge height of this optimal sedan front is higher than for the pedestrian models shorter than the 90th% male.

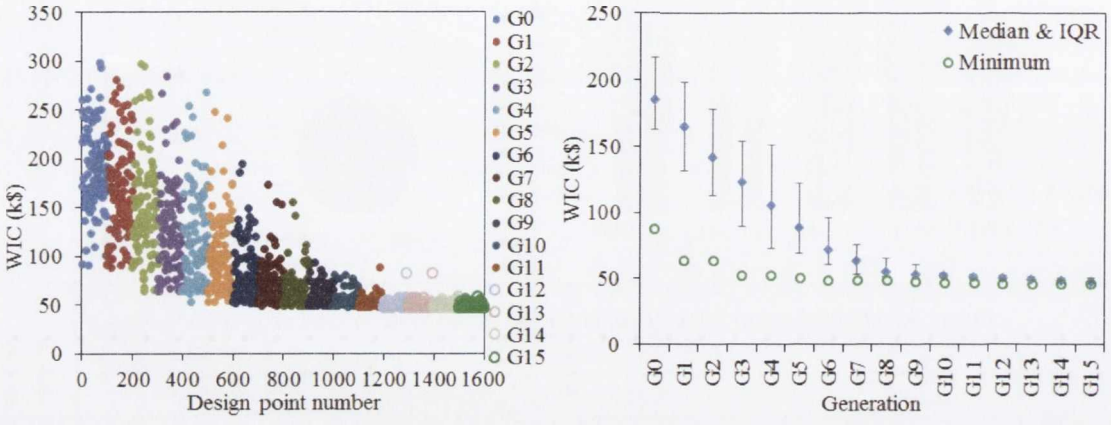

Figure 8.4 Predicted WIC data for design points (a) and generations (b) in the sedan optimization using the GAMBIT.

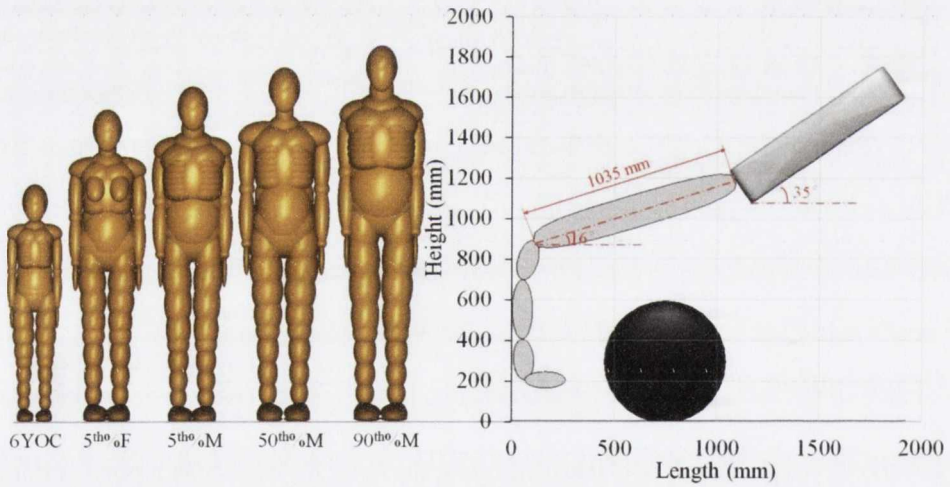

Figure 8.5 Optimal sedan front model predicted using the GAMBIT and pedestrian models.

Figure 8.6 compares the 'good' and 'poor' sedan shapes which were selected according the predicted WIC values: WIC<110 k$ for the 'good' sedan shapes and WIC>235 k$ for the 'poor' sedan shapes (same approach as before). There are obvious differences between the 'good' and 'poor' shapes observed using the GAMBIT, especially for the bumper and bonnet leading edge height.

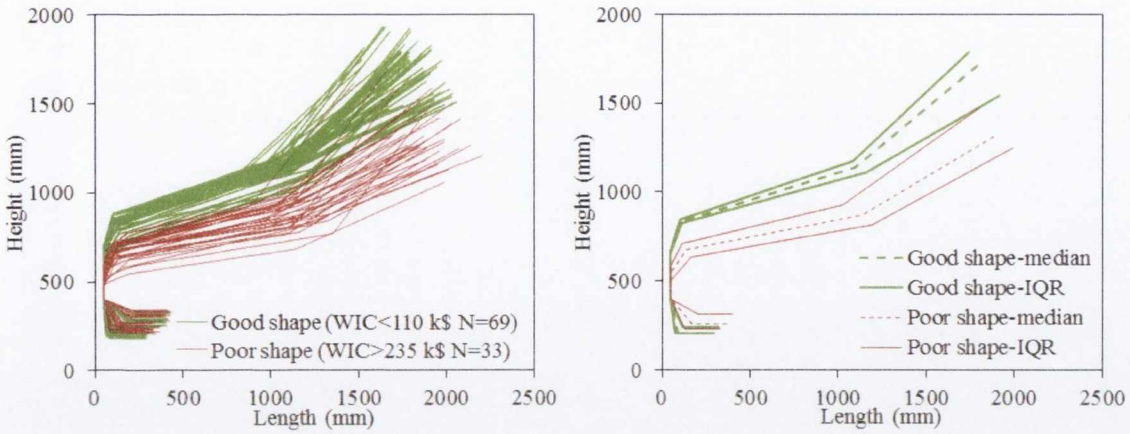

Figure 8.6 'good' and 'poor' sedan shapes observed using the GAMBIT (a) and their corridors (b).

8.4 Discussion

8.4.1 WRPMI vs WIC

The results in Figure 8.1 show a good convergence of the sedan front shape optimization based on the WRPMI. By using the WRPMI for weighting predicted injuries, the optimization framework can still find the optimal sedan front and distinguish the 'good' and 'poor' sedan front shapes, see Figure 8.2 and 8.3.

Figure 8.7 shows the predicted weighted injury outcome for different body regions as a function of the convergence process of the optimizations based on the WRPMI and WIC, respectively. The data predicted by the WIC was from the sedan front optimization conducted in Chapter 7 (Figure 7.16 (a)). The data in Figure 8.7 (a) shows that the predicted head and lower extremity WRPMI decrease with increasing generation, while the predicted thorax and pelvis WRPMI are not always reducing in the optimization process. Similar to the WIC, head and lower extremity WRPMI are the dominant parts of the overall predicted WRPMI. This again implies that the optimization algorithm can focus on reducing the main parts of the objective (head and lower extremity WRPMI) and find the sedan fronts to minimize the overall WRPMI.

Figure 8.7 also shows that the predicted lower extremity WRPMI is obviously higher than that

for the head when a broad range of sedan fronts are employed (the initial generation), while this trend is opposite in the WIC case. This is due to the differences in the weighting factors between WRPMI and WIC, where a higher weight is given to the lower extremity in the RPMI system than the injury cost system (Table 6.3 and Table 8.1). The effects of high weight for the lower extremity injuries in the RPMI are also reflected in the obvious difference in the bumper design between the 'good' and 'poor' sedan shapes observed from the optimization based on the WRPMI, see Figure 8.3. For the last generation, the head is the most important part for both predicted WRPMI and WIC, followed by the lower extremity and pelvis. This trend is similar for both optimizations.

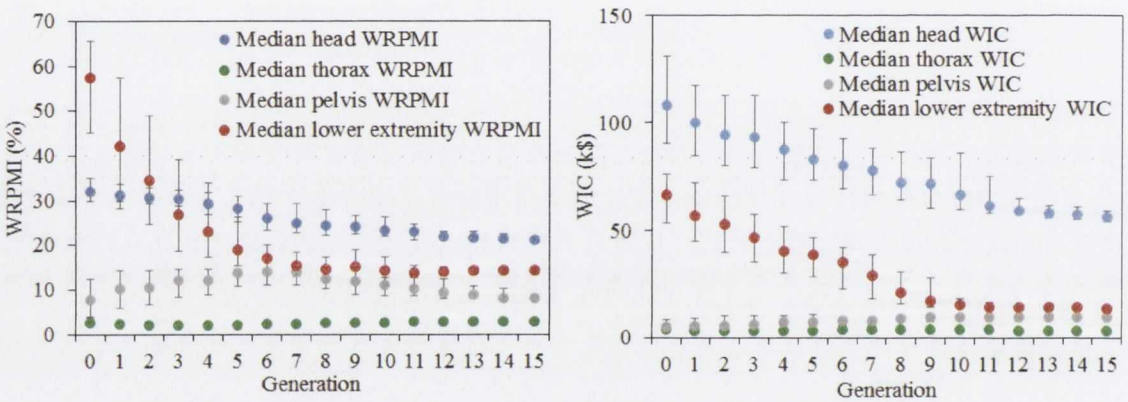

(a) WRPMI (b) WIC

Figure 8.7 Predicted weighted injury outcome for different body regions as a function of generation in the optimizations based on the WRPMI (a) and WIC (b).

To investigate the difference in the sedan front shape between the optimizations using WIC and WRPMI, Figure 8.8 compares the optimal sedan front and 'good' shape corridors predicted by these two optimizations. There is no obvious difference in the bumper and bonnet leading edge shape between the optimal sedan fronts predicted by WIC and WRPMI, but a difference in the bonnet angle (19° vs 11°) is observed between them (Figure 8.8 (a)). However, the difference in the bonnet angle may have no significant effect on the predicted overall injuries according to the sensitivity study conducted in Chapter 7 (Figure 7.21 (a)), where the predicted overall WIC for the case with a bonnet angle of 19° (WIC=79 k$) is close to that for the case with a bonnet angle of 11° (WIC=82 k$) when the bumper and bonnet leading edge design are fixed. Figure 8.8 (b) shows that the 'good' shape corridor predicted by the WIC is very close to that predicted by the

WRPMI. These results indicate that the optimizations based on the WRPMI and WIC have similar predictions for the optimal and 'good' sedan front shapes which pose a low injury risk to pedestrians, even though the injury weighting factors are different (Table 6.3 and Table 8.1). This is largely due to the fact that head and lower extremity are always the body regions dominating the optimization objective. This may also imply that the needs of a sedan front for reducing the HIC (head) and lower extremity bending are not strongly conflicting. Particularly, a wide bumper (high bumper upper edge) which is safe for pedestrian's lower extremity generally leads to a high bonnet leading edge then reducing the head impact speed on the vehicle body and head injury risk when a short bonnet is employed. This also to some extent validated the optimization outputs predicted by the proposed original optimization framework.

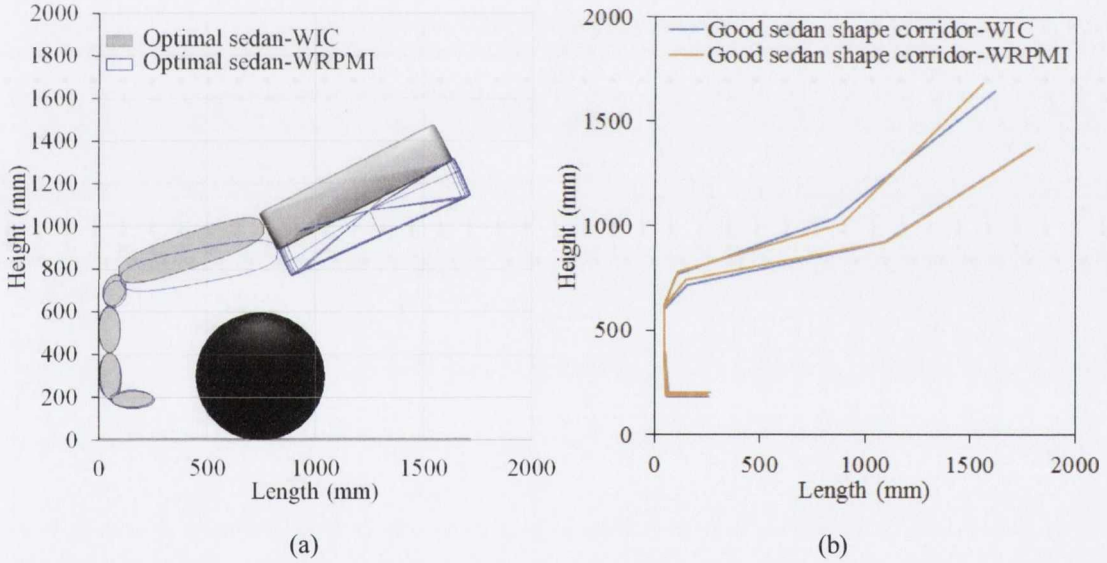

(a) (b)

Figure 8.8 Optimal sedan fronts (a) and 'good' sedan front shape corridors (b) predicted by the optimizations based on the WIC and WRPMI.

8.4.2 GAMBIT vs HIC

The results show a good convergence of the optimization for sedan front shape using the GAMBIT as the head injury criterion (Figure 8.4) and an optimal sedan front was observed based on the minimum predicted WIC (Figure 8.5). The optimization framework can also distinguish the 'good' and 'poor' sedan shapes based on the predicted WICs which were calculated based on injuries from different body regions where the head injuries were measured

by the GAMBIT (Figure 8.6).

To investigate the differences in the predictions between the optimizations using the GAMBIT and HIC, Figure 8.9 shows the predicted WICs for different body regions as a function of generation in both optimizations, where the data for the case using the HIC as the head injury criterion was predicted in Chapter 7 (Figure 7.16 (a)). The head injury cost can be reduced to a very low level (even lower than the pelvis WIC) if the head injuries are measured using the GAMBIT, but this cannot be achieved when the HIC is used as the head injury criterion (Figure 8.9). This is largely due to the difference in the mechanism of predicting head injuries between the GAMBIT and HIC, where the GAMBIT is based on the normalized combination of head linear and angular acceleration magnitude and the HIC is calculated from the combination of head linear acceleration magnitude and its duration time.

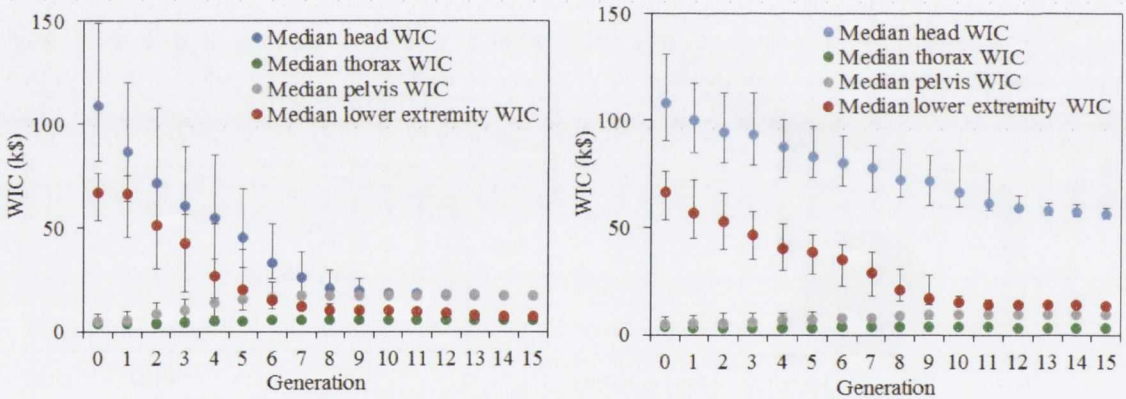

(a) GAMBIT (b) HIC

Figure 8.9 Predicted WIC for different body regions as a function of generation in the optimizations using the GAMBIT (a) and HIC (b) as the head injury criterion.

The distribution of the predicted WIC as a function of body region for generations 8-15 (Figure 8.9 (a)), where the head WIC is even similar to that for the pelvis, is suspect when comparing to that observed from the accident data (head WIC is dominant, see Figure 7.17 (a)). This suggests that the GAMBIT is not a credible criterion for head injuries, though further physical test analysis is needed for validation. The findings from a previous comparison study between multi-body and FE simulations also indicate that the HIC is generally more credible than the GAMBIT for predicting head injuries in vehicle-to-pedestrian collisions (Feist et al., 2009).

For a further understanding, Figure 8.10 compares the predicted optimal sedan fronts and 'good' shape corridors between the optimizations using the HIC and GAMBIT. The optimal and 'good' sedan fronts predicted using the GAMBIT has an obviously higher bumper upper edge and bonnet leading edge, and longer bonnet than that predicted by the HIC. These differences in the bonnet leading edge and bonnet design are mainly due to the difference in the mechanism of predicting head injuries between the GAMBIT and HIC. However the consistent lower bumper shape for reducing pedestrian lower extremity injury risk reflects the firm prediction of the optimization framework. Accordingly, Figure 8.11 shows the head contact location for different pedestrian models struck at different speeds by these optimal sedan fronts.

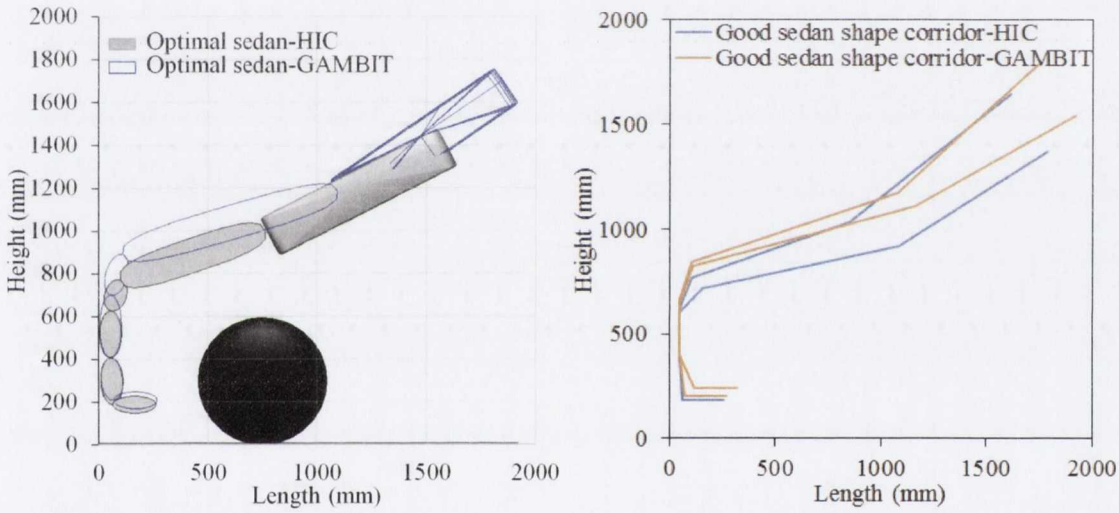

(a) (b)

Figure 8.10 Optimal sedan fronts (a) and 'good' sedan front shape corridors (b) predicted based on the HIC and GAMBIT.
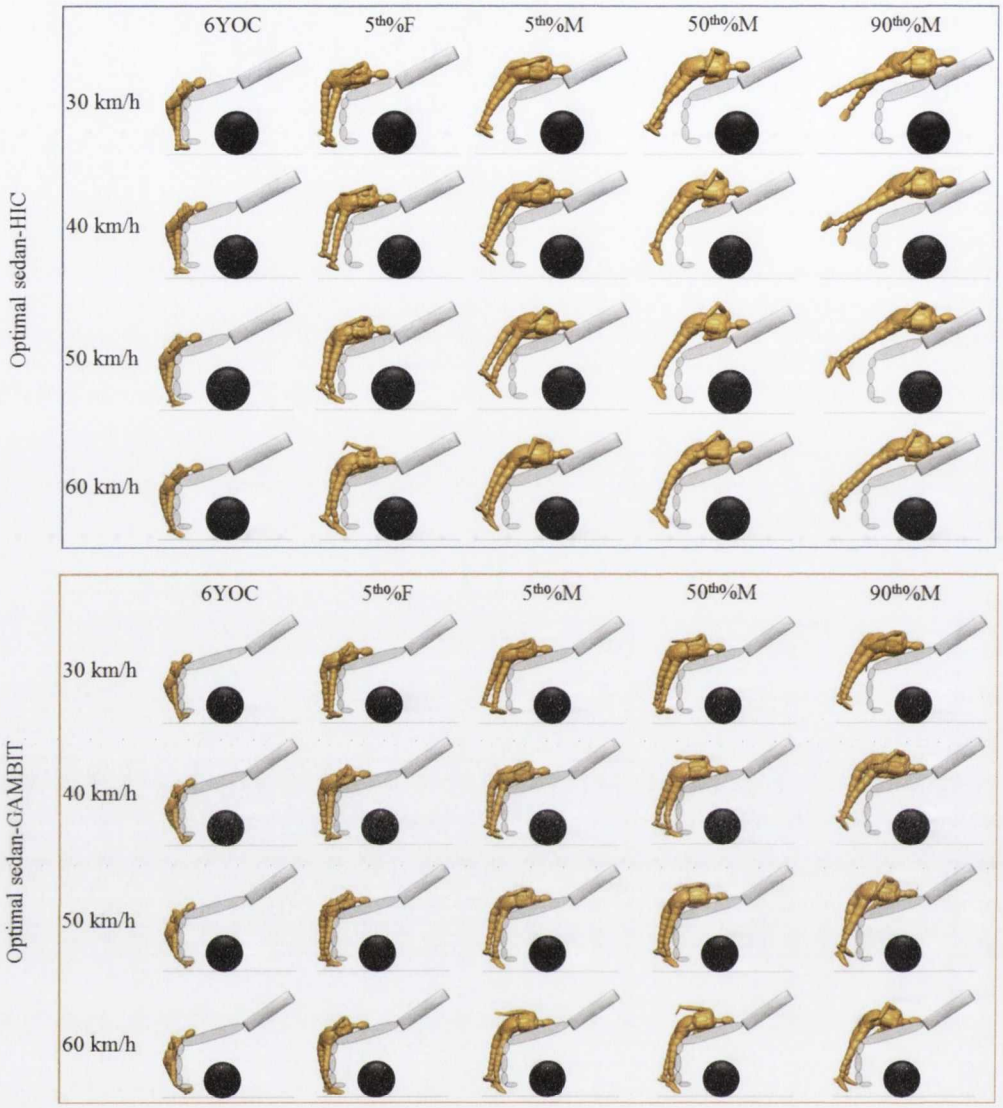
Figure 8.11 Comparison of pedestrian head impact location between impacts with the optimal sedan fronts predicted based on the HIC and GAMBIT.

The higher bonnet leading edge and longer bonnet of the optimal sedan predicted based on the GAMBIT result in a higher frequency of head-to-bonnet contacts than the optimal sedan-HIC (8.11). This may be mainly for reducing the peak head linear acceleration which is an important part of the GAMBIT (Eq. (2.2), Chapter 2), since the initial contact stiffness of the windscreen poses a higher peak for the head linear acceleration than the bonnet (Figure 7.20, Chapter 7). But the fracture of the windscreen modelled by the contact characteristics (Figure 5.8, Chapter 5) results in a lower HIC (narrow head linear acceleration peak) than the bonnet which leads to a wide head linear acceleration peak (Figure 7.20, Chapter 7), and then the 'good' sedan shapes

predicted by the HIC have a short bonnet (Figure 8.10). This also indicates that the predicted safer vehicle front shapes are strongly dependent on the stiffness distribution between vehicle front structures. The 'good' sedan front shapes predicted by the GAMBIT have a higher bumper upper edge and bonnet leading edge than that predicted from the optimization using the HIC, which leads to more head contacts on the bonnet area as a low GAMBIT score requires, consequently being able to have a higher bumper upper which is better for reducing lower extremity injury risk as observed in GIDAS accidents (Chapter 3). This leads to a higher consistency in the demand for a safe sedan between the head and lower extremity protection in the sedan optimization based on the GAMBIT, compared to the sedan optimization using the HIC.

Figure 8.12 shows the head linear and angular speed at the instant of head contact (on the vehicle body) for impacts with the optimal sedans predicted by the HIC and GAMBIT. Generally, the optimal sedan shape predicted by the GAMBIT (higher bonnet leading edge and longer bonnet) leads to a lower head linear speed but a higher head angular speed to pedestrians at the instant of contact with the vehicle body compared to the optimal sedan predicted by the HIC ('o' vs '+' in Figure 8.12). However, the peak head angular accelerations for the impacts with the optimal sedan shape predicted by the GAMBIT (higher head angular speed) are generally lower than for impacts with the optimal sedan shape based on the HIC (lower head angular speed), see Figure 8.13 ('o' vs '+'). This suggests that the peak head angular acceleration in vehicle impacts is the result of the combined effect of the head kinematics and loading boundary condition (contact force, neck force, etc.). Figure 8.14 compares the predicted HIC and GAMBIT (from contacts with the vehicle body) as a function of pedestrian size and impact speed for both optimal sedan front models shown in Figure 8.10 (a). Generally, the optimal sedan shape based on the minimum GAMBIT poses a higher HIC and a lower GAMBIT to pedestrians than the optimal sedan minimizing the HIC ('o' vs '+' in Figure 8.14). These differences are from the combined effects of head linear and angular impact speed, contact stiffness and head loading boundary conditions (neck force, torso and lower body motion, impact angle, etc.), however these are too complex for current understanding. The effects of bonnet leading edge height and bonnet shape on the predicted GAMBIT value also

explain the obvious differences in the 'good' and 'poor' sedan shapes observed from the optimization using the GAMBIT as the head injury criterion. Nevertheless, the results imply that the optimal/'good' sedan front shapes are highly dependent on the head injury criterion used in the optimization framework.

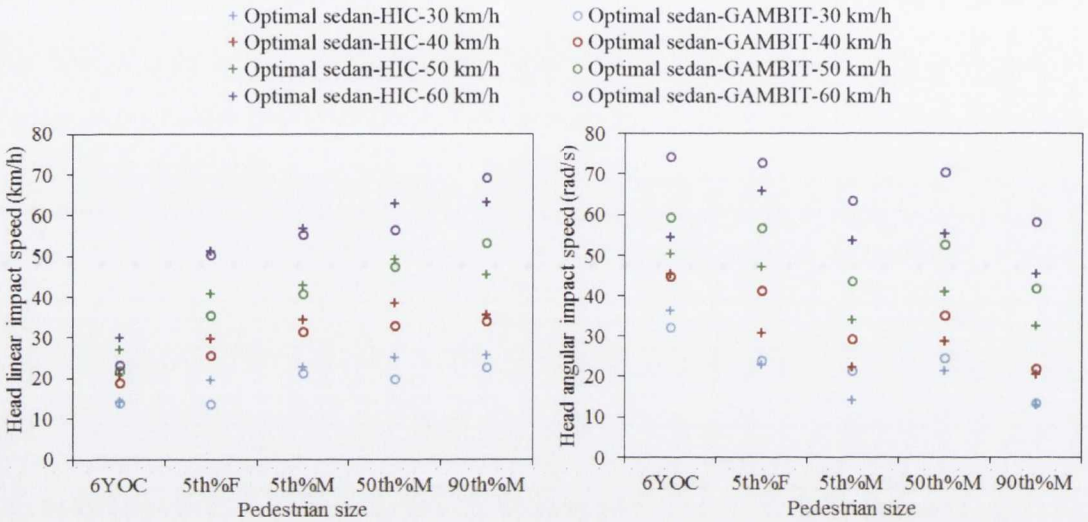

Figure 8.12 Head resultant linear speed curves (a) and head angular speed curves (b) for the optimal sedan fronts predicted based on the HIC and GAMBIT.

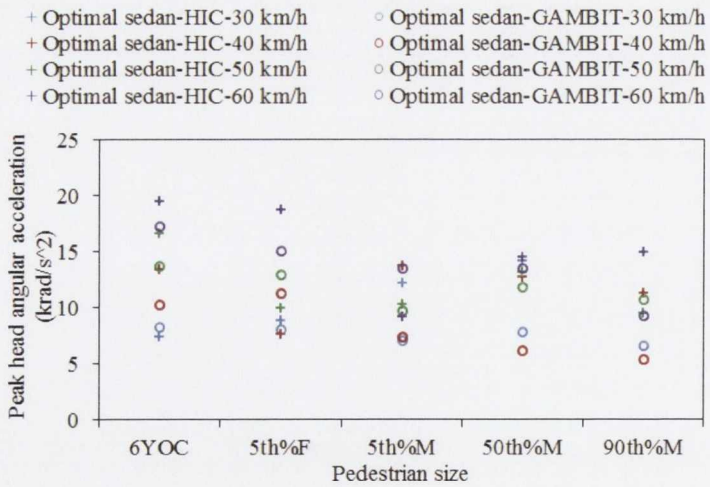

Figure 8.13 Peak head angular acceleration observed from the impacts with the optimal sedan fronts predicted based on the HIC and GAMBIT.

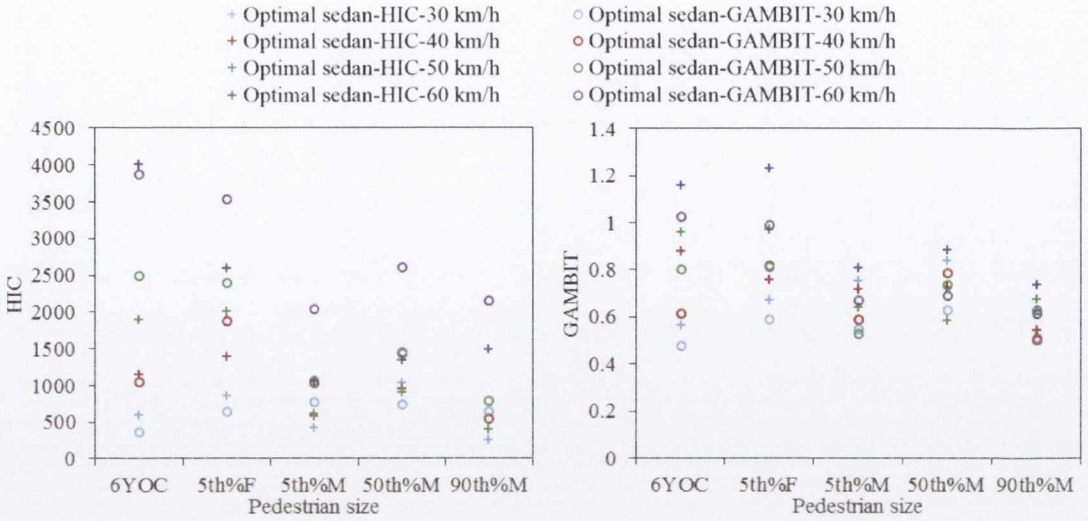

Figure 8.14 HIC (a) and GAMBIT (b) values observed from the impacts with the optimal sedan fronts predicted based on the HIC and GAMBIT.

To find further evidence to evaluate the predictions from the sedan front shape optimization based on the GAMBIT, the sedans meeting the 'good' shapes predicted by the GAMBIT were also extracted from the GIDAS accident data, see Figure 8.15 (a). These sedans were selected to keep a similar bonnet leading edge and bonnet design to the 'good' shapes in the GAMBIT prediction, since no real sedan in the GIDAS data matches both the bonnet leading edge and bonnet design and also has a similar bumper. The sedans (extracted from the GIDAS data in Chapter 7, see Figure 7.27 (a)) meeting the 'good' shapes predicted based on the HIC were also plotted in Figure 8.15 to show the difference. Then the injury costs were calculated for each accident case in GIDAS involved with the vehicles meeting the 'good' shapes based on the GAMBIT (in total 8 cases were observed). Figure 8.15 (b) compares the calculated average injury cost data between the sedans similar to the 'good' shapes from predictions based on the GAMBIT and HIC, which is also based on the condition that there is no statistically significant difference in pedestrian age (p=0.671) and impact speed (p=0.242) between these two groups when the Mann-Whitney U test was employed (data is not normally distributed). Clearly, the sedans similar to the 'good' shape predictions based on the GAMBIT have a higher average injury cost than those similar to the 'good' shape predictions from the HIC for all body regions. The higher average injury in the lower extremity for the sedans in the GAMBIT prediction

group is due to the higher bumper lower edge and the larger offset in the bumper lower structure. The sedans meeting the 'good' shapes of the GAMBIT prediction (higher bonnet leading edge and longer bonnet) have a higher average injury risk for the head, thorax and pelvis than those similar to the 'good' shapes of the HIC prediction. These findings suggest that the HIC is more reliable than the GAMBIT in the prediction of head injuries in vehicle collisions, even though these results were observed from small samples.

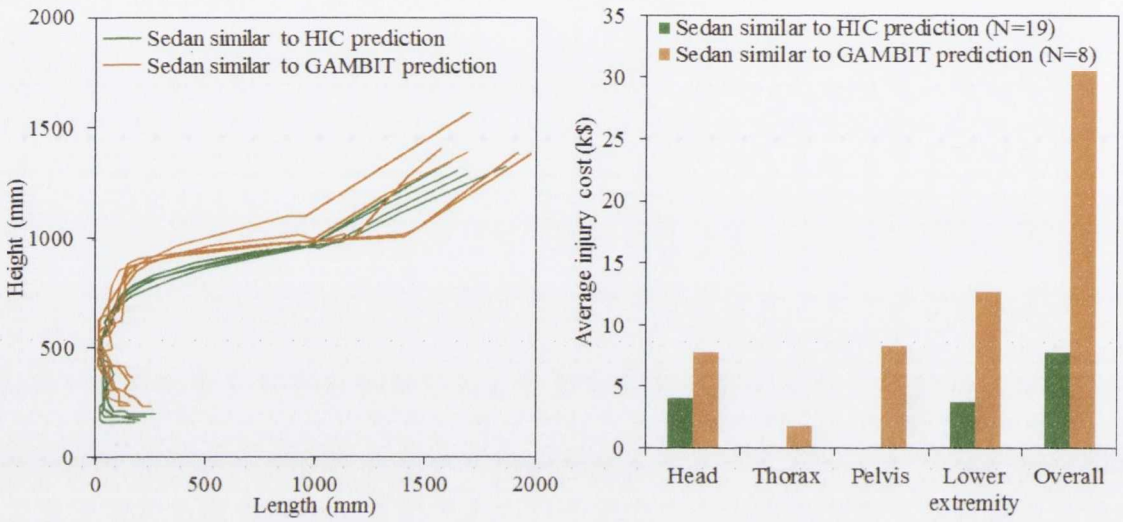

(a) (b)

Figure 8.15 Profiles of the sedans meeting the 'good' shapes predicted by the HIC and GAMBIT in the GIDAS data (a) and the average injury costs calculated from the cases involved these sedans (b).

8.5 Summary

Sensitivity studies were conducted in this chapter to investigate the effects of the injury weighting system and the choice of a head injury criterion used in the fitness function on the output of the sedan front shape optimization for pedestrian protection. In the sensitivity studies the risk of permanent medical impairment (RPMI) was employed for weighting predicted injuries instead of the injury cost, and the GAMBIT was used as the head injury criterion instead of the HIC, respectively. The results show that the safe sedan front shapes predicted using the weighted RPMI (WRPMI) are similar to those observed from the original optimization based on the weighted injury cost (WIC). But the safe sedan shapes predicted by the optimization using the GAMBIT have a higher bonnet leading edge and longer bonnet than

those predicted based on the HIC. The results again indicate that the needs of a sedan front for head and lower extremity protection are not strongly conflicting. These findings imply that the safe sedan front shapes predicted by the optimization framework are affected by the injury criteria employed, but which may not be influenced by the injury weight factor when the same injury criteria were used and a generally similar distribution of the weighted injuries as a function of body region is predicted. The findings of the current study also suggest that the GAMBIT is not a good choice for measuring head injuries in vehicle-to-pedestrian multi-body simulations.

Chapter 9 General Discussion

As the main group of vulnerable road users, pedestrians have a high risk of suffering serious injuries in vehicle collisions. Accident data from different countries and regions (Section 2.1) shows that there is still a need for safer vehicle designs to reduce pedestrian injury risk in road traffic accidents, even though much progress has been achieved for pedestrian protection. Both active and passive pedestrian protection approaches can help reducing pedestrian injury risk in road traffic accidents. Reducing the stiffness of the vehicle front structures and improving the vehicle front shape are the main methods used in passive pedestrian protection field (Simms and Wood, 2009). The effectiveness of reducing stiffness for pedestrian protection is generally understood and some local optimizations of vehicle front shape have been done for reducing pedestrian injury risk, such as adding the lower bumper structure (secondary bumper) to protect the lower extremity and using a rounded bonnet leading edge to reduce pelvis injury risk. However the global effects of the whole vehicle front shape on the overall pedestrian injury risk are still not clear, especially when considering a broad range of impact speeds, pedestrian population and initial positions. Thus an optimized vehicle front shape for pedestrian protection on a population level remains an elusive goal.

As discussed in Section 2.3.2, the current assessment systems for passive pedestrian protection performance of vehicle design only consider limited impact configurations using isolated impactors to represent the corresponding pedestrian body regions. It is reasonable to only use simplified subsystem tests in physical evaluation systems due to the high cost and low possibility of setting a broad range of impact configurations and using whole body pedestrian dummies in these tests. However, several studies have reported the shortcomings of using these subsystem test approaches for assessing vehicle front designs (Matsui et al., 2002; Matsui, 2004; Chalandon et al., 2007) compared to tests using a representation of the whole pedestrian body. Moreover, the broad variety of impact configurations which occur in real world accidents, but are not considered in the current subsystem tests, have a significant influence on the pedestrian injury outcome (Chapter 4; Untaroiu et al., 2009; Elliott et al. 2012b; Peng et al. 2012a). Finally, injuries from ground contacts are not considered in current vehicle pedestrian

safety performance evaluations and these account for a substantial proportion of pedestrian head injuries (Otte and Pohleman, 2001; Mizuno and Ishikawa, 2003) and are affected by the vehicle front shape and impact speed (Roudsari et al., 2005; Simms and Wood, 2006a and 2006b; Simms et al., 2011; Crocetta et al., 2015). Therefore a safe vehicle front shape for pedestrian protection should be designed based on tests using a whole pedestrian body and considering a broad range of impact configurations and ground contacts. However, none of the previous studies on the optimization of vehicle front shape for pedestrian protection has adequately considered these factors (Section 2.5, Chapter 2). Therefore, the aim of this thesis was to develop a valid and efficient optimization framework of vehicle front shape for pedestrian protection considering the above important factors. Given the difficulties in setting physical tests at a large-scale level, numerical simulation is probably the best approach to achieve this. Accordingly, several sub-studies were conducted in the current thesis to build and evaluate a valid and efficient optimization framework of vehicle front shape for pedestrian protection considering the broad range of pedestrian impact configurations and ground contacts. The following discussion will focus on the findings from each sub-study of the current thesis and how they connect to each other and to the published literature.

9.1 Effects of vehicle front shape on pedestrian injury risk

An analysis of the effects of vehicle front shape on pedestrian injury risk in accidents yields a basic understanding of what is needed for pedestrian protection and provides real world evidence for the evaluation of optimization outputs. A lot of studies have focused on this topic, however most were at the general level and based on accident data which is more than 15 years old (Section 3.1, Chapter 3). Therefore, a statistical analysis was conducted in Chapter 3 to investigate the detailed relationships between sedan (accounting for about 90% of pedestrian accidents in GIDAS data) front shape and pedestrian injury risk based on up-to-date pedestrian accident data (collected after 2000 by the GIDAS database) and logistic regression approaches. However the accident data simply provide the outcome of the accidents in terms of injuries and cannot in themselves provide biomechanical explanations. Accordingly, the multi-body simulations at the population level presented in the current thesis help to understand the effects

of vehicle front shape on pedestrian injury risk.

The accident data analysis results show that the AIS2+ lower extremity injury odds increase by 7% (CI: 1%-13%) and 6% (CI: 2%-10%) with every 1 cm increase in the bumper lower height (BLH, range 18-49 cm) and bumper lower depth (BLD, range 0-20 cm) respectively, when controlling for speed, age and the bumper upper height (BUH), see Table 3.7 and 3.8. The logistic regression results also show that every 1 cm increase in BUH (range 38-68 cm) results respectively in a 7% (CI: 1%-9%) or 7% (CI: 1%-14%) decrease in AIS2+ lower extremity injury odds when the BLD or BLH is fixed (also controlling the impact speed and pedestrian age). The multi-body simulations show that a low BLH and small BLD can significantly reduce lower extremity bending (Figure 7.24, Chapter 7) which is the key mechanism for pedestrian lower extremity injuries (Kerrigan et al., 2003a; Yang, 2005; Schmitt et al., 2010). The multi-body simulations in Chapter 7 also indicate that lower extremity injury risk decreases with increasing bumper upper height (BUH). Detailed analysis of the kinematics shows that a high BUH can help to reduce the upper lower extremity bending by relieving the loading from the inertia force of the upper body mass, see Figure 9.1. The statistical study also indicates that the pelvis/femur AIS2+ injury odds increase by 74% (CI: 16%-136%) with every 10% increase in the normalized bonnet leading edge height (NBLEH, range 62-102%), where the normalisation is with respect to the pedestrian hip joint. AIS2+ pelvis and lower extremity injury risk significantly increase with increasing impact speed and pedestrian age. This trend has also been observed in the sensitivity studies in Chapter 7 at the population level. This is mainly because the low bonnet leading edge can relieve direct pelvis impact (Figure 9.1) and hence reduce the pelvis contact force on the vehicle front.

The estimated trends for the effects of bumper lower shape (BLH and BLD) and bonnet leading edge height on the lower extremity and pelvis injury risk in the current study are generally in line with the findings reported in previous studies based on PCDS accident data (Matsui, 1999; Zhang et al., 2008; Pal et al., 2015) and multi-body simulations (Chapter 7; Pritz and Pereira, 1983; Liu et al., 2002). However, in the current study the quantified relationships between the sedan front shape and pedestrian injury odds are firstly observed from up-to-date accident data (Chapter 3). Secondly, this is the first time for the accident data and numerical simulations to

imply the benefits of a higher sedan bumper upper height for pedestrian lower extremity injury prevention.

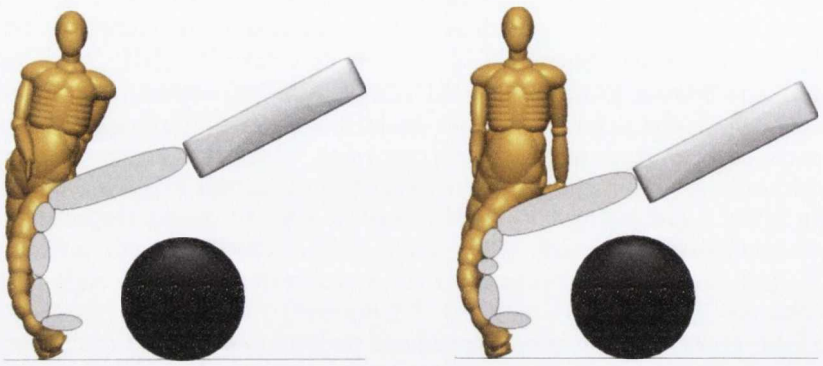

(a) (b)

Figure 9.1 Pedestrian kinematics when struck by the sedans with a high BUH/BLEH (a) and a lower BUH/BLEH (b).

According to the results in Chapter 3, no statistically significant effect was observed for the sedan front shape parameters and pedestrian age on the AIS3+ thorax and head injury odds. This is largely due to the complexity of upper body kinematics, especially for the head where a lot of factors (such as the sliding of the pelvis on the bonnet, the arm response, initial orientation, etc.) can affect its kinematics (Pass et al., 2015). The highly complex effects of the sedan bonnet leading edge height and bonnet angle on the overall head and thorax injury risk predicted in the multi-body simulations at the population level also suggest an uncertain relationship between the sedan bonnet leading edge/bonnet shape and pedestrian upper body injuries (Figure 7.18 and 7.19, Chapter 7). For the bonnet length, a short bonnet is suggested by multi-body simulations for head protection, but bonnet length is not significant for AIS3+ head injury odds in accidents under analysis of logistic regression. One reason for this difference might be that the effect of bonnet length is not linear (Figure 7.19, Chapter 7), and then logistic regression cannot detect this effect, but simulations can clearly show this complex trend and suggest a short bonnet for pedestrian protection. This difference between multi-body modelling and accident data might be also due to the fact that in real world accidents the stiffness varies from individual vehicles, while only one stiffness distribution is defined in the vehicle front model used in this work. Thus different stiffness distributions may affect the findings observed from

multi-body simulations in this work.

For windscreen angle, the multi-body simulation results in Chapter 7 show that reducing the sedan windscreen angle has a generally linear effect on decreasing the head weighted injury cost and a previous study (Lyons and Simms, 2012) shows that the sedan windscreen also has a linear effect on peak head linear and angular acceleration, even though the trends of the windscreen angle effect predicted from the current work and the previous study (Lyons and Simms, 2012) are not consistent due to the differences in the definition of the simulation (only the case of 50th% male struck at 40 km/h was considered in their study) and the head injury criteria (HIC vs peak head linear and angular acceleration) employed. These differences between multi-body simulations and accident data might be due to the limitations of multi-body simulations (reaction of the upper limbs, pedestrian impact angle, etc.) and the small size of the accident sample (N=90 with only 11 cases having AIS3+ injuries) for the windscreen angle effects. Thus further accident data collection is required to understand the effects of the windscreen angle on pedestrian head injuries and the choice of a head injury criterion is important for studying this issue.

Surprisingly, impact speed is not a significant predictor for head AIS3+ head injury risk when the head impact location is limited at the centre of the windscreen The significant influence of impact speed on AIS3+ head injury risk is widely recognized in previous studies (Zhang et al. 2008; Kong and Yang, 2010; Nie et al., 2015) and Chapter 3 based on the accident data without a clear inclusion criterion for the head contact location. This suggests that the insignificant effects of impact speed on head injury risk observed in Chapter 3 (head contact location was fixed in the windscreen centre) might be because the head injury risk from contacts with the windscreen centre is not as sensitive to the impact speed or some unclear reasons beyond current understanding (such as the motion of the whole body, neck reaction force, etc.). Further detailed analysis is needed to understand this.

Unfortunately, there are not enough accident cases to analyse the effects of SUV and van shape on pedestrian injury risk. Multi-body simulations at the population level suggest that the overall pedestrian head injury risk for the SUV bonnet leading edge heights around 1,100 mm are

generally lower than the cases for a lower or higher bonnet leading edge (Figure 7.28, Chapter 7). The effects of the van bonnet leading edge height on the overall pedestrian head injury risk are not straightforward (Figure 7.34, Chapter 7). However it is difficult to analyse all the underlying reasons for these effects since a number of pedestrian models and impact speeds were used.

The overall thorax and pelvis injury risk increases with increasing SUV bonnet leading edge height (Figure 7.28, Chapter 7), since a contact closer to these body regions generally leads to a higher load acting on them. This trend of the overall thorax injury risk was also found in the van case (Figure 7.34, Chapter 7). But a van bonnet leading edge height at the middle range (800-1,000 mm) of its limits (750-1,150 mm) is poor for the overall pelvis injury risk (Figure 7.34, Chapter 7). This might be due the effects from the weighting factor for the pedestrian population, but the detailed reasons for this are still not sure and further analysis is needed. The simulation results for both SUV and vans indicate that a flat (small BLD) and wide (vertical direction, low BLH and high BUH) bumper is beneficial for reducing the overall lower extremity injury risk by reducing lower extremity bending. The overall pedestrian head injury risk increases with increasing the bonnet angle of the SUV and van. This effect of the bonnet angle on the overall head injury risk (as measured by the HIC) in the SUV and van cases is in line with that from the windscreen angle in the sedan cases. However the underlying mechanisms are too complex for current understanding since different pedestrian models (heights), impact speeds and gait stances were considered in the simulation test sample and the effects of the bonnet and windscreen angle on the head kinematics and loading boundary conditions (contact reaction force, neck force, etc.) could vary from the initial impact definitions. Further studies are needed to understand these.

In the analysis of accident data, the stiffness of sedan structures has not been considered in this study due to the lack of data, and this is clearly an important influence on pedestrian injuries (Liu et al., 2002; Simms and Wood, 2009). The influence of sex on injury outcome was not considered due to the limited sample sizes available, but this is not a significant factor for pedestrian injury risk as observed in PCDS accident data (Zhang et al., 2008). The effects of

pedestrian initial gait position were not considered as these are uncoded, but gait stance does affect lower extremity injury risk (Chapter 4) and head injuries (Peng et al, 2012). Nevertheless, the effects of the sedan bumper and bonnet leading edge on the lower extremity and pelvis injury risk observed from the current analysis of accident data are in line with biomechanical analysis (Chapter 3 and Chapter 4) and numerical modelling (Chapter 7). The effects of vehicle front shape on pedestrian injury risk predicted from the multi-body simulations in the current work were for the first time observed at the population level. The multi-body simulations also indicate that the needs of vehicle front shape for one body region protection could be conflicting with the demands for another body region protection (such as lower extremity/head vs pelvis/thorax for the bonnet leading edge height). Thus a consideration of the importance of injuries between different body regions and the overall effect of the whole vehicle front shape will improve the reliability of the optimization of vehicle front shape.

9.2 Pedestrian gait stance study

The effects of pedestrian gait stance on lower extremity kinematics and injuries have not been analysed in previous studies and it is not practical to study this issue from real world accident data. Therefore, both finite element (FE) and multi-body simulations using 50^{th}% male models in different gait stances and sedan and SUV front models were conducted to understand this issue. Both FE and multi-body modelling results indicate that knee flexion can reduce lower extremity bending response and injuries. Particularly, the gait stances with the ipsilateral knee more flexed have a significantly lower lateral knee bending angle than other stances where the ipsilateral knee is straighter for both sedan and SUV impacts (Figure 4.7 and 4.16, Chapter 4). This trend is also observed in the predicted long bone (tibia and femur) von-Mises stress in the FE simulations and the bending moment of the leg and thigh predicted in the multi-body simulations (Figure 4.7 and 4.16, Chapter 4). These effects from knee flexion are due to the fact that the change in knee flexion/extension angle and the change in tibia internal/external rotation angle during the impact increase with increasing initial knee flexion angle (Figure 4.10, Chapter 4). These findings indicate that the internal/external rotation of the tibia during impact has a protective effect on knee injuries, which has also been observed in previous studies based on FE

simulations using a single gait stance (Masson et al., 2005; Mo et al., 2014). Moreover, knee flexion can also raise the centre of gravity of the leg, thus reducing the bending moment in the lower extremity, which is due to the inertia force from the part of the lower extremity which is lower than the bumper. The effects of knee flexion on lower extremity injury outcome predicted from the simulations are similar to those observed from four recent post-mortem human subjects (PMHS) tests considering two knee flexion angles (0° and 20°), where an initial flexion of the knee was associated with a reduced severity of knee ligament injuries (Petit et al., 2014).

This trend of gait stance on lower extremity injury risk has also been observed in the multi-body simulations where a broad range of pedestrian models (different heights) and impact speeds were considered (Figure 5.11, Chapter 5). These simulation results may imply that the FE and multi-body pedestrian models used in the current study are generally valid to model the passive response of the human knee joint in vehicle-to-pedestrian collisions in terms of the effects of knee flexion on its freedom of motion. The FE simulation results also show that the overlap between the legs of the pedestrian may influence the lower extremity injury risk due to the reaction force from leg to leg self-contact. This is the first time the effects of pedestrian gait stance on lower extremity kinematics and injuries using a broad range of gait stances and different vehicle fronts have been assessed. The findings of this gait stance study suggest that the straight lower extremity impactor used in the subsystem tests is perhaps a good choice since this captures the worst case in the gait stance, even though it does not reflect the effects of pedestrian gait stance on lower extremity kinematics and injuries.

9.3 Virtual test system (VTS)

The literature review (Chapter 2) and Chapter 4 suggest that the initial impact boundary conditions and ground contacts have a significant influence on pedestrian injury outcome. However, the broad range of pedestrian impact configurations and their distributions in accidents and the injuries from ground contacts are not considered by the existing assessment approaches for pedestrian protection performance of a vehicle front design, which usually uses a single impact speed of 30-40 km/h (EEVC, 2002; J-NCAP, 2011; C-NCAP, 2015). To develop a test method which can account for the

above factors, a virtual test system (VTS) was proposed in Chapter 5 based on accident data from the GIDAS and PCDS databases combined with multi-body simulations. This study was conducted to select a simulation set which can generally predict injury distributions in pedestrian accidents and keep the computational time at a reasonable level for optimization of vehicle front shape.

In the proposed VTS a simulation test sample (STS) considering a broad range of impact configurations which are formed using different impact speeds, pedestrian heights and pedestrian gait stances was firstly defined based on multi-body simulations. The STS can be created with any number of impact configurations according to the number of impact speeds, pedestrian heights and pedestrian gait stances considered. The simulations in the STS were defined to capture injuries from ground contacts for impacts at a speed lower than 40 km/h. The HIC, TTI, pelvis impact force, lower extremity (thigh and leg) lateral bending moment and knee lateral bonding angle were employed to assess the AIS level of injuries from the pedestrian head, thorax, pelvis and lower extremity respectively, and the number of AIS2+ injuries was calculated for each impact in the STS. Then an injury weighting system was defined to use the occurrence frequency of each impact configuration considered in the STS for weighting the AIS2+ injury number predicted from this impact configuration, see Eq. (5.1-5.3). This VTS can then be applied to assess the threat of a vehicle front design to pedestrians by using the weighted AIS2+ injury number (WIN) as the evaluation index.

Then three vehicle front models (sedan, SUV and van, which are the main vehicle types involved in pedestrian accidents) were tested via the VTSs with different STS sizes and the predicted WIN for each vehicle front model was then weighted further by the involving frequency of them in PCDS and GIDAS accidents and the sum of the further weighted WIN for these three vehicle types (for a given STS size) was named as the combined injury number (CIN), see Eq. (5.4-5.5).

The comparisons of the distributions of AIS2+ injuries as a function of body region, impact speed and vehicle type and average AIS2+ injury number between the predictions of the VTSs and the GIDAS data show good matches when a reasonable STS size ($\geq$60 impact configurations with $\geq$ 6 impact speeds) is applied. The relative differences in the AIS2+ injury distributions and average AIS2+ injury number between the predictions of the VTSs and the GIDAS data increase sharply when decreasing the STS size below 60 (Figures 5.12 and 5.13, Chapter 5). The number of groups

for all impact parameters (impact speed, pedestrian height and gait stance) considered in the STS has a significant influence on the injury predictive capability of the VTS since these parameters are all important factors for the pedestrian injury outcome in vehicle collisions. The results also show that the computational time increases linearly with increasing the STS size. Considering the absolute effects of these parameters on pedestrian injuries and the difference between discrete groups of each parameter, it is suggested to use more groups of impact speed (an interval bigger than 10 km/h may lead to a large different in the injury outcome) and pedestrian height (important for the head contact location and selection of a safe vehicle shape in the optimization) but less gait stances (most gait stances are similar to each other) in the simulation sample when controlling the STS size for the vehicle front shape optimization.

A STS with 60 impact configurations (6 impact speeds, 5 pedestrian heights and 2 gait stances) was then selected for vehicle front shape optimization for pedestrian protection based on its representativeness of pedestrian impact configurations, predictive capability with respect to injury distributions and consumption of computational time. The predictive capability of this STS was further evaluated using the PCDS data and the results show good matches (Figure 5.15, Chapter 5). In this study the STS was also found to be capable of distinguishing the aggressivity of different vehicle front types in accidents.

Although the modelling presented in Chapter 5 is substantially more representative of the range of real-world pedestrian collisions than has previously been considered, pedestrian accidents are complex events and there remain a number of significant assumptions and limitations. The simulation condition was defined as a purely lateral impact which does not fully match the real world cases and may affect the predicted injures (Chen et al., 2015). The contact functions were developed to generate reasonable contact forces in the pedestrian/vehicle interaction. However, detailed interactions and differences in stiffness between vehicle types have not been considered as they are not known. Only one vehicle model was used to represent the range of shapes within a vehicle type and variation in the structure away from the vehicle centreline was not included in the modelling. Nonetheless, this injury assessment approach can generally reflect the situation in accidents in terms of AIS2+ injury distribution and average AIS2+ injury rate. A simplified pedestrian/ground contact

characteristic was used and pedestrian ground contact injuries for vehicle impact speeds >40 km/h were not accounted for since at these speeds the injuries from vehicle contacts more serious than those from ground contacts (Ashton and Mackay, 1983; Guillaume et al., 2015). Moreover, the different sized pedestrian models were obtained by scaling the 50th% male model and have not been explicitly validated and the multi-body pedestrian models used here have some challenges with regard to both biofidelity and architecture (Kerrigan et al., 2009b). Only one injury was accounted for in each body part of the pedestrian models in the VTS and multi-injury conditions of bone fractures accompanied by damage to the internal organs cannot be predicted by the multi-body pedestrian model, and the effects of sex, age and weight on anthropometry and injury thresholds have not been considered in detail. All of these factors will influence the predictions of the VTS, but more considerations in the simulations will also require more information than is currently available and also lead to more challenges in the computational time.

The above discussion indicates that the good matches between the predictions of VTS and accident data are based on the combination of using reasonable injury criteria and thresholds, vehicle front shape and stiffness, as well as the injury weighting approach, accepting the basic capability of MADYMO pedestrian models for prediction pedestrian injury biomechanics. Nevertheless, the similar trend of the lower extremity injury risk as a function of pedestrian gait stance in the multi-body and FE simulations, the general matches between the injury predictions of the multi-body simulations and the GIDAS and PCDS data (Chapter 5) and the predicted sensitivity of the pedestrian injury risk to the change of vehicle front design (Chapter 7) imply that the multi-body pedestrian models used in the current work are acceptable for the purpose of the current work on the optimization of vehicle front shape at the macro level.

9.4 Optimization framework and its applications

9.4.1 Optimization framework

An optimization framework of vehicle front shape for pedestrian protection has been developed in Chapter 6, based on the approaches proposed in the virtual test system (VTS). The 60 impact configurations proposed in the VTS, which are formed by 6 impact speeds (20-70 km/h with an

interval of 10 km/h), 5 pedestrian heights (117 cm, 153 cm, 165 cm, 174 cm and 185 cm) and 2 gait stances (ipsilateral lower extremity forward and backward) (Table 6.1 and Figure 6.1, Chapter 6), were used as the inputs for the simulations in the optimization framework. Then a geometric dimension chain (crossing the centre of the six ellipsoids which form the vehicle centre-line profile of the lower bumper, bumper, bonnet leading edge, bonnet and windscreen, see Figure 6.2, Chapter 6) was developed as a string of numerical parameters to describe the centre-line geometry of the vehicle front. Nine parameters (Figure 6.2, Chapter 6), which can be modified by MATLAB code and input to the MADYMO simulation, were defined to control the overall vehicle front shape. The geometric dimension chain is novel and its controlling parameters allow new shapes to be generated automatically in the optimization process and this geometric dimension chain can also keep a continuous vehicle shape without any gaps between each ellipsoid during the optimization. Then 60 simulations (using the 60 impact configurations) can be defined and conducted for a given vehicle front shape in the optimization.

For each impact simulation in the simulation test sample (for a given vehicle front model) injuries predicted for the head, thorax, pelvis and lower extremity can be classified into corresponding AIS levels based on the injury criteria for each body region derived from the literature (Table 6.2, Chapter 6). To assess the aggressivity of a vehicle front to pedestrians, each predicted injury was first weighted using an injury cost system which includes the medical and auxiliary cost calculated based on AIS levels of injuries to the body regions. Then the sum of the injury costs for a given simulation in the simulation test sample (for a given vehicle front model) was weighted further by the frequency of occurrence of this impact configuration in the GIDAS data and the sum of the weighted injury costs (named as WIC) for all 60 impact simulations for a given vehicle front model was calculated as the objective function of the optimization. Thus the WIC score is the weighted average cost of all injuries (head, thorax, pelvis and lower limbs) recorded per impact configuration in the simulation test sample and can be used as a metric to distinguish the aggressivity of different vehicle front shapes when the broad range of impact configurations in accidents and overall pedestrian injuries (also ground contacts at impact speeds lower than 40 km/h) are considered. The approaches proposed and

validated in the virtual test system (Chapter 5) and the good matches in the injury cost distributions as a function of body region between the WIC and GIDAS accident data (Figure 7.17, Chapter 7) proved the reliability of using the WIC as the objective of the global vehicle front shape optimization for pedestrian protection.

Based on the WIC (objective) and nine parameters in the geometric dimension chain (design variables and constraints) a genetic algorithm (GA) defined in the MATLAB Global Optimization Toolbox was employed to search the optimal vehicle front shape(s) within a design space (the lower and upper boundaries of the design variables). The optimization framework defined in the current thesis is a system implementing the impact configurations and vehicle front models (shapes) in multi-body simulations, and then processing injury predictions to calculate the WIC, and analysing the effects of the vehicle front shape on the WIC and searching and outputting the optimal vehicle front shapes for minimizing the WIC. This optimization framework could also be modified at each part, such as using a different simulation test sample, injury prediction and weighting system, vehicle modelling approach, optimization algorithm and so on. Sensitivity studies were conducted in Chapter 8 to investigate the effects of some of the changes in the optimization framework on its predictions (discussed later).

In summary, the current optimization framework is the first to consider a number of impact speeds and their proportions and ground contacts for the evaluation of pedestrian safety performance of a vehicle front design in the optimization of vehicle front shape, compared to the previous studies on the same topic (Carter et al., 2005; Subramanian et al., 2012 and 2016; Kausalyah et al. 2014 and 2015). Furthermore, it is also the first to use a continuous geometric dimension chain to generate and control the vehicle front shape, which is reliable to ensure a multi-body vehicle front model without any gaps between the ellipsoids for avoiding invalid contacts between the pedestrian model body segments and vehicle structures which occurred in a previous study on vehicle front shape optimization (Subramanian et al., 2016).

9.4.2 Applications of the optimization framework

In Chapter 7 the optimization framework was applied for find the optimal vehicle front shapes for pedestrian protection for the sedan, SUV and van vehicle types respectively, since these have practical applications on the real world. Firstly, design spaces were defined for these three vehicle types based on shape corridor data extracted from real world accidents from different countries. These design spaces were employed in the genetic algorithm (GA) to control the vehicle shapes that generally correspond to the three vehicles types. Then a preliminary study was conducted to find a reasonable crossover fraction for the genetic algorithm (GA) used in the optimization framework and a reasonable stopping criterion (maximum generation number) for each optimization, based on a simplified simulation test sample. This preliminary study indicated that the GA yielded the best outputs when a crossover fraction of 0.8 was defined and the optimizations for the front shape of the sedan, SUV and van showed good convergence after 14, 10 and 12 generations, respectively. To ensure a valid output, a crossover fraction of 0.8 and a stopping criterion of 15 (sedan), 11 (SUV) and 13 (van) were defined. Then optimizations were conducted for the sedan, SUV and van front shapes applying the optimization framework and the above definitions for the GA, with the purpose of reducing the overall pedestrian injury risk.

9.4.2.1 Feasibility of the optimization framework

The optimization results show that all vehicle types (sedan, SUV and van) had a good convergence and the framework can clearly distinguish the 'good' (design points leading to a WIC in the lowest quarter of the WIC range) and 'poor' (design points leading to a WIC in the highest quarter of the WIC range) shapes for each vehicle type. The application of the optimization framework can strongly reduce the threat of the vehicle front design for pedestrians, and the median WIC decreased by more than 50% for all vehicle types from the 'poor' group to the 'good' group. Detailed analysis of the predicted WIC for different body regions as a function of generation number in the optimization indicates that the genetic algorithm (GA) focuses on reducing the WICs from the dominant body regions (lower

extremity and head) and generates optimal vehicle front shapes by keeping a balance between different body regions to minimize the overall WIC. This shows the importance of the distribution of injury predictions as a function of body region in the optimization of vehicle front shape for pedestrian protection. The optimization results indicate that the needs for head and lower extremity protection are not really conflicting, since both head and lower extremity WIC decrease with a higher bonnet leading edge height (within limits). The demands for thorax and pelvis protection are generally similar (low bonnet leading edge height), and thus there is a compromise between this and head/lower extremity protection. These are also in line with the results of sensitivity studies for the effects of the vehicle front shape on pedestrian injury risk. Some design parameters of the optimal vehicle fronts reached the design boundary, for example all optimizations almost selected the lowest bumper lower edge height and offset as the optimal design. However, the dimensions of the optimal bonnet leading edge, bonnet and windscreen did not reach their limits.

The good matches in the distributions of AIS2+ injuries between the prediction of the multi-body simulation test sample and accident data (GIDAS and PCDS) in Chapter 5 (Figure 5.9 and Figure 5.15) ensure the general validity of the optimization framework. Moreover, good matches were also observed in the distribution of the injury cost as a function of body regions between the optimization framework (WIC) and that calculated from GIDAS data (Figure 7.17, Chapter 7). This data also validated the injury predictive capability of the optimization framework in terms of injury distribution as a function of pedestrian body region which is crucial for the optimization of vehicle front shape for pedestrian protection. However, the predicted difference in the aggressivity between different vehicle types (sedan, SUV and van) is not distinguishable when the predicted injuries were weighted by the injury cost (Figure 7.16, Chapter 7). But this difference was remarkable when using the weighted AIS2+ injury number (WIN) as the index for vehicle front aggressivity (Figure 5.17, Chapter 5). This is mainly due to the fact that the costs for the pelvis and thorax injuries, which account for a big proportion of the AIS2+ injury number for the SUV and van impacts (Figure 5.17, Chapter 5), are generally lower than that for the lower extremity injuries (Table 6.3, Chapter 6) which is more important for the sedan case (Figure 5.17, Chapter 5), then the overall weighted injury

cost (WIC) are similar for these three vehicle types (Figure 7.16, Chapter 7).

Sensitivity studies indicate that the optimal front shape for each vehicle type predicted by the optimization framework has the lowest overall WIC when comparing to the designs where only one dimension (such as the bonnet angle or windscreen angle) was modified based on the optimal shape. This implies that the optimal shapes were at least from a local minimum, even though finding the global minimum cannot be guaranteed since this is a highly non-linear optimization and the preliminary study results indicated that the optimal vehicle front shape is affected by the crossover fraction and the value 0.8 used in the optimizations might not be absolutely the best. However further benefits from the crossover fraction are probably marginal (Figures 7.1 and 7.2, Chapter 7) and it is not practical to check further for a global minimum. In light of this, it might be reasonable to focus more on the predicted 'good' shapes rather the optimal shapes.

For all vehicle types the 'good' shapes have a lower bumper lower height, a higher bumper upper height and bonnet leading edge and a smaller offset in the lower bumper structure than the poor shapes, and all these differences between the 'good' and 'poor' shapes are statistically significant. The comparisons of the predicted WICs and pedestrian kinematics between the impacts with 'good' and 'poor' shapes show that the wide and flat bumper in the good shapes can significantly reduce pedestrian lower extremity bending and hence lower extremity injury risk, which is in line with the findings observed from accident data (Chapter 3). These comparisons also indicate that the high bonnet leading edge can help to reduce the head impact speed on the vehicle front, similar to that reported in previous studies based on multi-body modelling (Pritz and Pereira, 1983; Liu et al., 2002), FE simulations (Han et al. 2010) and dummy and cadaver tests (Kerrigan et al., 2009a; Matsui et al., 2002). This is the first time to show this trend based on a broad range of impact configurations. However the sensitivity studies for the bonnet leading edge height indicate complex effects on the overall head injury risk of a population of pedestrians and these effects vary between vehicle types. The low influence of the bonnet leading edge on head injury risk was also observed in the GIDAS accident data (Chapter 3). This implies that the use of a broad range of impact configurations

may be more successful to investigate the effects of the vehicle front shape on overall pedestrian injury risk.

For the sedan case, the 'good' shapes have a shorter bonnet than the 'poor' shapes. This short bonnet together with a high bonnet leading edge significantly increases the frequency of the head-to-windscreen contacts, reducing the head injury risk since bonnet contacts in the multi-body simulations lead to a higher HIC than windscreen contacts. It is also seen from the simulation results that the predicted head WICs for the impacts with a long bonnet sedan are generally higher than for shorter bonnet sedans (designs for the bumper, bonnet leading edge and windscreen are the same), excepting the cases which lead to head contacts with both bonnet and windscreen. This exception is due to the fact that when the head contacts with both bonnet and windscreen the reaction forces from both parts were accounted for in the modelling, resulting in an obviously higher peak head acceleration and HIC than the head contacts with only either the bonnet or the windscreen. This difference in the HIC prediction between the bonnet, windscreen and their interface is generally in line with the real situation observed from impactor tests (Mizuno et al., 2001). However, a previous analysis of the accident data captured before 1992 indicates that 'short' bonnet (>950 mm and <1,200 mm) sedans lead to a higher head injury risk than the 'long' bonnet (>1,200 mm) sedans (Otte, 1994b), which is not in line with the trend observed from the current work. This is due to the fact that the 'short' bonnets in those accident cases are in the 'poor' sedan corridor of the current work (Figure 7.7 and 7.19, Chapter 7), which lead to a high frequency of head contacts with the bonnet rear end and/or windscreen lower edge. For the SUV and van cases, there are few head to windscreen contacts and a shallow bonnet surface is beneficial for head protection for these cases as discussed before (Section 9.1). Thus a shallower bonnet was predicted for the 'good' shapes than the 'poor' shapes for the SUV and van. The above findings imply that interactive effects of stiffness and shape have a significant influence on pedestrian injury outcome. Therefore the optimization predictions observed in this work are only for the current stiffness distribution, but which could be affected by using different stiffness distributions. For example a long bonnet may be suggested by the optimization framework for pedestrian protection when a very soft bonnet is defined. Further study is needed to investigate safer vehicle front shapes under

different stiffness distributions.

For the sedan optimization, accident data shows that the sedans with a similar design as the predicted 'good' shapes have a lower threat to pedestrians in the accidents than those sedans matching the 'poor' shapes. This strongly supports the predictions of the optimization framework, though this finding was based on small samples in the accident data and the effect of stiffness was not considered. The findings observed from the application of the optimization framework in Chapter 7 were based on only one stiffness definition, one injury weighting system, one injury criterion for each body part and one design space for each vehicle type. These factors may have a significant influence on the predictions of the optimization framework. Nevertheless, the above discussion implies that it is generally feasible to apply the optimization framework defined in the current thesis for vehicle front optimization for overall pedestrian protection and the predicted 'good' vehicle front shapes are acceptable for future vehicle design for pedestrian protection.

Figure 9.2 shows the optimal vehicle front compared with the real world fleets for each vehicle type. Generally the modern fleets have a similar bumper shape to the optimal predicted sedan front, while the old model vehicles have a sharp and narrow (vertical direction) bumper. This suggests that the subsystem test for the bumper used in NCAPs has improved the bumper design for lower extremity protection. The overall shape of the optimal sedan front is between the mini-size and small-size class, the optimal SUV is at the full-size level and the optimal van front is at the upper-medium-size level. However, the pedestrian safety rating of a vehicle in the NCAPtests is only weakly shape dependant. Figure 9.3 shows an example where significantly different ratings were obtained from the Euro-NCAPtests for two very similar shaped sedans. The lower extremity protection performance is similar for these two sedans, but there are big differences in the pelvis and head protection performance between these very similar shaped sedans. This also affirms the efficiency of the subsystem test using the lower extremity impactor. But the subsystem tests for pelvis and head protection mainly focus on the stiffness rather than the shape, as it is well known that reducing vehicle front stiffness is very helpful for pedestrian head protection. However the injury risk of the pelvis is also highly dependent on

the bonnet leading edge height as observed from both accident data (Chapter 3) and numerical modelling (Chapter 7) in the current work. Moreover, the head injury risk also shows shape dependency in the multi-body simulation (Chapter 7), even though no evidence from the accident data is available. The isolated head impactors used in the subsystem tests also cannot reflect the head kinematics accumulated as a chain effect from the whole body motion and the neck force during the impact. These analyses indicate that the global shapes of the safer vehicle fronts predicted from this work are worthy for reference in future vehicle front safety design.

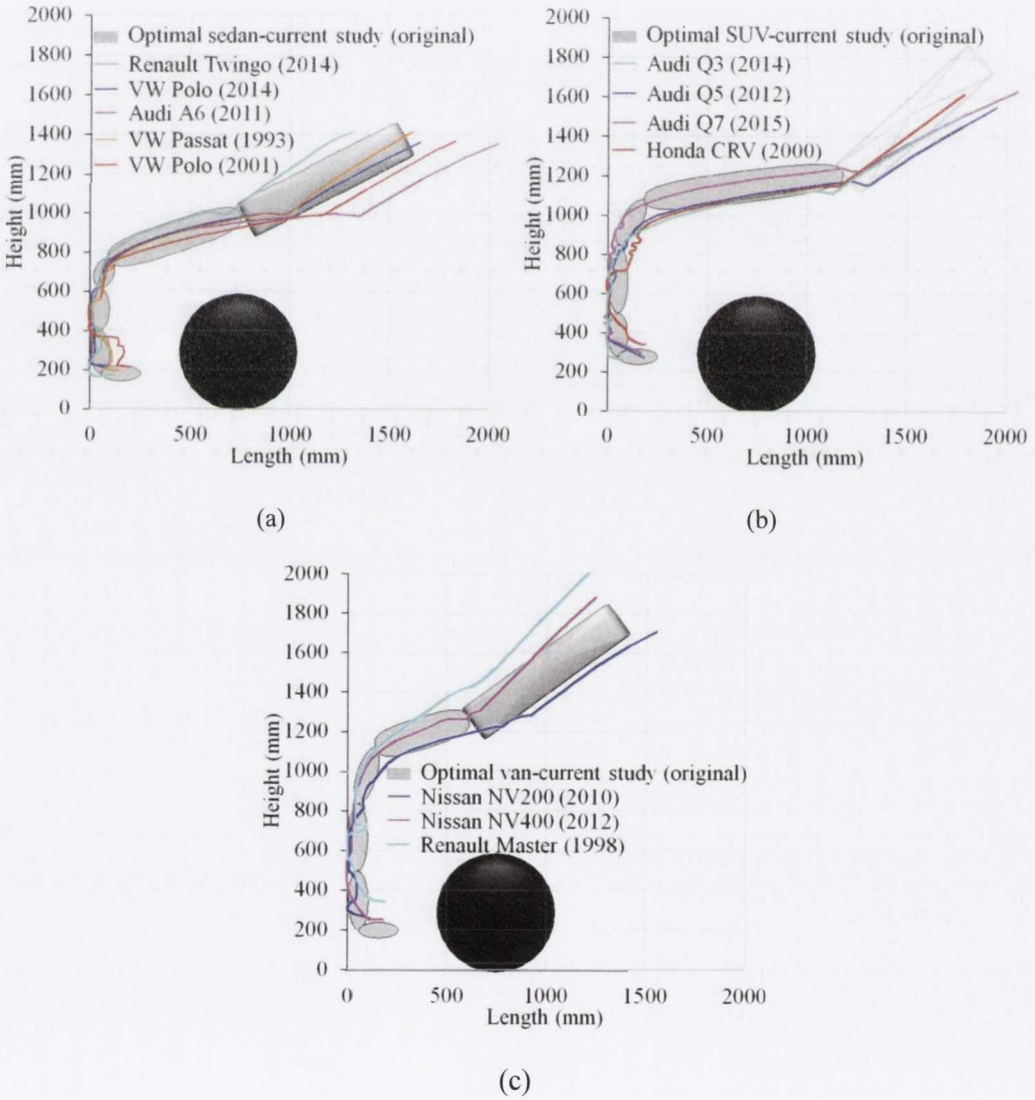

Figure 9.2 Comparisons of the optimal vehicle fronts predicted by the optimization framework and the real world vehicle fleets for the sedan (a), SUV (b) and van (c).

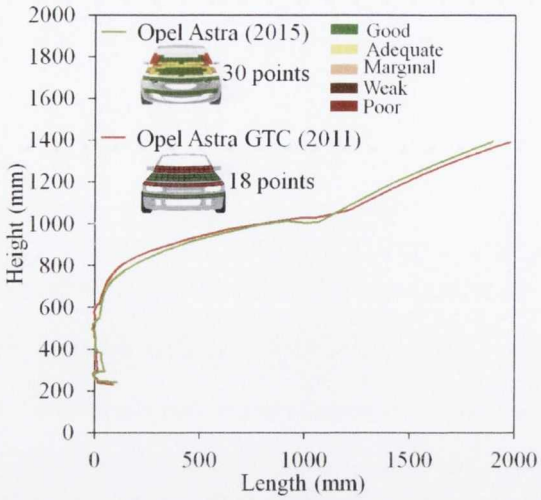

Figure 9.3 Different Euro-NCAP ratings for similar shaped sedans.

To evaluate the combined benefit from the optimal shapes of different vehicle types for pedestrian protection, the combined injury cost (CIC) was calculated by the weighted injury cost (WIC) values from different vehicle types using the proportion of each vehicle type involved in GIDAS (p_{sed}-sedan = 0.93, p_{suv}-SUV/pick-up = 0.01 and p_{van}-van = 0.06, see Figure 5.1) and PCDS (p_{sed}-sedan = 0.68, p_{suv}-SUV/pick-up = 0.18 and p_{van}-van = 0.14, see Figure 5.1) data respectively, based on the Eq. (9.1). The CICs for the optimal vehicle fronts and the vehicle front models which have been used to represent the average shape in Chapter 5 (Figure 5.7) were calculated via Eq. (9.1) and compared in Figure 9.4. The WIC data for each vehicle front in the PCDS case was calculated based on the proportions of the impact configurations involved in this database (Figure 5.15, Chapter 5).

$$CIC = WIC_{sed} * p_{sed} + WIC_{suv} * p_{suv} + WIC_{van} * p_{van}, \quad (9.1)$$

Figure 9.4 shows that the optimal vehicle front shapes significantly reduced the predicted overall combined injury cost (CIC) for both GIDAS (57%) and PCDS (43%) inputs, especially for the head (55% for the GIDAS and 40% for the PCDS) and lower extremity (80%). This indicates that implementation of the predicted optimal vehicle front shapes may bring a big societal benefit.

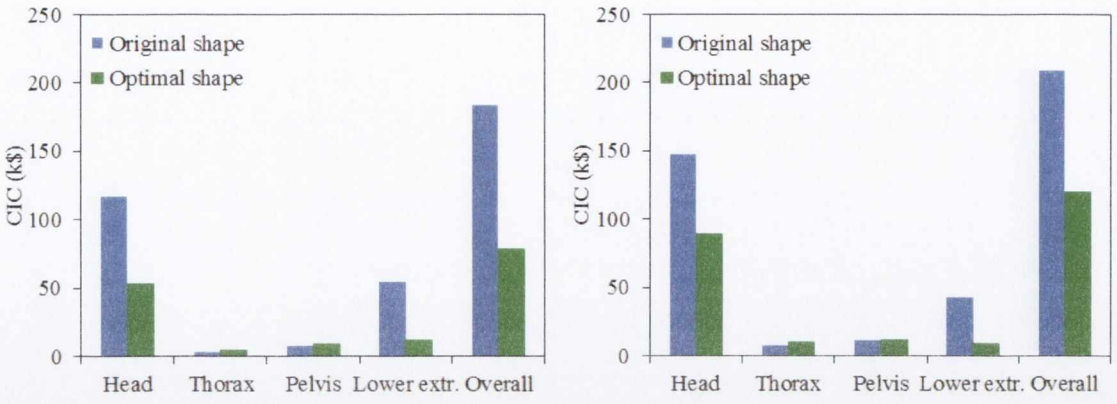

Figure 9.4 Comparisons of the predicted CIC between the original shapes and optimal shapes for the GIDAS (a) and PCDS (b) inputs.

9.4.2.2 Considerations in the optimization framework

In the optimization framework, a broad range of impact configurations and their distributions in accidents, injuries from ground contacts at low impact speeds (<40 km/h), injuries to different body regions (head, thorax, pelvis and lower extremity) and weighting of predicted injuries were considered. These factors each have their own influences on the predictions of the optimization framework.

The comparison between the impacts with 'good' and 'poor' vehicle front shapes indicates that the weight factors between the pedestrian models (heights) are important for the predictions of good and poor shape. Particularly, the difference in the predicted WIC between the 'good' and 'poor' shapes is mainly from the 5th% male (165 cm) model which represented a large proportion of individuals in accidents (a high weight is given in the WIC calculation, see Table 6.1, Chapter 6). Similarly the effects of the weight factors between the pedestrian models (heights) were observed in the sensitivity study for sedan bonnet length, where the cases with a bonnet length leading to a head contact with both bonnet and windscreen for the 5th% male (165 cm) model have a significantly higher overall WIC than other cases (Figures 7.19 and 7.20, Chapter 7). These findings imply that the consideration of a broad range of pedestrian heights and its distribution in the optimization framework has a strong influence on the predictions. However, the predicted high bonnet leading edge for safe vehicle fronts may be not

a good choice for child protection (Pritz and Pereira, 1983). This has also been observed in the current optimizations where the optimal SUV and van shapes are not the best for child protection, see Figure 9.5. Therefore the optimal vehicle front shapes for child protection might be different than the current predictions and further analysis is needed for this. However the optimal vehicle front shapes are not particularly poor for child protection.

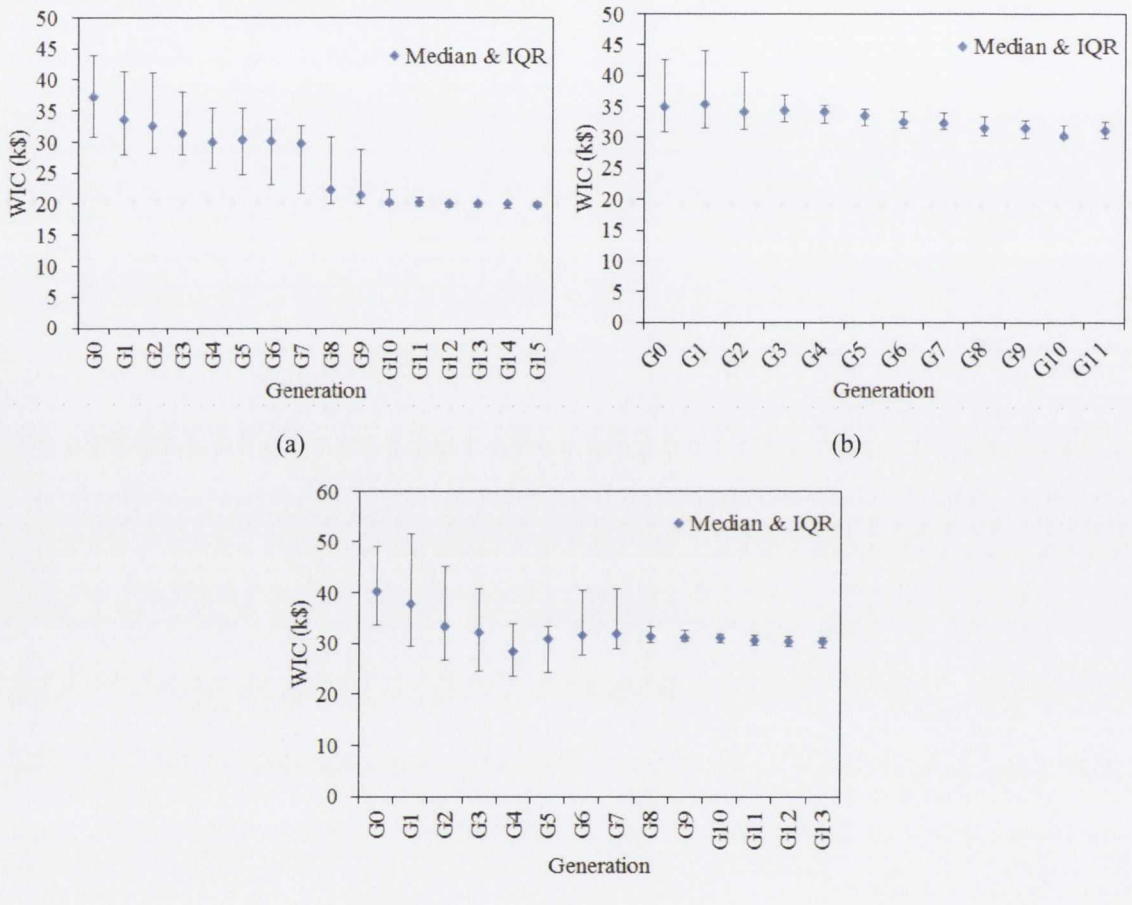

Figure 9.5 Predicted WIC for the child model (6YOC) as a function of the generation number in optimizations for sedan (a), SUV (b) and van (b) front shape.

The difference in the predicted WIC between the 'good' and 'poor' shapes is mainly from the impact speed range 30-60 km/h. The effect of the vehicle front shape on pedestrian risk is very weak at high impact speed (70 km/h) and the effect is highly dependent on ground contacts for low impact speeds (20 km/h). These findings indicate the importance of accounting for a broad range of impact speeds and its distribution in the optimization. However, the simulation results show that there is no obvious difference in the 'good' bumper shape between the predictions

using a broad range of impact speed and a single impact speed of 40 km/h (Figures 7.22 (b), 7.30 (b) and 7.36 (b), Chapter 7). This implies that in multi-body simulations the effects of the bumper shape on lower extremity injuries which are predicted by the lateral bending response at 40 km/h can generally represent the situation combined from all impact speeds. However, in the sedan case there is a clear difference in the bonnet leading edge shape between the 'good' vehicle front corridors predicted using a broad range of impact speed and a single impact speed of 40 km/h. Particularly, the bonnet leading edge for the 'good' sedan fronts predicted at 40 km/h is generally higher than that predicted using a broad impact speed range (Figure 7.22 (b), Chapter 7). This might be mainly because for the sedan impacts (with the predicted 'good' shapes from optimizations using the original STS and 40 km/h) both the bonnet and windscreen are involved in head contacts, and the head impact locations (different pedestrian heights) in the 40 km/h case may therefore need a different shape to reduce the overall head injuries than when using a broad range of impact speeds. But the details are too complex for our current understanding since a large number of variations were considered in the optimization framework. For the SUV and van cases, there is almost no difference between the 'good' vehicle fronts predicted using a broad range of impact speed and a single impact speed of 40 km/h. This is largely because for these cases the bonnet is the only important part for head contacts (Figures A.2 and A.3, Appendix), and then the need for a safe bonnet leading edge and bonnet design for impacts at 40 km/h is similar to that for the combination of all impact speeds. These findings suggest that the consideration of a broad range of impact speeds in the optimization framework is not so important for optimization of SUV and van shapes.

Injuries from ground contact, mainly to the head, are considered in the optimization framework for impacts at speeds lower than 40 km/h. The simulation results show that for some cases where a head-to-ground first contact occurred the head injuries from the ground contact are more serious than those from the vehicle contacts. To understand the effects of the ground contacts on the predictions of the optimization framework, a subsequent optimization was conducted for the van front shape, which may lead to a high head-to-ground impact speed (Crocetta et al., 2015), using an STS considering only the predicted injuries from vehicle contacts. Figure 9.6 compares the 'good' shape corridors between the predictions from the van

optimizations with (original) and without a consideration of ground contact injuries. The 'good' van shape corridors are generally similar, but there is a difference in the design of the lower bumper and bonnet leading area (Figure 9.6). This suggests that those structures might have a distinguishable influence on the pedestrian-to-ground impact kinematics (e.g. a large lower bumper offset may lead to a downward load to the leg, hence affecting the upper body kinematics). However, how the vehicle shape will affect pedestrian-to-ground impact kinematics is still not very clear and further analysis is needed to understand this. A previous study also indicates that the vehicle front shape and impact configuration (impact speed, pedestrian height and gait stance, etc.) have a significant influence on the kinematics of pedestrian-to-ground impacts (Crocetta et al., 2015). Therefore the evaluation method for vehicle-to-pedestrian safety performance should consider the injuries from ground contacts.

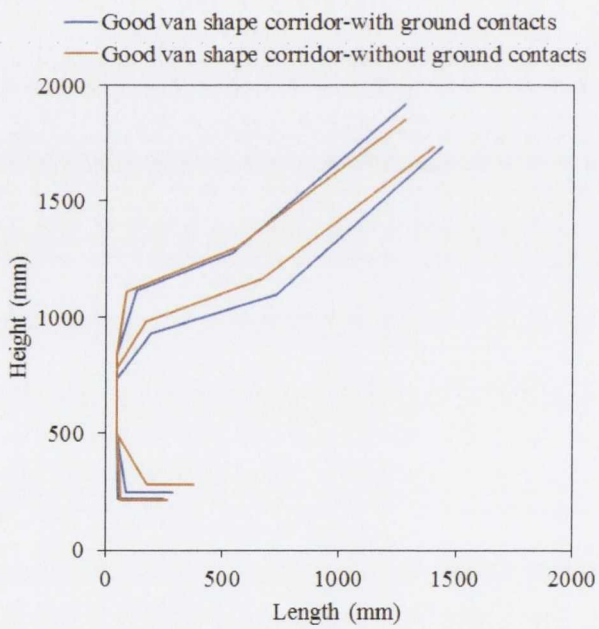

Figure 9.6 Comparison of 'good' van shape corridors between optimizations with and without a consideration of ground contacts.

The sensitivity study in Chapter 8 indicates that when a head injury criterion based on different mechanisms (such as the GAMBIT versus the HIC) was employed the prediction of the 'good' sedan front shapes of the optimization framework is affected. Particularly the 'good' sedan front shapes predicted using the GAMBIT have a higher bonnet leading edge and a longer bonnet than that predicted based on the HIC. This is because the demand of a safe sedan for the

GAMBIT is to reduce the peak head linear and angular acceleration and the higher bonnet leading edge and longer bonnet can move the head contacts from the windscreen to the bonnet area, leading to a lower peak head linear acceleration than for a windscreen contact. But the demand for a safe sedan for the HIC is a small area under the head linear acceleration curve and the head contacts with the windscreen are better than the contacts with the bonnet. Then a relatively lower bonnet leading edge and shorter bonnet (than the GAMBIT case) was predicted as the good design for head injury prevention based on the HIC. This reinforces the crucial need for a valid injury criterion for the evaluation of the pedestrian safety performance of a vehicle front design. A consistency in the demands for a safe sedan considering head and lower extremity protection was also found in the sedan optimization using the GAMBIT, where a higher bonnet leading edge helps to keep more head contacts on the bonnet area as a low GAMBIT requires, consequently being able to have a higher bumper upper height which is better for reducing lower extremity injury risk as observed in GIDAS accidents (Chapter 3). But the demands for a safe sedan between head and lower extremity protection are not consistent when the bonnet leading edge is higher than 750 mm in the HIC optimization (Figure 7.18, Chapter 7), thus the genetic algorithm (GA) controlled the bumper upper height (and consequently the bonnet leading edge height) to keep a balance between head and lower extremity protection (Figure 7.4, Chapter 7). The simulation results and accident data (small sample) indicate that the predictions based on the HIC are generally more credible for head injuries in vehicle-to-pedestrian collisions, and this was also suggested by Feist et al. (2009) in a comparison study between multi-body and FE simulations.

The weighting system takes the severity and body region of the predicted injuries into consideration when evaluating the pedestrian safety performance of a vehicle front shape. As discussed above, this weighting effect forces the optimization algorithm to focus on improving the vehicle front structure(s) to reduce the weighted injuries from the most important body regions. Thus the optimization algorithm tries to keep the balance of requirements from these body regions, which are mainly the head and lower extremity in the multi-body simulations and also in the GIDAS and PCDS accident data. The optimizations suggest using the lowest bumper lower height for the best benefit for lower extremity protection, but this lead to a higher

ankle injury risk (Aldman et al., 1979). Thus a consideration of ankle injuries may affect the shape of a safe lower bumper. All the predicted 'good' shapes have a relatively high bonnet leading edge in their corresponding vehicle type. For the sedan case, this is due to the low injury risk for mid-body regions (thorax and pelvis) and the conflictions between head/lower extremity and thorax/pelvis protection. However for the SUV and van cases, the relatively weightings for mid-body injuries in the WIC system also affected the prediction, since a high bonnet leading edge is obviously poor for mid-body protection (Chapter 7; Simms and Wood, 2006b). Therefore, relatively higher weightings for the mid-body injuries may lead to different predictions for the SUV and van optimizations. The sensitivity study results in Chapter 8 show that a higher lower extremity injury weighting has no significant influence on the predicted safe sedan front shapes since the 'good' shapes predicted using the weighted injury cost (WIC) are similar to those predicted by the weighted risk of permanent medical injury (WRPMI) where a higher weight was given to the lower extremity than the WIC. This also implies that the needs of a safe sedan for reducing the HIC (head) and lower extremity bending are not substantially conflicting. Particularly, a wide bumper (high bumper upper edge) which is safe for a pedestrian's lower extremity leads to a generally high bonnet leading edge, thereby reducing the head impact speed on the vehicle body (apart from for children) and the head injury risk measured by the HIC when a short bonnet is employed to encourage head to windscreen contact. These findings show that the weighting system for the predicted injuries is crucial for the prediction of the optimization framework and both the injury cost and risk of permanent medical injury are acceptable given their backgrounds (developed based on accident and medical data) and predictions in the optimizations.

The biofidelity of the pedestrian models is also important for optimization results since the optimal/'good' shapes were predicted based on the demands for protecting different body regions. A good biofidelity can reflect more valid sensitivity between pedestrian injury outcome and vehicle front shape. The current optimization predictions are mainly based on reducing lower extremity bending and head HIC. It is well known bending is the most important biomechanics for lower extremity injuries (Kerrigan et al., 2003a; Yang, 2005Schmitt et al., 2010), thus the predicted safer bumper shapes are biomechanically plausible. However, HIC is

still debatable for predicting head injuries, especially for brain injuries which account for about half of all head AIS2+ injuries in GIDAS accidents. Therefore, the predicted safer shapes from bonnet leading edge to windscreen might be debatable, as it is still not clear if the demands for reducing HIC can reflect the requirements for real head injuries in vehicle-to-pedestrian collisions. Further analysis is needed to understand this issue. Nevertheless, the predicted 'good' vehicle front shapes lead a lower head impact speed than the 'poor' shapes. This fairly supports the predictions of the proposed optimization framework.

9.4.2.3 Comparison of vehicle front shape optimizations from different studies

Recent studies on the optimization of the overall vehicle front shape for pedestrian protection considering different pedestrian heights were mainly from Kausalyah et al. (2014) and Subramanian et al. (2012; 2016). Kausalyah et al. (2014) used multi-body simulations with a response surface model and genetic algorithm (GA) to optimize the overall vehicle front geometry with the purpose of reducing head injury risk in an adult and a child pedestrian model. In this study a mathematical relationship between the combined HIC (weighting the HICs from both adult and child) and the vehicle shape parameters was estimated based on the response surface method, and then the GA was employed to predict the optimal sedan front shape to minimize the combined HIC based on the mathematic response surface function. In this study only the combined head injury risk (predicted by the HIC) from two different pedestrian heights (50^{th}% male and 6 years old child) at the impact speed of 40 km/h was considered. The optimal sedan shape predicted from this study of Kausalyah et al. (2014) is shown in Figure 9.7. Subramanian et al. (2012 and 2016) proposed a similar approach of using the multi-body simulation and GA to optimize the vehicle front centre-line geometry by considering the cost of injuries (from vehicle contacts) for five body regions (head, neck, thorax, pelvis and lower extremity). In their studies, different pedestrian sizes (6-year-old child, 5^{th}% female, 50^{th}% male and 95^{th}% male for the study of 2012, while 6-year-old child, 5^{th}% female, 50^{th}% male for the study of 2016), one gait stance and one impact speed (40 km/h) were considered. The optimal vehicle front shapes predicted from the studies of Subramanian et al. (2012 and 2016) are also shown in Figure 9.7.

It is clear from Figure 9.7 that there is a significant difference in the bumper shape between the

optimal sedan fronts predicted from the current work and that from the study of Kausalyah et al. (2014). Particularly, the optimal sedan front in the study of Kausalyah et al. (2014) has a sharp bumper which is aggressive for pedestrians. This is mainly due the fact that Kausalyah et al. (2014) only considered the head injury risk in their optimization, and then the bumper shape was not seriously optimized in their study. This highlights how it is necessary to consider injuries from different body regions in the optimization of the overall vehicle front shape.

For the studies from Subramanian et al., the sharp bumper of the optimal sedan front predicted from their study in 2012 does not make sense for pedestrian lower extremity protection. This is mainly because the peak contact force in the leg and thigh of the pedestrian model was used as the lower extremity injury criterion in their study of 2012 (Subramanian et al., 2012), and this probably does not reflect the key lower extremity injury mechanism from bending (Kerrigan et al., 2003a; Schmitt et al., 2010; Yang, 2005). In their study of 2016, the Femur Force Criterion (FFC) and tibia index (TI) were used as the lower extremity injury criteria (Subramanian et al., 2016), where the FFC is calculated based on the compression force transmitted axially on each femur and the TI is determined by the bending moments and axial force in the tibia (Schmitt et al., 2010). Both FFC and TI were defined in the ECE R94[3] for assessing lower extremity injuries to vehicle occupants in a frontal collision. Then a flat and wide bumper similar to the current work was predicted in their optimization with the consideration of the bending moment in the leg by the TI (Subramanian et al., 2016), see Figure 9.7. However the bonnet of the optimal sedan front from the study of Subramanian et al. (2016) is significantly longer than that predicted from other studies even though the same head injury criterion was used. This might be due to the differences in the definition of the impact configuration, design space, contact stiffness and so on. Nevertheless, the optimal vehicle front shapes predicted from the studies Subramanian et al. (2012 and 2016) have not been evaluated and validated by comparing to accident data and the big gaps between the ellipsoids (especially for the bonnet leading area) in

[3] ECE R94 is one of the World Forum for Harmonization of Vehicle Regulations, which was proposed for testing the protection of the occupants in the event of a frontal collision

their models may have a significant influence on the predictions of the multi-body simulations. Moreover, the GIDAS accident data (small samples) shows that the sedan fronts which have a higher bonnet leading edge and a longer bonnet (similar to the optimal sedan front shape predicted from the study of Subramanian et al. (2016)) compared to the profile of the 'good' sedan shapes predicted by the original optimization framework of the current work lead to a higher average injury cost to the pedestrians in accidents than the latter (Figure 8.15, Chapter 8).

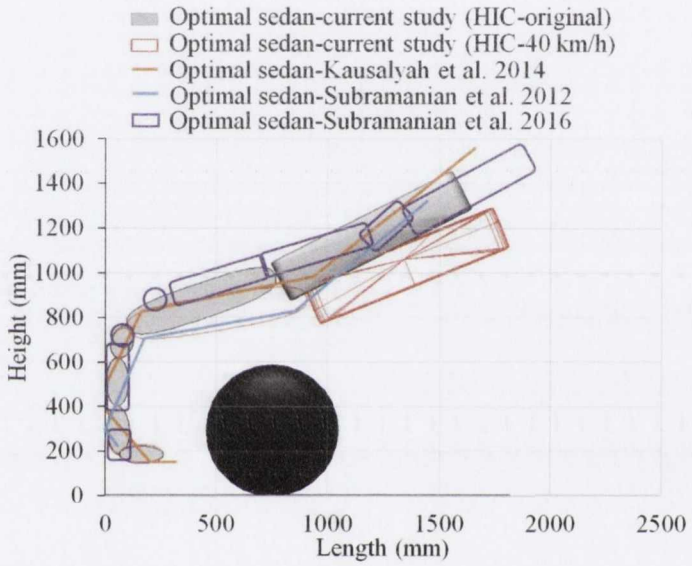

Figure 9.7 Comparison of the optimal sedan fronts predicted from different studies.

The above discussion implies that including the broad range of impact configurations (impact speed, pedestrian height and pedestrian gait stance) and their distributions, ground contacts, valid injury criteria and weighting of predicted injuries from different body regions as considered in the current optimization framework is crucial to the success of vehicle front shape optimization for pedestrian protection.

Chapter 10 Conclusions and Future Work

10.1 Conclusions

The main conclusions of the thesis are summarized as follows:

1. The GIDAS accident data indicates that a low bumper lower edge, a small offset at the bumper lower edge, a high bumper upper edge up to the femur area, and a low bonnet leading edge benefit pedestrian lower extremity and pelvis protection. These findings have also been observed based on multi-body simulations at the population level for the first time. The effects of sedan bonnet leading edge height on the upper body injury risk are complex as observed in the GIDAS data and multi-body simulations. The multi-body simulation results show that the head injury risk predicted by the HIC based on population tests considering six impact speeds, five pedestrian heights and two gait stances is generally lower for a shallow windscreen in the sedan impacts and for a shallow bonnet for the SUV and van impacts than that for a steep design of these structures. However these trends have not been observed in the GIDAS data.

2. The GIDAS accident data shows surprisingly that the impact speed and pedestrian age are not significant predictors for head injury risk when the head contact location is fixed at the sedan windscreen centre. Further detailed analyses are needed to understand these issues.

3. The results of the pedestrian gait stance modelling study show that flexion of the ipsilateral knee can reduce lower extremity injury risk by allowing more freedom of the knee joint in flexion/extension and internal/external rotation during vehicle collisions. The flexed knee also reduces the leg and thigh loading by raising the lower extremity to yield a lower bending moment caused by the inertia force from the part of the leg below the bumper. For the gait stances where self-contact between the two legs occurred, the reaction force from this contact may affect the lower extremity injuries.

4. The study of the virtual test system suggests that a set of multi-body simulations with a reasonable sample size (N≥60, considering a broad range of impact speeds (≥6), pedestrian heights and gait stances) is able to generally predict similar pedestrian injury distributions (as a function of pedestrian body region and height, impact speed, and vehicle type) to those observed from PCDS and GIDAS data, when the corresponding proportions of the impact parameters (impact speed, pedestrian height and gait stance) and vehicle types in accidents were employed for weighting the predicted injuries. The resultant output of the virtual test system (VTS) can generally distinguish the aggressivity of different vehicle front shapes to pedestrians. It is therefore acceptable to use the approaches defined in the VTS for evaluating the pedestrian safety performance of an overall vehicle front design.

5. The optimization results and their corresponding analysis indicate that the predictions of the optimization framework are generally reasonable and plausible, in terms of predicting the pedestrian injury distributions and the effects of the vehicle front shape on pedestrian injury risk. All optimizations have a good convergence. The applications of the proposed optimization framework show that it is feasible to use the combination of MATLAB and MADYMO to develop an efficient numerical based approach for the vehicle front shape optimization for pedestrian protection.

6. The optimizations of vehicle front shape using the proposed optimization framework mainly focus on improving the design for reductions of head and lower extremity injury risk. All optimal vehicle fronts have a flat and wide bumper (low bumper lower edge and high bumper upper edge) and a generally high bonnet leading edge. The demands for lower extremity and head protection are not strongly conflicting. But there is a balance to be kept for the bonnet leading edge design for the protection of different body regions, such as the pelvis versus lower extremity/head for the sedan case and thorax versus head for the SUV and van cases. The sedans meeting the predicted safe front shapes have a low injury risk to pedestrians in GIDAS accidents. The optimal vehicle front shapes show significant improvement for pedestrian protection in PCDS and GIDAS accidents when the involving

proportions of the impact configurations and vehicle types observed from these databases were employed for weighting the predicted injuries.

7. The impact configurations, injury criteria, and ground contacts affect the predictions of the optimization framework. The broad range of impact configurations and their distributions, injuries from different body regions and ground contacts, reasonable injury criteria and weighting of the predicted injuries considered in the current optimization framework are necessary for a successful and comprehensive optimization of vehicle front shape for pedestrian protection.

8. Stiffness shows strong interactive effects on pedestrian injury outcome with vehicle front shape. Therefore the predictions of the current optimization framework are stiffness dependent.

10.2 Further work

As shown in the discussion, there are some limitations in the current work and the underlying mechanisms for a number of conditions remain unclear. Thus further work can follow this project from different perspectives.

The accident data is still not sufficient for analysis of the detailed relationships between the vehicle front design and pedestrian upper body injury risk, which can provide the most direct and efficient information for improving the current vehicle front design. Further collection of in-depth accident data and a global pedestrian accident database would be helpful to understand these issues, especially for the head.

The current optimization framework is based on a simplified vehicle front model which only considers the centre line geometry of the vehicle front. Further application of the current optimization framework approach could focus on including more impact scenarios and using more biofidelic pedestrian models, more detailed vehicle front models and more representative accident datasets. An optimization framework using a vehicle model defined in detail with considerations of interaction between vehicle front shape and stiffness distribution and using

pedestrian models with better biofidelity may predict more reliable references for future vehicle front design of pedestrian safety.

The optimizations in the current work were conducted under regular constraints and some parameters of the predicted optimal vehicle front shapes reached their design constraints. Further work could also try to define an optimization framework which can generate 'fantastic' vehicle front shapes. The best vehicle front design for pedestrian protection might be beyond our current imagination.

The optimization predictions in the current work were based on simplified pedestrian models. The predictions might be affected by the biofidelity of pedestrian models since it is still not clear whether the sensitivities of upper body injury risk to vehicle front shape reflected by the current multi-body models were valid in real world case. Further work can focus on investigating whether a more detailed or a more simplified model would substantially change the resulting shape predictions.

The current optimizations of vehicle front shape focused on the overall population of pedestrians. Similar optimization framework could be defined for protection of a particular pedestrian population, such as children.

According to the findings of the current work, it is reasonable to improve the current assessment test system for pedestrian safety performance of vehicle front designs with a consideration of a broad range of impact configurations, ground contacts, the importance of injuries from different body regions and the loading linked between different body regions (such as the neck and head). Further work could focus on developing an advanced test systems to assess the overall threat of a vehicle front design to pedestrians.

The detailed mechanisms for head injuries in vehicle-to-pedestrian are still not very clear, especially when considering the global kinematics of the whole body and the head loading boundary conditions (contact force, neck force, etc.). Further research could be conducted to understand this issue and provide useful guidelines for future vehicle front safety design (such as the bonnet and windscreen angle).

The detailed effects of vehicle shape and impact boundary conditions on pedestrian-to-ground contacts and the effects of the kinematics of pedestrian-to-ground contacts on injuries are also not very clear. Detailed analysis of these issues can help to develop efficient strategies to reduce pedestrian injury risk from ground contacts.

Further improvement on vehicle front shape design can focus on combining requirements from different aspects, such as pedestrian safety, aerodynamics, and so on.

Further work can also try to find the optimal vehicle front shape for each potential impact configuration (impact speed, pedestrian height, etc.) and combine with active safety techniques to 'tune' the vehicle front shape in a pedestrian collision to minimizing its threat.

References

AAAM. (2005). AIS 2005: The injury scale (Eds. Gennarelli, T. and Wodzin, E.). Association of Advancement of Automotive Medicine (AAAM).

Akiyama, A., Okamoto, M., Ito, O., Takahashi, Y. (2009). Development of Omni-directional injury criteria for a pedestrian dummy for evaluating rib fracture. SAE Technical Paper No. 2009-01-1210.

Akiyama, A., Okamoto, M., Rangarajan, N. (2001). Development and application of the new pedestrian dummy. Proceedings of the 17th International Technical Conference of Enhanced Safety of Vehicles (ESV).

Aldman, B., Lundell, B., Thorngren, L., Bunketorp, O., Romanus, B. (1979). Physical simulation of human leg-bumper impacts. Proceedings of the 1979 International Conference on the Biomechanics of Impacts (IRCOBI).

Aldman, B., Kajzer, J., Cesari, D., Bouquet, R., Zac, R. (1985). A new dummy for pedestrian test. Proceedings of the 10th International Technical Conference of Enhanced Safety of Vehicles (ESV).

Anderson, R., Streeter, L., Ponte, G., Mclean, A. (2007). Pedestrian reconstruction using multi-body MADYMO simulation and the polar-II dummy: A comparison of head kinematics. Proceedings of the 20th International Technical Conference of Enhanced Safety of Vehicles (ESV).

Antona-Makoshi, J., Davidsson, J., Ejima, S., Ono, K., Brolin, K., Anata, K. (2013). Correlation of global head and brain tissue injury criteria to experimental concussion derived from monkey head trauma experiments. Proceedings of the 2013 International Conference on the Biomechanics of Impacts (IRCOBI).

Arnoux, P.J., Cesari, D., Behr, M., Thollon, L., Brunet, C. (2005). Pedestrian lower limb injury criteria evaluation: A finite element approach. Traffic Injury Prevention, 6 (3): 288-297.

Ashton, S. J., Mackay, G. M. (1983). Benefits from changes in vehicle exterior design–field accident and experimental work in Europe. SAE Technical Paper No. 830626.

ATSB. (2013). Road Deaths Australia 2012 Statistical Summary. Australian Government, Australian Transport Safety Bureau (ATSB) Research and Analysis Report, Road Safety.

Bacon, D., Wilson, M. (1976). Bumper characteristics for improved pedestrian safety. SAE Technical Paper No. 760812.

Ballesteros, M.F., Dischinger, P.C., Langenberg, P. (2004). Pedestrian injuries and vehicle type in Maryland, 1995-1999. Accident Analysis & Prevention, 36 (1), 73-81.

Björklund, M., Zheng, Q. (2001). Development and evaluation of a pedestrian anthropomorphic test device. MSc thesis, Chalmers University of Technology, Göteborg, Sweden.

Belsley, D. A., Kuh, E., Welsch, R. E. (2005). Regression diagnostics: identifying influential data and sources of collinearity (Vol. 571). John Wiley & Sons.

Bose, D., Bhalla, K. S., Untaroiu, C. D., Ivarsson, B. J., Crandall, J. R., Hurwitz, S. (2008). Injury tolerance and moment response of the knee joint to combined valgus bending and shear loading. Journal of Biomechanical Engineering, 130(3), 031008.

Bouquet, R., Ramet, M., Bermond, F., Cesari, D. (1994). Thoracic and pelvis response to impact. Proceedings of the 14th International Technical Conference of Enhanced Safety of Vehicles (ESV).

Brach, R. M., Brach, R. M. (2005). Vehicle accident analysis and reconstruction methods.

Bonfield, W. (1987). Advances in the fracture mechanics of cortical bone. Journal of Biomechanics, 20(11-12), 1071-1081.

Bunketorp, O., Romanus, B., Hansson, T., Aldman, B. (1983). Experimental study of a compliant bumper system. SAE Technical Paper No. 831623.

CARE. (2010). Traffic Safety Basic Facts 2010, pedestrian. http://ec.europa.eu/transport/road_safety/specialist/statistics/care_reports_graphics/index_en.htm.

Carter, E, Ebdon, S, Neal-Sturgess, C. (2005). Optimization of passenger car design for the mitigation of pedestrian head injury using a genetic algorithm. Proceedings of the 2005 Conference on Genetic and Evolutionary Computation (GECCO).

Cavanaugh, J. M., Zhu, Y., Huang, Y., & King, A. I. (1993). Injury and response of the thorax in side impact cadaveric tests. SAE Technical Paper No. 933127

Cesari, D., Ramet, M. (1982). Pelvic tolerance and protection criteria in side impact. SAE Technical Paper No. 821159.

Chalandon, S., Serre, T., Masson, C., Arnoux, P., Perrin, C., Borde, P., Cesari, D. (2007). Comparative study between subsystem and global approaches for the pedestrian impact. Proceedings of the 20th International Technical Conference of Enhanced Safety of Vehicles (ESV).

Chen, H.P., Fu, L.X., Zheng, H.Y. (2009). A comparative study between china and IHRA for the vehicle-pedestrian impact. SAE Technical Paper No. 2009-01-1205.

Chen, H., Poulard, D., Crandall, J. R., Panzer, M. B. (2015). Pedestrian response with different initial positions during impact with a mid-sized sedan. Proceedings of the 24th International Technical Conference of Enhanced Safety of Vehicles (ESV).

Chen, X., Yang, J.K. (2012) .Optimization of longitudinal beam for improvement of crashworthiness in frontal and offset impacts. Proceedings of the 3rd International Conference on Digital Manufacturing & Automation (ICDMA2012), pp.582-585.

Chidester, C., Isenberg, R. (2001). Final report-the pedestrian crash data study. Proceedings of the 17th International Technical Conference on the Enhanced Safety of Vehicles (ESV).

Chong, E. K., Zak, S. H. (2013). An introduction to optimization (Vol. 76). John Wiley & Sons.

C-NCAP. (2015). China New Car Assessment Programme. The Protection for Pedestrians in the Event of a Collision. China.

Coley, G., de Lange, R., de Oliveira, P., Neal-Sturgess, C. E., Happee, R. (2001). Pedestrian human body validation using detailed real-world accidents. Proceedings of the 2001 International Conference on the Biomechanics of Impacts (IRCOBI).

Crocetta, G., Piantini, S., Pierini, M., Simms, C. (2015). The influence of vehicle front-end design on pedestrian ground impact. Accident Analysis & Prevention, 79, 56-69.

Dobson, A.J. 2002. An introduction to generalized linear models. Chapman & Hall/CRC press.

Dokko, Y., Anderson, R., Manavis, J., Blumburgs P., Mclean, J., Zhang, L.Y., Yang K.H., King, A.I. (2003). Validation of the human head FE model against pedestrian accident and its tentative application to the examination of the existing tolerance curve. Proceedings of the 18th International Technical Conference on the Enhanced Safety of Vehicles (ESV).

Edwards, K.J. and Green, J.F. (1999). Analysis of the interrelationship of pedestrian leg and pelvis injuries. Proceedings of the 1999 International Conference on the Biomechanics of Impacts (IRCOBI).

EEVC. (1994). EEVC working group 10 report – proposals and methods to evaluate pedestrian protection for passenger cars. European Experimental Vehicles Committee.

EEVC. (1998). EEVC working group 17 report – improved test methods to evaluate pedestrian protection afforded by passenger cars. European Enhanced Vehicle-Safety Committee.

EEVC. (2002). Improved test methods to evaluate pedestrian protection affordable by passenger cars, technical report. European Enhanced Vehicle-safety Committee, Working Group17 Report, December 1998 with September 2002 updates.

Elliott, J., Lyons, M., Kerrigan, J., Wood, D., Simms, C. (2012a). Predictive capabilities of the MADYMO multi-body pedestrian model: three-dimensional head translation and rotation, head impact time and head impact velocity. IMechE Journal of Multi-body dynamics, 226(3) 266-277.

Elliott, J.R., Simms, C.K., Wood, D.P. (2012b). Pedestrian head translation, rotation and impact velocity: The influence of vehicle speed, pedestrian speed and pedestrian gait. Accident Analysis & Prevention. 45, 342-353.

Eppinger, R., Morgan, R., and Marcus, J. (1984). Development of dummy and injury index for NHTSA's thoracic side impact protection research program. SAE Technical Paper No. 840885.

Euro-NCAP. (2013). European New Car Assessment Programme. Pedestrian Testing Protocol, Version 4.3.

Feist, F., Gugler, J., Arregui-Dalmases, C., Del Pozo de Dios, E., Lopez–Valdes, F., Deck, D., Willinger, R. (2009). Pedestrian collisions with flat-fronted vehicles: injury patterns and importance of rotational accelerations as a predictor for traumatic brain injury (TBI). Proceedings of the 21st International Conference on the Enhanced Safety of Vehicles (ESV).

Fredriksson, R., Flink, E., Bostrom, O., Backman, K. (2007a). Injury mitigation in SUV-to-pedestrian impacts. Proceedings of the 20th International Conference on the Enhanced Safety of Vehicles (ESV).

Fredriksson, R., Zhang, L., Boström, O., Yang, K. (2007b). Influence of impact speed on head and brain injury outcome in vulnerable road user impacts to the car hood. Stapp Car Crash Journal, Vol. 51, pp.155-167.

Garrett, M. (1998). Head impact modeling using MADYMO simulations of documented pedestrian accidents. Proceedings of the Conference on Pedestrian Safety.

Gennarelli, T. A., Adams, J. H., Graham, D. I. (1981). Acceleration induced head injury in the monkey. I. The model, its mechanical and physiological correlates. In Experimental and Clinical Neuropathology (pp.23-25). Springer Berlin Heidelberg.

Gennarelli, T., Thibault, L., Ommaya, A. (1972). Pathophysiologic responses to rotational and translational accelerations of the head. SAE Technical Paper No. 720970, pp.269-308.

Gennarelli, T. A., Wodzin, E. (2006). AIS 2005: a contemporary injury scale. Injury, 37(12), 1083-1091.

Guillaume, A., Hermitte, T., Hervé, V., Fricheteau, R. (2015). Car or ground: which causes more pedestrian injuries? Proceedings of the 24th International Conference on the Enhanced Safety of Vehicles (ESV).

GTR. (2009). Global Technical Regulation No. 09. Pedestrian Safety.

Haffner, M. (1985). Synthesis of pelvic fracture criteria for lateral impact loading. SAE Technical Paper No. 856022.

Han, Y., Yang, J.K., Mizuno, K. (2011). Virtual reconstruction of long bone fracture in car-to-pedestrian collisions using multi-body system and finite element method. Chinese Journal of Mechanical Engineering, Vol. 24, No. 6, pp.1045-1055.

Han, Y., Yang, J., Nishimoto, K., Mizuno, K., Matsui Y., Nakane D., Wanami, S., Hitosugi, M. (2012). Finite element analysis of kinematic behaviour and injuries to pedestrians in vehicle collisions. International Journal of Crashworthiness 17:2, 141-152.

Hertz, E. (1993). A note on the head injury criterion (HIC) as a predictor of the risk of skull fracture. 37th Annals of Advances in Automotive Medicine (AAAM), pp.303-312.

Hoof, J. van, Lange R. de, Wismans J. (2003). Improving pedestrian safety using numerical human models. SAE Technical Paper No. 2003-22-0018.

Hu, J., Klinich, K. D. (2012). Toward designing pedestrian-friendly vehicles. Michigan: The University of Michigan Transportation Research Institute, 2012: 1-53.

Huang, S.N., Yang, J.K. (2010). Optimization of a reversible hood for protecting a pedestrian's head during car collisions, Accident Analysis & Prevention, 42 (4): 1136–1143.

Huang, S., Yang, J., Eklund, F. (2008). Evaluation of remote pedestrian sensor system based on the analysis of car-pedestrian accident scenarios. Safety Science, 46:1345-1355.

Huang, T.J., McDonald, J., Artis, M., Rangarajan, N., Shams, T., White, R., Beach, D., Campbell, R., Akiyama, A., Yoshida, S., Ishikawa, H., Konosu, A. (1999). Development of a biofidelic dummy for

car-pedestrian accident studies. Proceedings of the 1999 International Conference on the Biomechanics of Impacts (IRCOBI).

Ishikawa, H., Kajzer, J., Ono, K., and Sakurai, M. (1992). Simulation of car impact to pedestrian lower extremity: influence of different car front shapes and dummy parameters on test results. Proceedings of the 1992 International Conference on the Biomechanics of Impacts (IRCOBI).

ISO. (2000). Passenger cars and light truck vehicles-pedestrian protection-Impact test method for pedestrian head. ISO/TC22/SC10/WG2, Document N623.

ISO: 13232-5. (2005). Motorcycles-Test and analysis procedures for research evaluation of rider crash protective devices fitted to motorcycles. Part 5: Injury indices and risk/benefit analysis.

ITARDA. (2011). Annual Traffic Accident Report in 2010. Institute for Traffic Accident Research and Data Analysis of Japan (ITARDA).Tokyo, Japan.

Ivarsson, B. J., Kerrigan, J. R., Lessley, D. J., Drinkwater, D. C., Kam, C. Y., Murphy, D. B., Kent, R. W. (2005). Dynamic response corridors of the human thigh and leg in non-midpoint three-point bending. SAE Technical Paper No. 2005-01-0305.

Jakobsson, L., Broberg, T., Karlsson, H., Fredriksson, A., Gråberg, N., Gullander, C., Lindman M. (2013). Pedestrian airbag technology-A production system. Proceedings of the 23th International Conference on the Enhanced Safety of Vehicles (ESV).

J-NCAP. (2011). Japan New Car Assessment Programme. Pedestrian Testing Protocol, Japan.

Kajzer, J., Cavallero, C., Bonnoit, J., Morjane, A., Ghanouchi, S. (1993). Response of the knee joint in lateral impact: Effect of bending moment. Proceedings of the 1993 International Conference on the Biomechanics of Impacts (IRCOBI).

Kajzer, J., Matsui, Y., Ishikawa, H., Schroeder, G. Bosch, U. (1999). Shearing and bending effects at the knee joint at low-speed lateral loading. SAE Technical Paper 1999-01-0712.

Kajzer, J., Schroeder, G. (1992). Examination of different bumper system using Hybrid II, RSPD, subsystem and cadavers. SAE Technical Paper No. 922519.

Kajzer, J., Schroeder, G., Ishikawa, H., Matsui, Y., Bosch, U. (1997). Shearing and bending effects at the knee at high speed lateral loading. SAE Technical Paper No. 973326.

Kausalyah, V., Shasthri, S., Abdullah, K. A., Idres, M. M., Shah, Q. H., Wong, S. V. (2014). Optimisation of vehicle front-end geometry for adult and pediatric pedestrian protection. International Journal of Crashworthiness, 19(2), 153-160.

Kausalyah, V., Shasthri, S., Abdullah, K. A., Idres, M. M., Shah, Q. H., Wong, S. V. (2015). Vehicle profile optimization using central composite design for pedestrian injury mitigation. Applied Mathematics & Information Sciences, 9(1), 197.

Kerkeling, C., Schaefer, J., Thompson, G. (2005). Structural hood and hinge concepts for pedestrian protection. Proceedings of the 19th International Conference on the Enhanced Safety of Vehicles (ESV).

Kerrigan, J., Arregui, C., Crandall, J. (2009a). Pedestrian head impact dynamics: comparison of dummy and PMHS in small sedan and large SUV impacts. Proceedings of the 21th International Conference on the Enhanced Safety of Vehicles (ESV).

Kerrigan, J., Bhalla, K., Madeley, J., Funk, J., Bose, D., Crandall, J. (2003a). Experiments for establishing pedestrian impact lower limb injury criteria. SAE Technical Paper No. 2003-01-0895.

Kerrigan, J., Crandall, J., Deng, B. (2007). Pedestrian kinematic response to mid-sized vehicle impact. International Journal of Vehicle Safety, Vol. 2, No. 3, pp.221–240.

Kerrigan, J., Crandall, J., Deng, B. (2008a). A comparative analysis of the pedestrian injury risk predicted by mechanical impactors and post mortem human surrogates. Stapp Car Crash Journal, Vol. 52 (November 2008), pp.527-67.

Kerrigan, J., Drinkwater, D., Kam, C., Murphy, D.B., Ivarsson, B., Crandall, J., Patrie, J. (2004). Tolerance of the human leg and thigh in dynamic lateral-medial bending. International Journal of Crashworthiness, 9(6), 607–623.

Kerrigan, J., Ivarsson, B., Bose, D., Madeley, N., Millingtion, S., Bhalla, K., Crandall, J. (2003b). Rate sensitive constitutive and failure properties of human collateral knee ligaments. Proceedings of the 2003 International Conference on the Biomechanics of Impacts (IRCOBI).

Kerrigan J, Murphy D, Drinkwater D, Kam C, Bose D, Crandall J. (2005). Kinematic corridors for PMHS tested in full-scale pedestrian impact tests. Proceedings of the 19th Conference on the Enhanced Safety of Vehicles (ESV).

Kerrigan, J. R., Parent, D. P., Untaroiu, C., Crandall, J. R., Deng, B. (2009). A new approach to multibody model development: pedestrian lower extremity. Traffic injury prevention, 10(4), 386-397.

Kerrigan, J., Rudd, R., Subit, D., Untaroiu, C., Crandall, J. (2008b). Pedestrian lower extremity response and injury: A small sedan vs. a large sport utility vehicle. SAE Technical Paper No. 2008-01-1245.

KinX Learning eBooks. (2014). Volume 2: The knee joint. http://www.kinxlearning.com.

Kleinberger, M., Sun, E., Eppinger, R., Kuppa, S., Saul, R. (1998). Development of improved injury criteria for the assessment of advanced automotive restraint systems. NHTSA Docket, (1998-4405), 9.

Klinich, K. D., Schneider, L. (2003). Biomechanics of pedestrian injuries related to lower extremity injury assessment tools: a review of the literature and analysis of pedestrian crash database (No. HS-043 604, UMTRI-2003-25). University of Michigan, Transportation Research Institute.

Kong, C.Y., Yang, J.K. (2010). Logistic regression analysis of pedestrian casualty risk in passenger vehicle collisions in China. Accident Analysis & Prevention, 42(4):987-993.

Konosu, A., Issiki, T., Tanahashi, M. (2005). Development of a pedestrian lower extremity protection car using a biofidelic flexible pedestrian legform impactor. Proceedings of the 19th Conference on the Enhanced Safety of Vehicles (ESV).

Konosu, A., Tanahashi, M. (2003). Development of a biofidelity pedestrian legform impactor-Introduction of JAMA JARI legform impactor version 2002. Proceedings of the 18th Conference on the Enhanced Safety of Vehicles (ESV).

Kramer, F., Appel, H. (1990). Evaluation of protection criteria on the basis of statistical biomechanics. Proceedings of the 1990 International Conference on the Biomechanics of Impacts (IRCOBI).

Kuehn, M., Froeming, R., Schindler, V. (2005a). Assessment of vehicle related pedestrian safety. Proceedings of the 19th Conference on the Enhanced Safety of Vehicles (ESV).

Kuehn, M., Froeming, R., Schindler, V. (2005b). An advanced testing procedure for the pedestrian-car-collision. Proceedings of the 19th Conference on the Enhanced Safety of Vehicles (ESV).

Kuwahara, S., Hosokawa, T., Okada, K., Mizuno, K. (2007). Finite element analysis of pedestrian lower extremity injuries in car-to-pedestrian impacts. SAE Technical Paper No. 2007-01-0755.

Lefler, D.E., Gabler, H.C. (2004). The fatality and injury risk of light truck impacts with pedestrians in the United States. Accident Analysis & Prevention, 36(2): 295-304.

Li, G., Nie, J., Yang, J. (2012). A study on injuries and kinematics in pedestrian accidents involved minivan and sedan. Proceedings of the 5th International Conference on Expert Symposium Accident Research (ESAR).

Li, G., Yang, J., Simms, C. (2014). Predicting the effects of pedestrian gait on lower limb injuries. Proceedings of the 2014 International Conference on the Biomechanics of Impacts (IRCOBI).

Liers, H., Hannawald, L. (2011). Benefit estimation of secondary safety measures in real-world pedestrian accidents. Proceedings of the 22nd International Conference on the Enhanced Safety of Vehicles (ESV).

Liu, Q., Xia, Y., Zhou, Q., Wang, J.T. (2009). Design analysis of a sandwich hood structure for pedestrian protection. Proceedings of the 21st Conference on the Enhanced Safety of Vehicles (ESV).

Liu, X., Yang, J., Lovsund, P. (2002). A study of influences of vehicle speed and front structure on pedestrian impact responses using mathematical models. Traffic Injury Prevention, 3, 31–42.

Linder, A., Clark, A., Douglas, C., Fildes, B., Yang, K., Sparke, L. (2004). Mathematical modeling of pedestrian crashes: Review of pedestrian models and parameter study of the influence of the sedan vehicle contour, 2004 Road Safety Research, Policing and Education Conference, Perth, Australia.

Lissner, H. R., Lebow, M., Evans, F. G. (1960). Experimental studies on the relation between acceleration and intracranial pressure changes in man. Surgery, Gynecology & Obstetrics, 111, 329-338.

Longhitano, D., Henary, B., Bhalla, K., Ivarsson, J., Crandall, J. (2005). Influence of vehicle body type on pedestrian injury distribution. SAE Technical Paper No. 2005-01-1876.

Lyons, M., Simms, C. (2012). Predicting the influence of windscreen design on pedestrian head injuries. Proceedings of the 2012 International Conference on the Biomechanics of Impacts (IRCOBI).

MADYMO. (2012). Human Body Models Manual Release 7.4.1.

Kerrigan, J., Arregui, C., Crandall, J. (2009a). Pedestrian head impact dynamics: comparison of dummy and PMHS in small sedan and large SUV impacts. Proceedings of the 21th International Conference on the Enhanced Safety of Vehicles (ESV).

Kerrigan, J., Bhalla, K., Madeley, J., Funk, J., Bose, D., Crandall, J. (2003a). Experiments for establishing pedestrian impact lower limb injury criteria. SAE Technical Paper No. 2003-01-0895.

Kerrigan, J., Crandall, J., Deng, B. (2007). Pedestrian kinematic response to mid-sized vehicle impact. International Journal of Vehicle Safety, Vol. 2, No. 3, pp.221–240.

Kerrigan, J., Crandall, J., Deng, B. (2008a). A comparative analysis of the pedestrian injury risk predicted by mechanical impactors and post mortem human surrogates. Stapp Car Crash Journal, Vol. 52 (November 2008), pp.527-67.

Kerrigan, J., Drinkwater, D., Kam, C., Murphy, D.B., Ivarsson, B., Crandall, J., Patrie, J. (2004). Tolerance of the human leg and thigh in dynamic lateral-medial bending. International Journal of Crashworthiness, 9(6), 607–623.

Kerrigan, J., Ivarsson, B., Bose, D., Madeley, N., Millington, S., Bhalla, K., Crandall, J. (2003b). Rate sensitive constitutive and failure properties of human collateral knee ligaments. Proceedings of the 2003 International Conference on the Biomechanics of Impacts (IRCOBI).

Kerrigan J, Murphy D, Drinkwater D, Kam C, Bose D, Crandall J. (2005). Kinematic corridors for PMHS tested in full-scale pedestrian impact tests. Proceedings of the 19th Conference on the Enhanced Safety of Vehicles (ESV).

Kerrigan, J. R., Parent, D. P., Untaroiu, C., Crandall, J. R., Deng, B. (2009). A new approach to multibody model development: pedestrian lower extremity. Traffic injury prevention, 10(4), 386-397.

Kerrigan, J., Rudd, R., Subit, D., Untaroiu, C., Crandall, J. (2008b). Pedestrian lower extremity response and injury: A small sedan vs. a large sport utility vehicle. SAE Technical Paper No. 2008-01-1245.

KinX Learning eBooks. (2014). Volume 2: The knee joint. http://www.kinxlearning.com.

Kleinberger, M., Sun, E., Eppinger, R., Kuppa, S., Saul, R. (1998). Development of improved injury criteria for the assessment of advanced automotive restraint systems. NHTSA Docket, (1998-4405), 9.

Klinich, K. D., Schneider, L. (2003). Biomechanics of pedestrian injuries related to lower extremity injury assessment tools: a review of the literature and analysis of pedestrian crash database (No. HS-043 604, UMTRI-2003-25). University of Michigan, Transportation Research Institute.

Kong, C.Y., Yang, J.K. (2010). Logistic regression analysis of pedestrian casualty risk in passenger vehicle collisions in China. Accident Analysis & Prevention, 42(4):987-993.

Konosu, A., Issiki, T., Tanahashi, M. (2005). Development of a pedestrian lower extremity protection car using a biofidelic flexible pedestrian legform impactor. Proceedings of the 19th Conference on the Enhanced Safety of Vehicles (ESV).

Konosu, A., Tanahashi, M. (2003). Development of a biofidelity pedestrian legform impactor-Introduction of JAMA JARI legform impactor version 2002. Proceedings of the 18th Conference on the Enhanced Safety of Vehicles (ESV).

Kramer, F., Appel, H. (1990). Evaluation of protection criteria on the basis of statistical biomechanics. Proceedings of the 1990 International Conference on the Biomechanics of Impacts (IRCOBI).

Kuehn, M., Froeming, R., Schindler, V. (2005a). Assessment of vehicle related pedestrian safety. Proceedings of the 19th Conference on the Enhanced Safety of Vehicles (ESV).

Kuehn, M., Froeming, R., Schindler, V. (2005b). An advanced testing procedure for the pedestrian-car-collision. Proceedings of the 19th Conference on the Enhanced Safety of Vehicles (ESV).

Kuwahara, S., Hosokawa, T., Okada, K., Mizuno, K. (2007). Finite element analysis of pedestrian lower extremity injuries in car-to-pedestrian impacts. SAE Technical Paper No. 2007-01-0755.

Lefler, D.E., Gabler, H.C. (2004). The fatality and injury risk of light truck impacts with pedestrians in the United States. Accident Analysis & Prevention, 36(2): 295-304.

Li, G., Nie, J., Yang, J. (2012). A study on injuries and kinematics in pedestrian accidents involved minivan and sedan. Proceedings of the 5th International Conference on Expert Symposium Accident Research (ESAR).

Li, G., Yang, J., Simms, C. (2014). Predicting the effects of pedestrian gait on lower limb injuries. Proceedings of the 2014 International Conference on the Biomechanics of Impacts (IRCOBI).

Liers, H., Hannawald, L. (2011). Benefit estimation of secondary safety measures in real-world pedestrian accidents. Proceedings of the 22nd International Conference on the Enhanced Safety of Vehicles (ESV).

Liu, Q., Xia, Y., Zhou, Q., Wang, J.T. (2009). Design analysis of a sandwich hood structure for pedestrian protection. Proceedings of the 21st Conference on the Enhanced Safety of Vehicles (ESV).

Liu, X., Yang, J., Lovsund, P. (2002). A study of influences of vehicle speed and front structure on pedestrian impact responses using mathematical models. Traffic Injury Prevention, 3, 31–42.

Linder, A., Clark, A., Douglas, C., Fildes, B., Yang, K., Sparke, L. (2004). Mathematical modeling of pedestrian crashes: Review of pedestrian models and parameter study of the influence of the sedan vehicle contour, 2004 Road Safety Research, Policing and Education Conference, Perth, Australia.

Lissner, H. R., Lebow, M., Evans, F. G. (1960). Experimental studies on the relation between acceleration and intracranial pressure changes in man. Surgery, Gynecology & Obstetrics, 111, 329-338.

Longhitano, D., Henary, B., Bhalla, K., Ivarsson, J., Crandall, J. (2005). Influence of vehicle body type on pedestrian injury distribution. SAE Technical Paper No. 2005-01-1876.

Lyons, M., Simms, C. (2012). Predicting the influence of windscreen design on pedestrian head injuries. Proceedings of the 2012 International Conference on the Biomechanics of Impacts (IRCOBI).

MADYMO. (2012). Human Body Models Manual Release 7.4.1.

Maeno, T., Hasegawa, J. (2001). Development of a finite element model of the total human model for safety (THUMS) and application to car-pedestrian impacts. Proceedings of the 17th Conference on the Enhanced Safety of Vehicles (ESV).

Malm, S., Krafft, M., Kullgren, A., Ydenius, A., Tingvall, C. (2008). Risk of permanent medical impairment (RPMI) in road traffic accidents. 52nd Annals of Advances in Automotive Medicine (AAAM), pp.93-100.

Marjoux, D., Baumgartner, D., Deck, C., Willinger, R. (2008). Head injury prediction capability of the HIC, HIP, SIMon and ULP criteria-New injury criteria for the head. Accident Analysis & Prevention, 40(3): 1135-1148.

Martin, J. L., Lardy, A., Laumon, B. (2011). Pedestrian injury patterns according to car and casualty characteristics in France. 55th Annals of Advances in Automotive Medicine (AAAM), pp.137-146.

Martinez, L., Guerra, L.J., Ferichola, G., Garcia, A., Yang, J.K. (2007). Stiffness corridors of the European fleet for pedestrian simulation. Proceedings of the 20th Conference on the Enhanced Safety of Vehicles (ESV).

Masson, C., Serre, T., Cesari, D. (2007). Pedestrian-vehicle accident: analysis of 4 full scale tests with PMHS. Proceedings of the 20th Conference on the Enhanced Safety of Vehicles (ESV).

Matsui, Y. (2004). Evaluation of pedestrian subsystem test method using legform and upper legform impactors for assessment of high-bumper vehicle aggressiveness. Traffic injury prevention, 5(1), 76-86.

Matsui, Y. (2005). Effects of vehicle bumper height and impact velocity on type of lower extremity injury in vehicle-pedestrian accidents. Accident Analysis & Prevention, 37 (4): 633-640.

Matsui, Y., Ishikawa, H., Sasaki, A. (1999). Pedestrian injuries induced by the bonnet leading edge in current car-pedestrian accidents. SAE Technical Paper No. 1999-01-0713.

Matsui, Y., Schroeder, G., and Bosch, U. (2004). Injury pattern and response of human thigh under lateral loading simulating car-pedestrian impact. SAE Technical Paper No. 2004-01-1603.

Matsui, Y., Wittek, A., and Konosu, A. (2002). Comparison of pedestrian subsystem safety tests using impactors and full-scale dummy tests. SAE Technical Paper No. 2002-01-1021.

Midi, H., Sarkar, S.K., Rana, S. (2010). Collinearity diagnostics of binary logistic regression model. Journal of Interdisciplinary Mathematics 13(3):253-267.

Mizuno, Y. (2005). Summary of IHRA pedestrian safety working group activities – Proposed test methods to evaluate pedestrian protection offered by passenger cars. Proceedings of the 19th Conference on the Enhanced Safety of Vehicles (ESV).

Mizuno, Y., Ishikawa, H. (2003). Summary of IHRA pedestrian safety working group activities-Proposed test methods to evaluate pedestrian protection offered by passenger cars. Proceedings of the 18th Conference on the Enhanced Safety of Vehicles (ESV).

Mizuno, K., Kajzer, J. (1999). Compatibility problems in frontal, side, single car collisions and car-to-pedestrian accidents in Japan. Accident Analysis & Prevention, 31(4), 381-391.

Mizuno, K., Kajzer, J. (2000). Head injuries in vehicle-pedestrian impact. SAE Technical Paper No. 2000-01-0157.

Mizuno, K., Yonezawa, H., and Kajzer, J. (2001). Pedestrian headform impact tests for various vehicle locations. Proceedings of the 17th Conference on the Enhanced Safety of Vehicles (ESV).

Mo, F., Arnoux, P.J., Cesari, D., Masson, C. (2014). Investigation of the injury threshold of knee ligaments by the parametric study of car-pedestrian impact conditions. Safety Science. 62 (2014), 58-67.

Mo, F., Arnoux, P.J., Jure, J.J., Masson, C. (2012). Injury tolerance of tibia for the car-pedestrian impact. Accident Analysis & Prevention, 46 (2012) 18- 25.

Mo, F., Arnoux, P.J., Zahidi, O., Masson, C. (2013a). Injury thresholds of knee ligaments under lateral-medial shear loading: An experimental study. Traffic Injury Prevention, 14:6, 623-629.

Mo, F., Masson, C., Cesari, D., Arnoux, P.J. (2013b). Coupling lateral bending and shearing mechanisms to define knee injury criteria for pedestrian safety. Traffic Injury Prevention, 14:4, 378-386.

Mo, F. (2012). Towards lower limbs new injury criteria for pedestrian safety based on realistic impact conditions. PhD thesis, Université d'Aix-Marseille, Marseilles, France.

Mohan, D., (2002). Safety and health in Indian cities. Journal of Transport and Infrastructure 9, 79–92.

Nagatomi, K., Hanayama, K., Ishizaki, T., Sasaki, A., Matsuda, K. (2005). Development and full-scale dummy tests of a pop-up hood system for pedestrian protection. Proceedings of the 19th Conference on the Enhanced Safety of Vehicles (ESV).

Nahum, A. M., Smith, R., & Ward, C. C. (1977). Intracranial pressure dynamics during head impact. SAE Technical Paper No. 770922.

NCAC. (2008). Finite element model of Toyota RAV4, model year 1997, version 1. National Crash Analysis Center Vehicle Model Library. http://www.ncac.gwu.edu/vml/models.html.

Neale, M. S., Hardy, B. J., Lawrence, G. J. L. (2003). Development and review of the IHRA (JARI) and TNO pedestrian models. Proceedings of the 18th Conference on the Enhanced Safety of Vehicles (ESV).

Neal-Sturgess, C., Carter, E., Hardy, R., Cuerden, R., Guerra, L., Yang, J. (2007). APROSYS European in-depth pedestrian database. Proceedings of the 20th Conference on the Enhanced Safety of Vehicles (ESV).

Netter, F.H. Carios, A.G. (2003). Interactive atlas of human anatomy version 3.0. Germany.

Newman, J. (1986). A generalised acceleration model for brain injury threshold (GAMBIT). Proceedings of the 1986 International Conference on the Biomechanics of Impacts (IRCOBI).

Newman, J., Shewchenko, N., Welbourne, E. (2000). A proposed new biomechanical head injury assessment function-The maximum power index. SAE Technical Paper No. 2000-01-SC16.

NHTSA. (2012). Traffic Safety Facts 2012: a compilation of motor vehicle crash data from the fatality analysis reporting system and the general estimates system. National Highway Traffic Safety Administration (NHTSA), National Center for Statistics and Analysis, U.S. Department of Transportation, Washington,

DC 20590.

Nie, J., Li, G., Yang, J. (2015). A study of fatality risk and head dynamic response of cyclist and pedestrian based on passenger car accident data analysis and simulations. Traffic Injury Prevention, 16:1, 76-83.

Okamoto, M., Akiyama, A., Takahashi, Y. (2009). Pedestrian dummy pelvis impact responses. SAE Technical Paper No. 2009-01-1214.

Okamoto, Y., Sugimoto, T., Enomoto, K., Kikuchi, J. (2000). Pedestrian head impact conditions depending on the vehicle front shape and its construction-full model simulation. Proceedings of the 2000 International Conference on the Biomechanics of Impacts (IRCOBI).

Otte, D. (1994b). Influence of the front hood length for the safety of pedestrians in car accidents and demands to the safety of small vehicles. SAE Technical Paper No. 942232.

Otte, D. (1994a). Design and structure of the windscreen as part of injury reduction for car occupants, pedestrians and bicyclists. SAE Technical Paper No. 942231.

Otte, D., Haasper, C. (2005). Technical parameters and mechanisms for the injury risk of the knee joint of vulnerable road users impacted by cars in road traffic accidents. Proceedings of the 2005 International Conference on the Biomechanics of Impacts (IRCOBI).

Otte, D., Haasper, C. (2007). Characteristics on fractures of tibia and fibula in car impacts to pedestrians and bicyclists-influences of car bumper height and shape. 51st Annals of Advances in Automotive Medicine, pp.63-79.

Otte, D., Pohleman, T. (2001). Analysis and load assessment of secondary impact to adult pedestrians after car collisions on roads. Proceedings of the 2001 International Conference on the Biomechanics of Impacts (IRCOBI).

Pal, C., Okabe, T., Vimalathithan, K., Manoharan, J., Shinada, M. (2015). Effect of vehicle's front end profile on pedestrian's lower extremity injury pattern in real world and verification by large male FE human model. SAE Technical Paper No. 2015-01-1467.

Paas, R., Davidsson, J., Masson, C., Sander, U., Brolin, K., Yang, J. (2012). Pedestrian shoulder and spine kinematics in full-scale PMHS tests for human body model evaluation. Proceedings of the 2012 International Research Council on the Biomechanics of Injury (IRCOBI).

Paas, R., Masson, C., Davidsson, J. (2015). Head boundary conditions in pedestrian crashes with passenger cars: six-degrees-of-freedom post-mortem human subject responses. International Journal of Crashworthiness, 20(6), 547-559.

Payne, A.R., Patel, S. (2001). Occupant Protection & Egress in Rail Systems (OPERAS) Project 427519. http://www.eurailsafe.net/subsites/operas. MIRA, 2001, Date accessed: 27 September 2014.

Peng, Y., Chen, Y., Yang, J., Otte, D., Willinger, R. (2012a). A study of pedestrian and bicyclist exposure to head injury in passenger car collisions based on accident data and simulations. Safety science, 50(9), 1749-1759.

Peng, Y., Deck, C., Yang, J., Willinger, R. (2012b). Effects of pedestrian gait, vehicle-front geometry and impact velocity on kinematics of adult and child pedestrian head. International Journal of Crashworthiness, 17:5, 553-561.

Peng, Y., Han, Y., Chen, Y., Yang, J.K., Willinger, R. (2012c). Assessment of the protective performance of hood using head FE model in car-to-pedestrian collisions. International Journal of Crashworthiness 17(4), pp.415-423.

Petit, P., Trosseille, X., Dufaure, N., Dubois, D., Potier, P., Vallancien, G. (2014). The effect of upper body mass and initial knee flexion on the injury outcome of post mortem human subject pedestrian isolated legs. Stapp Car Crash Journal, 58, 197.

Phelps, J. B., Hubbard, G. B., Wang, X., Agrawal, C. M. (2000). Microstructural heterogeneity and the fracture toughness of bone. Journal of Biomedical Materials Research, 51(4), 735-741.

Pinecki, C., Zeitouni, R. (2007). Technical solutions for enhancing the pedestrian protection. Proceedings of the 20th Conference on the Enhanced Safety of Vehicles (ESV).

Pritz, H., Hassler, C., Herridge, J., Weis, E. (1975). Experimental study of pedestrian injury minimization through vehicle design. SAE Technical Paper No. 751166.

Pritz, H., Pereira, J. (1983). Pedestrian hip impact simulator development and hood edge location consideration on injury severity. SAE Technical Paper No. 831627.

Ramet, M., Bouquet, R., Bermond, F., Caire, Y. (1995). Shearing and bending effects at the knee joint tests in quasi-static lateral load. Proceedings of the 1995 International Conference on the Biomechanics of Impacts (IRCOBI).

Renaud, F., Tapia, F. (2004). Development of a mechanical neck for a 6-year-old pedestrian dummy. MSc thesis, Chalmers University of Technology, Göteborg, Sweden.

Rosén, E., Sander, U. (2009). Pedestrian fatality risk as a function of car impact speed. Accident Analysis & Prevention, 41(3):536-42.

Roudsari, B., Mock, C., and Kaufmann, R. (2005). An evaluation of the association between vehicle type and the source and severity of pedestrian injuries. Traffic Injury Prevention 6, 185-192.

Schmitt, K.U., Niederer, P.F., Muser, M.H., Walz, F. (2010). Trauma biomechanics. Third edition, Springer.

Schuster, P. (2006). Current trends in bumper design for pedestrian impact. SAE Technical Paper No. 2006-01-0464.

Shea, M., Wittenberg, R., Edwards, W., White, A., Hayes, W. (1992). In vitro hyperextension injuries in the human cadaveric cervical spine. Journal of Orthopaedic Research, 10(6), 911-916.

Simms, C., Ormond, T., Wood, D. (2011). The influence of vehicle shape on pedestrian ground contact mechanisms. Proceedings of the 2011 International Conference on the Biomechanics of Impacts (IRCOBI).

Simms, C., Wood, D. (2006a). Effects of pre-impact pedestrian position and motion on kinematics and injuries from vehicle and ground contact. International Journal of Crashworthiness, 11(4), 345-355.

Simms, C., Wood, D. (2006b). Pedestrian risk from cars and sport utility vehicles-a comparative analytical study. Proceedings of the Institution of Mechanical Engineers, Part D: Journal of automobile engineering, 220(8), 1085-1100.

Simms, C., Wood, D. (2009). Pedestrian and cyclist impact: a biomechanical perspective (Vol. 166). Springer Science & Business Media.

Shigeta, K., Kitagawa, Y., Yasuki, T. (2009). Development of next generation human FE model capable of organ injury prediction. Proceedings of the 21st International Technical Conference on the Enhanced Safety of Vehicles Conference (ESV).

Shin, J., Lee, S., Kerrigan, J., Darvish, K., Crandall, J., Akiyama, A., Takahashi, Y., Okamoto, M., Kikuchi, Y. (2006). Development and validation of a finite element model for the Polar II upper body. SAE Technical Paper No. 2006-01-0684.

Snedeker, J. G., Walz, F. H., Muser, M. H., Lanz, C., Schroeder, G. (2005). Assessing femur and pelvis injury risk in car-pedestrian collisions: comparison of full body PMTO impacts, and a human body finite element model. Proceedings of the 19th International Technical Conference on the Enhanced Safety of Vehicles Conference (ESV).

Sobotta, J. (1997). Atlas der Anatomie des Menschen. Band 1 & 2, Urban und Schwarzenberg; München, Germany.

Solomon, D.H., Simel, D.L., Bates, D.W., Katz, J.N., Schaffer, J.L. (2001). Does this patient have a torn meniscus or ligament of the knee? Value of the physical examination. JAMA. 2001; 286(13):1610-1620.

Strandroth, J., Rizzi, M., Sternlund, S., Lie, A., Tingvall, C. (2011). The correlation between pedestrian injury severity in real-life crashes and Euro NCAP pedestrian test results. Traffic injury prevention, 12(6), 604-613.

Subramanian, H., Göhlich, D., Mukherjee, S., Chawla, A. (2012). A bio-mechanics based methodology to optimize vehicle front profile for pedestrian safety, Proceedings of 10th International Symposium on Biomechanics and Biomedical Engineering.

Subramanian, H., Chawla, A., Mukherjee, S., Goehlich, D. (2016). Optimisation study on multibody vehicle-front model for pedestrian safety. International Journal of Crashworthiness, 21(1), 63-78.

TABC. (2010-2015). Statistics of Road Traffic Accidents in P.R. of China. Traffic Administration Bureau of China, Ministry of Public Security, Beijing, P.R. China. (In Chinese).

Takahashi, Y., Okamoto, M., Akiyama, A., Kikuchi, Y. (2009). Estimation of knee ligament injury measures for a pedestrian dummy. SAE Technical Paper No. 2009-01-1212.

Takahashi, Y., Kikuchi, Y., Konosu, A., Ishikawa, H. (2000). Development and validation of the finite element model for the human lower limb of pedestrians. Stapp Car Crash Journal, 44, pp.335-355.

Takhounts, E.G., Craig, M.J., Moorhouse, K., McFadden, J., Hasija, V. (2013). Development of brain injury criteria (BrIC). Stapp Car Crash Journal, 57, pp.243-266.

Takhounts, E.G., Eppinger, R.H., Campbell, J.Q., Tannous, R.E., Power, E.D., Shook, L.S. (2003). On the development of the SIMon finite element head model. Stapp Car Crash Journal, 47, pp.107-133.

Takhounts, E. G., Hasija, V., Ridella, S. A., Rowson, S., & Duma, S. M. (2011, June). Kinematic rotational brain injury criterion (BRIC). Proceedings of the 22nd Enhanced Safety of Vehicles Conference (ESV).

Talantikite, Y, Brun-Cassan, F, Lecoz, J, Tarriere, C. (1993). Abdominal injury protection in side impact-injury mechanisms and protection criteria. Proceedings of the 1993 International Conference on the Biomechanics of Impacts (IRCOBI).

Tandeter, H., Shvartzman, P., Stevens, M. (1999). Acute knee injuries: use of decision rules for selective radiograph ordering. American Family Physician, 60(9), 2599-2608.

Tefft, B.C. (2013). Impact speed and a pedestrian's risk of severe injury or death. Accident Analysis & Prevention, 50: 871-878.

The-Blueprints, 2015. http://www.the-blueprints.com/. Date accessed: 18th December 2015.

Tinard, V., Bourdet, N., Deck, C., Willinger, R. (2007). Active pedestrian head protection against windscreen. Proceedings of the 20th Enhanced Safety of Vehicles Conference (ESV).

Toyota Motor Corporation. (2011). THUMS User's Manual.

UNECE. (2007). Proposed draft global technical regulation (GTR) on pedestrian protection. http://unece.org/trans/doc/2004/wp29grsp/ps-116.pdf.

Untaroiu C, Darvish K, Crandall J, Deng B, Wang J. (2005) A Finite Element Model for the Lower Limb for Simulating Pedestrian Impacts. Stapp Car Crash Journal, Vol. 49, pp.157–181.

Untaroiu, C., Meissner, M., Crandall, J., Takahashi, Y., Okamoto, M., Ito, O. (2009). Crash reconstruction of pedestrian accidents using optimization techniques. International Journal of Impact Engineering, 36, 2, 210-219.

Van Rooij, L., Bhalla, K., Meissner, M., Ivarsson, J., Crandall, J., Longhitano, D., Kikuchi, Y. (2003). Pedestrian crash reconstruction using multi-body modeling with geometrically detailed, validated vehicle models and advanced pedestrian injury criteria. Proceedings of the 18th International Technical Conference on the Enhanced Safety of Vehicles (ESV).

Vary Mutation and Crossover. (2016). http://uk.mathworks.com/help/gads/vary-mutation-and-crossover.html. Date accessed: 10th January 2016.

Versace, J. (1971). A review of the severity index. SAE Technical Paper No. 710881.

Viano, D, Lau, I, Asbury, C., King, A, Begeman, P. (1989). Biomechanics of the human chest, abdomen, and pelvis in lateral impact. Accident Analysis & Prevention, 21(6):553-574.

Watanabe, R., Miyazaki, H., Kitagawa, Y., Yasuki, T. (2011). Research of collision speed dependency of pedestrian head and chest injuries using human FE model (THUMS version 4). Proceedings of the 22nd International Technical Conference on the Enhanced Safety of Vehicles Conference (ESV).

WHO. (2013). Global Status Report on Road Safety: Time for Action. World Health Organization, Geneva.

Willinger, R., Baumgartner, D. (2003). Human head tolerance limits to specific injury mechanisms. Journal of Crashworthiness 8(6), 605–616.

World Bank Group. (2011). Road Safety. http://www.worldbank.org/ transport/ roads/safety.htm.

Yang, J. (2005). Review of injury biomechanics in car-pedestrian collisions. International Journal of Vehicle Safety, 1(1-3), pp.100-117.

Yang, J. (2011). Investigation of brain trauma biomechanics in vehicle traffic accidents using human body computational models. Computational Biomechanics for Medicine, pp 5-14.

Yang, J., Lovsund, P. (1997). Development and validation of a human-body mathematical model for simulation of car-pedestrian impacts. Proceedings of the 1997 International Conference on the Biomechanics of Impacts (IRCOBI).

Yang, J., Otte, D. (2007). A comparison study on vehicle traffic accident and injuries of vulnerable road users in China and Germany. Proceedings of the 20th International Technical conference on the Enhanced Safety of Vehicles (ESV).

Yang, J., Xu, W., Otte, D. (2008). Brain injury biomechanics in real world vehicle accident using mathematical models. Chinese Journal of Mechanical Engineering, 32 (4): 81-86.

Yang, K.H., Hu, J., White, N.A., King, A.I. (2006). Development of numerical models for injury biomechanics research: A review of 50 years of publications in the Stapp Car Crash Conference. Stapp Car Crash Journal, Vol. 50 (November 2006), pp.429-490.

Yao, J., Yang, J., Fredriksson, R. (2011). Development of a pedestrian dummy FE model for the design of pedestrian friendly vehicles. International Journal of Vehicle Design. Vol. 57 (2011), 2/3, p. 254-274.

Yao, J., Yang, J., Otte, D. (2008). Investigation of head injuries by reconstructions of real-world vehicle-versus-adult-pedestrian accidents. Safety Science, 46(7): 1103-1114.

Yasuki, T. (2007a). Mechanism analysis of pedestrian knee-bending angle by sedan-type vehicle using human FE model. International Journal of Crashworthiness, 12:4, 329-339.

Yasuki, T. (2007b). Mechanism analysis of pedestrian knee-bending angle by SUV type vehicles using human FE model. International Journal of Crashworthiness, 12:6, 645-651.

Yoganandan, N., Pintar, F., Sances, A., Walsh, P., Ewing, C., Thomas, D., Snyder, R. (1995). Biomechanics of skull fracture. Journal of Neurotrauma. 12(4), 658–668.

Zhang, G., Cao, L., Hu, J., Yang, K. (2008). A field data analysis of risk factors affecting the injury risks in vehicle-to-pedestrian crashes. 52nd Annals of Advances in Automotive Medicine (AAAM), pp.199-214.

Appendix

Table A.1 Information for VTSs with different STS sizes (impact scenarios).

Test	VTS name	Number of vehicle impact speed	Number of pedestrian height	Number of pedestrian gait stance	Number of impact scenario
1	VTS-12-10-10/1200	12	10	10	1200
2	VTS-12-10-6/720	12	10	6	720
3	VTS-12-10-4/480	12	10	4	480
4	VTS-12-7-10/840	12	7	10	840
5	VTS-12-7-6/504	12	7	6	504
6	VTS-12-7-4/336	12	7	4	336
7	VTS-12-5-10/600	12	5	10	660
8	VTS-12-5-6/360	12	5	6	360
9	VTS-12-5-4/240	12	5	4	240
10	VTS-9-10-10/900	9	10	10	900
11	VTS-9-10-6/540	9	10	6	540
12	VTS-9-10-4/360	9	10	4	360
13	VTS-9-7-10/630	9	7	10	630
14	VTS-9-7-6/378	9	7	6	378
15	VTS-9-7-4/252	9	7	4	252
16	VTS-9-5-10/450	9	5	10	450
17	VTS-9-5-6/270	9	5	6	270
18	VTS-9-5-4/180	9	5	4	180
19	VTS-6-10-10/600	6	10	10	600
20	VTS-6-10-6/360	6	10	6	360
21	VTS-6-10-4/240	6	10	4	240
22	VTS-6-7-10/420	6	7	10	420

23	VTS-6-7-6/252	6	7	6	252
24	VTS-6-7-4/168	6	7	4	168
25	VTS-6-5-10/300	6	5	10	300
26	VTS-6-5-6/180	6	5	6	180
27	VTS-6-5-4/120	6	5	4	120
28	VTS-6-3-4/72	6	3	4	72
29	VTS-6-5-2/60	6	5	2	60
30	VTS-6-5-1/30	6	5	1	30
31	VTS-6-3-2/36	6	3	2	36
32	VTS-3-5-4/60	3	5	4	60
33	VTS-3-3-4/36	3	3	4	36
34	VTS-3-3-2/18	3	3	2	18
35	VTS-3-3-1/9	3	3	1	9

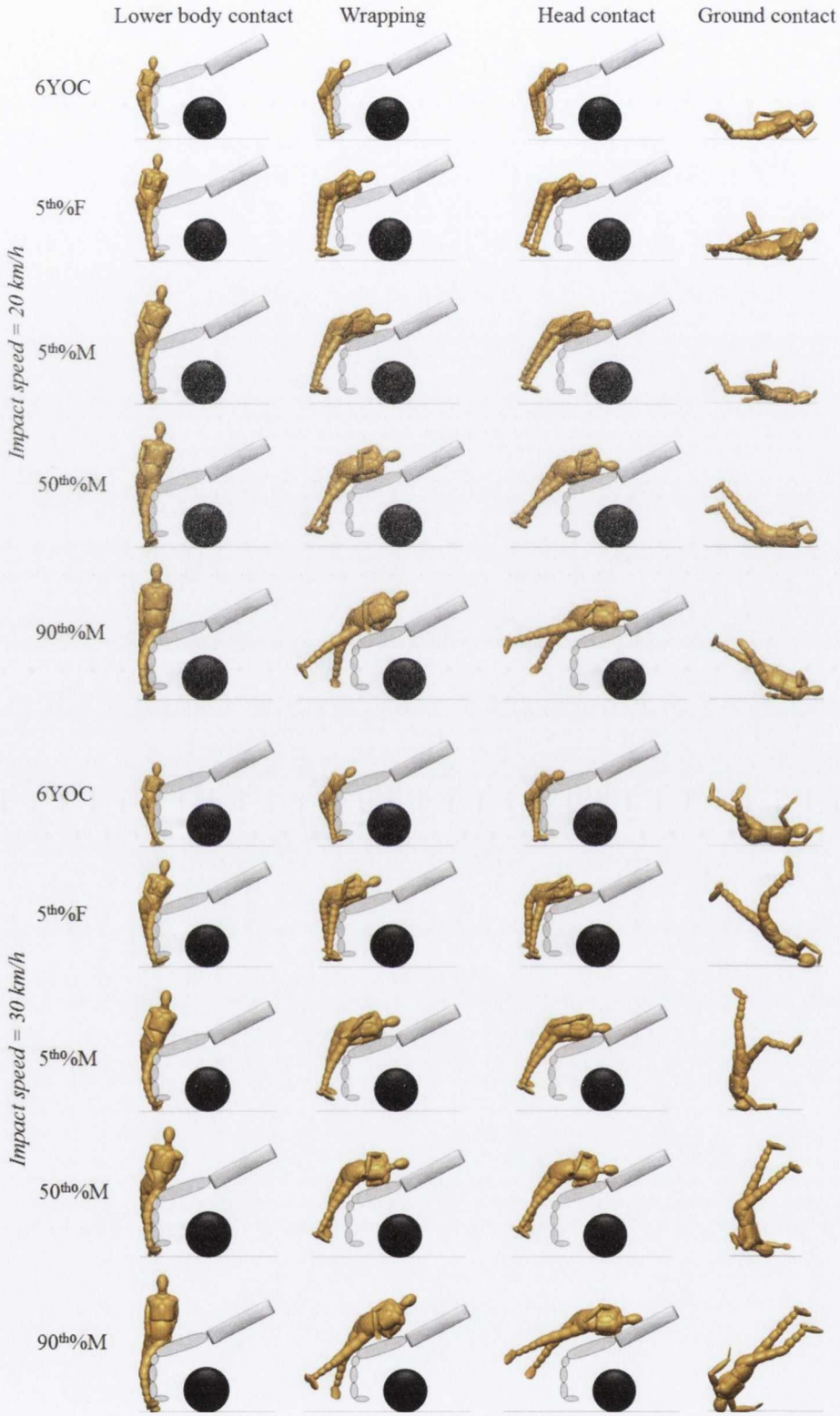
Lower body contact
Wrapping
Head contact
Ground contact
Impact speed = 20 km/h
6YOC
5th%F
5th%M
50th%M
90th%M
Impact speed = 30 km/h
6YOC
5th%F
5th%M
50th%M
90th%M

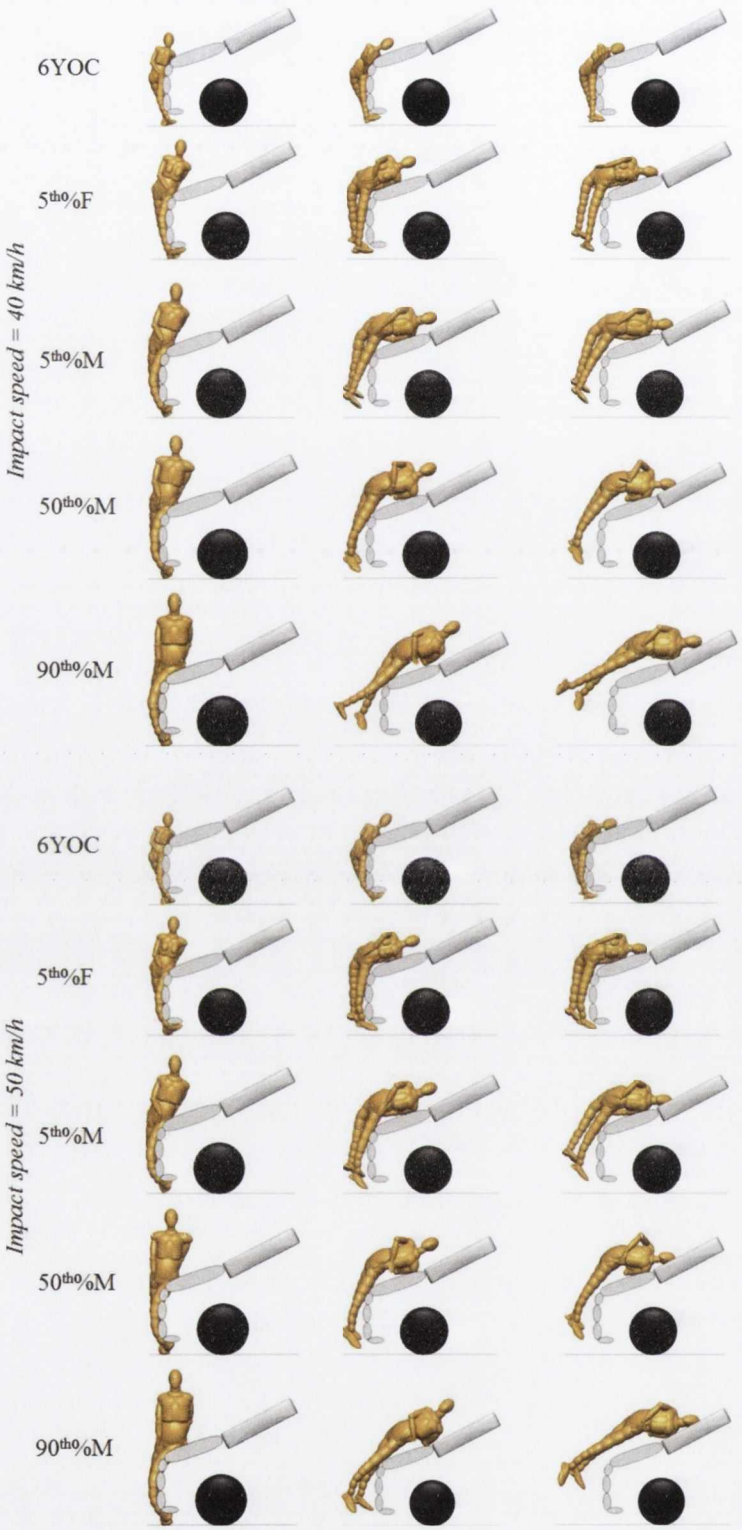
Impact speed = 40 km/h
6YOC
5th%F
5th%M
50th%M
90th%M
Impact speed = 50 km/h
6YOC
5th%F
5th%M
50th%M
90th%M

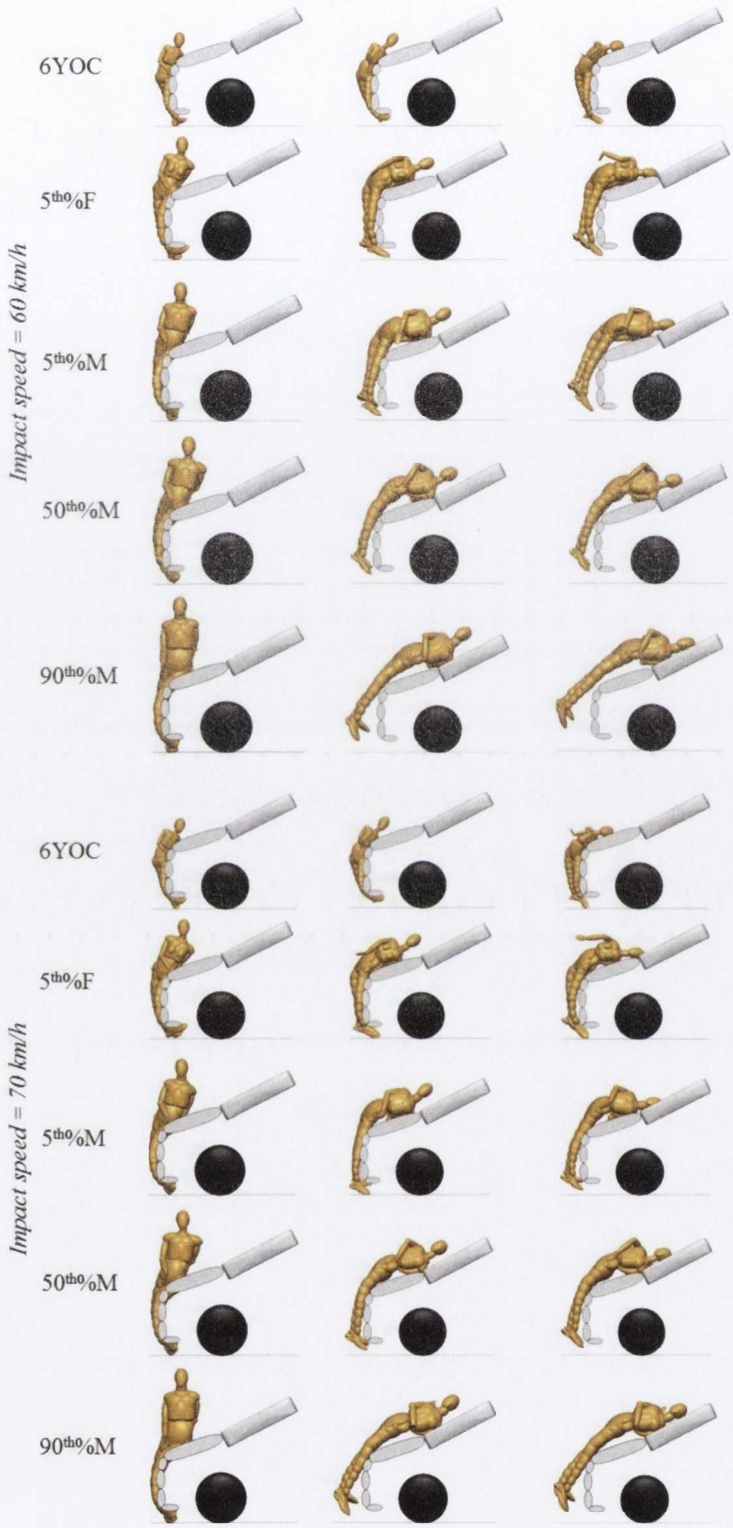

Figure A.1 Kinematics of different pedestrian models struck by the optimal sedan front at different impact speeds.

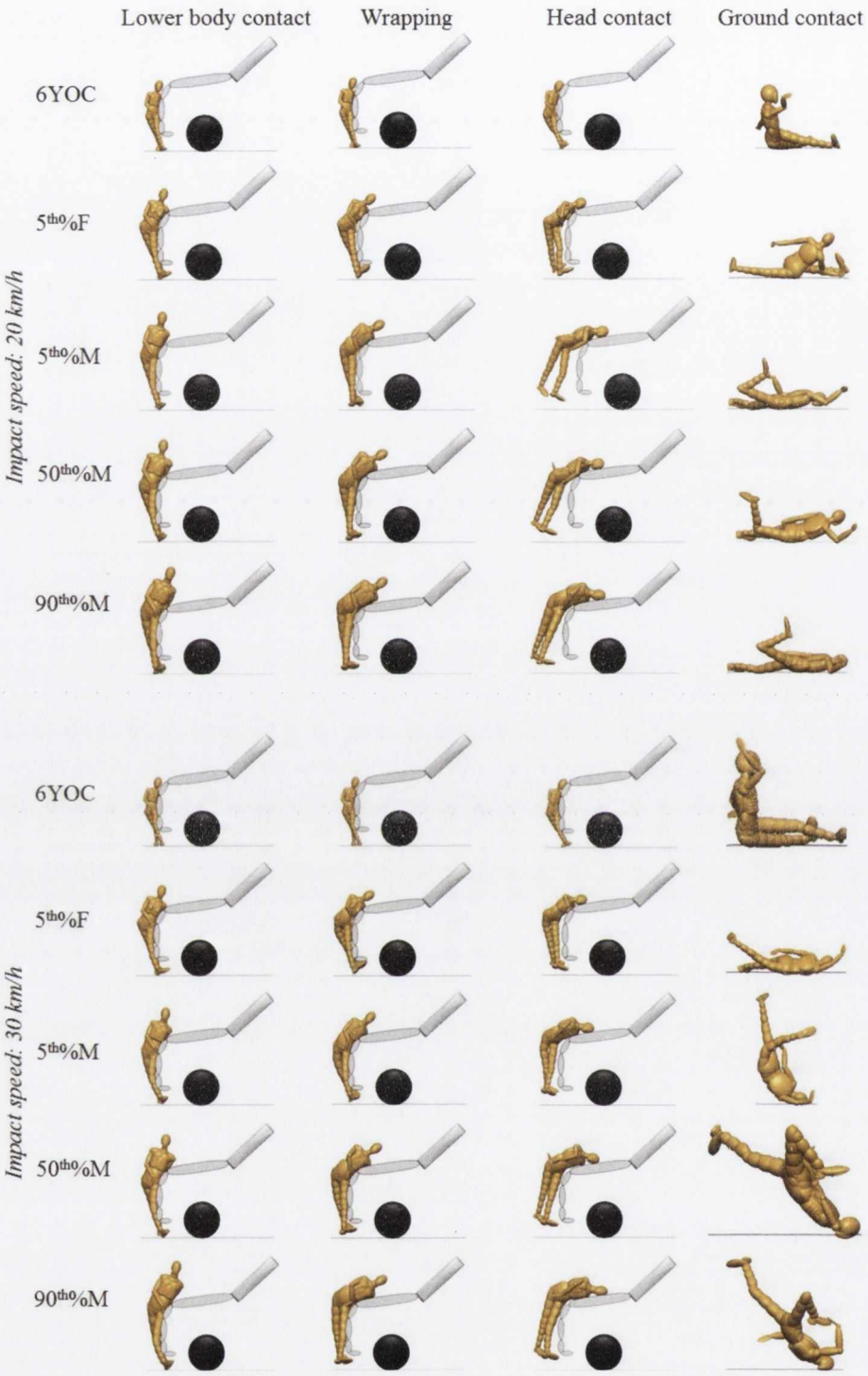
Lower body contact
Wrapping
Head contact
Ground contact
Impact speed: 20 km/h
6YOC
5th%F
5th%M
50th%M
90th%M
Impact speed: 30 km/h
6YOC
5th%F
5th%M
50th%M
90th%M

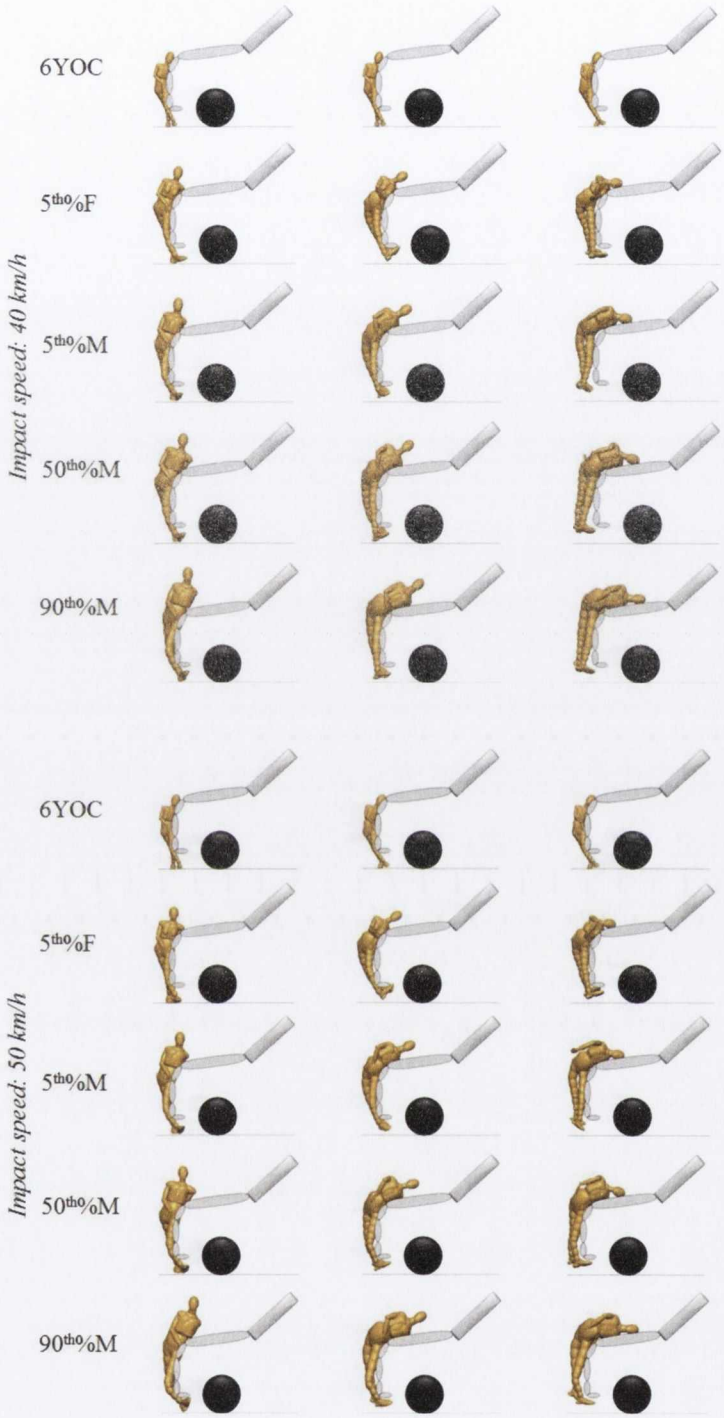
Impact speed: 40 km/h
6YOC
5th%F
5th%M
50th%M
90th%M
Impact speed: 50 km/h
6YOC
5th%F
5th%M
50th%M
90th%M

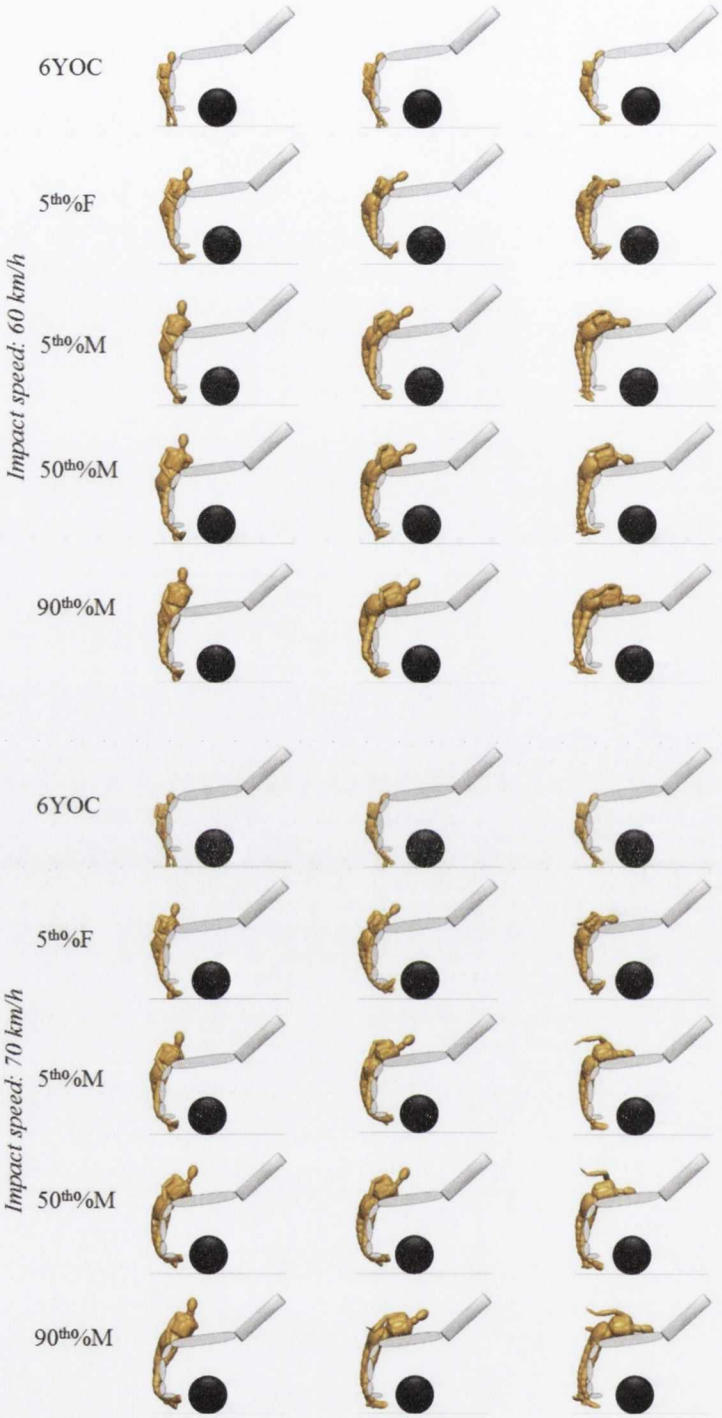

Figure A.2 Kinematics of different pedestrian models struck by the optimal SUV front at different impact speeds.

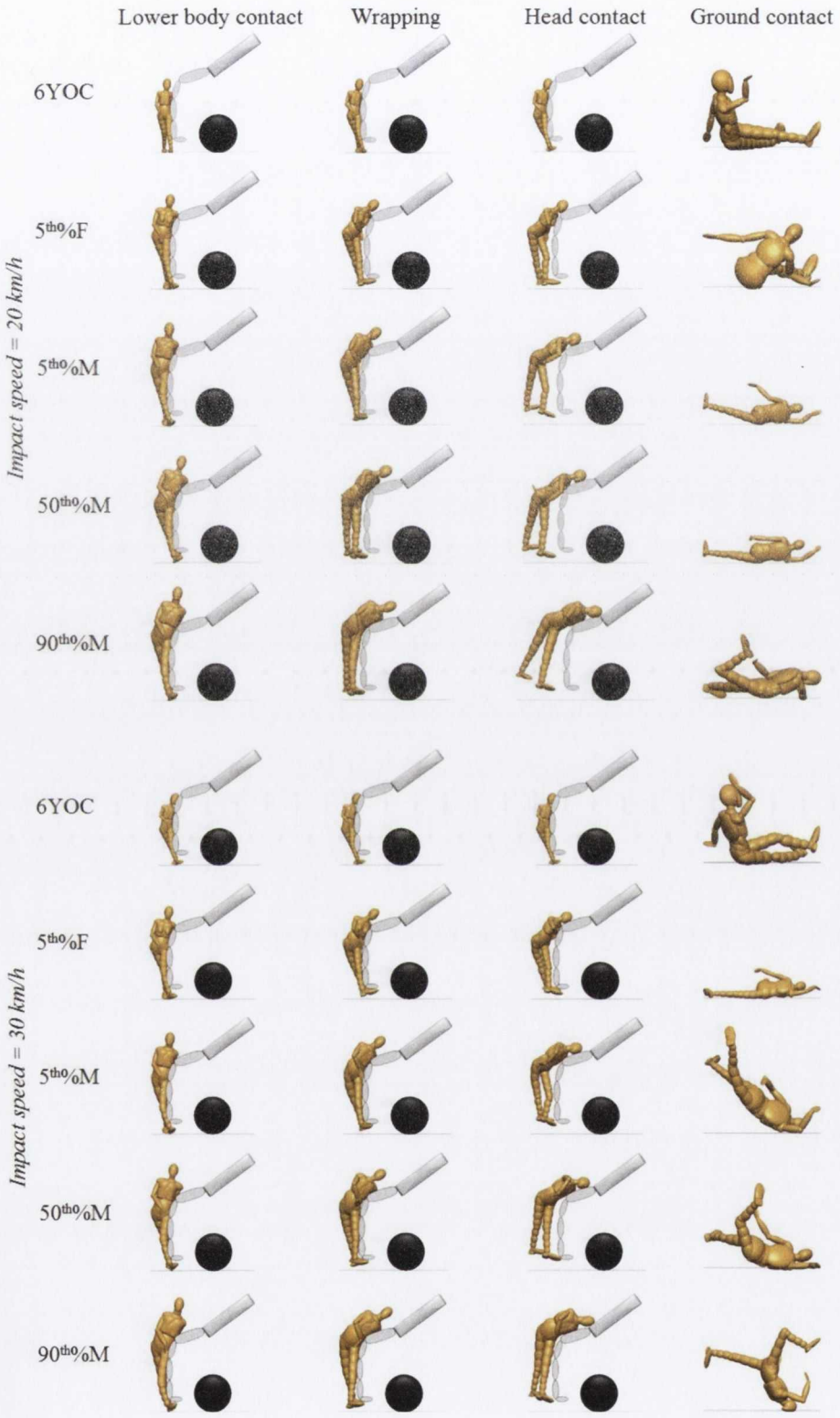
Lower body contact
Wrapping
Head contact
Ground contact
Impact speed = 20 km/h
6YOC
5th%F
5th%M
50th%M
90th%M
Impact speed = 30 km/h
6YOC
5th%F
5th%M
50th%M
90th%M

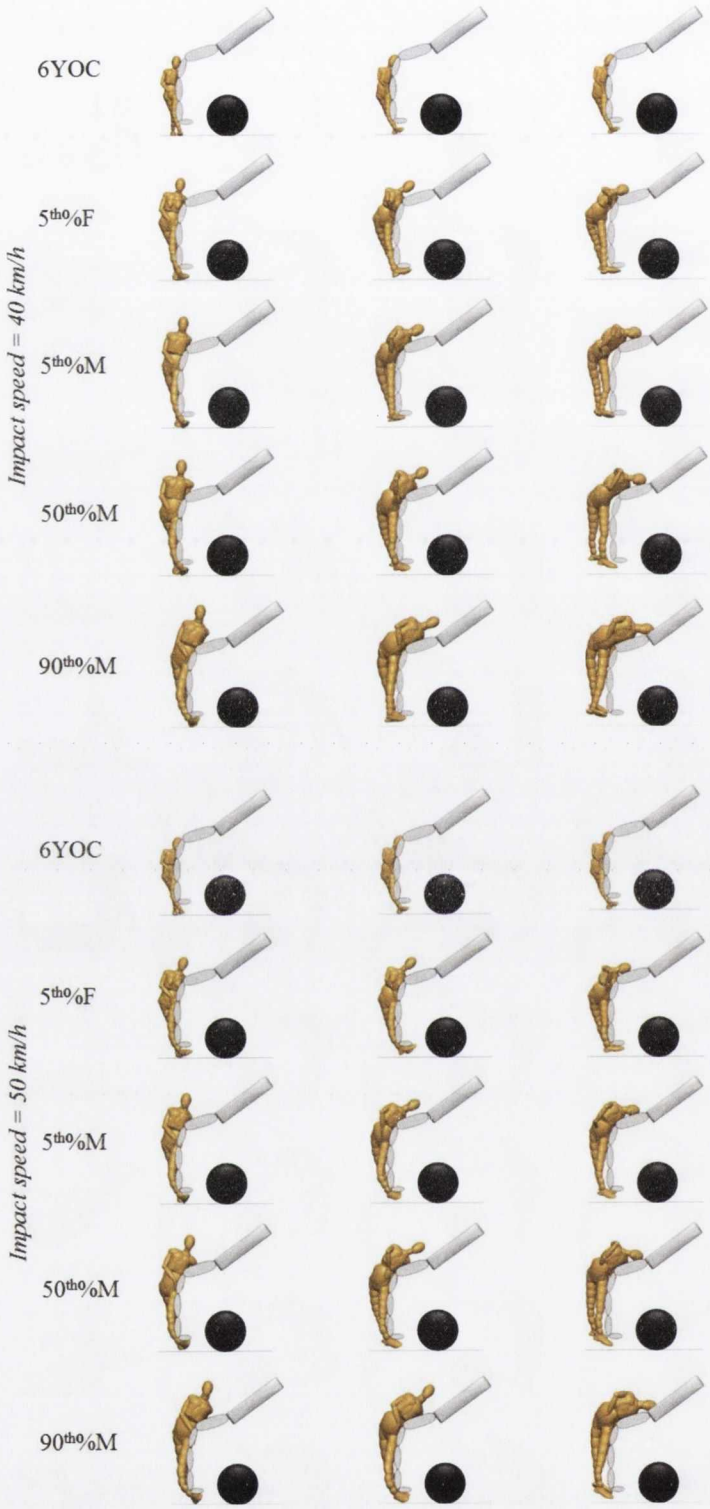
Impact speed = 40 km/h
6YOC
5th%F
5th%M
50th%M
90th%M
Impact speed = 50 km/h
6YOC
5th%F
5th%M
50th%M
90th%M

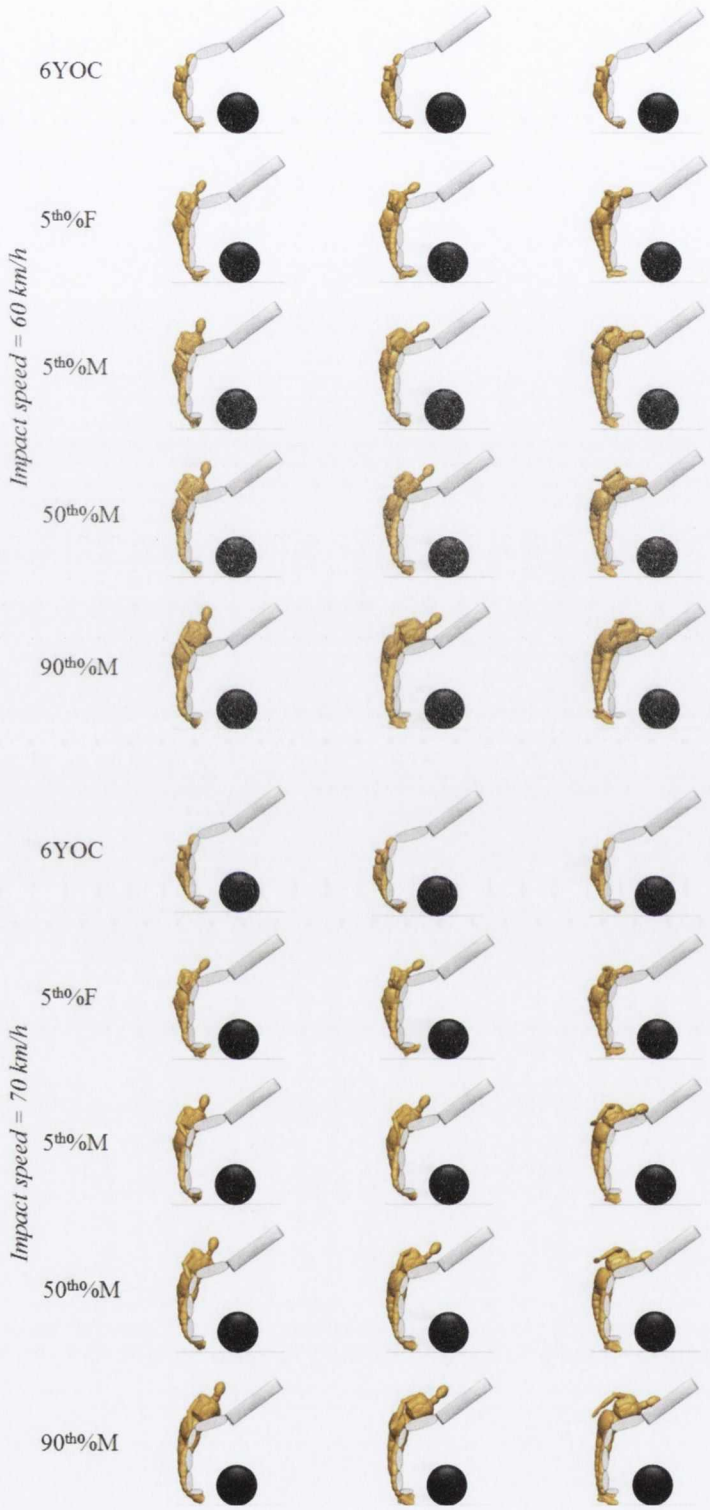

Figure A.3 Kinematics of different pedestrian models struck by the optimal van front at different impact speeds.